Global Automatic Telescopes Exploring the Sun (GATES): Building a New Network for Synoptic Space Weather Observation

by

Fallon Patrice Konow

XXXVIII cycle

Under the Direction of **Prof. Francesco Berrilli**, **Dr. Petrus Martens**
Dr. Neil Murphy, and **Dr. Stuart M. Jefferies**

A Dissertation Submitted in Partial Fulfillment of the Requirements for the Degree of

Doctor of Philosophy Astronomy

in the College of Arts and Sciences Georgia State University

and

Doctor of Philosophy of Astronomy, Astrophysics, and Space Sciences

in the Department of Physics "Sapienza Università di Roma"

ABSTRACT

This dissertation is an effort to add to technology for space weather monitoring and prediction through the introduction of a new network of ground-based telescopes. This network, Global Automatic Telescopes Exploring the Sun (GATES), currently consists of two nodes, the Tor Vergata Synoptic Solar Telescope (TSST) and the Mojave Solar Observatory (MSO). Both instruments are designed as low-cost, robotic facilities that use Magneto-Optical Filter (MOF)-based instruments to acquire full-disk, simultaneous line-of-sight (LoS) velocity and magnetic field maps (Dopplergrams and magnetograms, respectively). The TSST employs two channels: a potassium K I D1 769.6 nm centered MOF for photospheric Doppler- and magnetogram observations and a narrowband Hα Daystar telescope for chromospheric intensity images. MSO consists of a dual-MOF-based telescope with channels centered on K I D1 769.6 nm and sodium Na I D2 589.0 nm for photospheric and low-chromospheric Doppler- and magnetogram observations, respectively. Additionally, the GATES team at MSO has developed and tested a helium He I 1083 nm MOF for probing the velocity and magnetic field dynamics of the upper chromosphere. The two active GATES nodes are mounted at locations separated by $\sim$150° of longitude to enable near-synoptic observations to contribute to solar physics research and space weather monitoring/prediction. To show a proof-of-concept for this multi-nodal MOF-based network, GATES conducted a successful three-phase observing campaign during the summer of 2025: Phase 1: dual-site observing with the TSST and MSO, Phase 2: extended dual-height observing with MSO, and Phase 3: He MOF observing. Overall, this dissertation details the design, construction, preliminary observing campaign, and novel developments of the GATES Network. The success of the dual-site GATES observing run and the He I 1083 nm observations exhibits the notable impact the GATES Network can have on solar physics and space weather research.

INDEX WORDS: Heliophysics, Space Weather, Synoptic Telescope, Solar Instrumentation, Magneto-Optical Filter, Dopplergram, Magnetogram, Helium 1083

Global Automatic Telescopes Exploring the Sun [GATES]: Building a New Network for Synoptic Space Weather Observation

by

Fallon Patrice Konow

Committee Chair:	Fabien Baron
Committee:	Viacheslav Sadykov
	Benedetta Vulcani
	Mario Zannoni

Electronic Version Approved:

Office of Graduate Studies

College of Arts and Sciences

Georgia State University

March 2026

DEDICATION

To all the boy bands of the world: every day, I consider how much more of this dissertation I'd remember if my brain weren't full of your lyrics (but nonetheless, thank you for helping me get through it).

ACKNOWLEDGMENTS

Forgive me if my acknowledgments are twice as long as normal; with a cotutelle, I have twice as many people to thank.

I acknowledge the multiple funding sources that have supported me and my work throughout the past six years. The 2nd Century Initiative Fellowship, which funded my initial work at GSU; the Georgia Space Grant Consortium, which funded my internship at JPL; the Georgia State University Dissertation Grant, which funded parts for the MSO telescope; the AASS PhD, which funded my stipend and travel while in Rome, and the NASA FINESST Fellowship (award #80NSSC24K1872), which funded my stipend, travel, and instrumentation parts during the final 2 years of my PhD. Additionally, I'd like to give a special acknowledgment to the California Department of Forest and Fire Protection for all of their hard work fighting the January 2025 Southern California wildfires.

To my absolute squad of supervisors, Francesco, Luca, Neil, Piet, Stuart, and Wayne: thank you for agreeing to take part in my quest for a PhD in two countries; I am honored to have gotten to learn from all of you. Francesco, thank you for taking on a crazy American student and providing me the opportunity to join the amazing group out at UTOV. Luca, thank you for all you have taught me in the lab and your support throughout my time in Italy. Neil, thank you for taking on an instrumentation student in the height of COVID, your constant support both academically and in life out in CA, and always encouraging me to find balance in work and life. Piet, thank you for taking on an extra student when Stuart

was on leave and dealing with the extra work that came along with a dual-internationally-enrolled project. Stuart, thank you for starting me on this instrumentation journey, for always encouraging me to captain my own ship, and doing everything in your power to help me reach my destination. Wayne, thank you for opening up your workshop and home to me; you have allowed me to have an incredibly unique PhD project.

To the rest of my committee members, Fabien and Meredith: thank you for rounding out my PhD career. Fabien, thank you for continually being a supportive presence. Meredith, thank you for agreeing to serve on a PhD committee for a PhD topic outside your field and for being such an aspirational mentor. To my first advisor Seth, thank you for introducing me to research and being with me for every step in my research journey so far. To Don: thank you for your tireless help with all things MSO-related; without you, I'm sure everything I've done would've taken 10x longer.

To my GSU cohortmates, Aman, Dan, Emma, Julian, and Varun: thank you for supporting me even through my atrocious spelling errors, horrendously spaced code, and continuing 2D presence. Emma and Julia, thank you for being my grad school day ones and my boots-on-the-ground at GSU whenever I wasn't there. Varun, thank you for being my research twin, answering all my last-minute questions, for all of your help with my code/solar understanding, and keeping me sane. Aatiya, thank you for being my conference buddy and always being willing to read over everything I write. Andrew, thank you for being an amazing AstroPAL, helping me find my place as a grad student in the crazy time of COVID, and checking in on me even when I was no longer a baby grad. Aparna, thank you for

your MOF-based support on all fronts. Deborah, thank you for letting me cry to you about instrumentation and always making sure I knew I could do it. Justin, thank you for being a support both as a fellow grad student and as a professor, supporting my career aspirations. To all of the other GSU grads I have had the pleasure of working alongside, whether it be in 2 or 3D, thank you for showing me how supportive our field can be, even across oceans.

To my UTOV Solar and Space Sciences group, Andrea, Archana, Letizia, Matteo, Raffaele, Ronish, Simone, and Simone: thank you for being my support when I was far from home and struggling through PhD work; I think you guys made me crazier, but in the best possible way. Andrea, thank you for embarking on the journey of building a telescope with me and dealing with my constant, incredibly dumb instrument questions. Archana, thank you for being such an amazing support system, no matter where we both are: in the lab, in Italy, in the US, and even from India. Letizia, thank you for bringing joy into the lab and providing much-needed balance in my work/life. Matteo, thank you for brightening my days and always being a supportive presence. Raffaele, thank you for continually helping me complete administrative tasks and always reminding me to worry less. To all of the other AASS PhD grads, thank you for putting up with my Americanness and lack of Italian; you were all really too kind to me.

To my day one astronomy family, WesAstro (Rogue Addition), Ben, Gil, Kim, and Hunter: I can't imagine better people to have started my astronomy journey with. Thank you for always making me laugh and continuing to study and hang out with me even when we went our separate ways in grad school. Kim, thank you for being my support system out

in California; from picking me up when I first arrived, Zoom study sessions, and everything in between, you and Tom have been an integral part of my PhD.

To all of my friends who have helped me along the way – Lucy, Shannon, Lauren, Mandy, Sarah, Sarah, Emma, Kelsey, and so many others – thank you for sticking with me, keeping me sane during my crazy academic endeavors, providing me wake up calls, and always pretending you care about what I was saying when I talked about work.

Most importantly, to my amazing family: Courtney, Vlad, Sebastian, and Aurelia: thank you for letting me stay with you for my first year of grad school and whenever I needed in a pinch. I would not have made it through this degree or life without you. Johnny, Jalyn, and Kieran: thank you for being people to look up to and compete with for best email signature. Every day you inspire me to follow my dreams. Kara and Dillon: thank you for keeping me sane in my (many) times of distress and being my first astronomy teachers. You are a support I can always count on. Audrey and Sean: thank you for always being there whenever I'm floundering, whether I realize it or not, and knowing exactly what I need. I am forever grateful I was put on this Earth a twin. Mom and Dad: thank you for tirelessly supporting and encouraging me throughout my life, no matter what I chose to do. You've shown me what hard work and dedication are and instilled in me a sense of curiosity. I can never thank you enough for all you have done and continue to do for me.

Finally, to everyone past, present, and future reading this, whoever you are: thank you for believing in me and my work enough to open my dissertation. Please know that if I could do it, you can too.

"Remember kids, the only difference between screwing around and science is writing it down."

-Adam Savage, *Mythbusters*

TABLE OF CONTENTS

LIST OF TABLES

LIST OF FIGURES

LIST OF ABBREVIATIONS

AI/ML	Artificial Intelligence / Machine Learning
AIA	Atmospheric Imagining Assembly
AR	Active Region
AU	Astronomical Unit
BiSON	Birmigham Solar-Oscillations Network
BBSO	Big Bear Solar Observatory
BS	BeamSplitter
BW	Blue Wing
CAD	Computer Aided Design
CCD	Charge-Coupled Device
CME	Coronal Mass Ejection
CMOS	Complementary Metal-Oxide Semiconductor
DKIST	Daniel K. Inouye Solar Telescope
DT	Display Tech
EB	Ellerman Bomb
ESA	European Space Agency
EUV	Extreme UltraViolet
FADOF	Faraday Anomalous Dispersion Optical Filters
FFT	Fast Fourier Transform
FINESST	Future Investigators in NASA Earth and Space Science and Technology
FOV	Field of View
FPI	Fabry Pérot Interferometer
FWHM	Full Width at Half Maximum

GATES	Global Automatic Telescopes Exploring the Sun
GOES	Geostationary Operational Environmental Satellite
GONG	Global Oscillations Network Group
GSU	Georgia State University
GUI	Graphical User Interface
HMI	Helioseismic and Magnetic Imager
HWP	Half Wave Plate
IAC	Institution de Astrofísica de Canarias
INAF	Italian National Astrophysics Institute
IPBS	Incomplete Paschen-Back Splitting
IR	InfraRed
JPL	Jet Propulsion Laboratory
JSOC	Joint Science Operations Center
KSO	Kanzelhöhe Solar Observatory
LCVR	Liquid Controlled Variable Retarder
LHCP	Left-Hand Circular Polarization
LoS	Line-of-sight
LOWl	LOW degree l
LTE	Local Thermodynamic Equilibrium
MHD	Magneto-Hydro-Dynamics
MDI	Michelson Doppler Imager
MOF	Magneto-Optical Filter
MOTH	Magneto-Optical filters at Two Heights
MSO	Mojave Solar Observatory
NASA	National Aeronautics and Space Administration

ngGONG	Next Generation Global Oscillations Network Group
NIR	Near InfraRed
NOAA	National Oceanic and Atmospheric Administration
NSO	National Solar Observatory
ORM	Roque de Los Muchachos Observatory
OT	Teide Observatory
OCAN	Observatorios de Canarias
PIL	Polarity Inversion Line
PSF	Point-Spread Function
PSP	Parker Solar Probe
PTT	Phase Travel Time
QE	Quantum Efficiency
QWP	Quarter Wave Plate
RES3	Radiation in Earth, Sun, and Space Surroundings
RHCP	Right-Hand Circular Polarization
RODOMA	Rome Network for Doppeler and Magnetic Oscillations
RSSS	Remote Sensing for Space Sciences
RW	Red Wing
SAMM	Solar Activity Magnetic Monitor
SAMNet	Solar Activity Monitor Network
SC	Solar Cycle
SDO	Solar Dynamics Observatory
SDK	Software Development Kit
SEP	Solar Energetic Particle
SNR	Signal-to-Noise Ratio

SO	Solar Orbiter
SOHO	Solar and Heliospheric Observatory
SOLIS	Synoptic Optical Long-term Investigations of the Sun
SPSW	Solar Physics and Space Weather [Lab]
SSU	Samarkand State University
SuFI	Sunrise Filter Imager
SWERTO	Space WEatheR TOr vergata university
TNG	Telescopio Nazionale Galileo
TSST	Tor Vergata Synoptic Solar Telescope
UCCI	University College of the Cayman Islands
UTOV	University of Rome Tor Vergata
VAMOS	Velocity And Magnetic Observations of the Sun
WS	Wing Selector

CHAPTER 1
INTRODUCTION TO THE SUN AND SPACE WEATHER

The star of our Solar System, the Sun, is the closest star and the most accessible high-energy plasma laboratory available for observation. As such, it is a critical observational target for understanding the inner workings of other stars. However, perhaps more importantly, the Sun is intimately related to our daily lives on Earth, and therefore, it is imperative that we understand it. The Sun provides the main source of energy on Earth, allowing for the creation and sustainability of life. However, this energy from the Sun can also prove detrimental to life on Earth: high-energy radiation can be incredibly harmful to human life and technology. Especially in our increasingly digital world, it is crucial that we understand the Sun and its activity better so that we can preserve life on Earth.

1.1 *Solar Structure and Phenomena*

The Sun is a $G2V$ star with a mean luminosity $L = 3.83 \times 10^{26}\ W$, an effective temperature $T_{eff} = 5780\ K$, mass $M = 1.99 \times 10^{30}\ kg$, and a radius $R_\odot = 6.957 \times 10^{8}\ m$. The radius of the Sun is defined as the base of the photosphere, and is the point that divides the solar interior from the solar atmosphere (Figure 1.1).

The solar interior is made up of three distinct layers that can be probed with different helioseismic techniques. The innermost layer of the Sun is the core. The solar core reaches to 0.25 $R_\odot$ and has a temperature of $\sim 1.5 \times 10^{7}\ K$. This is the region where nuclear fusion occurs. The radiative zone lies above, extending from 0.25 $R_\odot$ to 0.7 $R_\odot$ and has a mean temperature of $2 \times 10^{6}\ K$. Here, high-energy photons released from the fusion in the core are

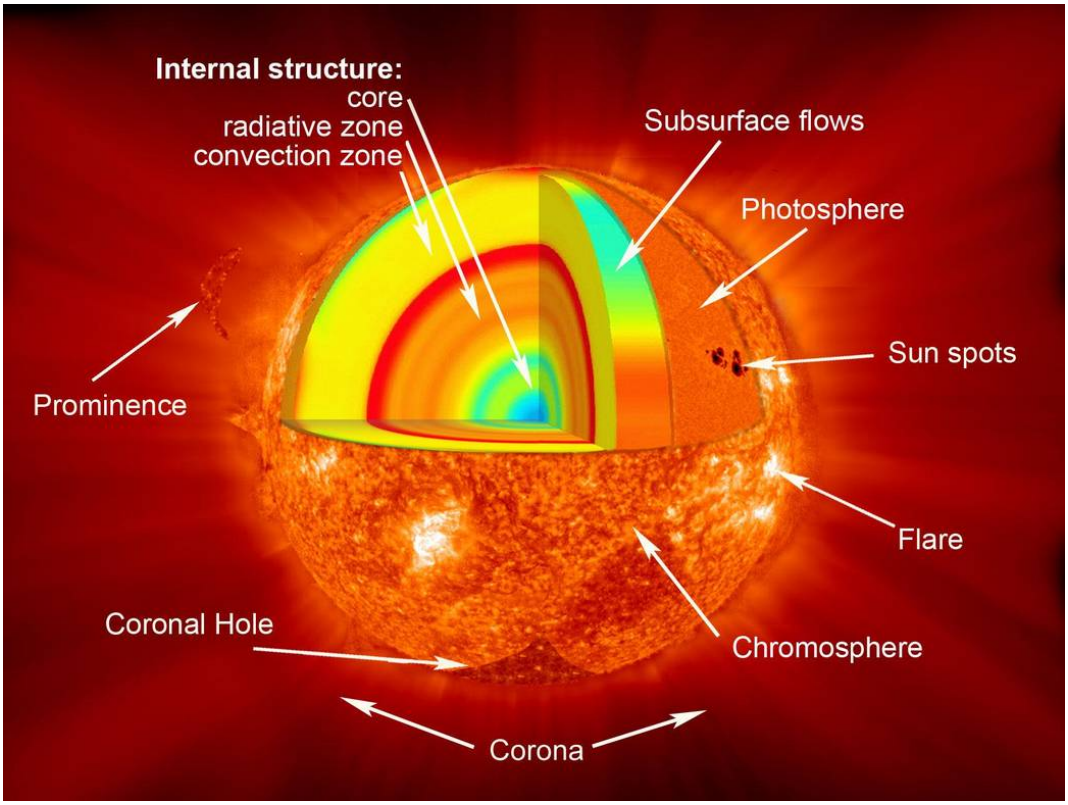

Figure 1.1 An illustration of the solar interior and atmospheric structure. Reproduce from NASA.

radiatively transported outward, losing significant amounts of energy in the process. The third layer of the solar interior is the convective zone. This layer extends from 0.7 $R_\odot$ to the solar surface and contains a temperature gradient from 2×10^6 K at the base of the convective zone to 6×10^3 K at the surface of the Sun. In this regime of the Sun, the solar plasma is unstable to convection, producing large convective cells at the surface of the Sun.

The division of the radiative zone and convective zone is called the tachocline. The tachocline divides the Sun not only in terms of energy release mechanisms, but in terms of rotational motion as well. Below the tachocline, the Sun rotates as a rigid body, while above it, the Sun exhibits differential rotation, with rotation rates depending on latitude (Duvall

& Harvey 1983; Spiegel & Zahn 1992). Additional plasma flows such as the meridional flow that rotates plasma between the equator and poles (Choudhuri et al. 1995), are also present in the convective zone. These variable motions – turbulent convection, differential rotation, and meridional flow – in the plasma of the Sun are key factors in creating the solar dynamo and solar variability (Charbonneau 2020). Figure 1.2 depicts a schematic of the solar dynamo flux transport processes from the solar interior to the surface.

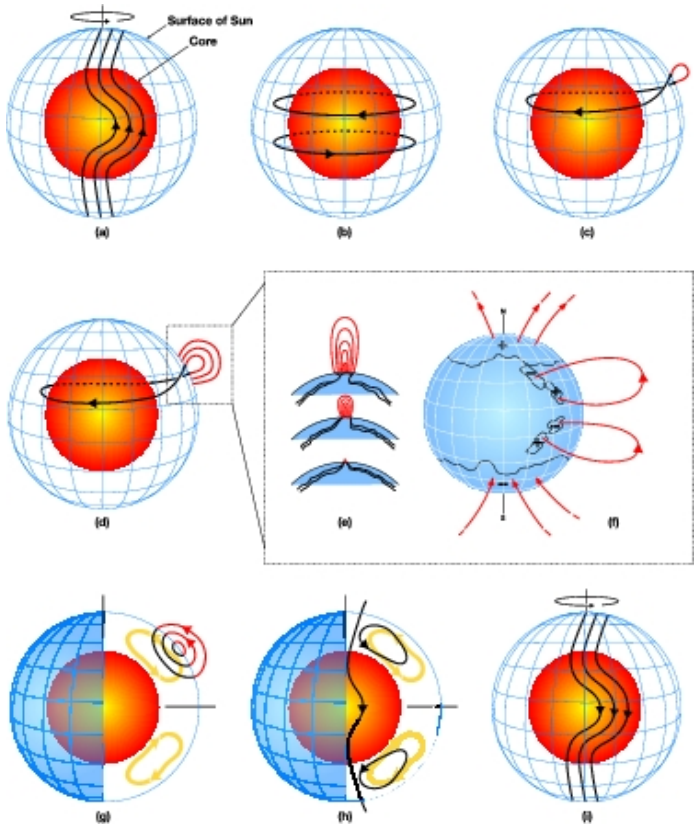

Figure 1.2 A schematic of solar dynamo flux transport processes reproduced from the High Altitude Observatory. Preexisting poloidal magnetic fields are transformed into toroidal fields due to differential rotation. Field lines twist as they reach the solar surface and become visible as sunspots in the visible spectrum and as active region loops in EUV and X-ray spectra. A new reversed-sign field is produced via the Babcock-Leighton effect (Babcock 1961; Leighton 1969).

The emergence of strong, twisted magnetic flux at the solar surface and throughout the solar atmosphere produces various visible phenomena collectively referred to as solar activity (Usoskin 2017). Solar activity is characterized by emission across a broad range of wavelengths, corresponding to active regions (ARs) (van Driel-Gesztelyi & Green 2015), and manifests through multiple distinct phenomena, including:

- *Sunspots* are the largest compact magnetic concentrations and appear darker than their surroundings with magnetic fluxes $\sim 5 \times 10^{20} \leq \Phi \leq 3 \times 10^{22}\ Mx$. They are a photospheric feature characterized by two regions: the central dark umbra, with a vertical magnetic field $\sim 2.5\ kG$, and a surrounding penumbra which is slightly brighter and has a nearly horizontal magnetic field (Hale et al. 1919; Skumanich et al. 1994). The left panel of Figure 1.3 shows an example of a sunspot.
- *Pores* are the smallest magnetic photospheric features that can be distinguished in white light. Their radii are $0.7 \leq R \leq 1.8\ Mm$, their magnetic flux is $2.5 \times 10^{19} \leq \Phi \leq 2.5 \times 10^{20}\ Mx$, and their typical magnetic field strength is $\sim 2\ kG$, oriented vertically (Schrijver & Zwaan 2008). They are small, dark points lacking penumbra, and constitute the first stage of sunspot evolution (Sobotka et al. 1999). The left panel of Figure 1.3 shows an example of a pore.
- *Faculae* are small bright features in the photosphere most easily observed close to the solar limb and are associated with magnetic field strengths $\sim 1.5\ kG$ (Hale 1922; Keller et al. 2004). They manifest in plages and remnants of ARs, and their increased abundance around sunspot maximum contributes to the slightly higher solar irradiance

observed at solar maximum. (Fröhlich 2002; Krivova et al. 2003). The right panel of Figure 1.3 shows an example of faculae.

- *Fibrils* are thin, elongated features that are traditionally considered a tracer of magnetic field lines in the chromosphere (de la Cruz Rodríguez & Socas-Navarro 2011; Pietarila et al. 2009). When they are located close to the solar limb, they are also referred to as spicules. Spicules/fibrils have a mass flux 100× that of the solar wind into the lower corona and are considered an important factor in mass and energy transport to the upper chromosphere/corona (Withbroe 1983). The left panel of Figure 1.4 shows an example of a fibril.
- *Loops* are bright, arch-shaped structures in the Sun's chromosphere (Merenda et al. 2011) and corona (Reale 2010), composed of hot, ionized plasma confined and directed by closed magnetic field lines that extend from one point (footpoint) on the photosphere to another. Their temperatures range from $10^5 - 10^7\ K$ (Reale 2010) and are often associated with flares and coronal heating phenomena. The center panel of Figure 1.4 shows an example of a coronal loop.
- *Jets* are transient, collimated plasma ejections originating in the chromosphere and propagating along magnetic field lines outwards into the corona. They have characteristic lengths $\sim 1 - 10\ Mm$ and velocities $\sim 10 - 150\ km/s$ (Shibata et al. 2007). Their presence implies smaller-scale magnetic reconnection throughout the chromosphere. The center panel of Figure 1.4 shows an example of a jet.
- *Coronal Holes* are large darkenings in the EUV and soft X-ray in the corona that

correspond to open magnetic field lines. They are characterized by cooler, lower-density plasma than the surrounding corona, which allows their plasma to escape into interplanetary space, forming high-speed solar wind streams (Cranmer 2009). Figure 1.5 shows an example of a coronal hole.

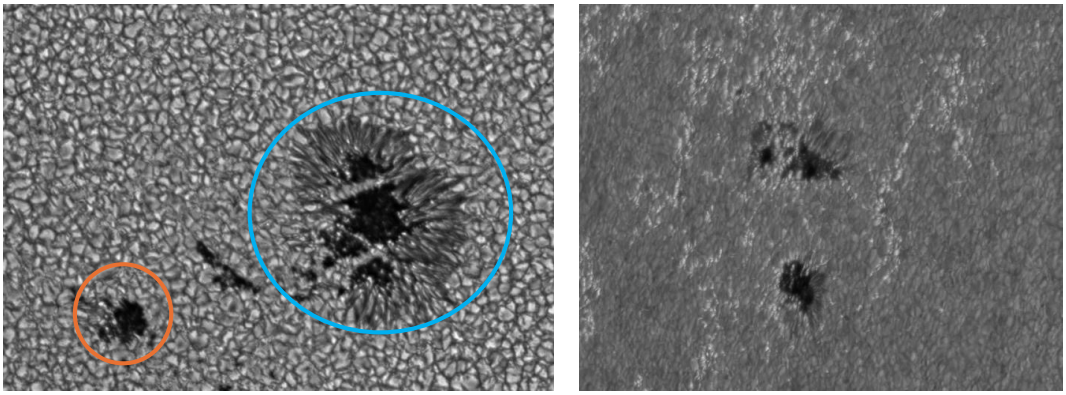

Figure 1.3 Photospheric phenomena: sunspot (left, blue circle) featuring a distinct umbra and penumbra, pores (left, orange circle), and faculae (bright points, right) captured in white light. Images from NASA.

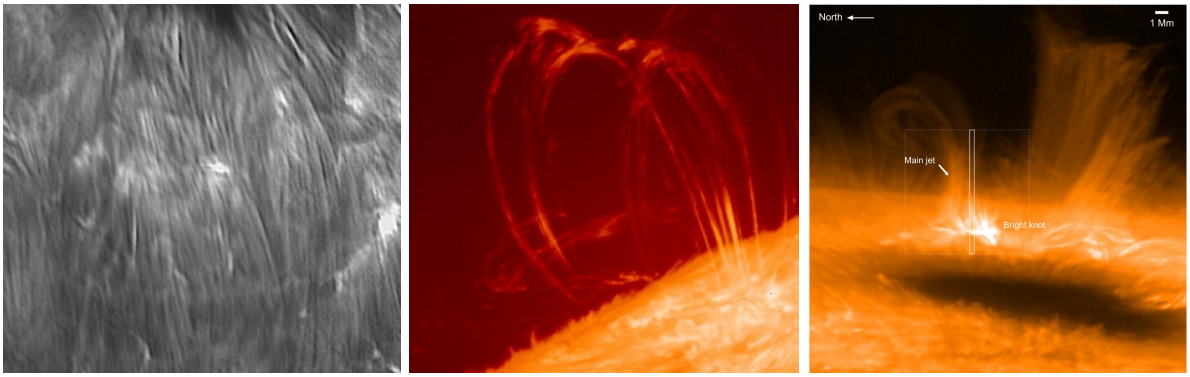

Figure 1.4 Chromospheric phenomena: fibrils (left) captured in Ca II H from SUNRISE/SuFI (Peter et al. 2021), loops (center) captured in Hα from NASA, and a jet (right) captured in Ca II H (Singh et al. 2024).

As these different solar activity phenomena originate from different physical processes, they require different environments to form and propagate, and are therefore characteristic

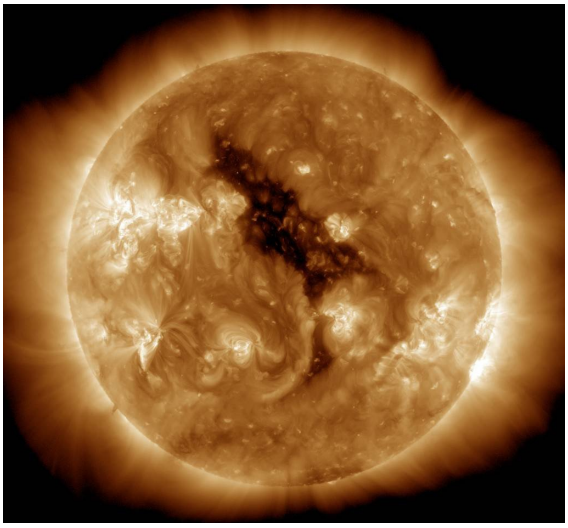

Figure 1.5 Image of a coronal hole captured by SDO/AIA 193Å.

of different layers of the solar atmosphere. The Sun's atmosphere consists nominally of four layers: the photosphere, the chromosphere, the transition region, and the corona. The base of the photosphere is often considered the "surface" of the Sun, and is the layer where photons in the optical continuum escape (Haberreiter et al. 2008). Different layers of the solar atmosphere are probed with different spectral lines, as the physical conditions of the plasma differ significantly in each atmospheric layer. Figure 1.6 shows some of the solar spectrum lines most frequently used to probe the different layers of the solar atmosphere. This figure also shows the variation of temperature as a function of height in the solar atmosphere.

An important concept when studying the solar atmosphere is the plasma-β parameter, which is defined at the ratio between the gas pressure P_{gas} and the magnetic pressure P_{mag}:

$$\beta = \frac{P_{gas}}{P_{mag}} = \frac{nk_BT}{B^2/2\mu_0}, \tag{1.1}$$

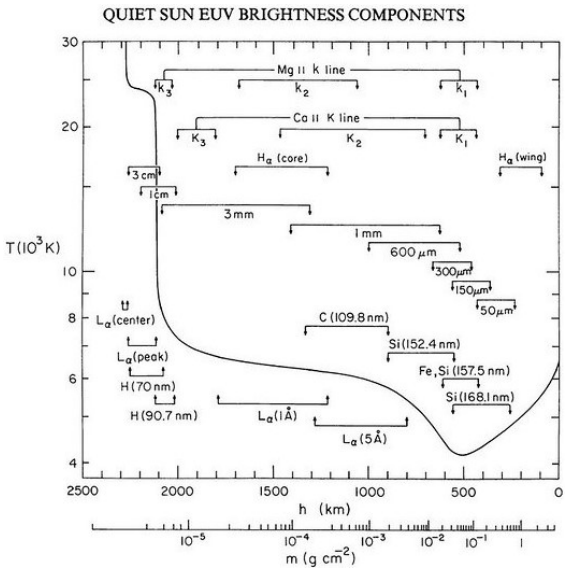

Figure 1.6 Temperature profile of the quiet Sun as a function of height (continuous line) with approximate heights where spectral line continua are formed (arrowed lines). Reproduced from Vernazza et al. (1981).

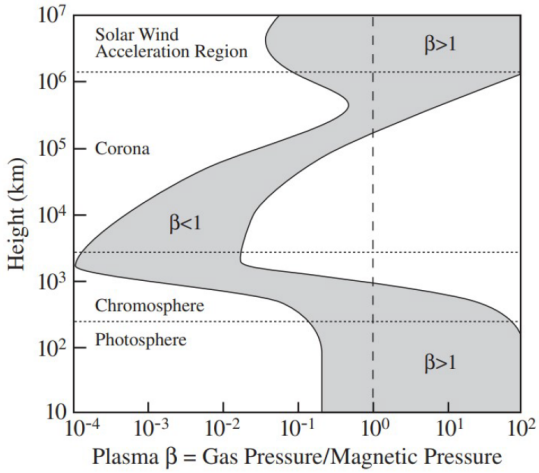

Figure 1.7 Plasma-β value across the solar atmosphere. Reproduced from Gary (2001).

where μ_0 is the magnetic permeability of free space, n is the number density of total particles contributing to the gas pressure, k_B is Boltzmann's constant, T is the temperature, and B is the magnetic field strength. The point at which the magnetic and gas pressures become comparable (i.e. the $\beta \sim 1$ layer) is expected to vary in height from 800 - 1600 km above the photosphere (Rosenthal et al. 2002), placing it in the chromosphere of the Sun. Figure 1.7 depicts the plasma-β values throughout the solar atmosphere.

The photosphere of the Sun ranges from 0 km to approximately 400 km and is characterized by a decreasing temperature profile with height (from 6500 to 4000 K). It consists of high-β plasma and is characterized by high density. Because of this high density, collisions

dominate the excitation mechanisms of photospheric diagnostic lines, and, consequently, the photosphere is assumed to be in local thermodynamic equilibrium (LTE). The photosphere exhibits multi-scale dynamic phenomena, with granulation patterns emerging from convective motions rising from the convective zone. These motions, along with larger-scale supergranulation flows, create a cascade of energy across spatial scales, from large convection cells down to small turbulent eddies, which helps shape magnetic structures such as pores, faculae, and sunspots. This cascading behavior contributes to the formation and evolution of the photospheric magnetic network and plays a role in generating waves and turbulence that propagate into the upper solar atmosphere (Schrijver & Zwaan 2008)

The chromosphere is the layer above the photosphere (400 to 2400 km above the solar surface). Here, the pressure drops by several orders of magnitude over a short distance (500 - 1000 km), and is consequently dominated by low-β plasma. The chromosphere also has an increasing temperature profile with height, reaching a peak temperature of around 35000 K at the top. Due to the low density, collisional rates are low and therefore, the approximation of LTE is typically invalid. The chromosphere is usually observed in the core of the strongest lines of the solar spectrum, like the hydrogen Balmer lines (Leenaarts et al. 2012). In fact, the chromosphere was defined by what is seen in the visibly red Hα 656.28 nm line by Lockyer (1868). The chromosphere is home to features quite different than the photosphere, including fibrils, loops, and jets.

The next layer of the solar atmosphere, the transition region, is the interface between the chromosphere and corona. It is relatively thin (ranging from 2400 to 3000 km) and

is characterized by an incredibly steep temperature gradient (temperatures increasing from 35000 to 10^6 K) as hydrogen and helium become fully ionized. The mechanisms for this dramatic heating are not yet fully understood and remain a highly interesting and debated area of research.

The hot, diffuse corona is the outer layer of the solar atmosphere and extends out up to 20 $R_\odot$. The corona is extremely low density (on the order of 10^{-10} g/cm^3) and has a temperature in the millions of kelvin. It is sampled by the lines of highly ionized species (typically in the extreme ultraviolet (EUV) and X-ray) and is characterized by large-scale magnetic loops and coronal holes. Coronal lines are formed under conditions known as "coronal equilibrium," which is characterized by collisionally excited and radiatively decaying electrons; linking the measured line intensities directly to the coronal temperature (Hubeny & Mihalas 2014).

Each layer of the solar atmosphere provides a unique link in the story of the Sun and space weather. The reason why the chromosphere and corona are so hot is still debated and referred to as the coronal heating problem (e.g. Klimchuk (2006, 2015); Parnell & De Moortel (2012)). Currently, the top theories are mechanical heating through the dissipation of Alfvén and magneto-acoustic waves (e.g. Alfvén (1942); Arregui (2015); Osterbrock (1961); Tomczyk et al. (2007)) and microflares (e.g. Brosius & Viall (2020); Hannah et al. (2011); Parker (1988)). In order to make more progress on this problem, a better understanding of wave propagation throughout the solar atmosphere, and in particular, throughout the chromosphere, is necessary.

1.2 *The Solar Cycle*

As described in the previous section, due to differential rotation, turbulent convection, and meridional flows, the solar magnetic field produces multiple phenomena on timescales ranging from minutes to years, collectively referred to as solar activity (Usoskin 2017). Solar activity ranges from flares (lasting minutes) to multi-decadal activity cycles and polarity inversion cycles.

From almost two centuries of solar direct monitoring (e.g., sunspot observations), a dynamic, cyclic pattern of magnetic activity known as the solar cycle (SC) (Hathaway 2015; Usoskin 2017) has been defined. These cycles (currently in SC 25), with an average period of eleven years, are characterized by a periodic growth and decay of the Sun's global magnetic field, which can most directly be observed by the overall sunspot number (Figure 1.8 bottom). Generally, sunspots appear between $\pm\,30^{\circ}$ latitude on the Sun – their average position throughout the SC will shift closer to the equator (Solanki et al. 2006). Tracking sunspot locations across time leads to a characteristic "butterfly diagram" which is also typically used to map SCs (Figure 1.8 top).

Periods with the largest number of sunspots are categorized as "solar maxima" and also correspond to a higher overall total solar irradiance and total number of ARs. Because sunspots are concentrations of magnetic activity, they are associated with eruptive events such as flares and coronal mass ejections (CMEs). These events, and specifically their effects on Earth, its technological systems, and spacecraft are classified as space weather. Consequently, the SC drives the frequency and intensity of space weather events.

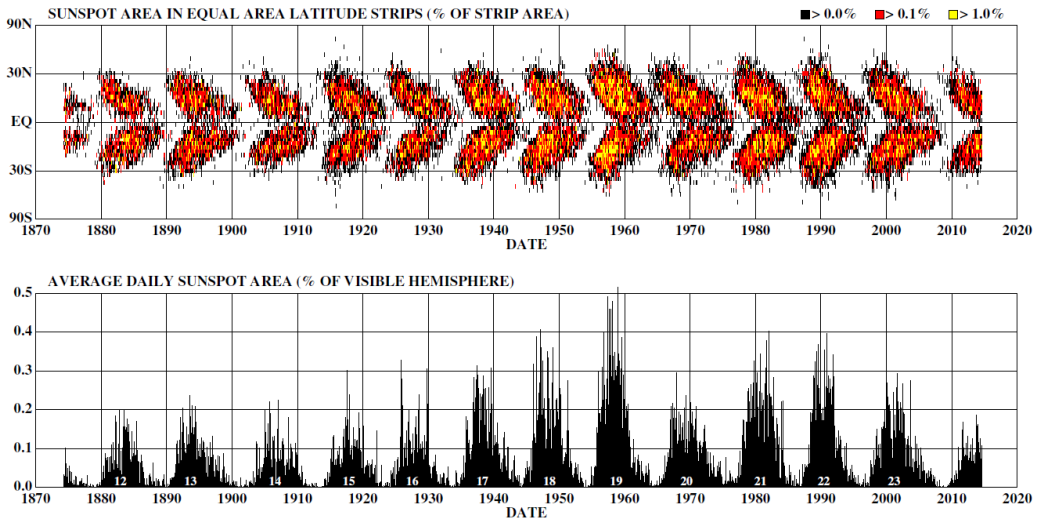

Figure 1.8 Solar Cycle diagrams from (Hathaway 2015). Top: "butterfly diagram" from sunspot latitudinal position vs. time. Bottom: average daily sunspot number vs. time.

1.3 *Space Weather*

Space Weather refers to the conditions on the Sun and in the solar wind, magnetosphere, ionosphere, and thermosphere that affect human life/health and technological performance (Glover et al. 2002). Of particular interest to space weather studies are solar eruptive events because of the high levels of radiation they can deliver to Earth. There are three main types of eruptive space weather events that we need to monitor: solar energetic particles (SEPs), coronal mass ejections (CMEs), and flares (Schwenn 2006).

SEPs consist of energetic protons, electrons, and ions that are accelerated during explosive solar events and travel through interplanetary space along interplanetary magnetic field lines (Reames 2013). They present energy spectra that span from a few keV to several GeV (Anastasiadis et al. 2019), and are particularly dangerous for astronauts' health. Figure 1.9 shows a CME and its corresponding SEPs.

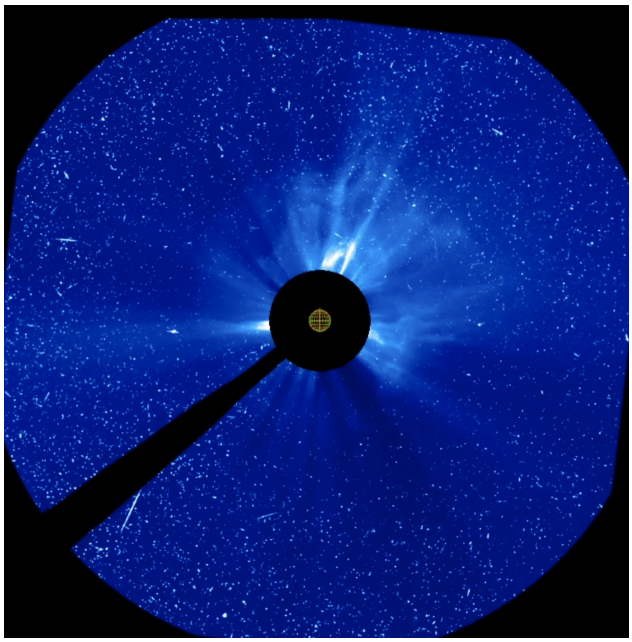

Figure 1.9 A Composite image of a CME from November 11, 2025 as captured by SOHO. Bright points and streaks are due to SEPs.

CMEs are the largest-scale eruptive phenomenon not only on the Sun but also across the solar system. They are characterized by AR-sized plasmas that are expanded and accelerated into interplanetary space. The bulk of the plasma has a typical mass of $10^{11} - 10^{13}\ kg$ and typical speeds of several hundred to a thousand km/s and (Chen 2011). CMEs break the flow of the solar wind and transport high energy particles to Earth, which, when trapped by Earth's magnetic field can cause catastrophic geomagnetic storms.

Most eruptive space weather events are associated with a flare, and consequently, understanding the initiation mechanisms of flares is one of the bases of space weather studies. A flare is observed as a brightening enhancement across the electromagnetic spectrum, but is classified specifically by its X-ray flux (1 - 8 Å) measured by the GOES series satellites (Table 1.1). Although the exact mechanism for flare initiation is not fully understood, the

standard model suggests that flares are the result of magnetic field line reconnection, which releases magnetic energy, accelerating particles into space or back to the footpoints of the reconnected field line (Figure 1.10). Caused by reconnection, flares are associated with magnetically active regions formed from sunspots. Their probability, occurrence, duration and strength increase with the solar cycle (Temmer et al. 2001), as does the frequency of their association with CMEs (Youssef 2012).

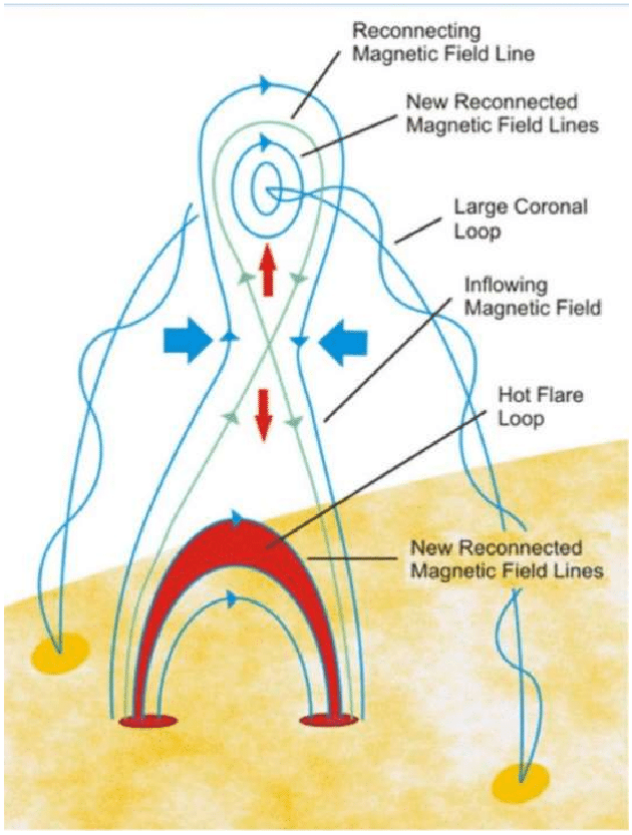

Figure 1.10 Standard model of a solar flare from NASA.

M- and X-class flares emit enhanced X-ray and extreme ultraviolet radiation that increases ionization in the terrestrial ionosphere, leading to radio blackouts. Their associated energetic particle events can also pose radiation hazards to astronauts and damage satellites.

Table 1.1 Solar flare classifications based on GOES X-ray flux in the 1 - 8 Å band.

Flare Class	Peak Flux $[W/m^2]$
A	$< 10^{-7}$
B	10^{-7} - 10^{-6}
C	10^{-6} - 10^{-5}
M	10^{-5} - 10^{-4}
X	$> 10^{-4}$

Nearly all other space weather phenomena – CMEs, SEPs, etc. – are frequently associated with flares, which is why a main goal of space weather forecasting is to fully understand, detect, and predict flares. To do this, it is imperative to study the Sun's magnetic field, atmospheric wave propagation, and subsurface flows to identify precursor signals for space weather events (Falkenberg et al. 2010; Korsós et al. 2015; Kosovichev & Sadykov 2023). Since space weather events are tied to magnetic activity, studying and characterizing AR magnetic fields is fundamental to our investigations of what triggers solar flares. Moreover, studies on subsurface flows reveal strong vortical and shearing flows during the emergence of magnetic flux and strong correlation between flow divergence and helicity in the active regions with their flaring activity.

Recent studies have used LoS and vector magnetograms obtained from space and ground-based observatories to obtain parameters that can be used as proxies for studying and predicting solar activity. A few examples of these parameters include the gradient of the magnetic field (Cui et al. 2006), the total unsigned current helicity (Zhang & Bao 1999), the total unsigned magnetic flux within $\sim 15\ Mm$ of a strong-field, high-gradient polarity separation

line R (Schrijver 2007), the free magnetic energy (Su et al. 2014), and topological counts of polarity inversion lines D (Cicogna et al. 2021). For a more extensive, but non-exhaustive, list of magnetic-field related flaring parameters, refer to Georgoulis (2012) and Barnes et al. (2016). Magnetograms are also powerful tools to characterize the complexity of active regions (ARs). Hale et al. (1919) first introduced the Mount Wilson (or Hale) classification, which groups ARs according to the distribution of magnetic field topology into three major classes: unipolar (α), bipolar (β), and multipolar (γ). Künzel (1960) and van Driel-Gesztelyi & Green (2015) expanded this system to include five major classes: α, β, $\beta\gamma$, γ, and δ. These classes have been shown to correlate to magnetic flux gradient strengths (Ireland et al. 2008) which indicates flare strength. An additional system for AR classification based on sunspots, the Zurich system (Kiepenheuer 1953) was expanded and given more quantitative definitions by McIntosh (1990). The McIntosh classification system categorizes sunspot groups using a three-part code (Zpc), where Z denotes the modified Zurich class (overall size and structure), p the penumbral class of the sunspot (the structure of the largest sunspot's penumbra), and c the compactness of the group of sunspots. Such classifications are strongly associated with flare rates (Bornmann & Shaw 1994), and the NOAA Space Weather Prediction Center uses this system operationally to estimate daily probabilities of M- and X-class solar flares (Barghouty & Falconer 2015).

LoS velocity maps, called Dopplergrams, are also fundamental to solar physics and space weather studies because they provide direct, spatially resolved information about plasma motions on and beneath the solar surface. Dopplergrams are essential for identifying and

characterizing plasma flows such as flux-emergence upflows, shear flows along polarity inversion lines, and sunspot-associated motions, which are associated with ARs and contribute to the build-up of magnetic stress preceding eruptive space weather events like flares and CMEs (e.g. Welsch et al. (2009)). These Dopplergram and magnetogram maps are obtained by observing magnetically sensitive lines and exploiting the Zeeman effect (Section 2.1.2) in the solar atmosphere. By leveraging observations of Zeeman splitting, co-spatial Dopplergrams and magnetograms can be acquired, providing a comprehensive view of the dynamic and magnetic structure of the Sun. The splitting of spectral lines in the presence of a magnetic field yields right- and left-circularly polarized ($\sigma^{\pm}$) components of light which correspond to Stokes formalism $I+V$ and $I-V$.The wavelength difference or intensity imbalance between these components is proportional to the LoS magnetic field, and allows a magnetogram to be constructed. Furthermore, measuring the overall wavelength shift of the spectral line yields a map proportional to a LoS Dopplergram. Additionally, Dopplergrams reveal insights into the dynamical processes that govern the transport of energy and magnetic fields in the Sun, such as convection, meridional flows, and oscillations of varying scales. These measurements are essential for helioseismology (Section 1.4), which uses solar oscillations to infer the Sun's internal structure and dynamics.

1.4 *Helioseismology*

As described in Section 1.1, the magnetic field, and therefore solar activity, originates in the interior of the Sun. The only way to study the structure and dynamics of the solar interiors

is via solar seismology (Duvall & Harvey 1983). Solar seismology, or helioseismology, is based on the study of velocity map time series and is fundamental to understanding the mechanism of the solar dynamo and interactions of solar plasma with magnetic fields (Christensen-Dalsgaard 2002). Helioseismology is traditionally broken into two categories: global and local helioseismology.

Global helioseismology uses resonant normal modes of the Sun to measure large-scale structures such as the radial sound-speed profile, differential rotation, and the meridional circulation (Christensen-Dalsgaard 2021; Dwivedi 2003). In global helioseismology studies, solar oscillations are decomposed into spherical harmonics and are defined by three types of waves: p-modes (pressure-driven), f-modes (fundamental surface gravity wave), and g-modes (gravity-driven). These wave patterns are standing acoustic waves trapped in resonant cavities, resulting from interference. The most ubiquitous of these modes is the 5-minute p-mode oscillation (Basu 2016). Local helioseismology studies the propagation of component waves near the Sun's surface, probing subsurface flows as they reach the photosphere, sound-speed perturbations, and sunspot structure (Duvall & Harvey 1983; Duvall et al. 1993; Gizon & Birch 2005; Rajaguru et al. 2013). It is categorized by the study of p-modes excited by convection and focuses on techniques such as time-distance helioseismology (measuring travel times between points on the solar surface; Duvall et al. 1993) and ring-diagram analysis (studying local power spectra of oscillations to determine flows and structural inhomogeneities; Basu et al. 1999; Hill 1989).

Classical helioseismic studies usually rely on analyzing waves below the acoustic cutoff

frequency, approximately 5.2 mHz (Christensen-Dalsgaard 2002; Fossat et al. 1992), which are consequently trapped in the acoustic cavity of the Sun. Therefore, these waves are mainly evanescent in the solar atmosphere and provide little insight into this region (Finsterle et al. 2004c). Waves above the acoustic cutoff frequency, which are free to propagate in the solar atmosphere, have been shown to refract and reflect when they cross a boundary with a change in the dispersive characteristics (for example, the $\beta \sim 1$ layer (Rosenthal et al. 2002)). Therefore, expanding helioseismology studies to the solar atmosphere allows us to infer the properties of the different layers of the solar atmosphere and provide greater insights into the internal drivers of solar activity. For example, Finsterle et al. (2004c) inferred the location of the $\beta \sim 1$ magnetic canopy; Jefferies et al. (2006) showed that inclined magnetic field lines at the boundaries of supergranules allow for low-frequency waves to propagate to through the solar atmosphere; Straus et al. (2008) and Straus et al. (2009) determined the height dependence of energy transported by waves in the solar atmosphere in the context of coronal heating; and Aparna (2022) linked perturbations in phase travel time of acoustic waves to flare precursors. These works motivate large-scale helioseismic studies of the solar atmosphere, which can only be accomplished through multi-height velocity measurements.

1.5 *Solar Observations and Telescopes*

Modern solar telescopes can generally be divided into two categories: high (≤ 0.5") and low ($\geq 1 - 2$") resolution. The diffraction-limited angular resolution is given by

$$\theta = 1.22\frac{\lambda}{D} \tag{1.2}$$

where θ is the angular resolution in radians, λ is the wavelength of observation, and D is the diameter of the telescope's primary aperture. For a given wavelength, high-resolution telescopes correspond to large-diameter telescopes and vice versa. Both large-diameter/high-resolution and small-diameter/low-resolution telescopes provide essential contributions to solar and space weather studies.

Large-diameter telescopes provide high-resolution images of the Sun down to spatial scales of kilometers. Solar satellites like Solar Orbiter (SO) provide resolutions as high as 0.5" (in the EUV), corresponding to a spatial resolution of 100 km at disk center (Rochus et al. 2020). Ground-based telescopes like the Daniel K Inouye Solar Telescope (DKIST) are specified to achieve diffraction-limited resolution of 0.026" arcsec at 500 nm, corresponding to a spatial scale of roughly 20 km on the Sun (Rimmele et al. 2020). Such telescopes are designed to resolve the fundamental spatial, temporal, and spectral scales at which solar magnetic and plasma processes operate. Their value lies in matching the physical scales of the solar atmosphere. At the photosphere and chromosphere, many key processes occur on spatial scales of tens of kilometers and evolve on timescales of seconds. High angular resolution ($\leq$ 0.1") is necessary to resolve individual magnetic flux tubes, the structure and dynamics of a sunspot penumbra, granular convection and the excitation of p-modes, and magnetic effects of p-modes and higher frequency acoustic waves (Thomas 1999). Solar activity and space weather events originate in small-scale magnetic structures and dynamics, so resolving these scales is essential for understanding the physics of flares, CMEs, and other eruptive phenomena. While high-resolution ground-based telescopes such as DKIST or space missions

like So provide this critical insight, they are not suitable for routine operational forecasting. Instead, observations from these high-resolution platforms guide the design and targeting of lower-resolution instruments that can provide continuous coverage for effective operational forecasts.

Small-diameter telescopes achieve lower angular and spatial resolutions, but can more easily provide full-disk images of the Sun, and have been just as impactful to solar studies. For example, the space-based Solar and Heliospheric Observatory (SOHO) achieved a maximum resolution of 2.6" ($\sim$1900 km) in the EUV (Domingo et al. 1995), and with over 25 years of solar monitoring, continues to be a cornerstone of solar and space weather studies, while the Solar Dynamics Observatory, launched in 2010, (SDO) continues to provide continuous full-disk imaging with higher spatial resolution (0.5, $\sim$ 360 km) and rapid cadence in multiple EUV channels, enabling detailed studies of dynamic solar phenomena (Pesnell et al. 2012). Moreover, smaller ground-based solar telescopes, such as those that make up the Global Oscillations Network Group (GONG) project (Harvey et al. 1996), achieve a comparable 2.5" resolution and, similarly, with 30+ years of near-continuous solar coverage, provide the standard for helioseismology studies. Furthermore, smaller FoV high-resolution telescopes do not allow the production of an image of the entire Sun and its activity. Despite having lower resolution, small-diameter telescopes with larger FoV provide the ability to simultaneously observe the full-disk of the Sun (angular diameter of $\sim$ 32'). As many space weather phenomena (e.g. flares, coronal holes, AR evolution, global magnetic field patterns, and long-term solar cycle trends) occur on global/large spatial scales and evolve over

timescales from hours to years (Temmer 2021), achieving full-disk observations is equally as critical to space weather studies as high-resolution imaging. Lastly, full-disk solar images enable Sun-as-a-star investigations, enabling direct comparison, drawing parallels to unresolved stellar observations (Brooks et al. 2018).

1.5.1 Synoptic Observations

Angular resolution and FoV are not the only important considerations for solar and space weather telescopes. The temporal resolution and coverage are also critical. As described in Section 1.2, solar activity varies on both long and short time scales. Although eruptive events such as flares last for minutes, the Sun's activity cycle follows an 11-year period and has even longer time-scale trends such as the 22-year polarity inversion cycle (Hale cycle) and periodic abnormalities. Consequently, long-term, continuous (synoptic) observations of the Sun are critical for monitoring eruptive events and constructing datasets suitable for understanding the Sun's long-term evolution. When attempting to perform synoptic observations of any astronomical object, there are three main techniques to achieve them: 1) observing with a space-based telescope, 2) observing from the Poles of the Earth, 3) using multiple, low-latitude sites for observations (Elsworth et al. 2015).

Space-based observations offers the strongest opportunity to achieve synoptic observations; with no diurnal rotation or weather to contend with, spacecraft can, in theory, achieve true synoptic coverage (if positioned in the proper orbit). Moreover, since spacecraft do not have to contend with atmospheric absorption and seeing, they can observe regions of the solar spectrum inaccessible from the ground and can often achieve diffraction-limited ob-

servations. There are many space missions currently operational, such as SOHO (Domingo et al. 1995), the Solar Dynamics Observatory (SDO: Pesnell et al. (2012)), and SO (Müller et al. 2013), and multiple planned for the upcoming decade, such as the MUlti-slit Solar Explorer (MUSE: De Pontieu et al. (2022)) and HelioSwarm (Klein et al. 2023). However, despite the scientific benefits, there are major drawbacks to space-based observing. The first is cost. For a given size of telescope, it costs 2-3x more to operate a spacecraft for 10 years as compared to a comparable ground-based instrument (Meredith 2022; Stahl & Allison 2020). Moreover, space-based telescopes have the disadvantage of being unserviceable (with the exception of few instruments onboard the ISS), meaning any system failure can cause the permanent shutdown of the instrument, and they often have a far shorter projected lifetime than ground-based instruments.

Conversely, the drawbacks of space-based telescopes become some of the biggest strengths of ground-based instruments. Ground-based telescopes, regardless of their location on Earth, are far more serviceable than spacecraft. Consequently, although system failures can often be catastrophic, they do not always mean full decommissioning of the telescope. Furthermore, being serviceable allows ground-based telescopes to be upgraded over time, whether to improve efficiency, output, or instrumentation. Although this is theoretically true for any ground-based site, in practice, it is more feasible to service low-latitude sites than to service polar sites.

Observations from the South Pole can provide extremely powerful ground-based observations. True synoptic observing is feasible for months at a time, and Antarctica has many

advantageous observational qualities, including low atmospheric water vapor, excellent sky transparency, prolonged periods of stable seeing (with median seeing of 0.27"), and minimal atmospheric disturbances such as those caused by Earth's rotation (Lawrence et al. 2004). However, because solar observations are available for only half the year, the South Pole alone is not suitable for synoptic observations. This can be remedied by placing a telescope at both Poles, but environmental factors make this option difficult to implement. First, the extreme weather at the Poles requires far more specialized equipment than most other observing sites. Moreover, extreme weather events can force the telescope into dormant modes, thereby losing observation time and failing to achieve synoptic observations. Additionally, obtaining a permanent observatory at the Poles is extremely difficult; most Antarctic solar observations come from specialized projects lasting at most a few austral summers. One of the longest-operating solar telescopes in Antarctica was the Polar Solar Observatory/Polar Solar Observatory-II, which operated from 1978 to 1982 (Pomerantz et al. 1981) and contributed to studies of long-period oscillations (Stebbins & Wilson 1983). In more recent times, the Magneto Optical Filters at Two Heights (MOTH) and MOTH II instruments were deployed to the South Pole three times (austral summers of 2002 - 2003, 2016 - 2017, and 2017 - 2018), collecting over 260 hours of multi-height data which has been used for many solar and space weather studies such as atmospheric seismology (Finsterle et al. 2004a), acoustic cut-off frequency mapping (Jefferies et al. 2019), wave reflection analyses (Chaturmutha et al. 2024), and flare precursor investigations (Aparna 2022).

Placing telescopes at low-latitude sites allows for the most cost-effective and accessible

instruments. Telescopes at low-latitude sites can be easily accessed in the event of a malfunction, readily upgraded, and monitored in person whenever necessary. The most obvious drawback of using low-latitude sites to achieve synoptic observations is that no single site can provide full synoptic coverage. The diurnal rotation and seasonal shift of the Sun mean that, at best, a low latitude sight can observe for a portion of the day. Moreover, as with the Poles, poor weather can mean that a low-latitude instrument is out of observing commission for days or weeks at a time. One way to work around these constraints is to build a network of telescopes at low-latitude sites so that at least one telescope is always taking observations, thereby achieving synoptic coverage. This technique runs into its own challenges, for example, calibrating observations between instruments and coordinating international observation agreements, but is by far the most cost-effective method to acquire synoptic observations. Moreover, multiple, low-latitude sites readily facilitate collaborations that can strengthen the telescopes' achievements.

Because of these numerous benefits, many solar studies have attempted to construct a ground-based network of synoptic telescopes. The most notable and longest-standing network is the GONG project, which comprises six identical Michelson-interferometer-based telescopes (Harvey et al. 1996) used for space weather prediction and helioseismology (e.g., Gallagher et al. (2002); Gough et al. (1996); Huang et al. (2024); Riley et al. (2014)). Another notable synoptically-designed solar telescope is the Synoptic Optical Long-term Investigations of the Sun (SOLIS), which is a suite of three instruments, which operated for $\sim$20 years starting in 2003 at Kitt Peak National Observatory (Keller et al. 2003) before being

relocated to Big Bear Solar Observatory (BBSO). It is used for a variety of solar physics studies such as flare productivity of ARs, sunspot correlation to the calcium II393.37 nm line, and comparative studies of magnetic fields across varying solar latitudes (e.g. Bertello et al. (2016); Jing et al. (2010); Petrie & Patrikeeva (2009)).

In addition to the currently active synoptic observatories, there are multiple proposed networks of ground-based telescopes for solar and space weather observations at various stages of development. The *Solaris* project is a proposed network of small radio telescopes designed to operate in Antarctica and other polar/mountainous sites, with the technical goal of enabling smart solar monitoring at high radio frequencies (Pellizzoni et al. 2024). The GONG project is also planning an upgrade, titled next-generation GONG (ngGONG), which aims to upgrade each of the current GONG observing sites to include a spectropolarimeter (photospheric/chromospheric), a narrow/broadband imager, and a Sun-as-a-star integrated spectrograph (Pevtsov et al. 2024). The Solar Activity Monitor Network (SAMNet) is a proposed network of Magneto-Optical Filter (MOF)-based instruments and white-light coronagraphs designed to observe velocity and magnetic field maps at multiple heights throughout the solar atmosphere for space weather studies (Erdélyi et al. 2022). Finally, the Global Automatic Telescopes Exploring the Sun (GATES) Network, the network I have worked to develop, (and what this dissertation is about) is a network of MOF-based instruments and Hα channels designed for multi-height synoptic observations of the Sun for monitoring the Sun for phenomena related to space weather, prediction, and helioseismic studies (Konow et al. 2024).

The majority of these upcoming networks not only leverage multi-site observations for synoptic coverage, but also emphasize the importance of multi-height observations of the solar atmosphere for space weather studies. Energetic events such as flares are rooted in flux emergence first seen in the photosphere which only fully develops in the chromosphere and corona. Therefore, to achieve a complete understanding of these processes, multi-height measurements of the solar magnetic field are necessary (Bertello et al. 2022). Moreover, with acoustic wave propagation as one of the possible solutions to the elusive chromospheric/coronal heating problems (Abbasvand et al. 2020), extending multi-height observations to include velocity maps throughout the solar atmosphere, especially in the upper chromosphere, is equally as important. It is increasingly evident that multi-height synoptic observations of velocity and magnetic fields in the solar atmosphere are essential for the future of solar physics, helioseismology, and space weather studies and prediction. Hence, developing instruments with spectropolarimetric capabilities is crucial to obtain simultaneous access to velocity and magnetic field information through the Doppler and Zeeman sensitivity of solar spectral lines.

1.6 *Dissertation Overview*

In this dissertation, I describe an attempt to advance space weather studies and prediction by developing a new ground-based network of MOF-based telescopes and conducting a valuable observational campaign using the GATES network. The rest of the document is organized as follows:

- Chapter 2 introduces the concept, history, operational modes, and data products of MOF-based telescopes.
- Chapter 3 details the concept, history, design, and preliminary performance of the Tor Verata Synoptic Solar Telescope (TSST). I highlight the work I conducted, including redesigning the telescope's mechanical design and the lab tests I ran to verify data quality.
- Chapter 4 mirrors Chapter 3, detailing the concept, history, design, and performance of the Mojave Solar Observatory (MSO), including the specific work I contributed to the telescope.
- Chapter 5 describes the Global Automatic Telescope Exploring the Sun (GATES) Network: its concept, data acquisition, reduction, and storage pipeline/techniques I developed, and the Summer 2025 Observing Campaign I conducted.
- Chapter 6 discusses my developments of a Helium 1083 nm MOF filter. I detail the historical progress on developing such a filter and the current successes/status of the GATES Network's He I 1083 nm MOF, including first light images with the He MOF and the brief observational campaign which acquired full-disk LoS magnetograms.
- Chapter 7 discusses preliminary results from the 2025 observational campaign I conducted with the GATES Network. This includes magnetogram comparisons to GONG/HMI, MSO-He comparisons to AIA, investigations of the magnetic/Doppler gradient using MSO-Na, and acoustic power spectrum analysis of the various MSO channels.
- Chapter 8 describes my efforts to model the MOF passbands of the GATES Network,

with specific emphasis on developing the model for the new He MOF.

- Chapter 9 details the next steps of the GATES' nodes, including the projected timeline of the networks' operation as well as potential future science investigations the GATES data can address.
- Chapter 10 concludes my findings, summarizing how my contributions to the development of a new space weather telescope network have progressed.

Following these sections, I include a collection of supplementary material, including the full parts list for both telescope nodes, Python codes I developed for reducing and analyzing this newly collected dataset, and additional instrumentation pictures/schematics.

CHAPTER 2
INTRODUCTION TO MAGNETO-OPTICAL FILTERS

Filtergraphs are narrow-band filters that can observe an extended field of view (FoV) and thus allow for full-disk spectropolarimetric studies. Within this class of instruments, Fabry-Pérot Interferometers (FPIs) have historically been used for high-resolution spectroscopic studies (Bailén et al. 2023) and Magneto-Optical Filters (MOFs) are gaining traction for their powerful ability to observe extremely narrow wavelength bands with intrinsic sensitivity to circular polarization. FPIs function by creating a resonant cavity between two mirrors; constructive and destructive interference allow only a selected resonant frequency to transmit through the second mirror, producing the desired narrow-band filtering effect. Although powerful for full-disk narrowband spectral selection, FPIs have some drawbacks that limit their effectiveness. Table 2.1 lists a few of these limitations and how MOFs rectify them.

MOFs operate as a fixed-band spectrograph which, when combined with polarization selection, provides an extremely narrowband image at selective wavelengths intrinsically sensitive to circular polarization (Agnelli et al. 1975; Cimino et al. 1968). MOFs have been historically developed for alkali metals (Potassium 769.9 nm and Sodium 589.0 nm, (e.g. Cacciani et al. (1971); Jefferies et al. (2005); Rhodes et al. (1988)) with new prototypes using Helium (Murphy et al. (2005) and Chapter 6) and Calcium (Rodgers et al. 2005) under development. These instruments have all been developed for spectropolarmetic studies of extended sources in our solar system — namely the Sun and Jupiter (e.g. Gulledge (2022); Shaw et al. (2022)).

Table 2.1 Highlights of the strengths of MOFs compared to FPIs.

FPIs	*MOFs*
- FPIs are *very sensitive to mirror spacing, tilt, and mechanical vibrations*; small instrumental vibrations can notably change transmission peaks (Bailén et al. 2023).	- MOFs are much more *mechanically stable*, and their transmission peaks are independent of interference.
- FPIs are *extremely sensitive to temperature* as temperature changes can alter the mirrors' spacing and refractive index, consequently shifting the passband.	- Although traditional MOFs use heated vapor cells, and are therefore sensitive to heating in this manner, their *passband operating wavelength is set by atomic transitions* and therefore is *extremely stable* (Cacciani & Fofi 1978).
- FPIs provide *relative wavelength filtering and can drift over time*, therefore require frequent recalibration for high-precision work (Santamarina Guerrero et al. 2024).	- MOFs are based on atomic spectral lines and, therefore, *provide an absolute wavelength reference*. Once they are spectrally characterized, they do not need to undergo recalibration and therefore have better long-term operational stability than FPIs (Cacciani & Moretti 1994; Sakurai et al. 1990).
- Since FPIs utilize interference, they transmit multiple peaks, which *often require higher-order filtering* for the most precise results.	- MOFs typically *provide single-order passbands*, simplifying their optical scheme.

The basic MOF, shown in the left panel of Figure 2.1, consists of a glass cell containing alkali metal vapor placed in a longitudinal magnetic field which is generated by a magnetic circuit of permanent bar magnets (right panel of Figure 2.1). The cell and magnetic assembly are placed between two crossed linear polarizers and the cells are heated to produce alkali vapor with their temperature maintained with designated electronics.

For a classic MOF, there are multiple cell designs; the two most prominently used designs (and the designs used by the GATES Network) are the reservoir cell and the ring cell (Figure 2.2). Both types of cells used in the GATES Network are comparable in size (length of 96.5

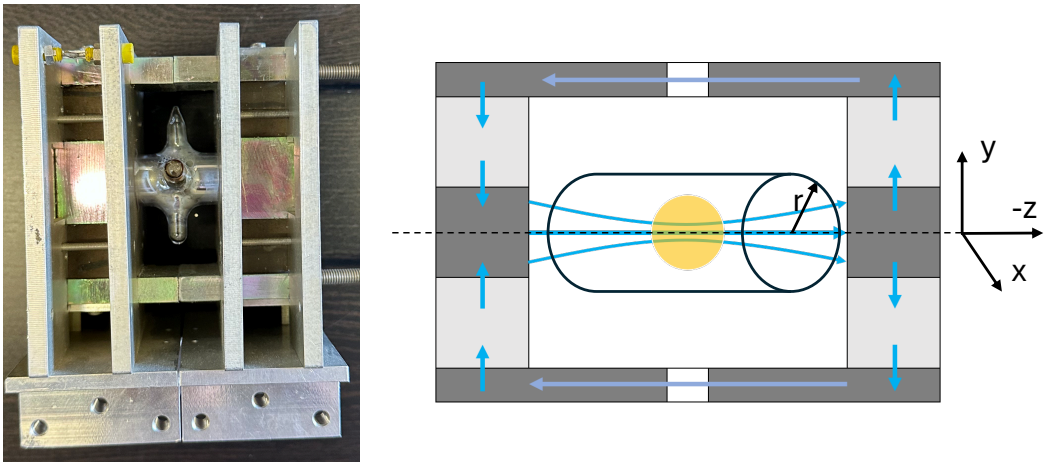

Figure 2.1 Image (left) and model (right) of a basic, alkali MOF. Blue lines indicate the direction of the magnetic field along the assembly. The coordinate system for the MOF cell/magnet assembly is present on the right. The z axis is defined along the optical beam path (longitudinal to the MOF cell), the x and y axes are respectively defined as the horizontal and vertical axes with respect to the telescope rail, and the r axis refers specifically to the MOF cell starting from the center and increasing outwards to the edge of the cylinder.

- 100 mm and a clear aperture of 19-20 mm). It is worth noting that the He cells, given their different operation, are built slightly differently. See Chapter 6 for more details.

Reservoir cells contain all of the alkali metal deposited in two wells, called reservoirs, near the center of the cell's cylinder. These reservoirs jut out along the x axis of the cells and are the only component that is heated. Ring cells consist of a "ring" of metal deposited onto the center of the body of the cell itself. Consequently, the column density of alkali vapor in the ring cell is far more uniform, and because of the larger surface area of the deposited metal, they can be operated at a lower temperature than the reservoir cells. The higher operation temperature of the reservoir cells results in wider MOF passbands than those produced by ring cells (Oliviero et al. 2011). However, this higher temperature also means that reservoir cells have a higher temperature gradient, which causes their windows to experience greater

stress. This can result in distortions that, combined with the higher operating temperature, lower the lifetime of the reservoir cells relative to ring cells.

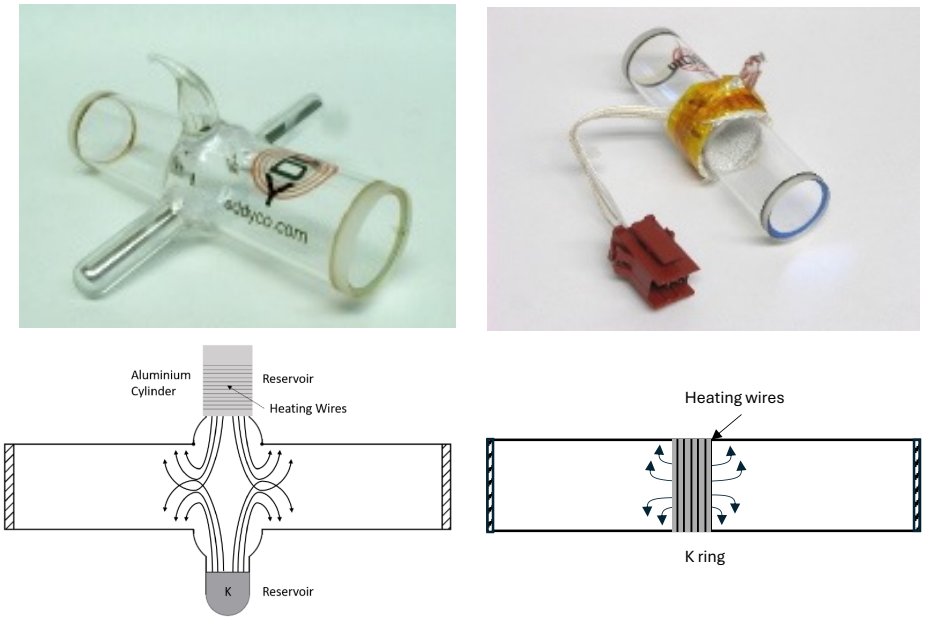

Figure 2.2 Images (top) and schematics (bottom) of reservoir cells (left) and ring cells (right). Images are from the Mojave Solar catalog. In the ring cell, the metal is deposited below the yellow thermal tape (on the inside of the cell). The pointed glass extension on both cells is not a metal reservoir, but rather the sealing location of the cell.

Within the cell, regardless of its design, two effects impact the light beam: the inverse Zeeman (Righi) and Macaluso-Corbino effects. These effects, along with polarization selection optics, allow MOFs to image each combination of red/blue wings of the σ^+/σ^- Zeeman components of light in the Sun (Stokes I+V and I-V, respectively) to produce filtergrams (R+, R-, B+, B-). Combining these filtergrams provides Dopplergram and magnetogram measurements of specific heights in the solar atmosphere. More specific information about how these effects work with the MOF cell is provided in the following subsections.

2.1 *Theoretical Principles of MOFs*

2.1.1 Polarization of Light

At the basis of all theoretical principles that MOFs exploit to produce Doppler- and magnetograms is the polarization of light. The polarization state of a wave of light describes the plane of the electric field vector with respect to the plane of light propagation. The three main types of polarization of linear, circular, and elliptical. Linear polarization is defined by the electric field vector oscillating along a fixed direction in a plane perpendicular to the light propagation: vertical or horizontal. Circular polarization is defined by the electric field vector which rotates with a constant magnitude, thus tracing a circle: right-hand circularly polarized (σ^+) or left-hand circularly polarized (σ^-). Elliptical polarization is the most general case and occurs when the electric field vector traces an ellipse; it is a combination of linear and circular polarization. To generalize these states, the Jones formalism is often used, in which a wave of light propagating in the z direction will be described as

$$\vec{E}(z,\omega,t) = E_{0,x}\exp\left[i(\omega t - kz + \phi_x)\right]\hat{e}_x + E_{0,y}\exp\left[i(\omega t - kz + \phi_y)\right]\hat{e}_y, \tag{2.1}$$

where $\omega = 2\pi\nu$ is the angular frequency, $k = 2\pi/\lambda$ is the wave number, ϕ_x, ϕ_y are the phases, and $E_{0,x}, E_{0,y}$ are the initial components' magnitudes along the x, y axis.

A particularly important remark for the operation of MOFs is that linearly polarized light can be described as the sum of two circularly polarized waves with opposite circular polarization states. In the Jones formalism:

$$\vec{E}(z,t) = \frac{E_0}{\sqrt{2}}(\hat{e_-} + \hat{e_+})e^{i(kz-\omega t)}, \tag{2.2}$$

where $\hat{e_-}, \hat{e_+}$ represent the left-handed and right-handed circular polarization vectors and $e^{i(kz-\omega t)}$ is the common plane-wave factor. The common plane-wave factor is the same for all polarization components of a specific wave of light. Consequently, for a given beam of light, we can simplify Equation 2.2 into its Jones matrix form:

$$\vec{E} = \begin{pmatrix} 1 \\ 0 \end{pmatrix} = \frac{1}{\sqrt{2}}(\hat{e_-} + \hat{e_+}) = \frac{1}{2}\begin{pmatrix} -i \\ 1 \end{pmatrix} + \frac{1}{2}\begin{pmatrix} i \\ 1 \end{pmatrix}. \tag{2.3}$$

2.1.2 The Zeeman and Inverse Zeeman Effects

The Zeeman effect is the splitting of atomic energy levels when an atom is placed in a magnetic field (Zeeman 1897). The atomic energy levels split according to the equation

$$\Delta E = h\Delta\nu = g_J M_J B \mu_B \tag{2.4}$$

where h is Planck's constant, ν_o is the atomic line's laboratory frequency, g_J is the Landè factor (defined in Equation 2.5 below), L, S, J are the orbital number, spin number, and total angular momentum, respectively, M_J is the magnetic angular momentum and must be an integer between $-J$ and J, B is the magnetic field, and μ_B is the Bohr magnetron.

$$g_J = 1 + \frac{J(J+1) + S(S+1) - L(L+1)}{2J(J+1)} \tag{2.5}$$

Expanding Equation 2.4 due to a transition from level J to level J' produces

$$\Delta\nu = \frac{\mu_B}{h} B(g_J M_J - g_{J'} M_{J'}) = \frac{\mu_B}{h} B g_{eff} \Delta M_J \tag{2.6}$$

where g_{eff} is the effective Landè factor and ΔM_J allows us to define the Zeeman components, which are pictured in Figure 2.3. We can define the π component when $\Delta M_J = 0$ and the $\sigma^{\pm}$ components when $\Delta M_J = \pm 1$. Considering Equation 2.6, we see that the π component does not have any shift with respect to the laboratory frequency; it is only the $\sigma^{\pm}$ components that have an effective shift. In wavelength space the $\sigma^{\pm}$ components shift is

$$\Delta\lambda \approx 4.67 \times 10^{-13} \lambda_o^2 g_{eff} B \tag{2.7}$$

where λ_0 is the laboratory wavelength of the absorption line in units of Å, and B is the magnetic field in units of Gauss.

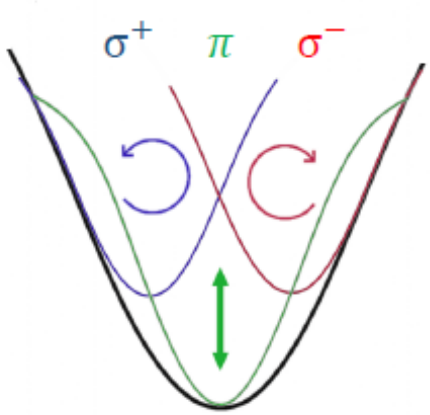

Figure 2.3 An exaggerated absorption line profile produced by the blending of the Zeeman triplet. The linearly polarized (π) line core is depicted in green, the right-hand circularly polarized (σ^+) blue wing is depicted in blue, and the left-hand circularly polarized (σ^-) red wing is depicted in red. Reproduced from Chiodini (2025).

When solar magnetic fields are present and detectable, the atomic lines we observe from the Sun have already been Zeeman-split. During the formation of the atomic lines on the Sun, the Zeeman effect has two impacts. Firstly, the rest frequency of the line will be split into three components (π, σ^+, σ^-) as defined by Equation 2.6. Secondly, the three split frequencies have different polarization states. The π component will have a linear polarization parallel to the LoS magnetic field, and the $\sigma^{\pm}$ components will have opposite circular polarization states perpendicular to the LoS magnetic field.

To measure the LoS velocity and magnetic fields of the Sun, MOF-based telescopes leverage the Zeeman effect again, but inversely. The MOF cells are filled with an atomic vapor that is initially unpolarized and placed in a longitudinal magnetic field (along the z axis). The light that enters the MOF cell corresponds to one of the $\sigma^{\pm}$ states from the Sun, which has been encoded in linearly polarized light thanks to the polarization selection portion of the telescope (Section 2.2.2).

Recalling that linearly polarized light can be thought of as a superposition of two circularly polarized components, the circularly polarized components of light interact with the M_J sublevels of the atomic vapor, preferentially exciting $\Delta M_J = \pm 1$ transitions. This splits the red and blue wings of the line (Figure 2.4) and allows the vapor to absorb one of the circularly polarized components (right-hand circularly polarized: RHCP or left-hand circularly polarized: LHCP). The width of the absorption bands depends on the temperature inside the cell and the intensity of the incoming light (Oliviero et al. 1998; Oliviero et al. 2011). As with the traditional Zeeman effect, the distance between the RHCP and LHCP bands

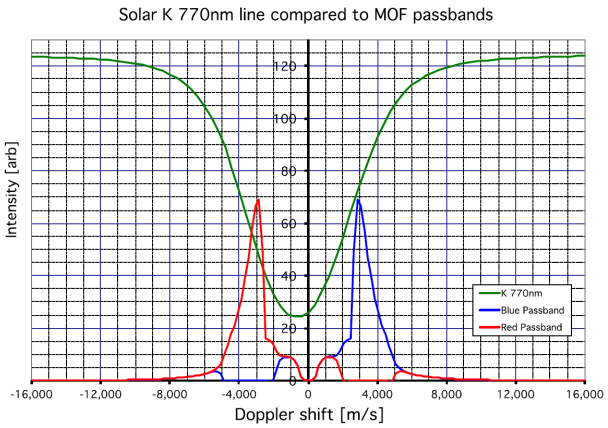

Figure 2.4 MOF transmission (red and blue wings) compared to the spectral absorption line as a function of wavelength. Reproduced from Calchetti et al. (2020a).

depends on the strength of the magnetic field within the cell. Moreover, in different magnetic field regimes, the way the Zeeman effect is leveraged alters slightly. See Section 2.2 for more details. The inverse Zeeman effect that occurs within the MOF cell can also be referred to as the Righi effect; the Righi effect is defined as the Zeeman effect observed in absorption or emission of light in the presence of a magnetic field, specifically when the splitting of spectral lines leads to polarization-dependent absorption or emission (Righi 1906).

2.1.3 The Faraday and Macaluso-Corbino Effects

The Faraday effect, also called Faraday rotation, is a magneto-optical phenomenon in which the polarization plane of linearly polarized light is rotated when the light travels through a medium that is subjected to a longitudinal magnetic field (oriented along the direction of light propagation). This phenomenon relies on the principle that linearly polarized light is the superposition of two circularly polarized components. In the presence of a magnetic field, these two circular components travel at slightly different speeds due to a difference

in the refractive index for each polarization state; this property is also known as circular birefringence (Fresnel & Putland 2021). This difference in speed produces a relative phase shift between the two components, resulting in a rotation of the overall phase plane (Faraday 1846). The amount of rotation (θ), described in Equation 2.8, is proportional to the magnetic field strength (B), the length of the medium (L), and the Verdet constant of the material (V):

$$\theta = VBL. \tag{2.8}$$

The Verdet constant is an experimentally determined parameter that quantifies the sensitivity of a medium's optical polarization to an applied magnetic field; it varies with wavelength, temperature, and material purity (Vojna et al. 2019).

If the medium in which the Faraday rotation occurs is an atomic vapor, a resonant regime of Faraday rotation can arise, and consequently, an enhanced rotation of polarized light near the atomic resonance line occurs; the resonant line's rotation becomes 90°. This phenomenon is called Resonant Faraday Rotation or the Macaluso-Corbino effect, after the two scientists who first discovered it experimentally (Macaluso & Corbino 1898). The physical result of the Macaluso-Corbino effect in the MOF is that the RHCP and LHCP components (wings) become linearly polarized and are therefore able to pass through the crossed linear polarizer at the end of the cell.

Using the Jones matrix formalism, assuming the incoming light entering the cell is linearly polarized, and therefore described by Equation 2.3, we begin by defining the refractive indices

(n) for σ^+ and σ^- as

$$n_\pm(\omega) = n_0(\omega) \pm \Delta(\omega, B) \tag{2.9}$$

where ω is the angular frequency of the light and B is the magnetic field. After propagating a distance L, the circularly polarized light components acquire different phase factors and can be defined by

$$J_{\mathrm{MC}}^{(\mathrm{circ})} = \begin{pmatrix} e^{ikn_+L-\alpha_+L} & 0 \\ 0 & e^{ikn_-L-\alpha_-L} \end{pmatrix} \tag{2.10}$$

where $k = \omega/c$ is the wave number, and $\alpha_\pm$ are the absorption coefficients for the circular components. We define the differential phase shift and average phase:

$$\Delta\phi = k(n_+ - n_-)L \qquad \phi_0 = k(n_+ + n_-)\frac{L}{2} \tag{2.11}$$

as well as the differential absorption:

$$\Delta\tau = \tau_+ - \tau_- \qquad \bar{\tau} = \frac{\tau_+ + \tau_-}{2} \tag{2.12}$$

The Jones matrix in circular form then becomes

$$e^{i\phi_o}e^{-\bar{\tau}L}\begin{pmatrix} e^{i\Delta\phi/2}e^{-\Delta\tau/2} & 0 \\ 0 & e^{-i\Delta\phi/2}e^{\Delta\tau/2} \end{pmatrix}. \tag{2.13}$$

In the case of pure Macaluso-Corbino effect, no ellipticity is introduced, and the Jones matrix can simplify into linear form as

$$e^{\tau^\pm}\begin{pmatrix} \cos\frac{\Delta\phi}{2} & -\sin\frac{\Delta\phi}{2} \\ \sin\frac{\Delta\phi}{2} & \cos\frac{\Delta\phi}{2} \end{pmatrix} \tag{2.14}$$

where $\frac{\Delta\phi}{2}(\lambda)$ is the phase retardation and $e^{\tau(\lambda)^\pm}$ is the global absorption factor for the σ^+ and σ^- polarizations states; both are functions of wavelength. The final transmitted intensity is

therefore

$$T(\lambda) = \frac{1}{4}(e^{-\tau^+} - e^{-\tau^2})^2 + \frac{1}{2}e^{-(\tau^+ + \tau^-)} \sin^2 \frac{\Delta\phi}{2} \tag{2.15}$$

where $\Delta\phi$ and τ remain a function of wavelength.

2.1.4 History of MOFs

The concept for the MOF began in the 1960s with the possibility to use the atomic-beam method for high-resolution spectroscopy (Blamont & Roddier 1961) and a way to leverage the Maccaluso-Corbino effect to make a gas in a longitudinal magnetic field behave as a birefringent medium (Öhman 1960). These concepts were combined by Cimino et al. (1968) to produce "a new kind of very narrow-passband filter...for detecting solar magnetic fields without a spectrograph"; the authors' follow-up works (Cacciani et al. 1971; Cimino et al. 1970), developed the theoretical description of the MOF and the first schematic of an MOF-based instrument (Figure 2.5). These first MOF cells were filled with Na and created filters around the Na I D1 (589.6 nm) and Na I D2 (589.0 nm) Fraunhofer lines.

This MOF-based instrument first acquired filtergram and intensitygram images of regions of the Sun on May 11, 1974 (Agnelli et al. 1975) (Figure 2.6). Several developments were made to the instrument (e.g. Cacciani (1981); Rhodes Jr et al. (1984)), before it achieved full-disk LoS Dopplergram and Magnetogram on June 17, 1987 (Cacciani et al. 1990a; Rhodes et al. 1988) (Figure 2.7). Employing the approach described in Appourchaux (1987), the Cacciani-Cimino style instrument was able to be adapted to operate as vector magnetograph at Big Bear Solar Observatory (Cacciani et al. 1991; Cacciani et al. 1990b).

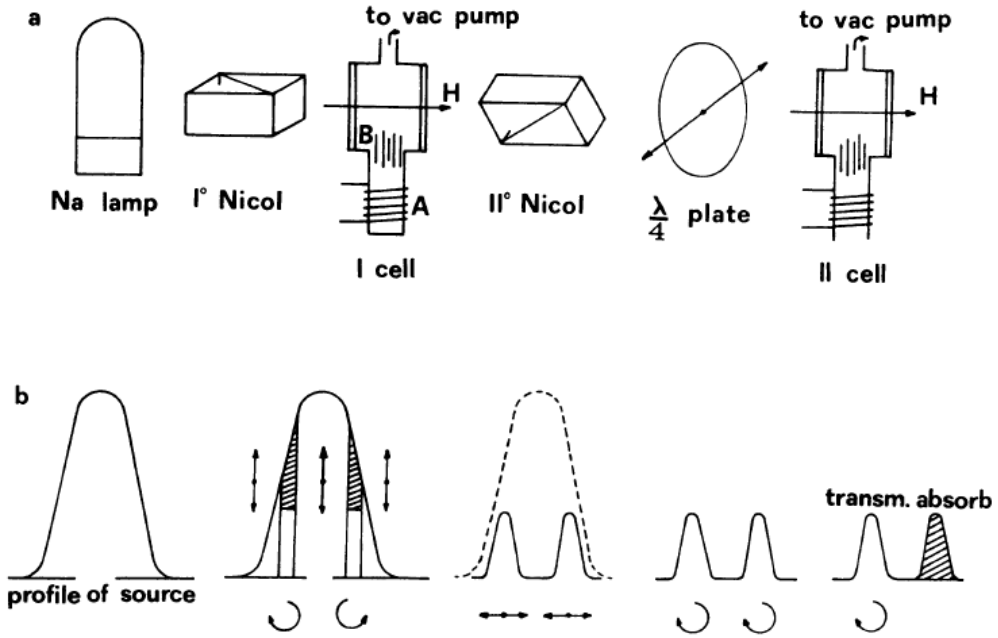

Figure 2.5 Schematic of first experimental MOF (a), and the corresponding light profiles at each step (b). Reproduced from Cacciani et al. (1971).

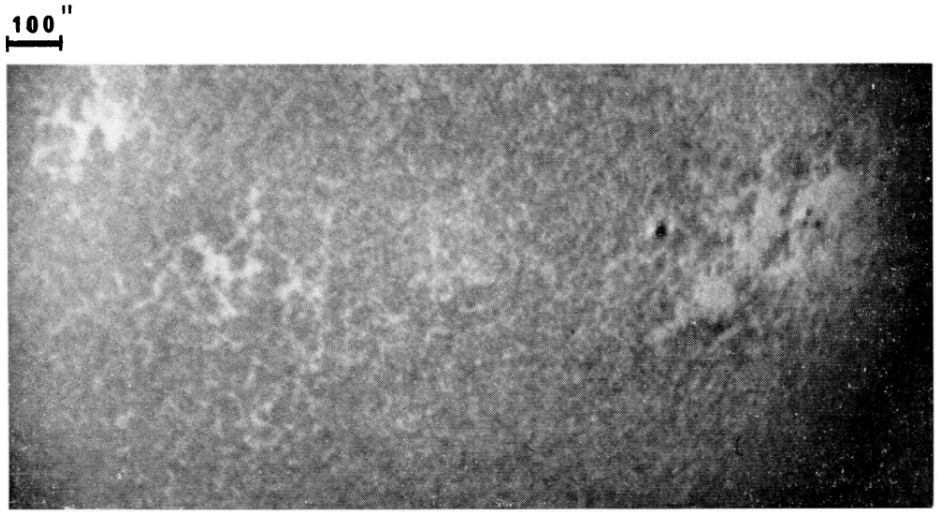

Figure 2.6 First solar image achieved utilizing an MOF. Acquired from Mount Wilson on May 11, 1974, at 11:40 UT. Image reproduced from Agnelli et al. (1975).

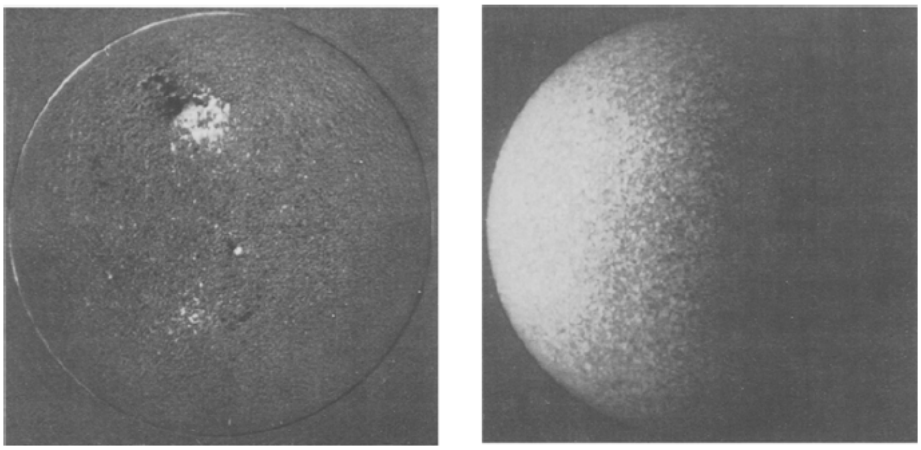

Figure 2.7 First magnetogram (left) and Dopplergram (right) achieved utilizing an MOF. Acquired from Mount Wilson on June 17, 1987. Image reproduced from Cacciani et al. (1990a).

Since the original MOF-based instruments' development, there have been multiple iterations of MOF-based instruments for solar studies. The most notable of these instruments include:

- Na MOF at Mount Wilson: developed in the late 1980s and mounted on the 60-foot solar tower of the Mount Wilson Observatory. This MOF-based instrument performed the first solar MOF observations on June 18, 19, and July 1, 1987. It operated in the Na I D1/D2 wavelengths (589.6 nm and 589.0 nm) with a 2.3" pixel size, and achieved both LoS Doppler- and magnetograms of the full disk of the Sun with a cadence of 25 s. The instrument operated with a simpler optical scheme than modern MOF-based instruments (see Figure 1 of Rhodes Jr et al. (1988)), but still achieved full-disk Doppler- and magnetograms.
- LOW degree l (LOW-l): developed in 1994 and mounted in the Mauna Loa Solar Observatory. This instrument operated at the K I D1 769.9 nm line and achieved a

25" spatial resolution on full-disk images acquired every 15 s (Cacciani et al. 1995; Tomczyk et al. 1995). LOW-l was designed to observe low-degree solar oscillations, and its data has been used for multiple helioseismic studies, such as constraining the structure of the tachocline (Charbonneau et al. 1999) and inferring the rotation rate of the solar core (Chaplin et al. 1999; Charbonneau et al. 1998).

- The Rome Network for Doppler and Magnetic Oscillations (RODOMA): originally developed in 1996 and consisted of two observatories, one at the Kanzelhöhe Solar Observatory in Austria and Eddy Co. Observatory in California, USA, which operated in 1998 (Cacciani et al. 1998b). These instruments operated at the Na I D1/D2 wavelengths (589.6 nm and 589.0 nm) and achieved full vector magnetic field measurements with a resolution of 1.5" with a maximum cadence of 1 *minute* (Cacciani et al. 1998). RODOMA's data was intended to provide ground-based support for helioseismological experiments such as SOHO, and was used for case studies of magnetic topology in active regions (Cacciani et al. 1998).
- Velocity And Magnetic Observations of the Sun (VAMOS): developed in 1998 and installed at the Capodimonte Observatory. This instrument operated at the K I D1 769.9 nm line and achieved a spatial resolution of 12" on full-disk images acquired with a cadence of 1 *minute* (Cacciani et al. 1997; Moretti et al. 1997; Oliviero et al. 1998). The VAMOS data has been used in studies such as investigating the source of solar oscillations (Moretti et al. 2001), measuring supergranulation patterns (Formicola et al. 2007), and determining the phase relationship between velocity and intensity

fluctuations in the photosphere (Magrì et al. 2008).

- Magneto-Optical filters at Two Heights (MOTH): developed in the early 2000s and used in multiple observing campaigns at the South Pole. This instrument was a dual-channel K I D1 769.9 nm and Na I D2 589.0 nm MOF instrument that achieved simultaneous LoS full-disk Doppler- and magnetograms at the two heights with a 5.3" resolution and an imaging cadence of 10 s (Cacciani et al. 2003). The longest of the MOTH's South Pole campaigns was during the austral summer of 2002-2003 where 260 hours 35 minutes of data was acquired (Finsterle et al. 2004b). The MOTH instrument was later updated and installed at the Mees Observatory in Hawaii, with the aperture being increased to 20 cm in 2007, prior to being redeployed to the South Pole for two additional observing campaigns in the austral summer of 2016-2017 and 2017-2018. Data from the various South Pole observing campaigns have contributed to studies such as mapping the acoustic cut-off frequency (Jefferies et al. 2019) and wave reflection (Chaturmutha et al. 2024) in the solar atmosphere, as well as determining phase perturbations throughout the atmosphere with respect to flare precursors (Aparna 2022).
- Solar Activity MOF Monitor (SAMM): achieved first-light images mounted on the roof of Avalon Instruments headquarters in Aprilia, Italy on October 10, 2019. SAMMs are K I D1 769.9 nm and Na I D2 589.0 nm MOFs with 0.8" and 0.65" resolution, respectively, designed to study smaller regions of the Sun (FoV $8.3 \times 9.8\ arcmin^2$) with a cadence of 80 s (Speziali et al. 2021; Stangalini et al. 2018). These instruments were

developed as part of the proposed Solar Activity Monitor Network (SAMNet), which has the goal of continuously monitoring the Sun's intensity, magnetic, and Doppler velocity fields at multiple heights in the solar atmosphere (Erdélyi et al. 2022)

- Global Automatic Telescopes Exploring the Sun (GATES) Network: a new network of MOF-based instruments built on the success of the MOTH team. GATES currently consists of two telescopes, the Tor Vergata Synoptic Solar Telescope (TSST: Chapter 3) and the Mojave Solar Observatory (MSO: Chapter 4). The TSST contains a K I D1 769.9 channel (TSST-K) nm MOF with 2.4" resolution and operates at a cadence of 50 s (Calchetti et al. 2020b; Giovannelli et al. 2020b). MSO contains a dual-channel K I D1 769.9 nm and Na I D2 589.0 nm telescope (MSO-K and MSO-Na, respectively), which operates simultaneously at a cadence of $5s$ and achieves 3.81" and 2.91" resolution, respectively. GATES is also designed to continuously monitor the Sun's intensity, magnetic, and Doppler velocity fields at multiple heights in the solar atmosphere (Konow et al. 2024) and has achieved dual-site first light images (Chapter 5).

Although to date the only operational MOF-based telescopes have been ground-based, there have been multiple MOF-based instruments proposed for space missions. A dual-band Na D1/D2 MOF-based instrument was initially proposed for SO and was considered for the NASA STEREO missions (Cacciani et al. 2001). Additionally, the Advanced Astronomy for HELIOphysics (ADAHELI) mission, which is a small-class Italian Space Agency (ASI) mission that has completed Phase-A feasibility, proposed a dual-channel Na I D2 589.0 nm

and K I 769.9 nm MOF channel (Berrilli et al. 2010; Moretti et al. 2010; Stangalini et al. 2011). Moreover, there have been two proposed compact MOF-spacecraft in recent times: the Solar Activity Investigation (SAI) was a proposed 6U CubeSat mission which proposed a single-channel K I 769.9 nm MOF channel (Murphy et al. 2017) and Calcines Rosario et al. (2023) proposed multiple designs for an ultra-compact Na MOF.

Furthermore, MOFs have been used for planetary studies, most notably to study Jupiter, as in Cacciani et al. (1998a), and with the Planetary Multilevel Oscillations and Dynamics Experiment (PMODE) instrument (Shaw et al. 2022). PMODE's main observational focus was dioseismology of Jupiter, and, through a 137-hour observational campaign in 2022, was able to place constraints on the global mode amplitudes of Jupiter's zonal winds. PMODE also obtained a rich dataset with 25 hours of Uranus observations and a spare few hours of Mars and Venus observations (Gulledge 2022).

2.2 *MOF-based Telescope Operating Modes and Schematics*

The basic MOF-based telescope can be divided into four sections: the broadband filtering section, the polarization selector section, the filter (MOF) section, and the wing selector (WS) section. Although the basic theoretical principles behind their operation remain the same, multiple mechanics and parameters within each section slightly alter the telescope's operation. There are broadly two different operating modes: Cacciani mode and Tomczyk mode, which leverage the inverse Zeeman effect differently and have different filtergram imaging sequences.

Cacciani mode is the classic operating mode of MOFs detailed in e.g. Agnelli et al. (1975); Cacciani & Fofi (1978); Cacciani et al. (1990a). In this mode, the MOF cell operates at a lower magnetic field than the WS cell (and an MOF cell in Tomczyk mode). The MOF cell, therefore, relies more heavily on the Macaluso-Corbino effect to rotate the polarization of incoming light than it does on the Zeeman effect to absorb one of the polarization states. Cells are also run hotter in Cacciani mode, resulting in broader passbands and higher transmission. Additionally, Cacciani mode employs a secondary polarization modulator in between the MOF and WS sections, so that filtergram states are imaged sequentially; the TSST-K operates in Cacciani mode.

Tomczyk mode is a polarization-modulation mode of MOFs, detailed in e.g., Rhodes Jr et al. (1984); Tomczyk et al. (1995). In this mode, the MOF cell and WS cell are operated at the same (higher compared to Cacciani mode) field strength. The higher field MOF cells do not rotate the light's polarization as much, but rather leverage the selective absorption of the Zeeman effect. For the incoming linearly polarized light (superposition of two circular components), the stronger Zeeman effect absorbs one of the circularly polarized components (superposition of two linear components), resulting in a transmission through the cell of half the intensity of the incoming beam. Despite this, Tomczyk MOF cells are designed such that their MOF passbands exactly align with their WS absorption bands (and have a further separation compared to Cacciani mode), thereby reducing cross-talk between the two bands. Furthermore, rather than having the polarization state rotated after the MOF, Tomczyk mode has light exiting the MOF that directly enters the WS, and utilizes a polarizing beam

splitter present after the WS to separate out the wings of a given circular polarization. This allows for a more compact optical design; all channels at MSO currently operate in Tomczyk mode.

It is worth noting that although the TSST-K operates in Cacciani mode and MSO operates in Tomczyk mode, optical specifications of the specific telescopes are not fully indicative of their operation mode. For example, TSST-K utilizes reservoir cells and MSO ring cells; however, either operating mode (Cacciani or Tomczyk) can use either cell. Additionally, MSO uses a liquid crystal variable retarder (LCVR) as a half-wave plate (HWP) in its polarization selection section, but again, LCVRs can be implemented in either operating mode. The optomechanical differences in Cacciani and Tomczky modes lie solely in the WS section, specifically in whether the polarized light is modulated before the WS cell or split after the WS cell (Section 2.2.4).

The subsections below provide more detail on each section of MOF-based telescopes and how the optics differ between the two GATES telescopes. Figures 2.8 (Cacciani mode: TSST) and 2.9 (Tomczyk mode: MSO) depict the general optical setup, along with the polarization state and passband of the light beam in different steps for both telescopes.

2.2.1 *The Broadband Filter Section*

When observing the Sun in a narrow band, as with an MOF, it is critical to have broadband filtering, or pre-filtering, at the front of the telescope for energy rejection. Since the Sun delivers an enormous amount of energy across a wide range of wavelengths, even for smaller objective telescopes, like those of the GATES telescopes, the concentration of all of the Sun's

energy can damage internal optics. Lenses, mirrors, and narrowband filters are subject to warping when overheated, which can greatly degrade their precision and therefore the image quality. Moreover, excess broadband light can cause thermal drift on narrowband filters, shifting the passband off of the spectral line. Furthermore, heat buildup within the telescope can cause air turbulence inside the enclosure, causing a "telescope seeing" effect which will also degrade the image quality.

To prevent these effects, all MOF-based telescopes have some type of broadband pre-filtering. For single-channel MOFs, like the TSST (see Chapter 3 for more specifics), pre-filtering is often done with high- and low-cut filters, which eliminate excess UV and IR light, followed by a wavelength-specific filter to further eliminate unwanted radiation. For dual-channel MOF telescopes such as MSO, the presence of high- and low-cut filters is still common, but can also be incorporated directly into the telescope's beam splitter/mirrors. As is the case with MSO, the presence of custom optics for light splitting allows for individual optics to act both as filters and mirrors (see Chapter 4 for more specifics).

2.2.2 The Polarization Selector Section

The Polarization Selector Section (steps 0 - 2 in Figures 2.8 and 2.9) consists of a quarter-wave plate (QWP) and a variable half-wave plate (HWP), which eliminates excess right- or left-handed circular polarization (σ^+ or σ^-) from magnetically active regions so that one state may be imaged at a time. The QWP, oriented at an angle 45° with respect to the first linear polarizer P1, changes the circularly polarized light from the Sun into linearly polarized light so that it can pass through P1 of the MOF section. The variable HWP

alternates between two states (parallel to P1 or at an angle 45°) to allow for either σ^+ or σ^-, encoded in a linear polarized state, to pass through P1 at a time.

With the TSST, the HWP is a mechanically rotating HWP that requires a full filtergram exposure before the other state can be imaged. At MSO, this HWP is a LCVR that alternates between states with an applied voltage, allowing both polarization states to be imaged within the same exposure. With the use of an LCVR, states are still imaged consecutively, but with rapid state changes, with a frequency on the order of kHz (Meadowlark Optics 2019), each polarization state's filtergram is populated near simultaneously.

2.2.3 The MOF Section

The MOF Section (steps 3 - 5 in Figures 2.8 and 2.9) consists of a vapor cell, filled with the ion of investigation, placed in a longitudinal magnetic field (see Figure 2.1, between crossed linear polarizers (P1 and P2). Due to the Inverse Zeeman effect and Macaluso-Corbino effect (Sections 2.1.2 and 2.1.3), only two narrow passbands of light, located in either wing of the corresponding ion's absorption line, are transmitted through the second polarizer; the separation of these passbands corresponds to the strength of the magnetic field and vapor density in the cell. As described above, Tomczyk mode operates the MOF at a lower cell temperature and higher magnetic field compared to Cacciani mode, resulting in a lower total transmission but with less crosstalk between bands.

2.2.4 The WS Section

The WS section (steps 6 - 8 in Figures 2.8 and 2.9) consists of an additional vapor cell/magnet assembly, an additional QWP (QWP2) and either an additional variable HWP (HWP2) or a polarizing beam splitter (PBS). The order of these optics depends on the operational mode, as does the resultant filtergram imaging.

Cacciani Mode: In Cacciani mode, the WS section consists of HWP2, QWP2, and the WS cell/magnet assembly. Light exiting the MOF Section first encounters HWP2, oriented parallel or 45° with respect to P2, which either maintains the light's polarization state or rotates is 90° to align with the wing-selecting passband. QWP2, oriented at 45° with respect to P2, then changes the linearly polarized light back to circularly polarized light. Upon entering the WS cell, the inverse Zeeman effect created an absorption band, eliminating one of the wings (red wing with RHCP and blue wing with LHCP will be absorbed) and consequently allowing the other wing to pass. Alternating the orientation of HWP2 inverts the polarization state of the wings, thus allowing the opposite wing to pass. This mode allows one filtergram to be obtained per exposure, and the limiting factor for the frame rate is the time required to change the HWPs' states.

Tomczyk Mode: In Tomczyk mode, the WS cell/magnet assembly is placed directly after the MOF Section, and is followed by QWP2 and a polarizing beam splitter (such as a Wollaston prism: WA). The linearly polarized light, which is a superposition of RHCP and LHCP states, exiting the MOF Section undergoes the same inverse Zeeman effect in the WS cell as in Cacciani mode. Consequently, the WS will absorb the RHCP of the red wing and

LHCP of the blue wing, resulting in a LHCP red wing and RHCP blue wing exiting the cell. QWP2 then converts this circularly polarized light into two orthogonal linearly polarized components. Finally, WA splits the light based on its linear polarization state and sends them to two different sensors or two different regions of the same sensor. This mode allows for two filtergrams to be imaged simultaneously. Since this mode operates using an LCVR for HWP1, the filtergrams of different states are rapidly alternated between, and all four filtergrams can be acquired within the same exposure time through a sum of brief frames.

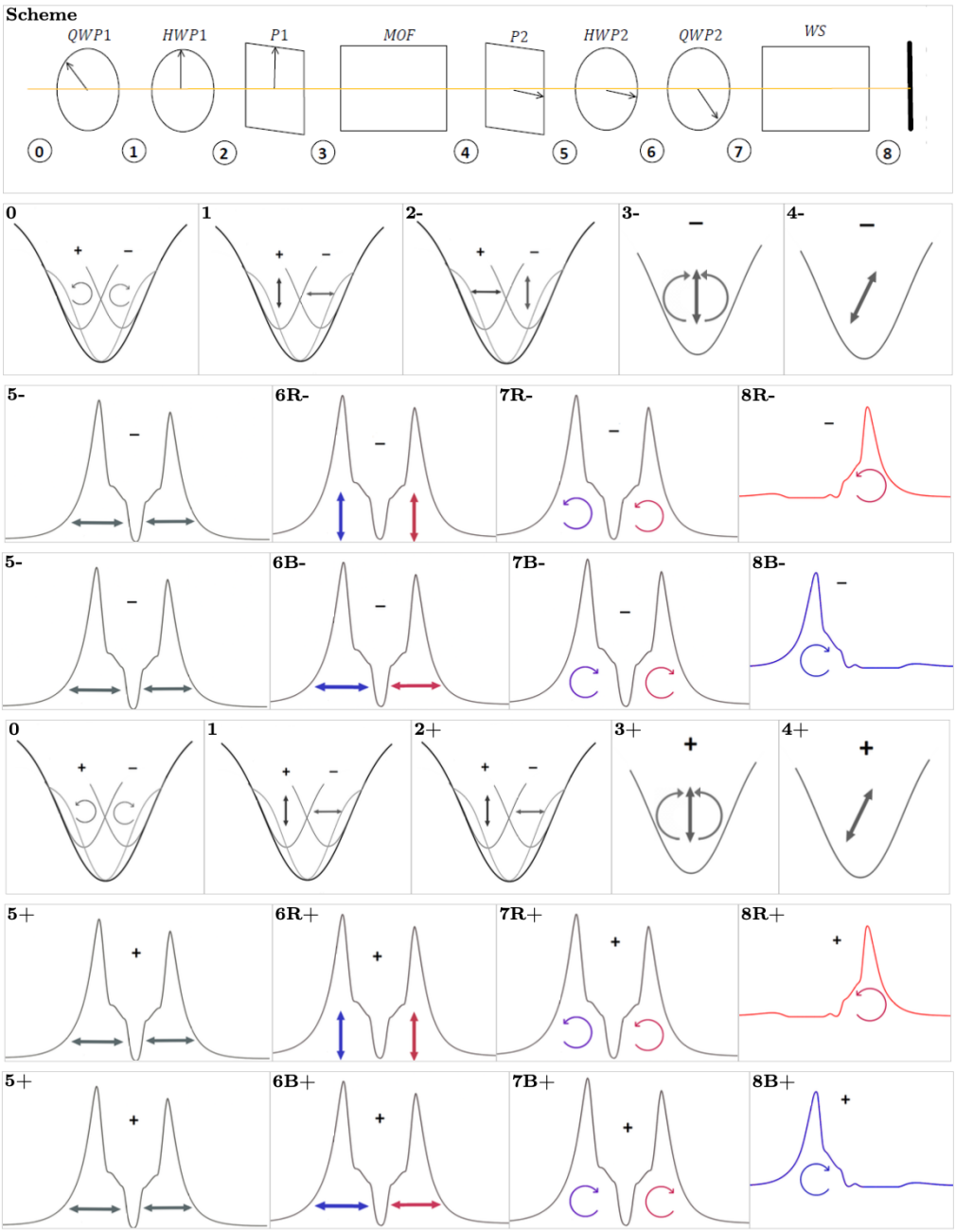

Figure 2.8 Simplified optical set-up (excluding imaging optics) of an MOF-based telescope operating in Cacciani mode (top row) and the resultant polarization state and passband shape at each point in the telescope. '+' and '-' refer to the circularly polarized states RHCP and LHCP as produced on the Sun. Rows 2 - 4 depict the imaging process for the solar σ^+ state $(I + V)$, with rows 3 and 4 depicting the red and blue wings of this state, respectively. Rows 5 -7 reproduce this scheme for the solar σ^- state $(I - V)$. Figure adopted from (Chiodini 2025); the transmission profiles depicted come from the TSST spectral characterization reported in (Calchetti et al. 2020b). In the MOF section (steps 3 - 4), part of the continuum is present, but is not shown for simplicity.

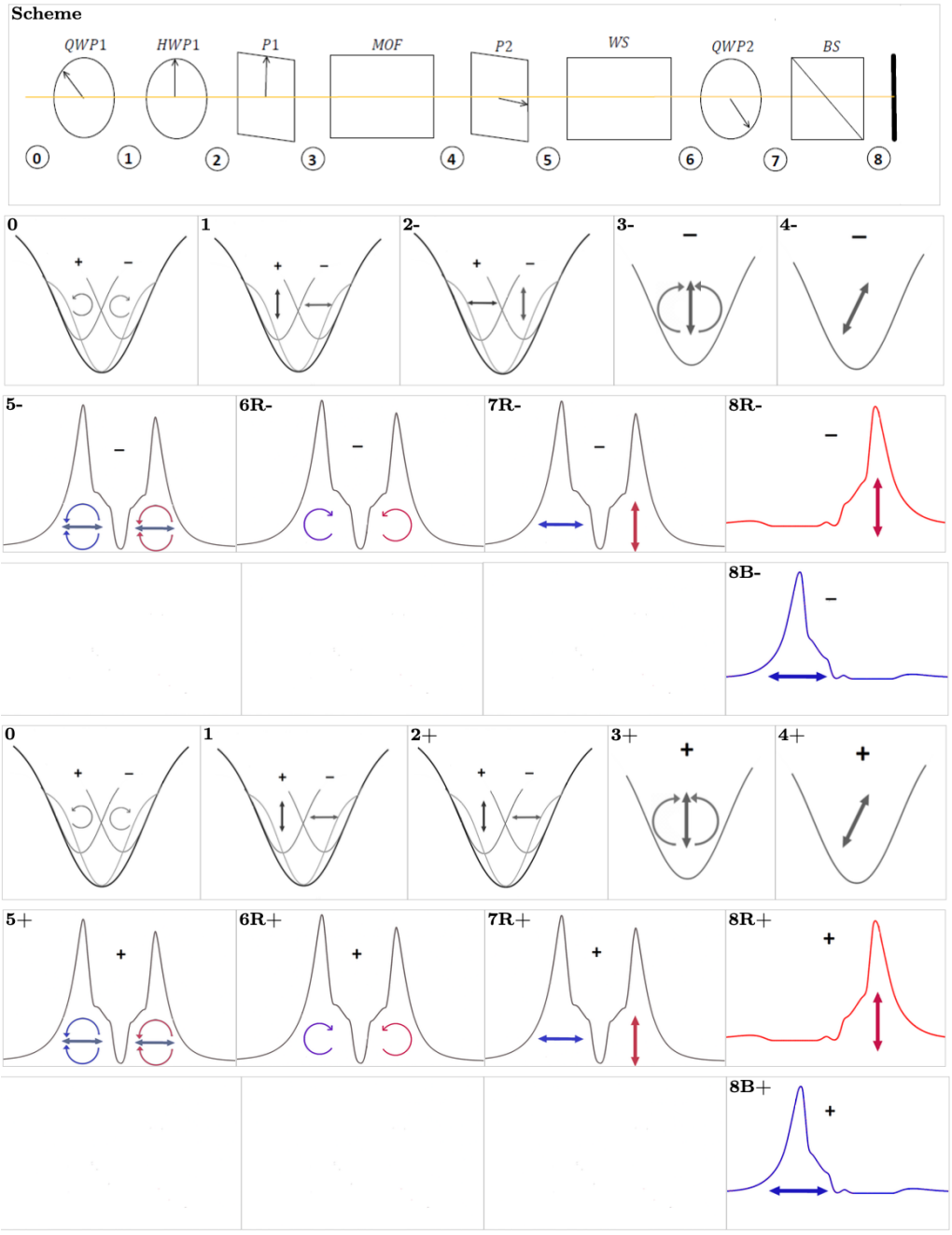

Figure 2.9 Same as Figure 2.5 for the Tomczyk mode.

2.3 *MOF Products*

The raw data products of MOF-based telescopes are intensity maps for a particular wing/polarization state. These maps are called filtergrams, and there are four in a full filtergram suite: red-wing RHCP, blue-wing RHCP, red-wing LHCP, blue-wing LHCP (R^+, B^+, R^-, B^- respectively). Figure 2.10 shows an example of a full filtergram suite. The sum of these filtergrams reproduces the intensity of the Sun at the given wavelength and is referred to as an intensitygram. Using the filtergrams, it is possible to generate the line-of-sight (LoS) Dopplergram (V^*_{Los}) and LoS magnetogram (B^*_{Los}) (Figure 2.11) using the equations from Cacciani et al. (1990a):

$$V^*_{LoS} = \frac{R^+ - B^+}{R^+ + B^+} + \frac{R^- - B^-}{R^- + B^-} \tag{2.16}$$

$$B^*_{LoS} = \frac{R^+ - B^+}{R^+ + B^+} - \frac{R^- - B^-}{R^- + B^-}. \tag{2.17}$$

These equations generate Doppler- and magnetogram maps proportional to the LoS velocity and magnetic fields. The calibration procedures to convert these maps into physical units are described in Oliviero et al. (1998), Vogt et al. (1999), and Oliviero et al. (2010). Additionally, the maps produced by Equations 2.16 and 2.17 contain the entire Doppler- and magnetograms, but there exists intermediate Doppler- and magnetograms that are also useful data products. By subtracting the two polarization states of a given wing from each other, so-called 'Red-Wing (RW) magnetograms' and 'Blue-Wing (BW) magnetograms' are produced. Similarly, by subtracting the red and blue wings of a given polarization state from each other, so-called 'RHCP Dopplergrams' and 'LHCP Dopplergrams' are produced. An

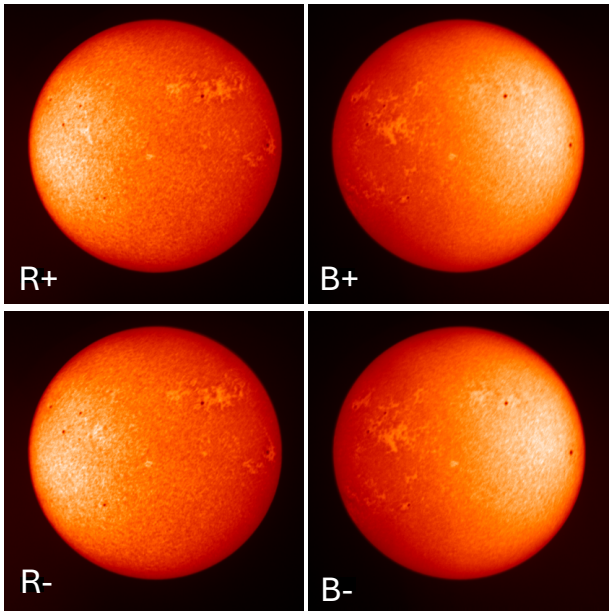

Figure 2.10 Examples of raw filtergrams (R^+, B^+, R^-, B^-) acquired by the MSO-Na channel on July 31, 2025.

example of these intermediate grams and their final products (from Equations 2.16 and 2.17 can be found in Figure 2.11.

$$B^*_{LoS:RW} = \frac{R^+ - R^-}{R^+ + R^-} \qquad B^*_{LoS:BW} = \frac{B^+ - B^-}{B^+ + B^-} \tag{2.18}$$

$$V^*_{LoS:RHCP} = \frac{R^+ - B^+}{R^+ + B^+} \qquad V^*_{LoS:LHCP} = \frac{R^- - B^-}{R^- + B^-} \tag{2.19}$$

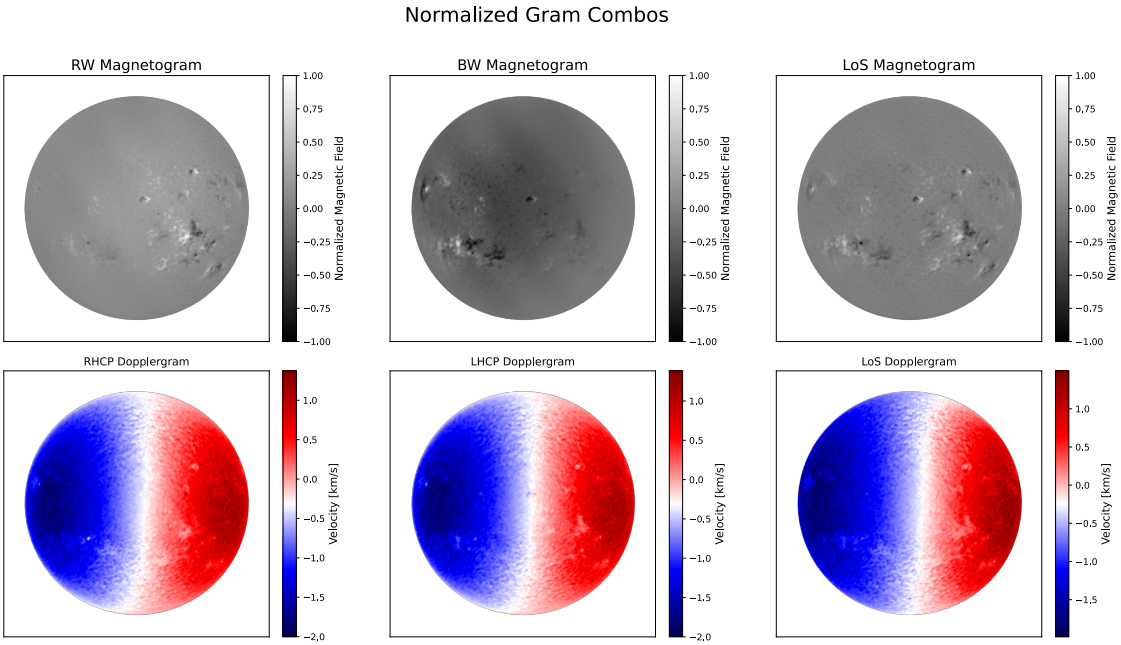

Figure 2.11 Magnetogram (top) and Dopplergram (bottom) combinations obtained using the filtergrams from Figure 2.10.

CHAPTER 3
THE TOR VERGATA SYNOPTIC SOLAR TELESCOPE

The Tor Vergata Synoptic Solar Telescope (TSST) is the first channel of the GATES Network; it is currently located in Rome, Italy at the University of Rome Tor Vergata in the Solar Physics and Space Sciences (SPSS) Lab with the final mounting location at the Roque de los Muchacos Observatory (ORM). The TSST is designed as a robotic, dual-channel facility, targeting space weather studies through the simultaneous acquisition of full-disk, LoS potassium K I 769.9 nm Doppler- and magnetograms as well as Hα intensity images. The TSST consists of two channels: a K I 769.9 nm MOF channel (henceforth TSST-K) and a Hα 656.28 nm narrow-band commercial telescope (henceforth TSST-Hα). The TSST-K is a modular, MOF-based instrument primarily constructed from off-the-shelf components (Figure 3.1); it acquires simultaneous Doppler- and magnetograms of the full-disk of the photosphere of the Sun. The Hα is a Daystar SR-127 QT (Figure 3.1) which obtains full-disk intensity images of the chromosphere of the Sun. Both TSST channels currently operate using a Basler a2A4504-18umPRO camera (see Appendix B for more details).

This chapter describes the TSST channels, preliminary performance/first light observations, facility plans, and inclusion into the Space WEatheR Tor vergata university (SWERTO) service. For a more thorough description of TSST's most recent observational campaign and role in the GATES Network and a more extended view of the dual-site observing campaign, refer to Chapters 5 and 7. Further technical specifications, including a full list of optomechanical components of the TSST, can be found in Appendix A.

Figure 3.1 Top: TSST-K on the bench at the Solar Station at UTOV prior to its enclosure box mounting. Bottom: TSST-Hα telescope.

3.1 *The Hα Channel*

The primary role of the TSST-Hα is the real-time detection of flaring regions through the identification of the flash and impulsive phases of the flare where the intensity reaches its maximum, similar to the techniques described in e.g. Piazzesi et al. (2012); Pötzi et al. (2018, 2015). The Hα line has been widely recognized for its importance in space weather monitoring (Kurokawa 1989) and its ability to detect and track chromospheric structures such as prominences and filaments (Leenaarts et al. 2012; Parenti 2014), which are often associated with flares and CMEs (Yan et al. 2011).

The passband of the TSST-Hα is 0.04 nm, allowing us to observe these active features in high contrast and serve as an effective flare detection channel. Moreover, this filter is the same as that used by the Hα telescopes in the GONG Network (Harvey et al. 1996), enabling

direct comparison of images between TSST-Hα and GONG. This comparison is useful for preliminary instrument data quality tests and future scientific studies and space weather monitoring. Supplementing the TSST-Hα observations with GONG's enables more synoptic coverage of the chromosphere while the GATES Network expands to additional nodes.

TSST-Hα is a commercially available Daystar SR-127 QT – an achromatic refracting telescope with a temperature-stabilized etalon filter. The telescope consists of a telecentric 2.7x Barlow lens with an internal temperature-stabilized Fabry-Perot interferometer to select for the Hα line located in the collimated beam. More specifications for the TSST-Hα can be found in Table 3.1.

Table 3.1 TSST-Hα telescope specifications.

Primary Aperture	127 mm
Central Wavelength	656.28 nm
Passband Width	0.04 nm
Distortion	$< 0.16\%$
Wavelength Stability	± 0.1 nm
Angular Resolution	1.3 arcsec
Pixel Scale	0.4 arcsec/pix (with 2x2 binning)
Field of View	15 $arcmin^2$ (without focal reducers, 2x2 binning)
Length	80 cm
Weight	6.2 kg

Due to the extended focal length of the TSST-Hα, the effective FoV when combined with the Basler camera is 15.9 $arcmin^2$. Since the primary purpose of the TSST-Hα – the real-time detection of solar flares – requires full disk and solar limb imaging, the optical design was adapted to include a focal reducer. The primary focal reducer of the TSST-Hα was a

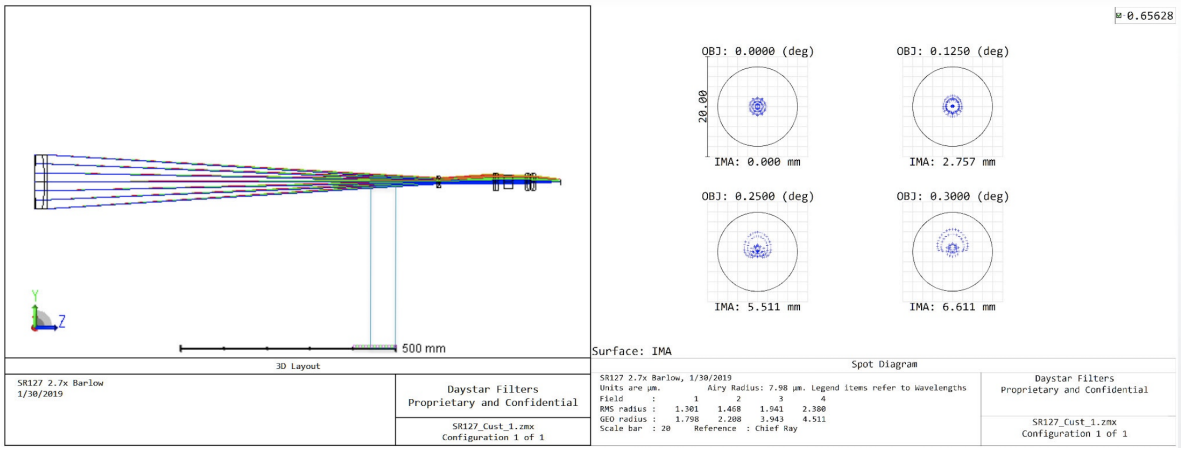

Figure 3.2 Optical scheme and spot diagrams of the Daystar SR-127 QT with the 0.36x focal reducer. Scheme provided by Daystar using Zemax software.

0.36x Daystar reducer, which additionally serves as a field curvature corrector. This focal reducer is made from two identical achromatic doublets whose design reduces focal length by a factor of 0.5x. For TSST-Hα, this focal reducer was placed 17 mm from the camera, thus having an effective reducing factor of 0.36x (corresponding to an effective focal length of 960 mm). The optical design and spot diagram of the TSST-Hα with the 0.5x Daystar focal reducer can be found in Figure 3.2.

Despite the theoretically flat focus of the TSST Hα using the optical design of Figure 3.2, test observations I conducted indicated the Daystar focal reducer produced a nonuniform focusing pattern across the disk of the Sun, preventing simultaneous observations of the disk center and limb. Additionally, the 0.5x focal length reduction proved insufficient for imaging the entire solar disk. To resolve these imaging aberrations, we implemented an additional field-flattener/focal-reducer (SkyWatcher 82ED). This focal reducer is also made from two achromatic doublets; its design reduced focal length by a factor of 0.9x. The simultaneous

inclusion of the Daystar and SkyWatcher reducers into the TSST-Hα optical scheme successfully allowed for simultaneous, full-disk observation with improved field flatness. However, the inclusion of the SkyWatcher introduced vignetting – likely caused by occlusion of the optics internal to the SR 127-QT body – and did not produce the expected optical quality. We continue to make adjustments to improve the image quality of the TSST-Hα so that it is optimally operational, maintaining a uniform, flat focus across the full disk of the Sun while achieving Nyquist sampling of the 1.3" angular resolution, prior to the TSST's deployment to its final mounting location at the ORM.

One potential solution is to implement a larger detector, such as the 9586 x 6380 pixel detector of the Sony IMX455 CMOS, without the focal reducer to eliminate any aberrations the additional optics introduce. This solution prevents full solar disk acquisition, cutting, on average, assuming a solar angular diameter of 1930", 3.8% of the solar disk from the image. If limited to the north and south solar poles, this small cut-off would still allow for eruptive monitoring of active solar latitudes. However, this would require additional pointing precision for the TSST and would eliminate the possibility to capture polar crown filaments. Consequently, we continue to make optical adjustments to find a solution that both maintains the full-disk FoV and achieves a uniform, flat focus.

Despite the continuing FoV and field curvature issues, TSST-Hα remains a valuable channel for the TSST. Our current image quality, capable of defining prominences and faculae regions, is comparable to GONG (Figure 3.3) and sufficient for flare detection techniques. We plan to continue to improve the optical quality of the TSST-Hα either through the inclusion

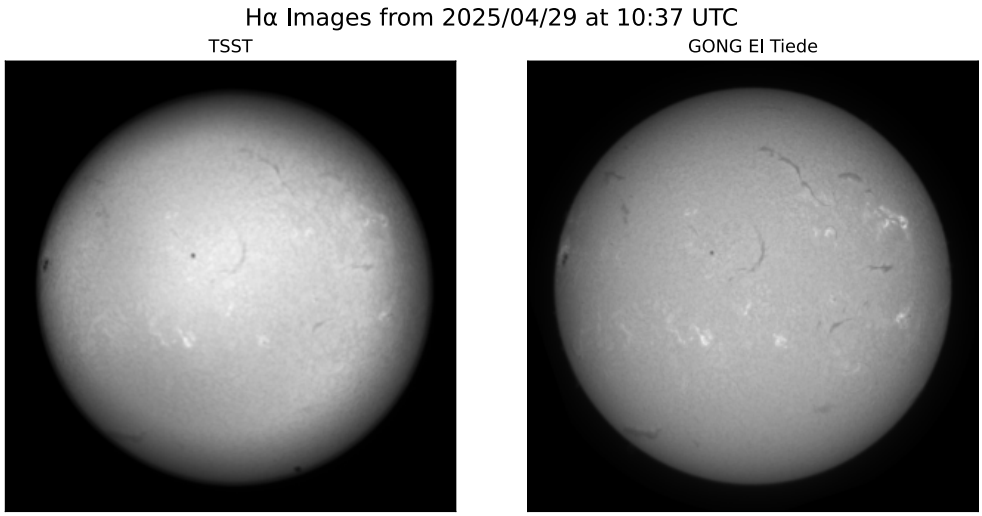

Figure 3.3 Hα observations from April 29, 2025 at 10:37 UTC. Left: TSST-Hα from UTOV. Right: NSO/GONG from El Tiede.The TSST-Hα image was acquired implementing both the Daystar and SkyWatcher focal reducers. The intensity gradient across the solar disk is a result of internal vignetting on the Hα telescope caused by the includion of the focal reducers.

of a different focal reducer, which better matches the Basler camera's sensor size and SR 127-QT's back focal length, or through a camera with a larger detector, which would allow for the DayStar focal reducer to operate at its nominal configuration. Moreover, to improve the TSST-Hα's remote and autonomous operation, we have installed a ZWO EAF motorized focuser and plan to include a motorized cover/flat fielder in the future (see Appendix A for further details).

3.2 *The K MOF Channel*

The role of the TSST-K is to produce Doppler- and magnetograms of the solar photosphere (line core 300 - 500 km above the solar surface: Figure 3.4) to study solar phenomena such as wave dynamics and flare probability. Dopplergrams have been widely used to study subsur-

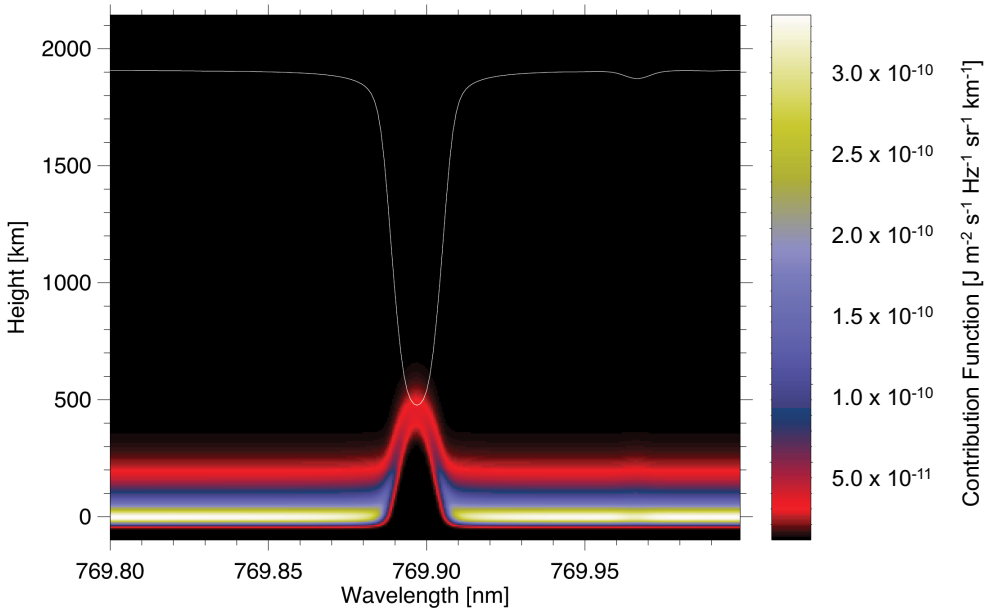

Figure 3.4 Contribution function of the K I 769.9 nm line in the solar atmosphere (Jefferies, private communication, 2026). The white curve plots the solar absorption line as a function of wavelength (on the x-axis) while the colored maps show the contribution height of the respective points of the absorption line. The core of the K I 769.9 nm line probes between 300 - 500 km in the solar photosphere, while the wings probe lower between 100 - 300 km.

face flows and wave propagation through the solar atmosphere (Basu 2016). In particular, MOF-based telescopes have been designed and proven successful in the study of seismology of the solar atmosphere (eg. Chaturmutha et al. (2024); Finsterle et al. (2004c); Jefferies et al. (2019), Section 1.4). Magnetograms can be used to estimate flare probability in active regions through various techniques, for example, using the Schrijver R parameter – total unsigned magnetic flux (Schrijver 2007) – or the D parameter – number of polarity inversion lines above a certain threshold (Cicogna et al. 2021). The TSST-K is designed so that its Doppler- and magnetogram data products can be used to further these seismic and flare prediction studies.

3.2.1 Design Specifications and Developments

The TSST-K was designed as a modular telescope comprising predominantly off-the-shelf components, such that it could be easily and cost-effectively reproduced. It is a double-Keplerian telescope consisting of an MOF centered on the $KI\ D1$ 769.9 nm absorption line operating in Cacciani mode. More specifications for the TSST-K can be found in Table 3.2.

Table 3.2 TSST-K channel specifications.

Primary Aperture	80 mm
Central Wavelength	769.9 nm
Angular Resolution	2.4 arcsec
Pixel Scale	1.17 arcsec/pix (with 2x2 binning)
Field of View	44 x 44 $arcmin^2$
Length	175.5 cm

As described in Section 2.2, the optical scheme of an MOF-based telescope can broadly be divided into four sections: the Broadband Filter Section, the Polarization Analyzer Section, the Filter Section (MOF), and the Wing Selector Section (WS). For compactness, the TSST-K implements two folding mirrors into its optical scheme such that these four sections are spread out over three branches of the telescope. In addition to containing these basic sections, the optical scheme of the TSST-K was designed under the following specifications:

- Designed as a refractive system to avoid pupil obstruction;
- Obtain an angular resolution of ~ 2 $arcsec$ (corresponding to a spatial resolution of 1.5 Mm in the solar photosphere at disk center) requiring an entrance pupil of 80 mm;
- Obtain full disk imaging, requiring a large FoV of at least 0.25° of half field cone angle;

- Both the MOF and WS cell should contain a pupil image to ensure spatially uniform, angle-independent spectral transmission and be fully traversed by a collimated beam;
- All polarization optics (polarizers, half and quarter wave plates) should also be traversed by a collimated beam to ensure uniform retardance and polarization selection;
- Include high-pass and low-pass filters to remove unwanted solar radiation from the telescope to prevent leakthrough noise and instrumental overheating;
- Maintain compactness in size and weight.

The MOF and WS cells' windows have a clear aperture of 20 mm. In order to meet all of the above specifications and reduce the beam size down to an appropriate diameter for the cells, the TSST-K requires two re-imaging systems comprised of lenses with shorter focal lengths than L1. These systems, L2-L3 and L3-L4, ensure pupil images, of the proper size, in the center of the cells and collimated beam space throughout the MOF and WS sections.

The original optical scheme of the TSST-K (Figure 3.5) consisted of an L-shaped design, with three branches, where all of the optics were mounted in the same orientation (with respect to the ground). Branch 1 held the Broadband Filtering Section and the first lens in the L2-L3 reimaging system. Following a folding mirror, Branch 2 held the Polarization Selector and MOF Section. After an additional folding mirror Branch 3 contained L3, the L4-L5 re-imaging system, and the WS Section. A more thorough description can be found in Viavattene et al. (2020) and Calchetti (2021).

Following preliminary calibrations and tests, I redesigned TSST-K optical scheme to improve compactness and maneuverability. The new, final optical design (Figure 3.6) maintains

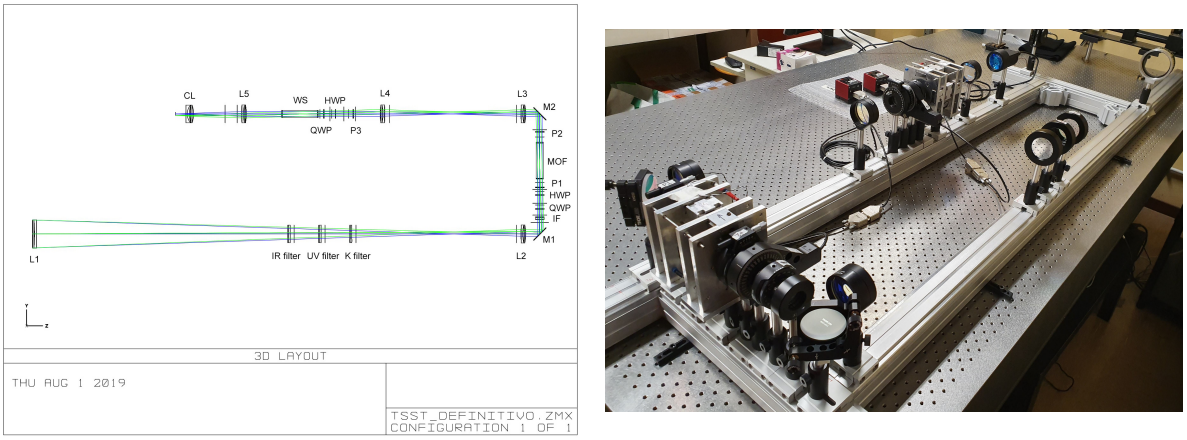

Figure 3.5 Left: Original optical scheme of the TSST-K created with Zemax software by Dr. Giorgio Viavattene. Right: Image of the TSST-K with its original design at the Solar Station at UTOV

a three-branch structure, but orients Branch 2 vertically, creating a T-shape and allowing both the top and bottom of a single telescope rail to be utilized. Additionally, the new design shifts the optical scheme such that Branch 1 contains only the Entrance Section, Branch 2 (now vertical) contains the first focus and L2, and Branch 3 contains the MOF, Re-Imaging, WS, and CAM sections. Aside from a dramatic decrease in overall size and weight, the main consequence of this redesign is the removal of the third polarizer (P3). In the original design, P3 was in place prior to the WS to eliminate any spurious polarization signal introduced by the second folding mirror (M2). Since the final design shifts the MOF after M2, the spurious signal being introduced after the MOF is no longer a concern. In addition to slightly simplifying the optical design, excluding P3 also reduces the number of possible sources of interference fringes.

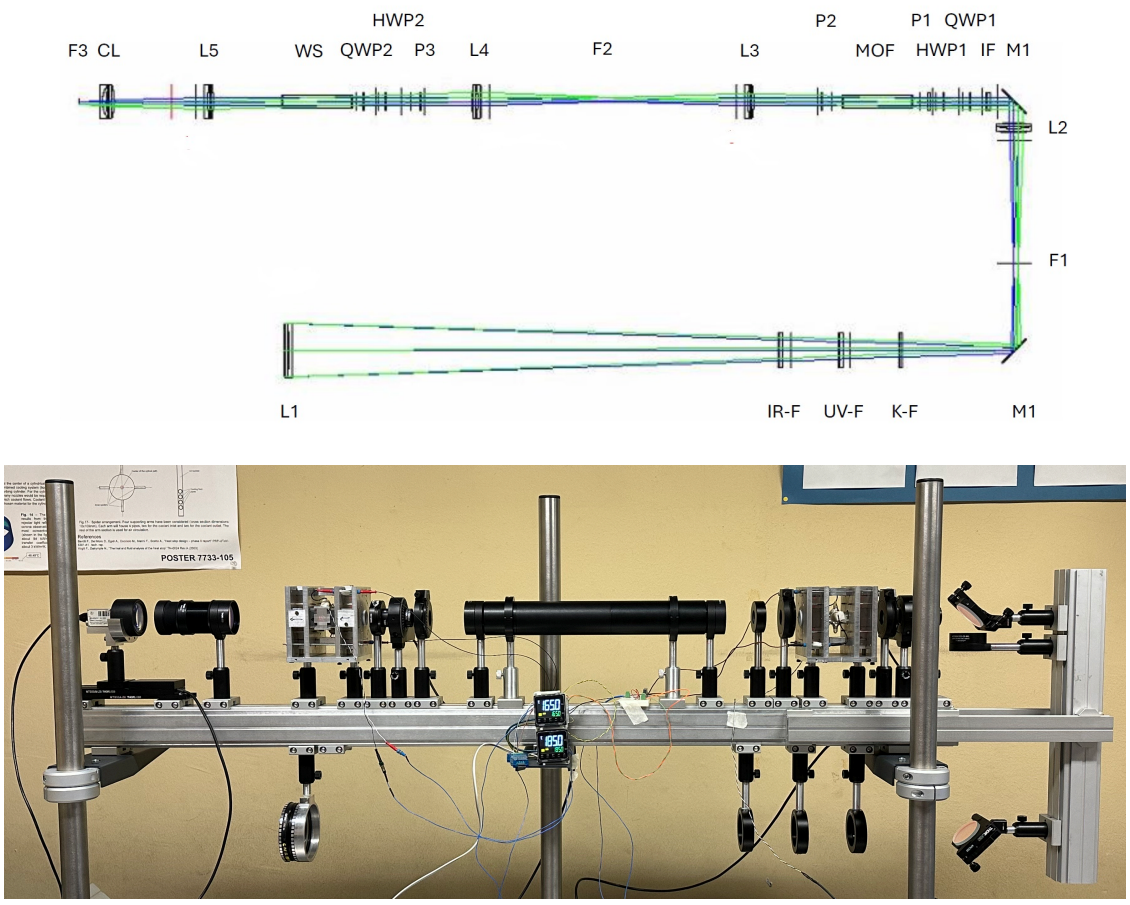

Figure 3.6 Top: Final optical scheme of the TSST-K created with Zemax software by Dr. Giorgio Viavattene. Bottom: Image of the TSST-K while mounted vertically at the Solar Station at UTOV.

3.2.2 Final Optomechanical Design

The updated optical design specified in Figure 3.6 for the TSST-K was finalized in 2023. I began construction/testing in 2023 and continued throughout 2024, with assistance from the GATES team at UTOV. Figure 3.7 shows a CAD model of the TSST-K channel with its MOF-specific sections labeled; each section and its optics are detailed below.

Broadband Filter: Red boxes in Figure 3.7. The Broadband Filter Section consists of three broadband filters to remove unused solar radiation from the beam path to prevent

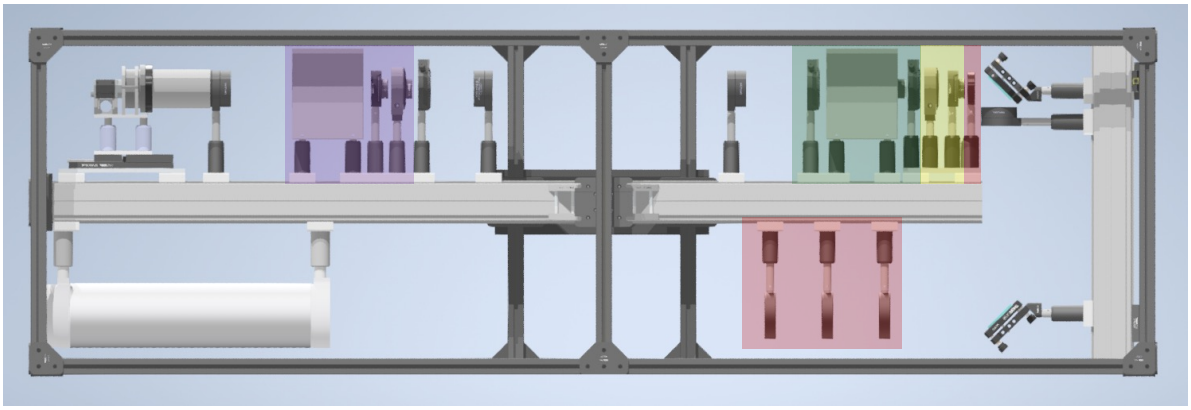

Figure 3.7 TSST-K telescope model produced by Andrea Chiodini. The red boxes indicates the filter section (including the 3 broadband filters on the first leg of the telescope and the IF on the third leg), the yellow box indicates the polarization selector, the green box indicates the MOF section, and the purple box indicates the WS section. All other optics are imaging optical elements.

overheating the optics. The section begins with an IR cut filter (eliminates $\lambda > 825\ nm$) and a UV cut filter (eliminates $\lambda < 700\ nm$) before passing through a broadband potassium filter ($\lambda \sim 769 \pm 1.72\ nm$). These three filters eliminate $\sim 88.5\%$ of the unused solar power entering the telescope, resulting in a $0.7\ W$ transmission to the main optics of the channel. After these filters, the beam is redirected up the vertical rail, where it is collimated by L2, and to the top of the rail via the two mirrors, M1 and M2. The Broadband Filter Section ends with a narrow-band interference filter, IF ($\lambda \sim 770 \pm 1\ nm$).

Polarization Selector: Yellow box in Figure 3.7. The polarization selector consists of the QWP1 and HWP1. The TSST-K QWPs and HWPs are crystalline quartz and magnesium fluoride-based optics from Thorlabs.

The light entering the Polarization Selector has been filtered for the channel's relevant wavelength and is composed of both polarized and unpolarized light. As described in Section

2.1, the goal of the MOF-based telescope is to select one of the circular polarization states produced in the solar atmosphere; therefore, these are the polarization states being selected by this section. QWP1, which is oriented with an angle of 45° with respect to P1, converts the Sun's circularly polarized light into linear polarization. After that, the HWP, which is oriented at 0° or 45° with respect to P1, changes the polarization of the linearly polarized beam by 90°. The consequence of this change is that one polarization state (for example σ^+) will remain parallel to the orientation of P1 (0°) and be allowed to pass through; P1 will eliminate the other. The orientation of HWP1 is mechanically rotated to switch between polarization states.

MOF Section: Green box in Figure 3.7. The MOF Section consists of P1, the MOF cell/magnet assembly, and P2 (oriented 90° with respect to P1). P1 and P2 are nanoparticle linear film polarizers from Thorlabs with an extinction ratio of 10^7. The MOF cells are reservoir cells. For additional specifications on the MOF cells/magnet assemblies, see Section 3.2.3.

The beam of light (consisting of one of the circular polarization states produced by the Sun, now encoded in a linearly polarized beam with 0° with respect to P1), which enters the MOF Section, passes through P1 such that only a single polarization state is transmitted. The selected polarization state then enters the MOF cell, where the Inverse Zeeman (Righi) and Macaluso-Corbino effects split the light into its red and blue wings, put them into emission, and rotate the polarization of the resonant wavelengths by 90°. The resultant beam is such that only the light from one polarization state can pass through P2.

WS Section: Blue boxes in Figure 3.7. The WS Section consists of HWP2, QWP2, and the WS cell/magnet assembly.

Light exiting the MOF section is re-imaged by L3 - L4, re-collimating the beam to produce a second pupil plane in the center of the WS cell. The collimated beam, encoded with a single linear polarization state, passes through HWP2, which is oriented at either 0° or 45° with respect to P2. HWP2 changes the polarization of the beam by 90°. QWP2, oriented 45° with respect to P2, transforms the linearly polarized beam into circularly polarized light prior to entering the WS. The combination of HWP2 and QWP2 ensures that only one wing (red or blue) of the resonant wavelength will pass through the WS; the Righi effect within the cell will absorb the other. This creates a single solar disk, encoded with the circularly polarized light from a single wing; each combination of red/blue wing and σ^+/σ^- light is imaged sequentially on the CMOS detector by rotating the HWP's positions.

Imaging Optics: Remaining optics in Figure 3.7. The entrance lens (L1) of the TSST-K is a Spindler & Hoyer doublet with a diameter of 80 mm and a focal length of 1185 mm. The system contains four additional lenses (L2 - L5) for re-imaging the system and resizing the beam. L2 - L5 are all Thorlabs achromatic doublets with a diameter of 50.8 mm and a focal length of 200 mm; they are coated with anti-reflective coating AR-B (650 - 1050 nm).

L2 images the entrance to create a collimated beam for the MOF section (with a pupil plane in the center of the MOF cell). L3 - L4 re-images the system to create a second collimated beam for the WS section (with an additional pupil plane within the WS cell). L5 focuses the beam towards the camera, which is equipped with a corrective lens (CL:

composed of a bi-convex and a plano-concave lens from Thorlabs with diameters 20.8mm and focal lengths 75 mm and -75 mm respectively) to ensure an aberration-free image of the whole solar disk fits on the detector. Two dielectric mirrors (M1 and M2), each with a diameter of 50.8 mm and optimized for the near-IR, are mounted on the vertical rail for optical path folding.

3.2.3 MOF Cells and Magnet Enclosures

The MOF cells utilized by TSST-K are reservoir cells (see Figure 2.2). They are 100 mm long with 20 mm clear-aperture windows with optical quality of $\lambda/4$. The cells are back-filled with argon gas to prevent metal condensation on the windows. The alkali vapor is generated by heating the reservoirs of the cell using NiCr wire with a total resistance of 20 Ω, powered by 24 V. The cell temperature is controlled by an OMRON E5SC controller with a stability of 0.1°C. See Table 3.3 for the operational temperatures of the MOF/WS cells.

The cells are situated in aluminum magnet enclosures, designed and produced at UTOV. The magnet enclosures utilize permanent bar magnets to produce a highly uniform longitudinal magnetic field centered at the center of the cell. The cells are free to rotate in the magnet enclosures to allow for adjustments to minimize interference fringes. See Table 3.3 for the operational magnetic fields of the two enclosures.

Table 3.3 TSST-K operational parameters for MOF and WS cells.

	MOF	WS
Temperature	166.5°C	185.0°C
Magnetic Field	1.23 kG	2.26 kG

3.2.4 Mechanical Structure

The main structure of the telescope consists of two 66 mm Thorlabs rails oriented in a T shape. The primary rail is 1.4 m long, and the secondary, vertical rail is 0.5 m long. Custom-machined aluminum plates support the vertical rail. All of the optics are mounted in Thorlabs mounts, which allow for adjustments in the y, z, and rotational planes. The TSST-K is enclosed in a modular, thermally insulated box constructed from Thorlabs 25 mm anodized aluminum rails and thermal insulation panels to protect the optics from dust and maintain thermal insulation. The interior of the panels is painted black to minimize internal reflections. Additionally, the exterior of the enclosure box will be coated with Mylar foil to reflect sunlight and prevent thermal runaway.

3.2.5 Spectral Characterization and Operating Parameters

Spectral characterization is an integral step for properly tuning and calibrating an MOF-based instrument. The process consists of tuning the magnetic field and temperature parameters and precisely measuring the peak transmission, the narrowband-filter passband width, and the passband separation. For the TSST, the goal of the spectral characterization were:

1. Obtain a separation of 0.02 nm between the red and blue passband peaks;
2. Match the MOF and WS passbands by tuning the WS magnetic field;
3. Optimize the WS temperature to fully remove one MOF passband.

Table 3.4 reports the TSST-K spectral characterization results for the MOF and WS operating at 166.5°C / 1.23 kG and 185°C / 2.26 kG respectively. Figure 3.8 shows the TSST-

K transmission and absorption profiles; for a full description of the spectral characterization, refer to Calchetti et al. (2020b) and Calchetti et al. (2020a).

Table 3.4 TSST-K spectral characterization results from Calchetti et al. (2020a).

	Blue	Red
Transmission Peak	48.9%	47.61%
FWHM	5.62×10^{-3} nm	5.11×10^{-3} nm
Contamination	$\sim$ 11%	$\sim$ 13%
Spectral stability	3×10^{-5} nm	
Doppler noise level	$\sim$ 10 m/s	
Velocity Saturation	$\pm$4 km/s	
Magnetic Saturation	$\pm$2700 G	

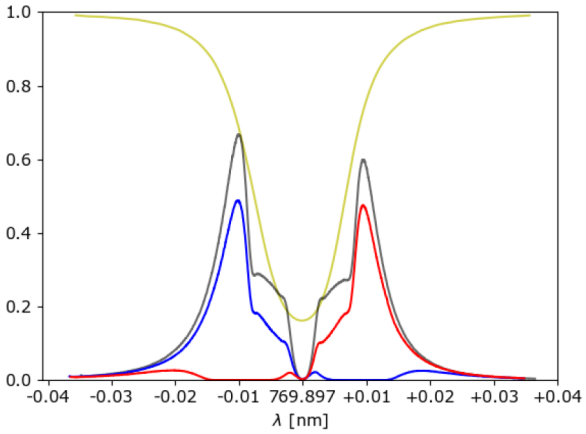

Figure 3.8 TSST-K transmission profile from Calchetti et al. (2020a). The yellow curve depicts the $KI\ D1$ 769.9 nm absorption line, the grey shows the composite MOF transmission profile, and the red and blue curves depict the red and blue wings.

3.3 *TSST Testing and Future Facilities*

During testing, first light acquisition, and the Summer 2025 observing campaign, the TSST has been utilizing the Solar Station at UTOV (Figure 3.9). The Solar Station is a heliostat

system that consists of a motorized alt-az mirror mounted on the roof, which directs sunlight to a fixed mirror on the optical bench in the Solar Lab. This system is equipped with an automatic tracking system comprising a tertiary mirror feeding a quad-cell photodiode. This system produces a stable solar beam, which was then fed into the TSST-K for tests/observations. Moreover, utilizing the Solar Station as the main testing facility for the TSST allowed for precise, real-time calibration/alignment corrections given the telescope is well supported on a TMC™ vibration-controlled optical bench.

Figure 3.9 Left: diagram of the Solar Station at UTOV. Center: heliostat alt/az mirror and entrance tube on the roof. Right: fixed mirror on the optical bench, which directs the solar beam to the table.

The TSST is designed to be a fully robotic facility with fully autonomous telescope and dome control systems. Autonomous operation requires the telescope data acquisition, mount, and dome control to work synergistically both during science-data acquisition and in case of emergency shutdown. The current acquisition and operation procedures can be found in Appendix B. In addition to the autonomy of the TSST system, its commercial reproducibility is a crucial aspect of the final TSST facility. Consequently, the TSST is planned to be integrated into a commercial clamshell dome (Figure 3.10), whose integration

is being carried out in collaboration with ADS International – an independent private firm specialized in designing and manufacturing advanced systems for astronomy, communication and defense. The telescope will be mounted on an equatorial mount to allow unrestricted telescope motion when the clamshell dome is fully open and to eliminate field rotation throughout the day. For a full list of dome specifications, refer to Appendix E of Chiodini (2025).

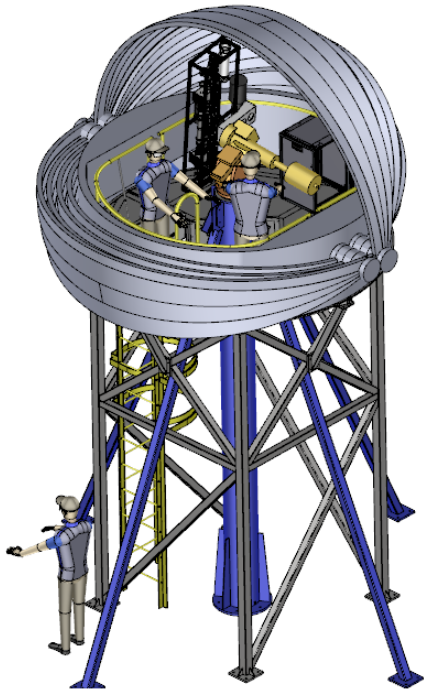

Figure 3.10 Current TSST dome render from ADS International.

In addition to automating the TSST, the final mounting site is crucial to the telescope's ability to contribute effectively to the GATES Network and, more broadly, to space weather studies. The final planned site for the TSST is located at the Roque de los Muchacos Observatory (ORM) on La Palma Island (28° 45' 15" N, 17° /; 53', 18", altitude: 2366 m).

ORM is one of the sites of the Observatorios de Canarias (OCAN) – the other site being Tiede Observatory (OT) on Tenerife Island. Due to their stable atmospheric conditions, low light pollution, and clear skies, these sites jointly host the telescopes and instruments of approximately 60 institutions from more than 20 countries and, consequently, were prime candidates for the TSST's final site. The exact site selection process ocurred in 2023 - 2024 and focused on finding a site that optimized proximity to existing infrastructure and clear horizon while avoiding protected areas of the national parks. (see Section 5.2 of Chiodini (2025) for more details).

3.4 *Space WEatheR TOr vergata university service*

The SWERTO service is a database for space weather prediction and notification. It is funded by the Regione Lazio and located in the Physics Department of UTOV. The service was designed to combine satellite and ground-based observations from external and internal sources, such as PAMELA, ALTEA, IBIS, GONG, and GATES. Its goal is threefold: 1) host a database with particle fluxes and photospheric spectro-polarimetric measurements; 2) exist in an open-access form to promote accessibility to regional industries affected by Space Weather events; 3) implement a tutorial and FAQ section to assist individuals and industries in accessing the risks of Space Weather events (Berrilli et al. 2018).

Currently, SWERTO collects data from different public databases such as GONG and SDO/HMI to provide a real-time view of the Sun and produce summaries on solar activity. With the inclusion of the TSST data, SWERTO will be able to expand its service to include

real-time flare notifications, using the data from the TSST-Hα, as well as live views of the Sun in Hα intensity, K LoS Doppler velocity, and K LoS magnetic field. Moreover, with the inclusion of current and future GATES nodes' data, the SWERTO service will be able to provide a more extensive – and ground-based synoptic – view of the Sun, including additional Doppler- and magnetogram channels such as Na and He.

3.5 *TSST-K First Light and Preliminary Data*

The first light of the TSST-K was acquired on February 7, 2020 using the Solar Station at UTOV and has been presented in Giovannelli et al. (2020a) and Calchetti (2021). TSST-K was in a preliminary assembly phase (Figure 3.5) using light fed into the lab from the heliostat. A Grasshopper GS3-U3-28S5M-C camera, with a 1920 x 1440 pixel detector (pixel size 4.54 μm), was used for the acquisitions. Intensity, leakthrough, and flat images in all four filtergram bands were acquired, and preliminary Dopplergrams were constructed (Figure 3.11) following the process described in Forte et al. (2020) and explained in Figure 5.2. The leakthrough and intensity images were produced by summing 40 ms exposures over a cadence of 1 s; the flat field images were acquired by summing 40 ms frames for 30 s, dithering the Sun across the FoV with a constant speed.

The quality of the 2020 first light images was affected by unpolarized leakage, caused by non-ideal polarizers, which resulted in interference fringes that were present in all of the filtergram bands (see Figure 2.16 in Calchetti (2021)). Additionally, a curvature of the zero-line Doppler velocity was present and likely caused by vignetting from the heliostat (as

identified in the 2025 new first light images). Despite these fringes, the 2020 first light tests found a robust signal-to-leakage ratio of ∼25, and provided excellent confirmation of the alignment of the optical elements/spectral calibration. Moreover, the Dopplergram images provided a positive proof-of-concept for the use of the TSST for photospheric velocity studies such as wave analysis.

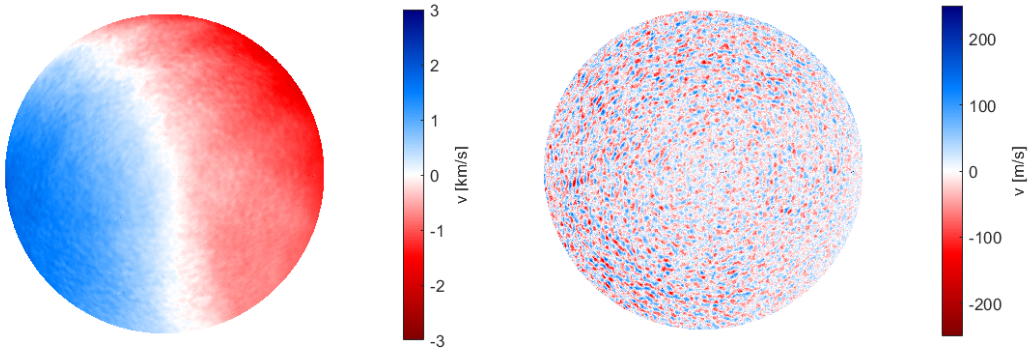

Figure 3.11 Dopplergrams from the February 7, 2020 first light campaign of the TSST-K; figure from Calchetti (2021). Left: LoS Dopplergram with the Sun's rotation being the dominant feature. Right: rotation-subtracted Dopplergram exhibiting supergranulation and p-mode patterns. Velocity scales reported from Giovannelli et al. (2020a).

Following the 2020 first light images, I, with the GATES team at UTOV, mechanically resigned the TSST-K to maximize compactness while maintaining a nearly identical optical scheme (Figure 3.6). Additionally, we made multiple upgrades to the assembly, including the new Basler camera, additional stray-light blocking tubes and baffles, and increasing motorization control on the polarization optics/camera. With this upgraded design, I conducted various "on-sky" (with the heliostat) tests with the TSST-K prior to the new first light science images which were acquired by the UTOV team on July 12, 2025, prior to the dual-site GATES observing campaign. Figure 3.12 displays the TSST-K magnetogram, Dopplergram,

and intensitygram from this day. Images were acquired by summing 50 ms exposures over a total integration time per filtergram of 5 s, resulting in a 50 s temporal resolution for the Doppler- and magnetograms.

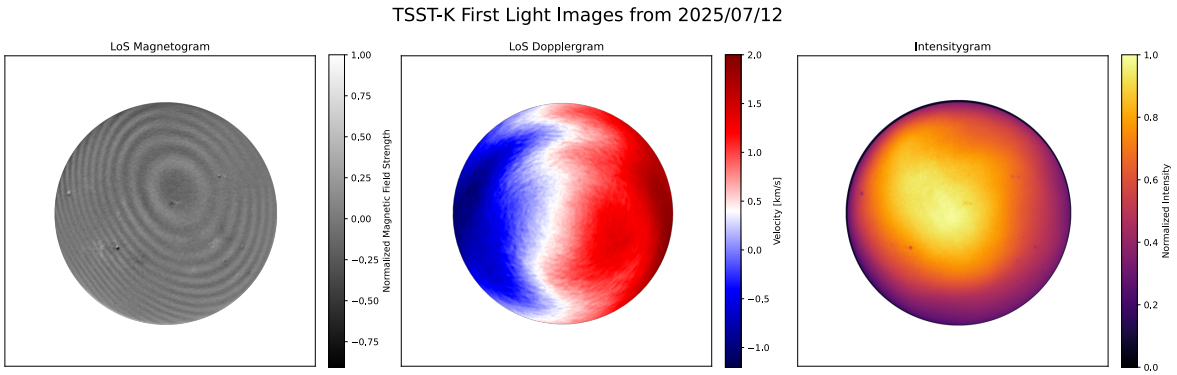

Figure 3.12 New first light images of the TSST-K acquired on 2025/07/12 at 16:06 UTC. Images acquired on the optical bench in the SPSW Lab with the TSST-K being fed with the heliostat.

A signal-to-leakage ratio of ∼20 was acquired for each filtergram state; this value is slightly lower than the 2020 observations, indicating that the rotational polarization alignment of the polarizers/retarders requires additional precision adjustment to account for the new optomechanical design. Despite the removal of P3, multiple fringe patterns persist in the TSST-K Doppler- and magnetograms, but are notably weaker in individual filtergrams compared to the 2020 data. Based on individual optics tests I conducted, the most likely cause of these patterns is aberrations arising from the MOF and WS cell windows. In the future, we aim to upgrade the cells to improve the image quality. In addition to the persistent fringes, the TSST first light data presented a notable intensity gradient across the solar disk (as seen in the intensitygram). The presence of this gradient introduces a kink in the Dopplergram's solar rotation zero-velocity line, similar to the 2020 first light images. It,

along with the fringe patterns, dominate the signal. The most likely cause of this gradient is vignetting on the heliostat system. At UTOV, we are working to realign the heliostat system and eliminate the need for its usage overall by conducting direct on-sky observations. Despite the fringes and system vignetting, both the Doppler and magnetograms acquired by TSST-K provide valuable data for cross-calibration between GATES nodes as well as studying velocity and magnetic dynamics in the photosphere. See Section 5.4 for comparison to other GATES channels.

CHAPTER 4
THE MOJAVE SOLAR OBSERVATORY

The Mojave Solar Observatory (MSO) hosts the second channel of the GATES Network. It is the private observatory of the Eddy Company and is located in Apple Valley, CA, USA. MSO is designed as a scaled-down version of the MOTH telescope (see Section 2.1.4) as a dual-channel MOF-based instrument. The mechanical design of MSO consists of two channels, which, over the GATES 2025 observing run, have rotated between three different MOFs: K I 769.9 nm (henceforth MSO-K), Na I D2 589.0 nm (henceforth MSO-Na), and He I 1083.0 nm (henceforth MSO-He). The original/standard design of MSO is constructed with MSO-K and MSO-Na active – consequently, when referring to "MSO" the instrument, this text is describing the MSO-K and MSO-Na setup. All three of the MSO channels are modular, MOF-based channels primarily constructed with off-the-shelf components (Figure 4.1); they acquire LoS Doppler- and magnetograms of the full disk of the photosphere and chromosphere of the Sun simultaneously. All MSO channels currently operate using an Alvium 1800 U-508M camera (see Appendix D for more details).

This chapter describes the MSO channels, performance/first light observations, and facility plans. For a more thorough description of MSO's role in the GATES Network, He MOF development, and extended summer observing campaign, please refer to Chapters 5, 6, and 7 respectively. Further technical specifications, including a full list of optomechanical components of MSO can be found in Appendix C.

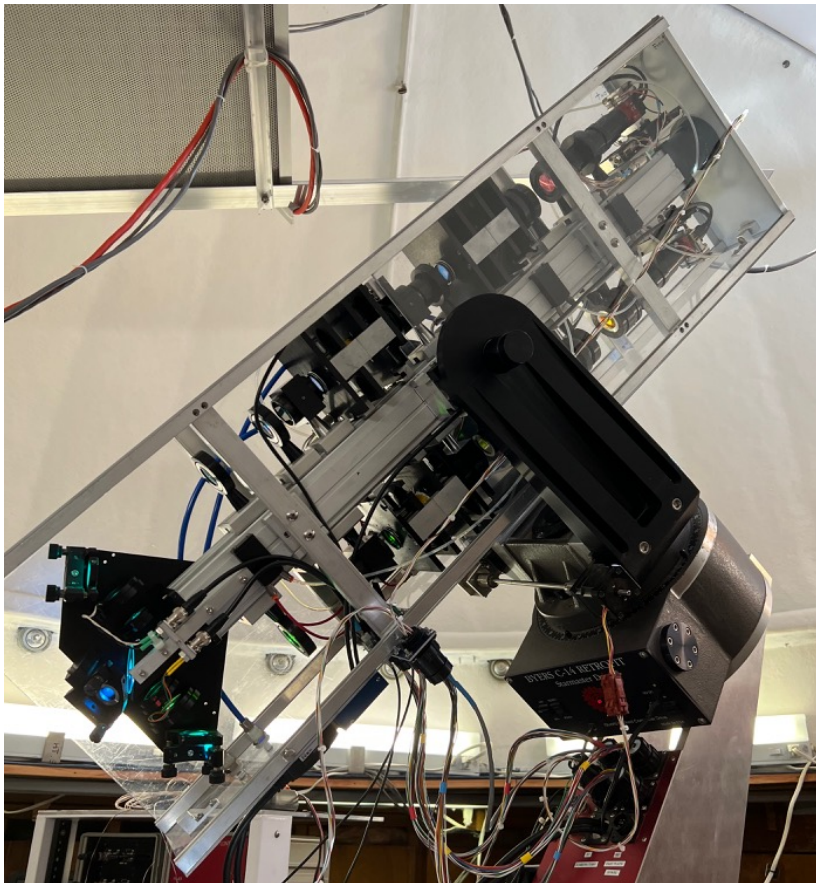

Figure 4.1 An image of the standard MSO telescope mounted in the dome prior to installing blackout foil on the enclosure box. MSO-K is the channel on top of the rail, and MSO-Na is the channel on the bottom of the rail.

4.1 *The K and Na MOF Channels*

Similar to TSST-K, the role of the MSO-K and MSO-Na is to produce LoS Doppler- and magnetograms to study solar phenomena such as wave dynamics and flare probability. MSO-K probes the photosphere of the Sun (line core 300 - 500 km above the solar surface: Figure 3.4) and MSO-Na probes the low chromosphere of the Sun (600 -800 km above the solar surface: Figure 4.2). The combined, multi-height observations of MSO-K and MSO-Na were designed specifically to contribute an independent co-registered (spatially and tempo-

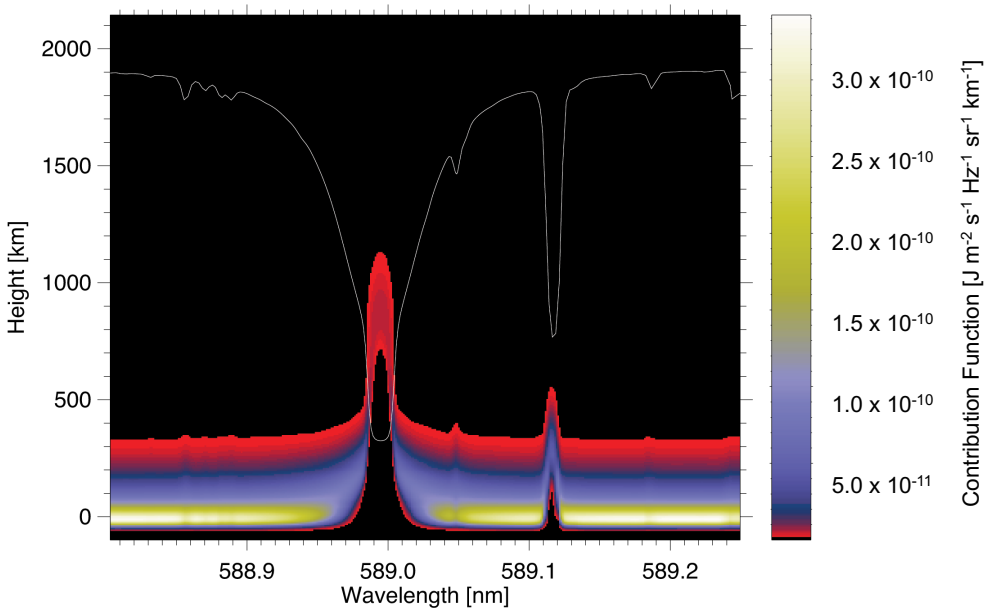

Figure 4.2 Contribution function of the Na I D2 589.0 nm line in the solar atmosphere (Jefferies, private communication, 2026). The white curve plots the solar absorption line as a function of wavelength (on the x-axis) while the colored maps show the contribution height of the respective points of the absorption line. The core of the Na I D2 589.0 nm line probes between 600 - 800 km in the solar photosphere/chromosphere, while the wings probe lower between 400 - 600 km.

rally aligned) data set to contribute to solar atmospheric seismology studies such as those described in Section 3.2. In addition to their scientific goals, since MSO-K and TSST-K operate at the same wavelength, MSO-K is designed to act as a calibration channel between the first two GATES nodes, ensuring consistency in physical unit calibration between the two nodes.

4.1.1 *Design Specifications*

MSO-K and MSO-Na were designed as dual-channel, modular telescopes comprising predominantly off-the-shelf components, making them consistent and straightforward to reproduce.

The two channels utilize the same primary aperture, are fed a wavelength-specific beam via a beamsplitter, and are mounted on opposite ends of the same rail. Optically, MSO-K and MSO-Na are designed as mirror channels; the only differences in their optics are the alignment position and the optical transmission/reflection coatings.

Both MSO-K and MSO-Na are double-Keplerian telescopes with their MOFs centered on the KI D1 769.9 nm absorption line and Na I D2 589.0 nm absorption line, respectively. Differing from TSST-K, the MSO MOF channels operate in Tomczyk mode. Specifications for MSO-K and MSO-Na can be found in Table 4.1.

Table 4.1 MSO channel specifications.

	MSO-K	MSO-Na	MSO-He
Primary Aperture	50.8 mm		
Central Wavelength	769.9 nm	589.0 nm	1083.0 nm
Angular Resolution	3.81"	2.92"	5.36"
Pixel Scale	2.39"/px	2.29"/px	2.38"/px
Field of View	39 $arcmin^2$		
Length (total)	105.41 cm (41.5 in)		

Despite operating in a different mode from the TSST-K, the MSO channels' optical design can be divided broadly into the same four sections: the Broadband Filtering Section, the Polarization Selector, the MOF Section, and the WS Section. The most notable difference between the TSST-K and MSO channels is the WS section. In addition to containing these basic sections, the optical scheme of the MSO telescope was designed under the following specifications:

- Designed as a refractive system to avoid pupil obstruction;
- Image both MSO-K and MSO-Na channels with the same intensity;
- Obtain an angular resolution consistent with average seeing in Apple Valley of ~ 4 *arcsec* (corresponding to a spatial resolution of 3 Mm in the solar photosphere);
- Obtain full disk imaging, requiring a large FoV of 0.25°of half field cone angle for each solar disk imaged simultaneously;
- Both the MOF and WS cell should contain a pupil image;
- Maintain compactness in size and weight.

The MOF and WS cells' windows have a clear aperture of 19 mm. In order to meet the above criteria and reduce the beam size to an appropriate diameter for the cells, the MSO-K and MSO-Na channels contain multiple reimaging systems comprised of lenses with shorter focal lengths than L1. These systems, L2-L3, L4-L5, and L6-L7, ensure the angular size of the beam is smaller than the polarization optics' acceptable angle of incidence and fits in the clear aperture of the cell windows. Moreover, they ensure pupil images are formed in the center of the MOF and WS cells.

4.1.2 Optomechanical Design

The optical design for the dual-channel MSO telescope was finalized in 2017 and the telescope was constructed that same year. After initial tests, it remained dormant until 2022, when I conducted realignment, lab tests, and began its integration into the GATES Network. Figure 4.3 shows a model of MSO telescope with the MOF-specific sections labeled; each

section and its optics are detailed below. Further specifications for individual optomechanical components can be found in Appendices A and B

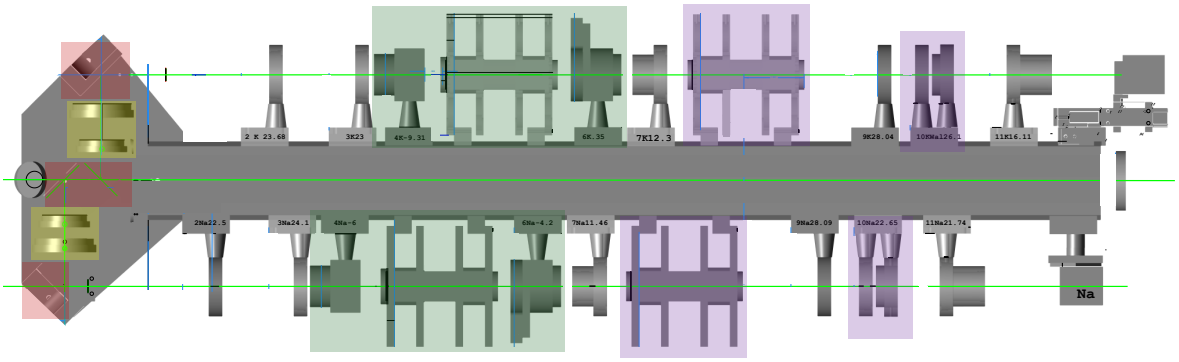

Figure 4.3 MSO telescope model. MSO-K is on the top and MSO-Na is on the bottom. Red boxes indicate the broadband filter sections, yellow boxes indicate the polarization selectors, green boxes indicate the MOF section, and blue boxes indicate the WS section. All other optics are imaging optical elements.

Broadband Filtering: Red boxes in Figure 4.3. Since the main beam of the MSO telescope feeds both the MSO-K and MSO-Na channels, the broadband filtering is done via a custom reflective beamsplitter (BS). The BS consists of two optics. BS1 is coated to transmit wavelengths less than 600 nm and reflect wavelengths greater than 600 nm; the reflected light feeds the MSO-K channel while the transmitted light feeds BS2. BS2 is coated to reflect light near 589 nm and transmit all other light. Its reflected light feeds the MSO-Na channel, and its transmitted light is relayed via a flat mirror to the fine-tracking quad-diode. Each channel utilizes an additional mirror for optical beam folding; these mirrors are custom-coated to further filter light for the channels' resonant wavelengths.

Polarization Selector: Yellow box in Figure 4.3. The polarization selector consists of the QWP1 and HWP. QWP1 is from Meadowlark Optics and is optimized for the respective

channel's wavelength. In the case of MSO, the HWP is an LCVR manufactured by Display Tech (DT) and is also optimized for the respective channel's wavelength. Rather than physically rotating, the LCVRs change the orientation of liquid crystal molecules within a cell when a voltage is applied. This changes the retardance of the incoming light and consequently the polarization state of the light as it passes through (Alvarez-Herrero et al. 2011).

The light entering the Polarization Selector has been filtered to the channel's relevant wavelength and contains both polarized and unpolarized light. As described in Section 2.2.3, the goal of the MOF-based telescope is to select one of the $\sigma^{\pm}$ components from the Zeeman splitting produced in the presence of a magnetic field in the solar atmosphere. QWP1, which is oriented with an angle of 45° with respect to P1, converts the Sun's circularly polarized light into linear polarization. After that, the LCVR's voltage is modulated to induce either a 0° or 90° polarization shift in the light. The consequence of this change is that one polarization state (for example σ^{+}) will remain parallel to the orientation of P1 (0°) and be allowed to pass through; P1 will eliminate the other. The orientation of the LCVR is modulated at such a frequency that both polarization states ($\sigma^{\pm}$) are populated within a single exposure time.

MOF Section: Green box in Figure 4.3. The MOF Section consists of P1, the MOF cell/magnet assembly, and P2 (oriented 90° with respect to P1). P1 and P2 are calcite linear polarizers with an extinction ratio 10^6. The MOF cells are ring cells manufactured by the Eddy Co. For additional specifications on the MOF cells/magnet assemblies, see Section

4.1.3.

The beam of light (consisting of the $\sigma^{\pm}$ Zeeman components produced by the Sun, now encoded with linear polarization and additional unpolarized light from the Sun), which enters the MOF Section, passes through P1 such that only a single polarization state is transmitted and all unpolarized light is filtered out. The selected polarization state then enters the MOF cell, where the Inverse Zeeman (Righi) and Macaluso-Corbino effects absorb one of the component RHCP or LHCP light that make up the linearly polarized light beam. This results in an orthogonal, linearly polarized beam (with respect to the beam entering the MOF) that transmits through P2 with half the intensity of the original beam.

WS Section: Blue boxes in Figure 4.3. The WS Section consists of the WS cell/magnet assembly, QWP2, a narrowband filter, and WA. The WS cell is manufactured by the Eddy Co. to the same specifications as the MOF cell. QWP2, similar to QWP1, is a Meadowlark Optic optimized to the relevant channel's wavelength. The narrowband filters are made by the Eddy Co., are 21 mm in diameter and have 2-3 nm passbands (for Na and K, respectively). Operating in Tomczyk mode, the MSO WS Section contains a polarizing beam splitter after the WS cell in the form of a 3-degree Wollaston prism (WA). The WA separates light into two linearly polarized outgoing beams with orthogonal polarization, allowing simultaneous imaging of the red and blue wings of a given circular polarization (encoded in linearly polarized light) on the same detector.

Light coming out of the MOF section consists of a single linear polarization state. A set of lenses re-images the beam, which immediately enters the WS and forms a pupil image in the

center of the cell. In the WS, the Righi effect produces two sharp extinction bands that absorb one of the polarization states. Consequently, the resultant beam leaving the WS consists of circularly polarized light of a single wing (red or blue) of the resonant wavelength. The circularly polarized light is transformed into linearly polarized light by QWP2. The presence of the narrowband filter eliminates any stray light before entering the WA; all optics after the WA are fully enclosed to prevent any other out of band stray light from entering the beam path. The WA then splits the beam into its component orthogonal linear polarizations. This creates two solar disks, encoded with the circular polarization information from the relevant wing, which are imaged simultaneously on the CMOS detector.

Imaging Optics: Black arrows in Figure 4.3. Both MSO channels share the entrance lens (L1), each channel contains six other imaging lenses (L2 - L7), and a set of camera focusing lenses. The shared entrance lens (L1) is an OptoSigma doublet with a diameter of 50 mm and a focal length of 1000 mm. All other lenses are Thorlabs achromatic doublets with a diameter of 25.4 mm; MSO-K optics are coated with anti-reflective coating AR-B (650 - 1050 nm), and MSO-Na optics are coated with anti-reflective coating AR-A (400 - 700 nm). For both MSO-K and MSO-Na, the optical functions and (relative) positions of the imaging lenses in the optical path remain the same.

L2 and L3 have a focal length of 200 mm, and acts as an achromatic doublet pair, imaging the focus of L1 to create a pupil image in the MOF cell. L4 and L5 have a focal length of 150 mm and re-image the pupil image in the MOF cell to produce an image in the WS cell. L6 and L7 have a focal length of 400 mm and re-image the WS's image to create a second

pupil image on the WA. The camera-correcting lenses, L8 and L9, consists of 2 achromatic doublets with focal lengths of 150 mm and 100 mm. These lenses focus the image from the WA for the CAM.

4.1.3 MOF Cells and Magnet Enclosures

The MOF cells utilized by both MSO-K and MSO-Na are ring cells (see Figure 2.2) designed and produced by the Eddy Co. They are 96.5 mm long with 19 mm clear-aperture windows. The windows are V-coated to less than 0.2% reflectivity and have optical quality of $\lambda/10$. The cells are back-filled with 35 torr of argon gas to prevent metal condensation on the windows. The alkali vapor is generated by heating the ring part of the cell using a NiCr wire, with a total resistance of 22 Ω. The heating wires are powered by a Stanford Research Systems (SRS) Programmable Temperature Control Unit (PTC10), which allows for variable input voltage and is able to maintain the temperature within 0.1 °C. See Table 4.2 for the operational temperatures of the MOF/WS cells.

The cells are situated in anodized aluminum magnet enclosures, also designed and produced by the Eddy Co. The magnet enclosures utilize permanent bar magnets to produce a highly uniform longitudinal magnetic field centered at the center of the cell. All cells in the MSO instrument are maintained at a 3 kG magnetic field, which facilitates the 0.02 nm separation between the red and blue passband peaks when operating at the lower temperature of Tomczyk mode. The cells are free to rotate in the magnet enclosures to allow for adjustments to minimize interference fringes. See Table 4.2 for more details.

Table 4.2 MSO-K and MSO-Na operational parameters for MOF and WS cells.

	K	Na
MOF Temperature	75°C	180°C
MOF Magnetic Field	3 kG	
MOF Ar Fill Pressure	35 $torr$	
WS Temperature	105°C	190°C
WS Magnetic Field	3 kG	
WS Ar Fill Pressure	35 $torr$	

4.1.4 Mechanical Structure

The main structure of the telescope consists of one 66 mm Thorlabs rail that is 0.81 m long; most of the MSO-K optics are mounted on the top of the rail, while most of the MSO-Na optics are mounted on the bottom. The entrance aperture, L1, is mounted to the end of the rail such that the beam travels through the hollow center of the rail before being split by the BS to feed the two channels. A custom-machined plate supports the BS and the Polarization Sector Section. All of the optic mounts are made by the Eddy Co. to allow for adjustments in the x, y, z, and rotational planes. The entire system, outside the MOF/WS cells, is water-cooled using a NesLab RTE111 system and maintained at 10°C.

The MSO instrument is enclosed in a modular box made from aluminum rails and plastic panels to protect the optics from dust and maintain thermal insulation. The interior of the box is lined with Thorlabs blackout aluminum foil to prevent stray light from entering the system and to minimize internal reflected light. The panels are designed with small ports to allow access to adjust the orientation of P1 and QWP2. Additionally, the panels can be removed individually while the telescope is mounted to enable further optical adjustments.

4.2 *The He MOF Channel*

The MSO-He was designed to produce Doppler- and magnetograms of the solar chromosphere (∼2000 km above the solar surface) to expand our helioseismic studies to the upper chromosphere and investigate wave heating of the upper solar atmosphere. He I MOFs have been most successfully used as a chromospheric probe (e.g. Leenaarts et al. (2025); Lites et al. (1985); Murphy et al. (2005)) and can also be used as a coronal hole diagnostic (e.g. de Toma et al. (2005); Landeros et al. (2025); Zirin (1975)). Additionally, as a gaseous MOF, MSO-He was developed to expand MOF technology into diagnostic wavelengths beyond those of the alkali metals.

MSO can currently only house two MOF channels due to structural limitations. This means that to test/observe with the He MOF, we had to sacrifice one of the currently operational channels. In October 2025, we substituted the MSO-K for the MSO-He. The choice to sacrifice the MSO-K as opposed to the MSO-Na was two-fold. Firstly, the wavelengths of K (769.9 nm) and He (1083.0 nm) are closer in spectrum than that of He and Na (589.0 nm). Since optical performance (transmission, reflection, centering) is wavelength-dependent, we chose the proximity of the K and He lines to minimize the risk of major optical aberrations. For example, the MSO-K channels' optics are coated with Thorlabs AR-B coating which has a transmission of 98.06% at 1083 nm while the MSO-Na optics are coated with Thorlabs AR-A which has a transmission $< 86\%$ at 1083 nm. Additionally, the AR-A coating has $\sim 20\%$ higher reflectivity at the 1083 nm wavelength as compared to the AR-B coating. Moreover, at 1083 nm, the AR-B coating has a focal length shift of ~ 0.14 nm compared

to the AR-A's focal length shift of $\sim$0.8 mm resulting in a necessary camera refocusing distance of $\sim$ 1.26 nm for the AR-B coated MSO-K channel and $\sim$7.2 nm for the AR-A coated MSO-Na channel. Secondly, by substituting MSO-K for MSO-He, MSO would become a fully chromospheric observatory, opening an opportunity to study the plasma dynamics across the chromosphere with inherently co-spatial and temporally aligned channels. As a consequence of being directly substituted in for the MSO-K channel, MSO-He is also a double-Keplarian telescope; its specifications can also be found in Table 4.1.

Due to notable differences between the alkali-based MOF instruments and the gaseous He-based MOF, I dedicate an entire chapter to the development, testing, and observations of MSO-He. Please refer to Chapter 6 for more details. The MSO-He tests I conducted in October 2025 were incredibly promising, acquiring 28 hours of He intensity images with preliminary LoS magnetic field observations including 23 hours of dual Na and He observations.

4.3 *MSO Facility*

The MSO Facility is the private observatory of Mojave Solar, the research subset of the Eddy Company. It is located in Apple Valley, CA, USA in the Mojave Desert (34°29' 45" N / 117°12' 52' W, altitude: 902 m). This location was chosen due to its relatively clear, dry climate and its proximity to the mechanical workshop/laboratory facilities at the Eddy Company. Apple Valley averages 73 cloudy days per year (including partially cloudy days), with only 25 rain days. The major limiting factor for observations at MSO is smoke coverage coming from wildfires. In particular, during the entire month of January 2025, 14 wildfires

ravaged Southern California, not only creating conditions non-conducive to observing but also depositing a notable amount of dust/soot on the observatory, which had to be properly cleaned before observing could resume.

Figure 4.4 Left: the MSO solar dome as seen from the outside. Right: the dome aperture from the inside.

The observatory consists of a custom 3.05 m (10 ft) dome with a 10 cm aperture equipped with four photodiodes for automatic solar tracking (Figure 4.4). The telescope itself is mounted on a Byers C-14 Retrofit alt-az mount with an equatorial wedge (making it act as an equatorial mount). The telescope system is equipped with an additional, fine-tune tracking system comprising four photodiodes on the front of the primary aperture, which feed into the dome control to ensure proper solar alignment. I have fitted both the dome and the telescope box with blackout equipment to prevent stray light from contaminating the beam and to assist with temperature control.

MSO was not originally designed to operate fully autonomously; however, since its integration into the GATES Network, the process of automating the telescope has begun. I

have installed programs to remotely control the dome, telescope, camera, and have ensured the HWPs and temperature control can operate automatically throughout the day (see Appendix D for operation procedures). The GATES team at MSO is currently working to transition all other controls, such as camera position and cell temperature adjustments to be accessed digitally so they can be made more autonomous. For more information about the future of MSO and its automation, please refer to Section 9.2.

4.4 *First Light and Preliminary Data*

MSO was designed as a scaled-down version of the MOTH telescope. It was conceptualized in the early 2000s after the successful MOTH observing campaigns at the South Pole, and began as a stand-alone telescope with planned operation under the Eddy Co. After its initial construction in 2017, MSO remained dormant for a period of time, before I reconstructed it, conducted a full realignment, recalibration, and software analysis for its integration into the GATES Network in 2022. From 2022 to 2025, to prepare the telescope to serve as a fully functional node in the GATES Network, I performed multiple upgrades, such as replacing the internal wiring, increasing the telescope's pointing precision, adding stray-light blocking baffles at the focus, and adding stray-light blocking box covers.

4.4.1 2022 and 2023 Data

I acquired first light images at MSO on November 15, 2022 with just the TSST-K channel. I completed two ten-minute acquisitions using a 5 s cadence, utilizing a preliminary version of the LabVIEW acquisition control algorithm that is operational today. Figure 4.5 shows

an intensitygram, Dopplergram, and Magnetogram from this day.

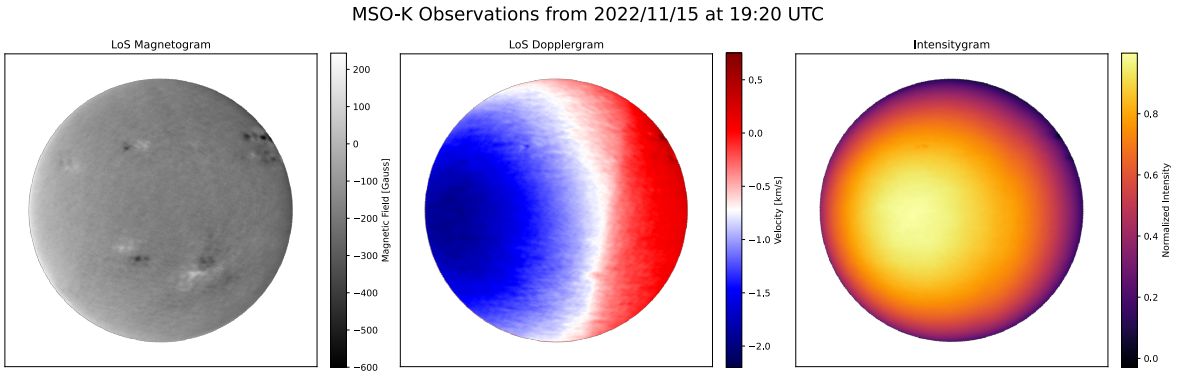

Figure 4.5 10-minute averaged magnetogram, Dopplergram, and intensitygram acquired by the MSO-K on November 15, 2022 at 19:24 UTC. The magnetic field units were matched off GONG El Teide at this time. We note the blurring in the magnetogram and the curved zero velocity line in the Dopplergram indicate the telescope is out of focus and the polarization optics are misaligned.

In addition to acquiring science images, the purpose of this first-light test was to confirm the functionality of the LabVIEW control and data saving algorithm. Furthermore, because the MSO facility had been dormant for an extended period, this test was performed to identify any additional observatory errors. Identified issues and their implemented solutions included:

- No magnetic signal attainable due to miscommunication between the control algorithm and the sensor, which modulates the voltage (and therefore position) of the LCVR HWP.
  - LabVIEW algorithm was updated to better control the HWP.
- Mismatched intensities present for the red and blue wings of a given polarization state.
  - I realigned the polarization optics of the MSO-K (and subsequently MSO-Na).

- Intermittent signal degradation during sensor readout, caused by an improper extension cable, leading to incomplete data frame where the upper portion of the array was not transmitted.
  - I upgraded and installed amplifying USB 3.0 cables for both cameras.
- A lack of data organization when saving (i.e. all data saved to the same folder).
  - LabVIEW algorithm was updated to create a new data folder every hour.
- Inconsistent solar tracking for the dome.
  - I replaced dome photodiodes and increased the temporal cadence on the dome adjustment algorithm for increased precision.

I, along with the GATES team at MSO, resolved the first two identified issues, misaligned and nonfunctional polarization optics, during the 2022 first light tests. I addressed all other matters between the 2022 first light and 2024 data acquisition. Additionally, during this period, I acquired a few days of test observations with the MSO-K to confirm the successful operation of the hardware and software upgrades. Figure 4.6 shows data I acquired on July 20, 2023 after the majority of the hardware and software upgrades were complete. During 2023, my main research focus was the TSST, so aside from these few days of test data, MSO remained dormant.

4.4.2 2024 Data

In 2024, I worked in parallel at MSO, developing the MSO-He MOF in the lab (see Chapter 6) and improving the observational function of the MSO-K and MSO-Na channels. The goal

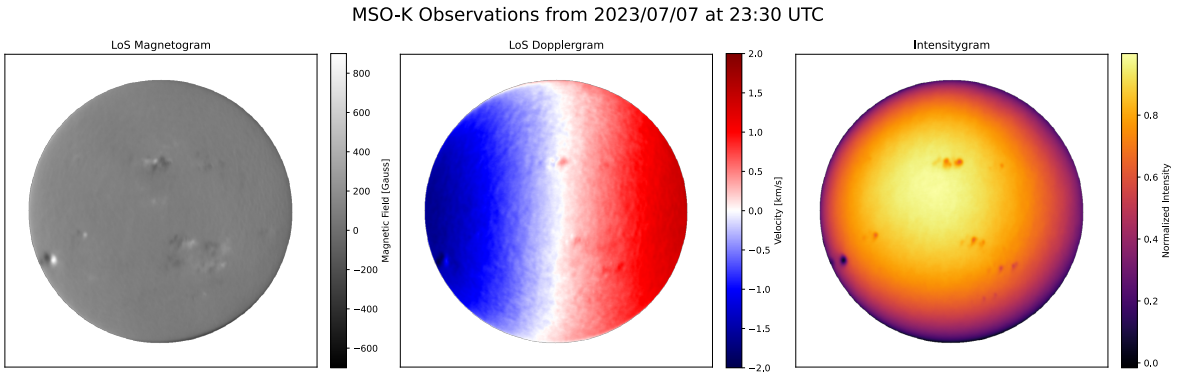

Figure 4.6 10-minute averaged magnetogram, Dopplergram, and intensitygram, from July 7, 2023 at 23:30 UTC. Magnetic field units were matched to GONG BBSO. Although the focus appears better than the 2022 test images, an intensity gradient most notable in the intensity gram indicates possible vignetting.

for MSO in 2024 was to bring the telescope to a point where it could conduct observing campaigns by the end of the year. Although unused for a shorter period in 2023 than its previous dormancy, MSO required many upgrades in 2024 to achieve this goal. Identified issues and solutions employed include:

- MOF and WS heating control was lost.
  - I rewired MSO-K and MSO-Na heating connections.
- MSO-K DT control was lost.
  - I replaced the camera sensor cable, which controls the DT signal.
- Fringing identified on the left side of the MSO-Na sensor, independent of the solar beam, caused by MOF cell window aberration.
  - I installed a blocking piece to cover aberration on the MOF window without blocking the solar beam.

- Stray light present, minimizing the contrast between the solar disk and background and increasing leakthrough light.
  - I installed Thorlabs BK4 blackout aluminum foil to the entire telescope box to minimize stray light entering the beam-path. I installed irises at the end of the rail and at the first focus of both channels to cut background light.
- Notable drifts in track throughout the day.
  - I installed an additional quad diode utilizing the excess light from the beamsplitter for fine-tuned tracking.

In addition to making the various improvements listed above, I conducted a new telescope optical alignment in the lab, followed by an on-sky polarization optical alignment (see Appendix C for more details). During the time these upgrades were being made, I obtained 28 hours of dual-height test observations (using MSO-K and MSO-Na) over 8 days. Figure 4.7 shows Doppler- and magnetograms from April 23, 2024.

The 2024 observations confirmed the Doppler velocity and magnetic field obtaining functions of both the MSO-K and MSO-Na channels. Slight spatial blurring in the MSO-K magnetogram indicated the need for improved focal alignment and image-registration precision. Additionally, the MSO-Na intensitygram exhibited strong intensity gradients over the disk, which were caused by vignetting on the MOF cell magnet enclosure. I address all of these aberrations prior to the 2025 GATES observing campaign. The observations from 2024 culminated in a two-day observing run on November 7 and 8, 2024, which I used to test MSO's automatic and remote capabilities.

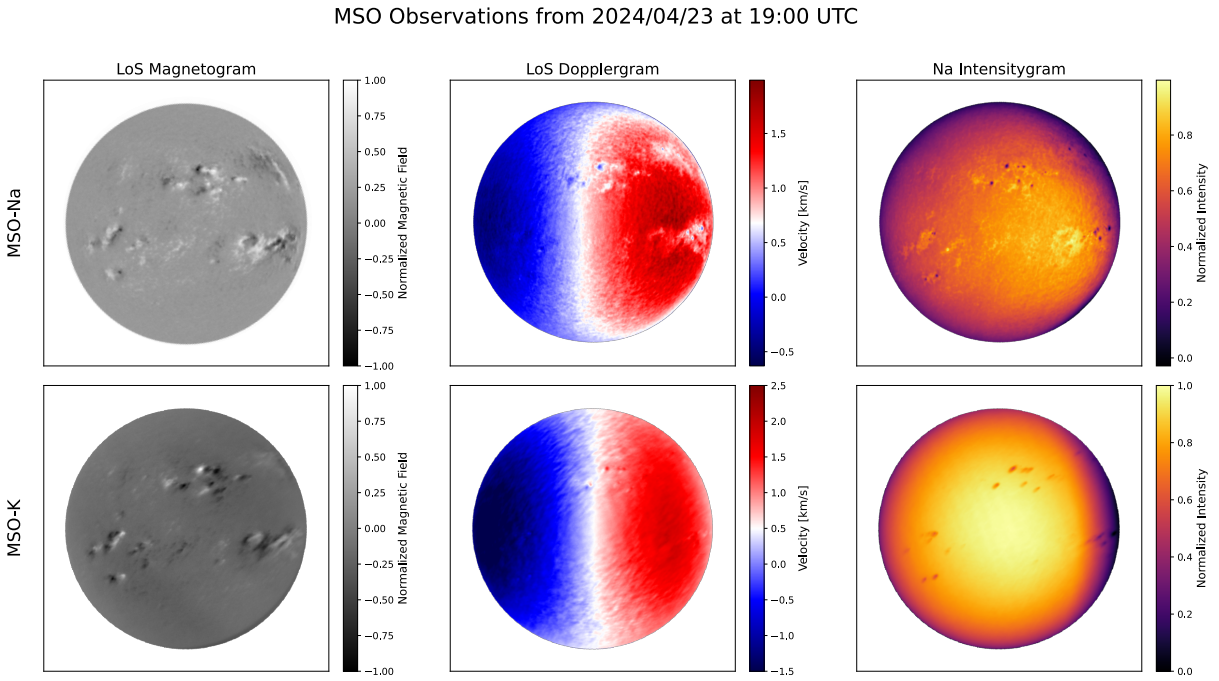

Figure 4.7 10-minute averaged magnetograms, Dopplergrams, and intensitygrams from the MSO-K and MSO-Na channels from April 23, 2024 at 19:00 UTC. The images are normalized and the Dopplergrams calibrated to ± 2 km/s as described by the reduction pipeline in Section 5.3. However, calibration images were not acquired at this time, so these observations are uncorrected for dark current, polarization optic leakthrough, and systematic aberrations (which flat field images address).

4.4.3 2025 Data

With the success of the 2024 data tests, I planned to begin dual-height observations in early 2025. However, due to the January 2025 wildfires in Southern California, MSO was forced to remain shut for the first few months of the year. Despite MSO's relative safety from the active fires, the smoke from the fires made observing conditions unfeasible, with the Sun being completely covered by smoke on some days. Additionally, the high winds brought additional dust and debris to MSO, covering the optics and requiring the telescope to be

deep-cleaned and realigned before it could be used again. Furthermore, the fires displaced some of the MSO team for multiple months, delaying observations.

In June 2025, I returned MSO to its fully operational capacity, realigned and cleaned the telescope (achieving a signal-to-leakage ratio of 18.56 and 16.35 for the MSO-K and MSO-Na channels, respectively), and established its calibration acquisition procedure (see Section 5.3.1.2), preparing MSO to participate in the GATES Network's proof-of-concept observing campaign. As part of the GATES Network, MSO had two observational goals for 2025: conduct a dual-site observing test with TSST and conduct an extended dual-height observing campaign with MSO-K and MSO-Na to investigate wave propagation. On July 23, 29, and 31, 2025, I observed with MSO alongside the UTOV team observing with the TSST for the GATES dual-site test (see Section 5.4.1); we acquired 8 hours of dual-site data between these two days. Between July and October 2025, I conducted an extended observing run at MSO, acquiring 440 hours of science observations over 56 days. These observations included 384 hours of dual-height MSO-K / MSO-Na observations and 43 hours of MSO-Na / MSO-He observations. As the first official observing run of the GATES Network, the details of the Summer 2025 observing campaign can be found in Section 5.4.2.

CHAPTER 5
THE GATES NETWORK

5.1 *Network Concept*

The GATES Network is an international collaboration of ground-based telescopes for space weather studies. It aims to produce a multi-height, synoptic data set of the solar atmosphere for real-time space weather predictions and notifications, as well as contribute to general solar physics studies. As a network of ground-based telescopes, GATES plans to leverage the observational coverage of multiple low-latitude sites to achieve fully synoptic observations.

The GATES Network currently consists of nodes: The Tor Vergata Synoptic Solar Telescope (TSST) and the Mojave Solar Observatory (MSO). As described in Chapter 3, the TSST is designed as a robotic, dual-channel telescope located in Rome, Italy, consisting of a Daystar SR-127 QT Hα telescope for chromospheric observations and flare detection and a modular K I 769.9 nm MOF-based telescope for photospheric LoS Doppler velocity and magnetic field measurements. As described in Chapter 4, MSO is a dual-MOF channel-based telescope located in Apple Valley, CA, USA, consisting of K I 769.9 nm and Na I D2 589.0 nm MOF channels to observe LoS Doppler velocity and magnetic fields in the photosphere and low chromosphere. MSO also has tested a He I 1083 nm MOF for higher chromospheric velocity and magnetic field measurements.

The telescopes of the GATES Network are designed modularly and utilize commercially available parts with the specific goal of being readily reproducible. With the ultimate goal of being a truly synoptic network, obtaining constant observations of the Sun, GATES requires

additional nodes to increase its temporal coverage. The commercially producible modular designs of the telescopes enable new nodes to be readily and cost-effectively added to the network. In addition to the two tested observation-ready GATES nodes, two new nodes are in the initial stages of potentially joining the network. Figure 5.1 depicts the current and future GATES nodes; Table 5.1 describes specific parameters of each node.

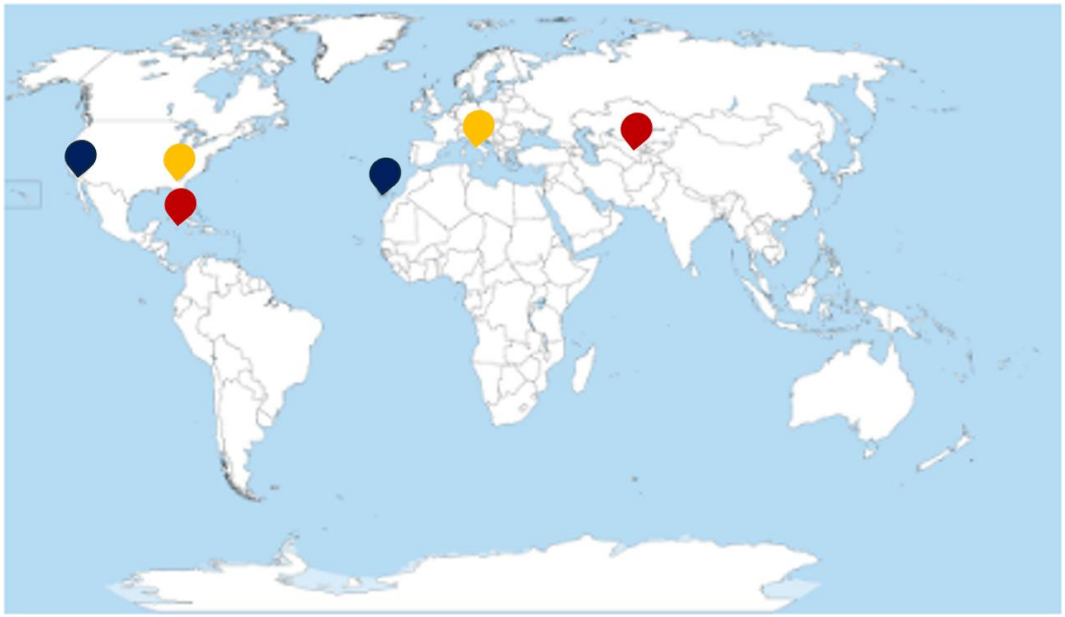

Figure 5.1 A map of the current and future nodes of the GATES Network. Yellow flags represent currently active institutions contributing resources, personnel, and administration. Blue flags represent the current/confirmed-near-future operational sites for GATES nodes. Red flags represent potential future collaborations.

5.2 *Data Acquisition Cadences*

The primary science driver of the GATES Network is space weather prediction and monitoring. To match the temporal cadences of current flare prediction models (e.g., Angryk et al. (2020); Bobra et al. (2014)), we require an observational cadence of 12 minutes or less. The

Table 5.1 List of GATES partners and observing nodes. Bolded nodes indicate currently operational nodes utilized in the Summer 2025 observing campaign. 'K MOF' refers specifically to the $K\ ID1$ 769.9 nm MOF, 'Na MOF' is the $Na\ I\ D2$ 5889.0 nm MOF, and 'He MOF' is the $He\ I$ 1083.0 nm MOF.

Name	Abbreviation	Latitude	Longitude	Altitude (m)	Role/Instrument
Georgia State University	**GSU**	**33° 45' 17" N**	**84° 23' 14" W**	**340** m	**Admin**
University of Rome Tor Vergata	**UTOV**	**41° 51' 14" N**	**12° 36' 17" E**	**50** m	**Admin** **Hα** **K MOF**
Eddy Company	**Eddy Co.**	**34° 29' 56" N**	**117° 10' 17" W**	**903** m	**Admin**
Mojave Solar Observatory	**MSO**	**34° 29' 45" N**	**117° 12' 52" W**	**902** m	**K MOF** **Na MOF** He MOF
University College of the Cayman Islands	UCCI	19° 20' 17" N	81° 18' 13" W	10 m	Hα MOF
Tor Vergata Synoptic Solar Telescope	TSST	28° 45' 15" N	17° 53' 18" W	2366 m	Hα K MOF
Samarkand State University	SSU	39° 38' 41" N	66° 57' 39" E	741 m	Hα K MOF

secondary scientific goal of the GATES Network is to investigate acoustic waves in the solar atmosphere, which requires an even higher cadence; to investigate high-frequency waves (10 - 50 mHz), like those theorized to contribute to coronal heating, a cadence of at least 10 s is necessary.

With these science drivers in mind, the MSO acquisition cycle is set to acquire a complete filtergram series, containing four R^+, B^+, R^-, B^- filtergrams used to construct Doppler- and magnetograms (see Section 2.3), every 5 s. Because MSO utilizes LCVRs, this cadence is both mechanically achievable and sufficient for SNR. Additionally, MSO's dual-height observational capabilities, combined with this achievable high cadence, make MSO the ideal node to designate for high-frequency wave data set acquisition. Moreover, a 5 s cadence is directly scalable to HMI's 45 s cadence, GONG's 60 s cadence, and sets an easily scalable cadence for all other GATES nodes.

The TSST acquisition cycle is limited by the rotational speed of the HWPs, and the necessity to acquire the filtergram series sequentially. The cycle is set so that each filtergram is acquired over 5 s. This cadence was chosen for multiple reasons. First, it matches the acquisition cadence at MSO, therefore allowing the intensities of particular filtergrams to be directly compared between the two sites. Second, factoring in an average HWP rotation time and frame-saving time of 4.7 s between filtergram acquisitions, we obtain a Doppler- and magnetogram every 50 s. This cadence is easily scalable to MSO 5s data, matches HMI's cadence, and allows us to Nyquist-sample acoustic frequencies down to 10 mHz.

5.3 *Data Reduction*

I adopted the data reduction pipeline for GATES data from the MOTH pipeline (Forte et al. 2020) and PMODE pipeline (Gulledge 2022). Both the MOTH and PMODE instruments were MOF-based and followed the general reduction framework shown in Figure 5.2. This framework breaks data reduction into three main steps: applying calibration images, spatially and temporally registering images, and computing Doppler- and magnetograms. In the subsections below, I detail the specific steps I implemented into the GATES pipeline. I have written the GATES pipeline using iPython notebook-style cells for increased accessibility and flexibility between the two GATES Networks.

As detailed in Sections 3.2.2 and 4.1.2, the two active GATES nodes operate in different MOF modes; consequently, their raw data is in slightly different formats. Due to MSO's usage of Wollaston prisms, two filtergrams are simultaneously imaged on the same detector. Additionally, MSO's use of LCVRs in place of a mechanical HWP1 allows all four filtergrams to be captured in a single acquisition. Moreover, MSO's acquisition software sums all frames within an acquisition prior to saving. Consequently, all four filtergrams are saved to a single two-dimensional array. Because the TSST relies on mechanically rotating HWPs, it observes a single filtergram per acquisition. Moreover, the TSST acquisition software saves every frame within an acquisition, producing a three-dimensional array for each filtergram. Figure 5.3 shows the difference in the raw data acquisition between MSO and TSST.

Because of their differing data acquisition methods, MSO and TSST data require different procedures for calibrating raw filtergrams. To account for this, I implemented separate

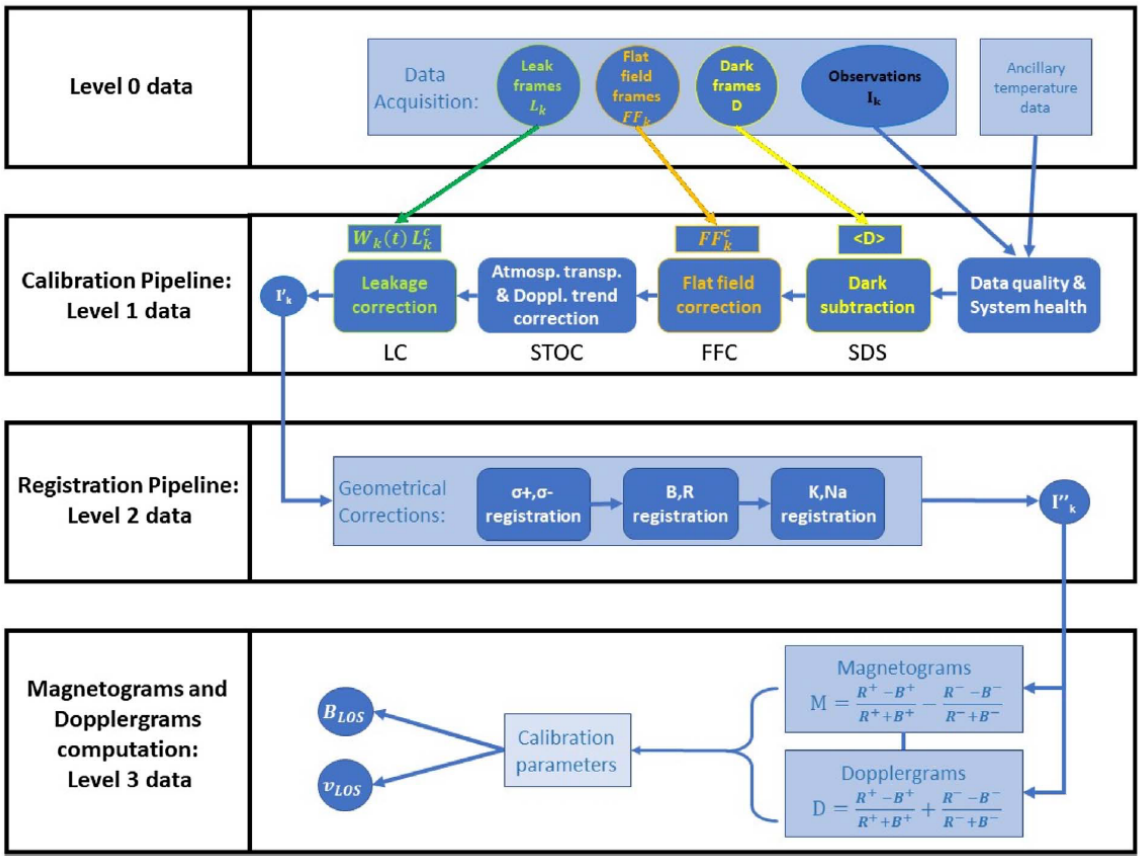

Figure 5.2 The general data reduction framework for MOF-based instruments as defined by MOTH data reduction pipeline from Forte et al. (2020).

calibration cells into the GATES pipeline for MSO and TSST filtergrams. This step ensures the two nodes' outputs are consistent with each other, allowing for the rest of the pipeline (registration and Doppler- and magnetogram computation) to be unified. The following subsections detail the individual processes within the GATES data reduction pipeline. Please see Appendix E for an example of the GATES reduction code.

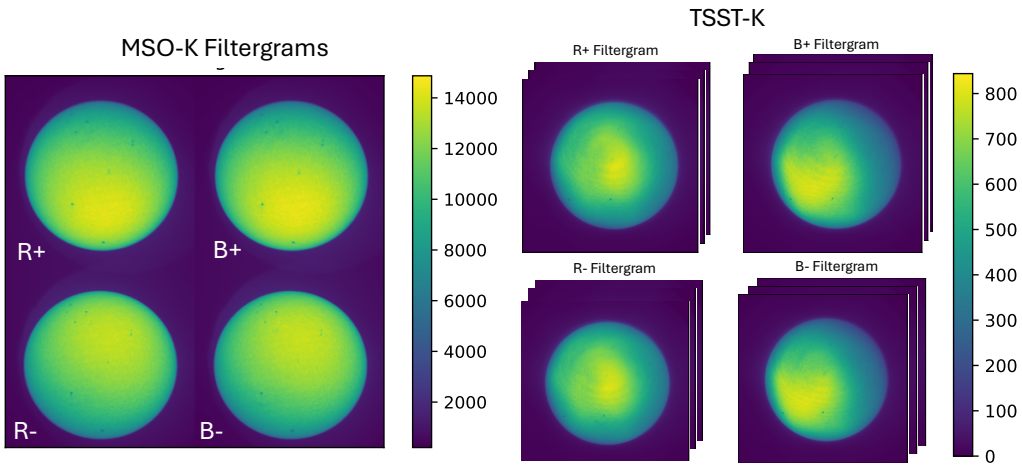

Figure 5.3 Left: Raw MSO filtergrams consist of a single, two-dimensional array with the entire acquisitions' exposure frames already summed. Right: Each raw filtergram from the TSST is saved to its own file in the form of a three-dimensional array containing all of the frames acquired during an acquisition. The different nodes' filtergrams are plotted on different count scales based on the acquisition time of each node.

5.3.1 *Calibration Pipeline: Level 1 Data*

The first step in the data reduction process is creating master calibration images. In addition to the typical flat-field and dark-current images, MOF-based telescopes have an additional calibration image called a leakthrough image. Leakthrough images measure the amount of light transmitted through the crossed polarizers P1 & P2 when the MOF cell is off. Since the passband of the MOF-based instruments is so narrow, both the TSST-K and MSO channels require the Sun to be used as a flat field image illumination source. For the summer 2025 GATES observing campaign, both telescopes utilized diffusive filters from LEE Filters to diffuse the solar disk and create a near-uniform illumination on the detectors. The flat field images were acquired with the respective channels' typical science acquisition procedure – maintaining stable pointing and observing a full filtergram series over a user-specified length

of time. For more information on flat field acquisition procedures and future upgrades, see Appendix B

5.3.1.1 TSST Calibration

Because the TSST saves each frame within an exposure, the first step in preparing any of the calibration or filtergram images for reduction is to sum all the frames within an exposure. This computation is performed as a "step 0" prior to any other reduction.

Calibration image acquisition and master calibration frame production begin with the dark-current images. To create the Master Dark, all dark images were scaled to match the filtergram exposure time of $5s$; the images were then averaged and, in consistency with the MOTH and PMODE pipelines, median-filtered (with a 3x3 kernel). An example TSST Master Dark is shown in the left panel of Figure 5.4.

The second calibration step is the flat field images. Flat-field images are acquired with both the MOF and WS cells on for each filtergram type. To produce the Master Flat, each flat-field exposure (a sum of individual frame stacks) is dark-corrected. Subsequently, the dark-corrected flat-field images for a given filtergram type were summed – in order to reach 30% - 70% of the detector's full well capacity – median-filtered, dark-corrected, and smoothed with a 4σ Gaussian filter. The Master Flat was then normalized, and a bias of 0.001 was added to prevent division-by-zero errors. The center panel of Figure 5.4 shows TSST Master Flats.

The final calibration image is the Master Leakthrough. Similar to the Master Dark, the Master Leakthrough was produced by scaling the summed leakthrough frames to match the

filtergram exposures. Subsequently, the Master Leakthroughs were median-filtered and dark corrected. The right panel of Figure 5.4 shows TSST Master Leakthroughs.

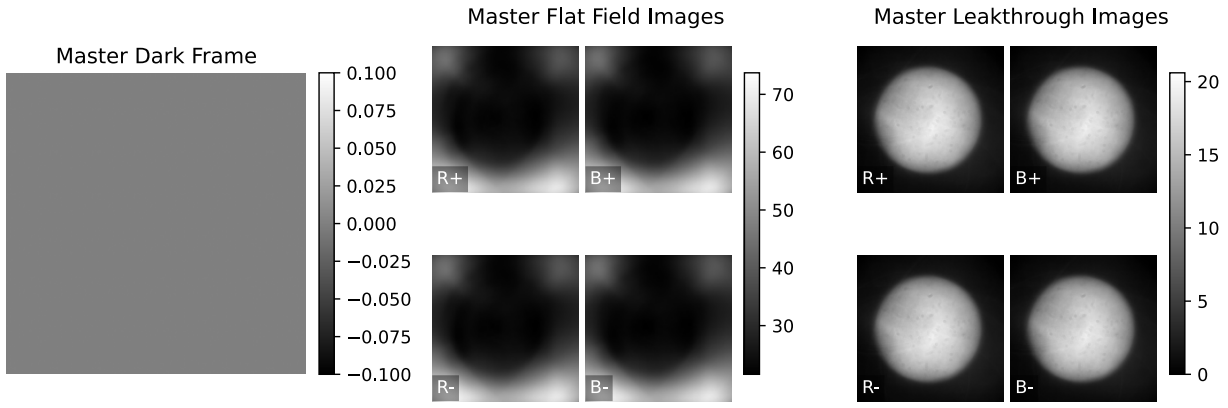

Figure 5.4 Master calibration images from the TSST-K on July 31, 2025. Left: Master Dark applied to all filtergrams/calibration images. Center: Master Flats corresponding to particular filtergram types. Right: Master Leakthroughs corresponding to particular filtergram types. The nonuniformity in the Master Flat indicated the need to implement a dithering procedure in the flat field acquisition.

Once the master calibration images are created, they are saved as .fits files in a new directory for application to the filtergrams. Each filtergram has its frames summed and is corrected for dark current by subtracting off the Master Dark. Then, each filtergram state has its corresponding Master Leakthrough subtracted off and its corresponding Master Flat divided out. These calibrated filtergrams are then stacked into a single three-dimensional array for the rest of the unified GATES reduction pipeline and saved as a single, calibrated 3-D .fits file. Figure 5.5 shows a filtergram series before and after the calibration pipeline is applied. The single filtergram series depicted in this Figure constitutes a single exposure of 62.5 ms. The calibrated series includes the step to sum all of the 5 s acquisition frames' 62.5

ms exposures. This produces a visible spatial blurring as the observing cadence is no longer below the seeing coherence time. In the future, we plan to implement image reconstruction and lucky imaging techniques to improve the angular resolution of the 5 s cadence.

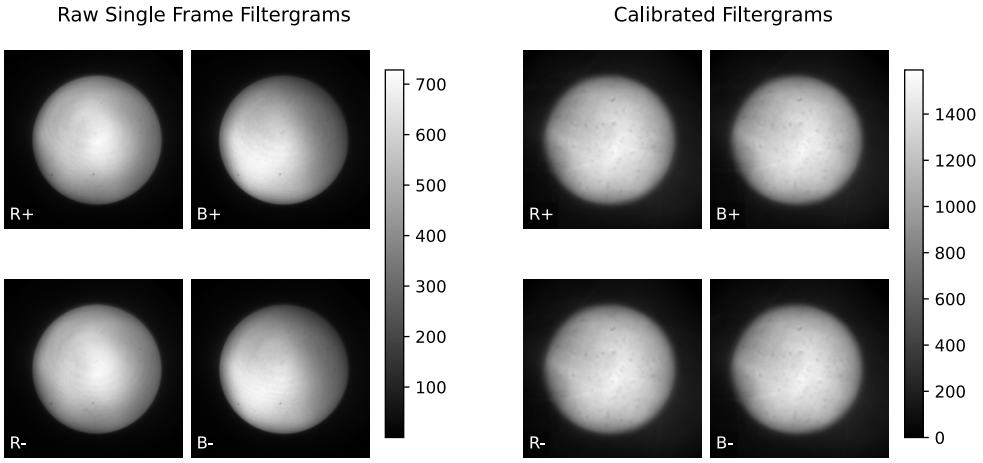

Figure 5.5 An example of a TSST filtergram series before (left) and after (right) the calibration pipeline has been applied from July 31, 2025. The precalibrated series shows a single exposure within the acquisition series; the calibration procedure sums all exposures within an acquisition frame prior to applying calibration images.

5.3.1.2 MSO Calibration

Because the MSO acquisition pipeline produces a single file for an entire filtergram series, all calibration images likewise contain the complete series within a single frame. All MSO Master Calibrations are produced/applied with this full-series filtergram prior to individual filtergrams being separated for Level 2 reduction. An additional divergence from the TSST calibration is the MSO's acquisition of flat-field images. All of the MSO channels acquire their flat-field images with only the MOF cell on to maximize detector illumination, but

maintain the procedure of consistent telescope pointing and full filtergram series acquisition.

The computations for the MSO Master Calibrations are nearly identical to the TSST's; the main difference is that MSO frames do not require "Step 0" frame summing since MSO acquisitions sum individual frames before saving exposures. The Master Dark is created by averaging all Darks and applying a median filter. The Master Flat is created by dark-correcting each flat-field frame, summing these frames to reach 30% - 70% of full well capacity, normalizing, median-filtering the resultant frame, applying a Gaussian filter, and giving a 0.001 bias. Lastly, the Master Leakthrough is produced by averaging the Leakthrough images, applying median filtering, and dark-correcting. Figure 5.6 shows an example of MSO Master Calibrations from July 31, 2025.

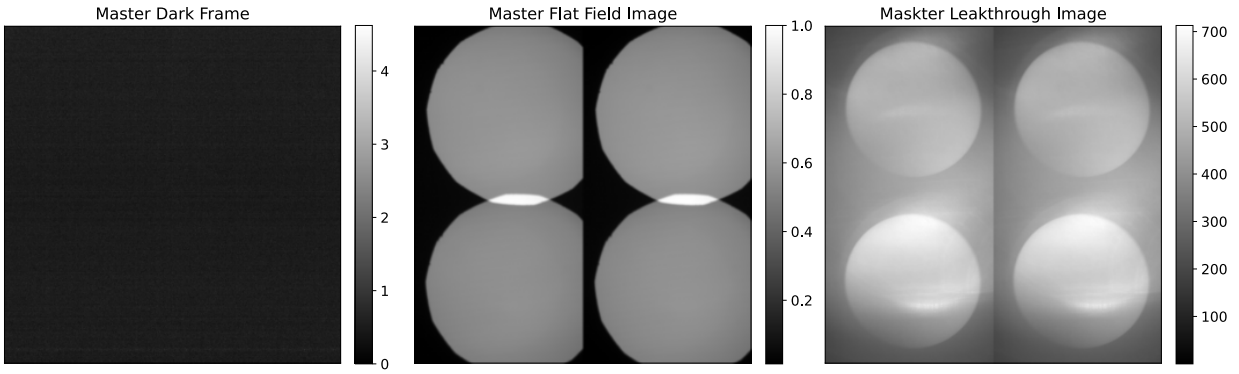

Figure 5.6 Master calibration images from MSO-K on July 31, 2025. Master Darks (left), Master Flats (center), and Master Leakthrough (right) are applied to all filtergrams since the MSO acquisition provides a single, stitched frame for all filtergrams. The Master Flat exhibits the pattern of the irises placed at the focus to block stray light.

Once the master calibration images are created, they are applied to the raw filtergram images in the same manner as the TSST calibration. At this point in the reduction process,

the MSO filtergram series is divided into individual filtergrams simply by cutting the arrays in half along both axes. The four calibrated filtergrams are then stacked into a single array, saved to a new .fits file, and fed to the rest of the unified GATES reduction pipeline. Figure 5.7 shows an MSO-K filtergram series before and after the calibration pipeline is applied.

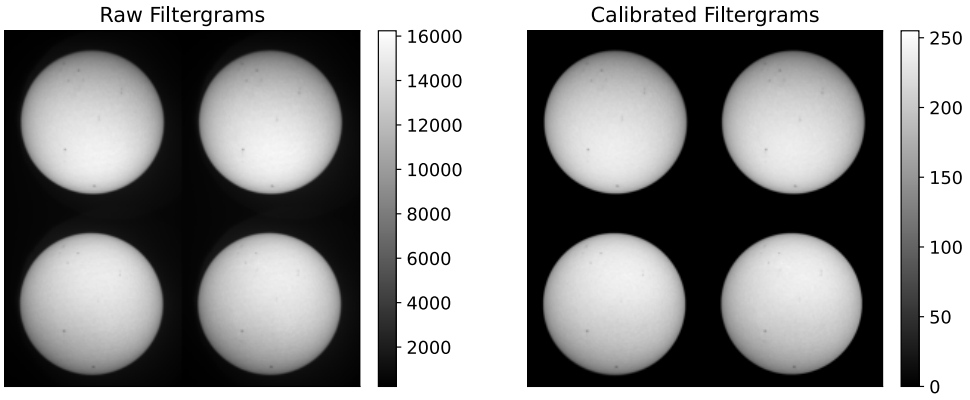

Figure 5.7 An example of an MSO-K filtergram series before (left) and after (right) the calibration pipeline has been applied. The irises present in the flat field images (as well as the raw images are masked out.

5.3.1.3 He MOF Calibration

The He MOF has an additional calibration step, correcting for spurious light entering the beam path from the emission of the ionized He within the MOF and WS cells. Since the He MOF operates probing a metastable He line, the neutral He within the cell must be ionized, producing a cell "glow", to allow the metastable line to populate via energy cascade from the ionized state (see Section 6.1 for more details). These emission images, referred to as the "glow frames", are acquired with no sunlight entering the telescope, and the MOF/ MOF+WS cells on. The Master Glow is created in the same way as the Master Leakthrough: by averaging all glow frames and applying median filtering. Figure 5.8 shows an example of

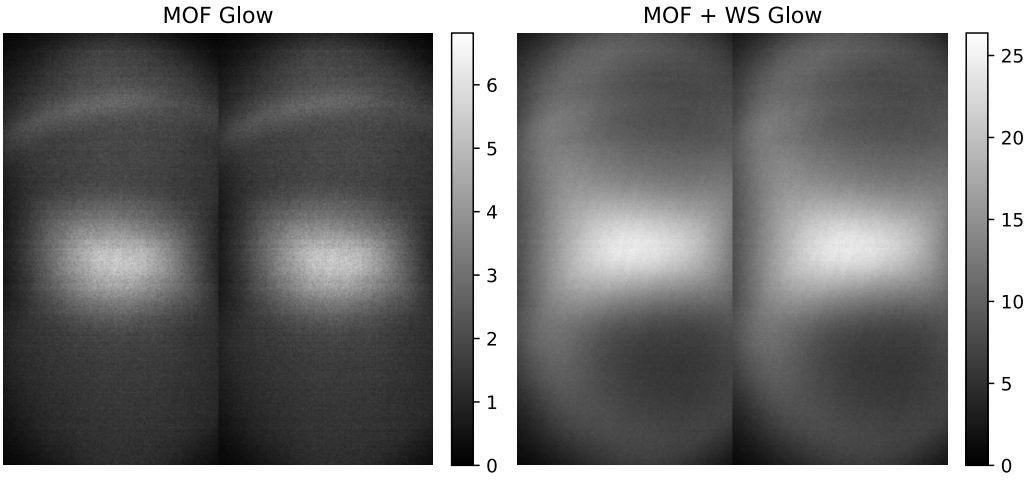

Figure 5.8 Master Glow images for just the MOF cell (left) and the MOF cell and the WS cell (right) acquired by the MSO-He on October 24, 2025.

Master Glows from October 24, 2025.

The necessity of glow frames requires the He calibration pipeline to deviate slightly from the typical GATES pipeline. The Master Dark and Master Leakthrough are created using the same process for MSO-He as the rest of the GATES channels. However, the MSO-He Master Flat is created by glow-correcting each flat-field frame, in addition to applying dark correction, prior to summing, normalizing, median-filtering, and Gaussian filtering. In addition to glow-correcting the Master Flat, each filtergram is glow-corrected before flat-field correction. Since MSO flat field images are taken with just the MOF cell active, the "Master MOF Glow" is the Master Glow that is applied in the Master Flat creation process, where the "Master MOF+WS Glow" is the Master Glow applied to each filtergram during its calibration. Figure 5.9 shows an MSO-He filtergram series before and after its calibration pipeline has been applied.

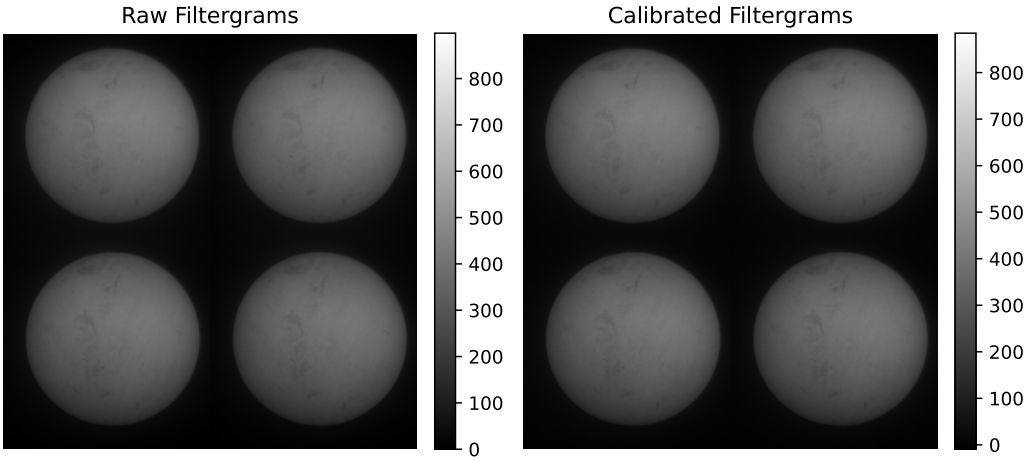

Figure 5.9 An example of an MSO-He filtergram series before (left) and after (right) the calibration pipeline has been applied from October 24, 2025. Despite the similar colorbars, the calibrated filtergrams have a notable amount of cell glow emission removed.

5.3.2 *Registration Pipeline: Level 2 Data*

The combination of small tracking losses (TSST$\sim 31.59"/hr$ and MSO $\sim 19.6"/hr$) and filtergram series splitting (MSO) requires individual filtergrams to be aligned prior to Doppler- and magnetogram computation. For each filtergram, a Hough transform (Duda & Hart 1972) is applied to identify the solar disk circle and disk center. Each filtergram is then shifted so that the center of the detected solar disk lies at the center of its array. Each filtergram is then scaled so that the solar disk size is consistent across filters and GATES channels. Since the Hough transform detects the solar disk post processing, it is sensitive to seeing effects; consequently, in addition to scaling the solar disk size so that it is consistent across GATES nodes, the calibration pipeline scales the disk to a consistent radius across observing days. Finally, a mask of the scaled disk size is created and applied to the filtergrams to mask out the background of the images; both the masked and unmasked data products are saved for

analysis. Figure 5.10 shows an example of the registration pipeline aligning, scaling, and masking an MSO-Na R+ filtergram.

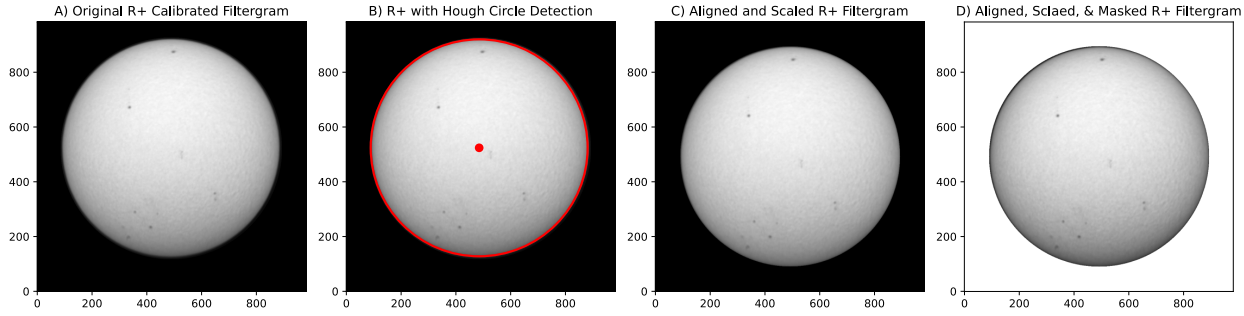

Figure 5.10 Intermediate steps of the registration pipeline as performed on an MSO-Na R+ filtergram. A) Original R+ filtergram; B) filtergram with Hough Circle detection; C) aligned and scaled filtergram; D) aligned, scaled, and masked filtergram. Similar to Figure 5.7, the iris from the optical path is masked out.

Once the filtergrams have been properly registered, the second half of the registration pipeline is to properly orient the images so that the solar north is aligned with the y axis of the images. This is necessary for cross-node calibration as well as comparison to other observatories such as GONG or HMI. Since MSO operates on an equatorially wedged mount and TSST's final mount will be equatorial, the correctional rotation required to align solar north with the y axis should remain constant. Therefore, it would be computationally expensive and unnecessary to check the rotational alignment for every intensitygram in the pipeline. Consequently, the pipeline takes a single input for the necessary rotation to correct each GATES channel's images to properly orient solar north. The calculation for the necessary rotation was done by aligning GATES intensitygrams to HMI intensitygrams outside of the pipeline.

Utilizing the masked filtergrams from the calibration pipeline, an intensitygam was com-

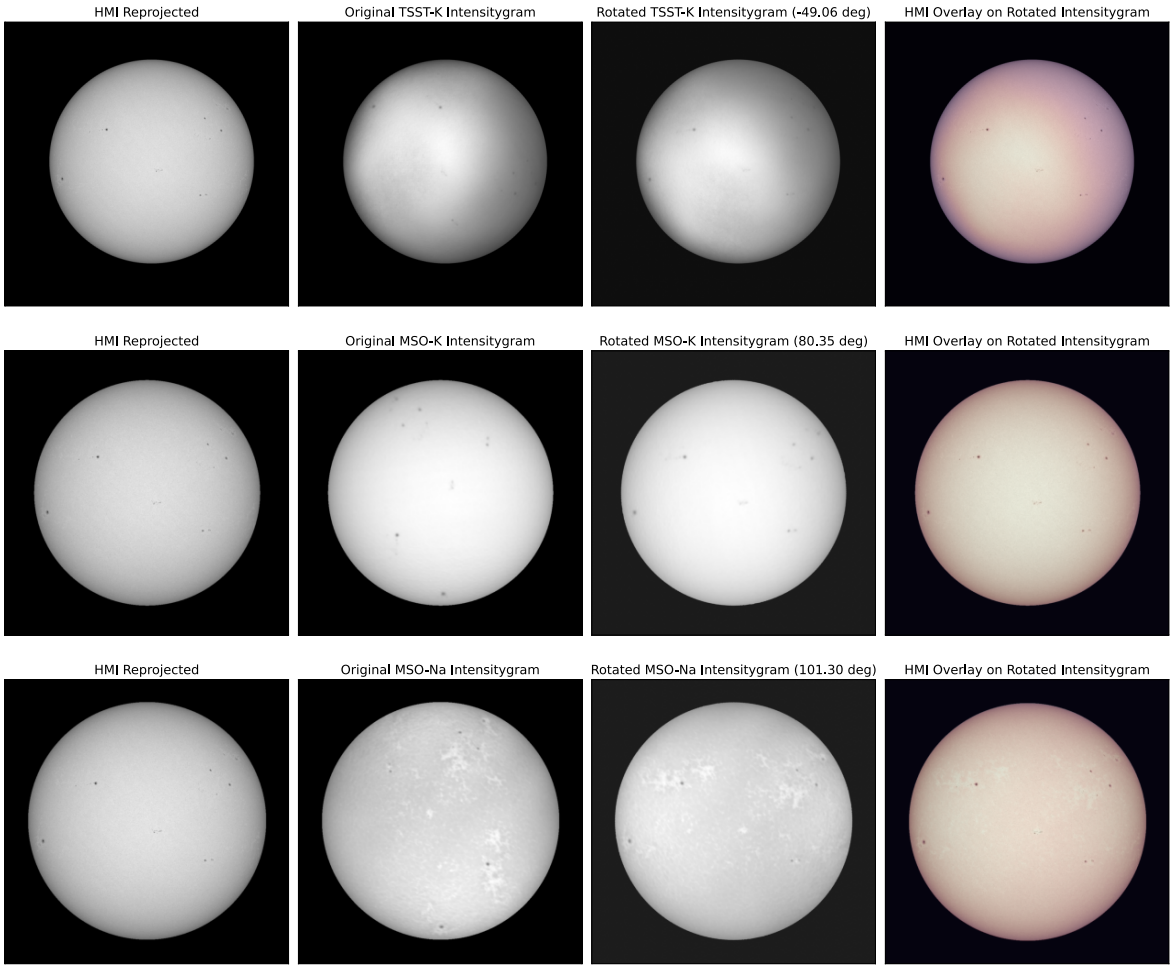

Figure 5.11 TSST-K (top), MSO-K (middle), and MSO-Na (bottom) rotationally corrected intensitygrams from comparison to HMI intensitygrams. Note that in addition to the rotation angle given, the MSO-Na intensitygram had to be flipped over the y-axis, given its channel is on the bottom of the MSO rail and its arrays are consequently saved upside-down.

puted, and a log-polar transform was applied. Both the GATES and HMI instensitygrams were smoothed with a 3σ Gaussian to minimize the effects of fringes (notable in TSST data) and to better match resolutions (degrading HMI's resolution). Subsequently, a phase-cross-correlation of the log-polar images was computed to determine the necessary rotation to orient the GATES intensitygram to match HMI properly. This technique aligns the GATES

data to HMI within 1 pixel, which corresponds to rotational precision of TSST=0.07°, MSO-K=0.143°, and MSO-Na=0.137°. The required rotation angle is saved to be included in the reduction pipeline and, in the future, the metadata of the calibrated images. Figure 5.11 shows an example of this process from all the GATES' MOF channels intensitygrams. The calculated rotation angles for each channel were then input into the pipeline. Although sufficient for MSO's equatorially wedged mount, since TSST operated with the alt-az configuration of the Solar Station's heliostat for the Summer 2025 observing campaign, its rotational position varied throughout the day at a rate of 15 $arcsec/sec$ (Chiodini 2025). Therefore, for the Summer 2025 observing campaign, the TSST data requires additional calibration to ensure it is properly aligned. Once both telescopes are mounted at their permanent locations, these correctional angles will be recomputed and the pipeline updated.

5.3.3 *Dopplergram and Magnetogram Computation: Level 3 Data*

The final step in the data reduction pipeline is to compute Dopplergrams and magnetograms. Although the most frequently used Doppler- and magnetograms are the normalized versions from Equations 2.16 and 2.17, there is scientific interest to investigate the individual RHCP and LHCP Dopplergrams as well as red-wing and blue-wing magnetograms (see Chapter 7). For example, the variation between the red-wing and blue-wing magnetograms of a particular channel allows us to investigate non-radial motions of the solar plasma at specific heights (Section 7.1.1). Additionally, investigating the RHCP and LHCP Dopplergrams of a single channel allows for instrumental diagnoses such as polarization-dependent instrumental effects. Moreover, a phase difference can be measured between the spectral power of the

MSO-Na RCHP and LHCP Dopplergrams, indicating that the individual wings can also be used as independent diagnostic heights (Section 7.2.1). Therefore, the GATES pipeline computes and saves the Doppler- and magnetograms in three-dimensional stacks. Figure 5.12 shows a masked example of the final Doppler- and magnetograms from the MSO-Na channel. Both masked and unmasked versions of these data products are created.

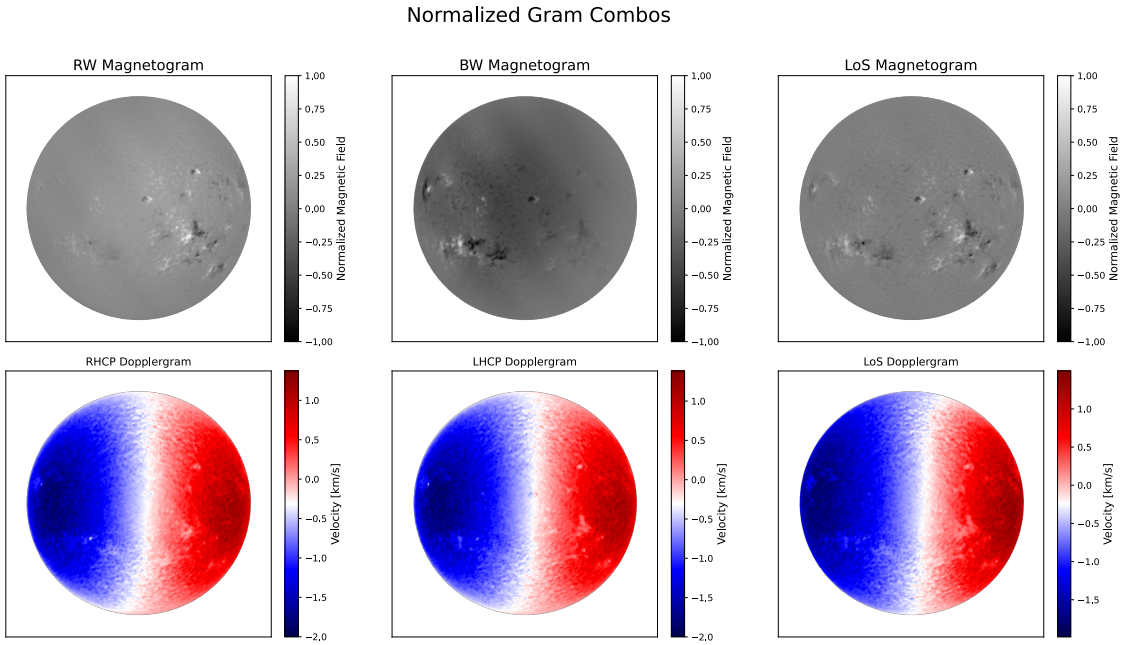

Figure 5.12 A quicklook image of calibrated, aligned Doppler- and magnetogram combinations from the MSO-Na channel on July 31, 2025 at 16:00 UTC. The magnetograms in the top row are saved to a single .fits file in this order, and a similar .fits file is made for the Dopplergrams in the bottom row.

The final computation for the Doppler- and magnetograms is to convert to physical units. The B_{LoS} and V_{LoS} values calculated by Equations 2.17 and 2.16 are proportional to the real solar values, and therefore require relative calibration factors to convert to physical units which can be obtained through laboratory calibration using known magnetic signals, theoretical calibration from the Zeeman effect, semi-empirical solar feature matching, or full

Stokes inversions. We plan a more robust physical unit calibration for the GATES reduction pipeline in the future. However, for preliminary data quality checking and analysis, cross-calibration to other instruments was employed.

The pipeline currently normalizes both the Doppler- and magnetograms to ± 1 and then scales the values for a zeroth order unit conversion. For the Dopplergrams, we account for the $\sim 4\ km/s$ Doppler shift difference between the Eastern and Western solar limbs (Aufdenberg 2003), such that the observed velocities range from approximately -2 km/s on the East limb to $+2\ km/s$ on the West limb (receding). This effect arises from, and is distinct from, the solar rotation (Carrington rotation $\sim$27 days), not the disk-uniform LoS velocity due to Earth's orbital motion.

Currently, the magnetograms are left in their normalized state with the option to scale the magnetograms to match the minimum/maximum values or the probability density functions to known instruments, such as GONG/HMI. This feature also enable the cross calibration between the TSST-K and MSO-K channels. This option provides a reasonable approximation for the physical units of the GATES photospheric channels (TSST-K and MSO-K), but it is far less accurate for the chromospheric (MSO-Na and MSO-He) channels. For these channels, a potential cross-calibration option is to utilize older SOLIS Ca II K 393.37 nm data, which is formed at a more consistent height in the solar chromosphere ($\sim 1 Mm$: Bjørgen et al. (2018)) with respect to the Na 589.0 nm and He I 1083 nm lines. Although useful for preliminary data quality checks and analysis, cross-calibration of physical units to other instruments introduces biases based on the difference in formation heights that the

instruments are probing. Therefore, the more robust, GATES-specific unit calibration tests and pipeline upgrades are one of the first planned improvements to the GATES reduction pipeline.

In addition to the Doppler- and magnetogram production of a standard MOF-based telescope reduction pipeline, the GATES pipeline has two additional optional procedures to begin initial data analysis. The first addition is for resampling the data to a new cadence. This is necessary for cross-calibration between the telescopes, since MSO produces a full Doppler/magnetogram every 5 s and the TSST requires 50 s. The cell takes a user-specified input for temporal rebinning and sums all the grams to the new cadence. The second addition to the GATES pipeline is a cell that applies rotation subtraction to Dopplergrams, thereby making supergranulation patterns visible (Figure 5.13). This procedure produces a smoothed rotational model from applying a $\sigma = 3$ Gaussian to the LoS Dopplergram. This model is then subtracted from the LoS Dopplergram, producing the rotation-subtracted Dopplergram (or supergranulation pattern).

5.4 *2025 Observing Campaign*

The main goal of my dissertation work was to show proof-of-concept of the GATES Network through a dual-site, dual-height observing campaign and to expand the technological capabilities of the He MOF. To achieve these goals, I, along with the GATES team, carried out a three-phase observational campaign during the summer/fall of 2025. The first two phases – Phase 1: dual-site observations (Section 5.4.1) and Phase 2: extended dual-height

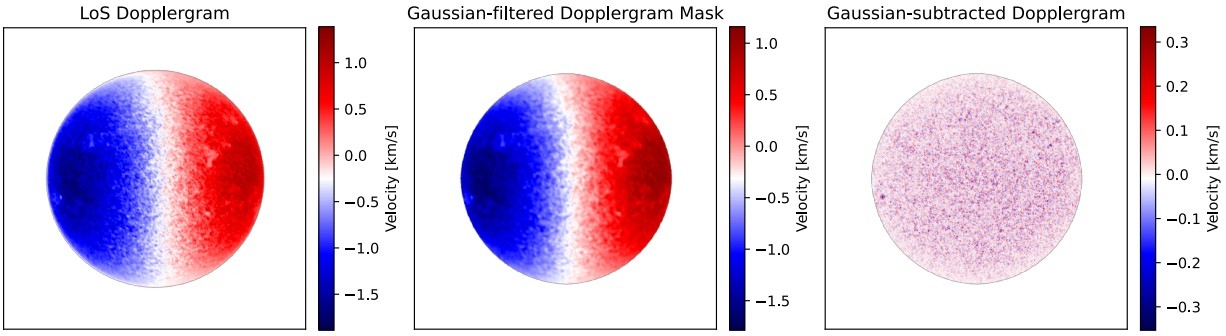

Figure 5.13 Example of the 2D polynomial fit rotation subtraction for obtaining Dopplergram supergranulation patterns. Dopplergram is a 10-minute summed image from MSO-Na on July 31, 2025 at 16:00 UTC.

observations (Section 5.4.2) – addressed the GATES Network's proof-of-concept and were carried out from July 21, 2025, through September 14, 2025; referred to as the Summer 2025 Observing Campaign. During this time, I conducted all observations at MSO. Phase 3 of the 2025 Campaign focused on testing the observational capabilities of the new He MOF. Following the successful conclusion of the Summer 2025 Campaign, I installed MSO-He in place of MSO-K and, after a month of testing, conducted a multi-day MSO-Na/MSO-He observing run. See Section 6.6 for more information about the He MOF observations.

5.4.1 *Dual-site Observations*

The purpose of Phase 1 of the Summer 2025 Observing Campaign was to test the acquisition capability of the TSST-K, to test the multi-nodal observation capability of GATES, and to obtain a dataset for cross-calibration between GATES nodes. During this time, the TSST-K was mounted on the optical bench at UTOV, fed by the Solar Station's heliostat, which is able to observe during the hours of 09:00 - 18:00 CEST (07:00 - 16:00 UTC), and operated

by the UTOV team. During this time, MSO's suitable observing hours were 06:00 - 18:00 PST (13:00 - 01:00 +1 UTC), and was operated by me. As such, we had three hours of possible observational overlap for the campaign (13:00 - 16:00 UTC).

Phase 1 was scheduled around the summer solstice to maximize daylight overlap between the two nodes. However, due to delays in the TSST-K's alignment, electrical and tracking issues at MSO, and poor weather, joint observations were not feasible until the end of July. The dual-site observations were conducted over the span of three days (July 23, 29 and 31, 2025), obtaining nine hours of simultaneous data.

July 31, 2025, was the longest simultaneous observing run with the fewest interruptions. TSST-K began observing at 12:16:56 UTC, from 14:12:00 - 16:04:38 UTC, both the TSST-K and MSO observed, and MSO continued observations until 2025/08/01 01:00 UTC. During this time, there were a few interruptions in acquisition with the TSST due to disconnections of the HWPs motorized mounts. This observing run caught eleven active regions and five C-class flares, two of which were observed by both TSST-K and MSO. Table 5.2 details the flares observed by GATES on this day, and Figure 5.14 shows GATES intensitygrams with the relevant active regions labeled. Figure 5.15 shows ten-minute averaged Doppler- and magnetograms from the three active GATES channels (TSST-K, MSO-K, and MSO-Na) from July 31, 2025 at 15:30 UTC. This time period encapsulates the rising phase of a C1.7 flare in region 4153. The quality of the GATES Doppler- and magnetograms were evaluated in comparison to other instruments (GONG/HMI); see Sections 7.2 and 7.1 for more details.

There are notable aberrations in each GATES node's data. The TSST-K suffers from

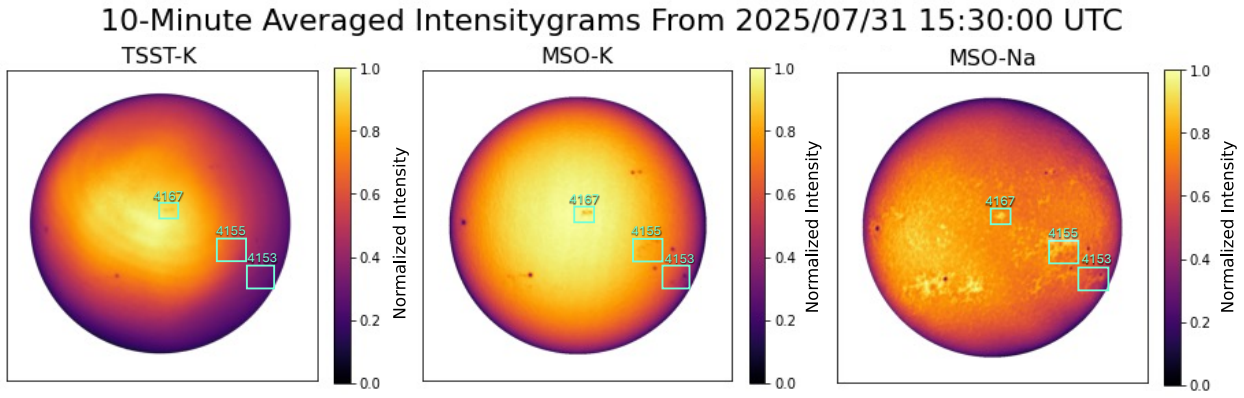

Figure 5.14 TSST-K(left), MSO-K (center), and MSO-Na (right) intensitygrams from July 31, 2025 at 15:30 UTC. Active regions highlighted with cyan boxes, and NOAA AR numbers, indicated regions with flares this day.

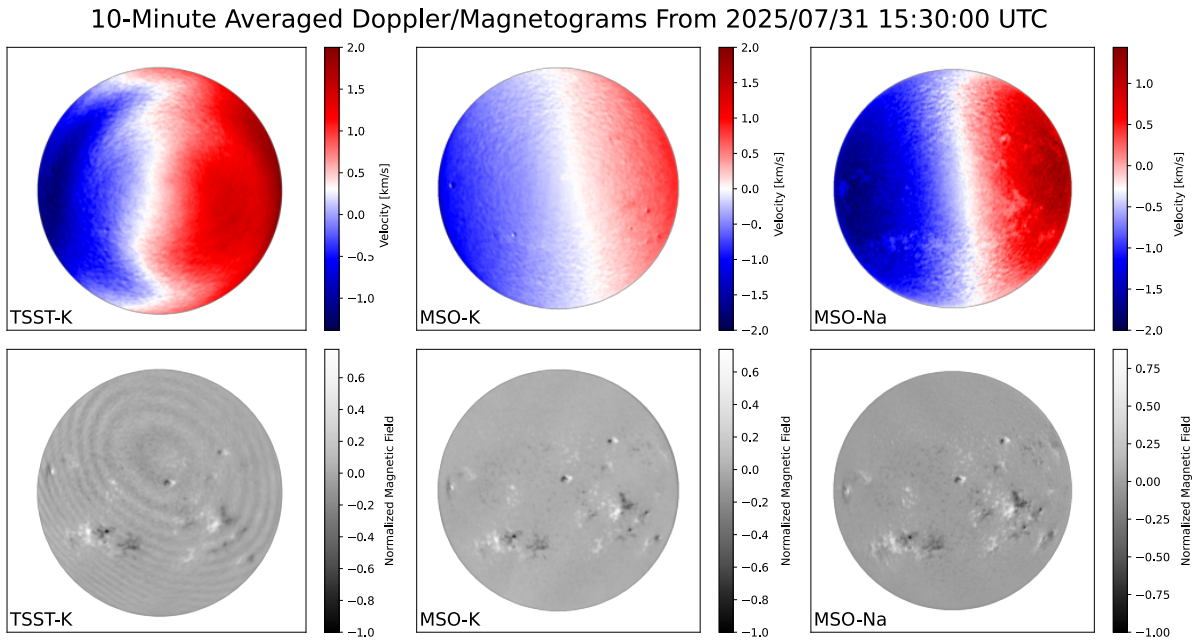

Figure 5.15 Ten-minute averaged Dopplergrams (top) and Magnetograms (bottom) from July 31, 2025 at 15:30 UTC. Dopplergrams have been normalized and scaled for ± 2 km/s across the disk.

Table 5.2 Flares observed by GATES on July 31, 2025 during the dual-site campaign. All times provided in UTC

Active Region	Flare Class	Start	Max	End	Observed by
NOAA AR 4153	C1.5	14:34	14:53	15:11	TSST-K/MSO
NOAA AR 4155	C1.7	15:30	15:43	15:53	TSST-K/MSO
NOAA AR 4153	C1.6	18:29	18:52	19:03	MSO
-	C1.3	19:47	19:51	20:00	MSO
4167	C1.9	21:55	21:59	22:04	MSO

elliptical fringing patterns, likely caused by interference from the cell windows, which dominate the magnetogram signals. Additionally, the TSST-K Dopplergrams exhibit a significant inhomogeneity in the zero-velocity reference plane (which should be approximately aligned with the North-South plane at the disk center) most likely due to heliostat vignetting which introduces an intensity gradient across all of the filtergrams similar to an artificial Doppler signal. MSO-K suffers from fringing as well, likely caused by interference between the polarization optics. These aberrations currently limit our ability to effectively cross-calibrate between nodes. However, the visually consistent magnetic signals between the two nodes provide promising results for the dual-site test.

5.4.2 Extended Observing Run at MSO

The purpose of Phase 2 of the Summer 2025 Observing Campaign was to produce a data set suitable for wave-travel time analysis. Phase 2 was completed solely using MSO with the MSO-K and MSO-Na channels active. From July 15, 2025, through September 15, 2025, I acquired 378 hours of dual height K-Na observations over 45 days. Although truly continuous

observations were limited by the diurnal cycle, the Phase 2 Campaign averaged 8.4 observing hours per day, with 23 10+ hour days. Additionally, the longest consecutive observing run lasted fifteen days, from July 21, 2025 through August 4, 2025 (encapsulating both of the dual-site GATES observations). During this time, MSO observed 83 C-class and 6 M-class flares. Table 5.3 lists the parameters of the observed M-class flares.

Table 5.3 M-class flares observed by the extended MSO-K/MSO-Na (*due to MSO-Na camera malfunctions, the flare on 2025/08/03 was only observed by MSO-K) observing run in Summer 2025. Dates and times given in UTC. Only flares where MSO observed the entire flare are included. Note: the last three flares listed in the table are not officially associated with NOAA AR 4168 as it had rotated off the limb.

Date	Active Region	Flare Class	Start	Max	End
2025/08/03*	NOAA AR 4168	M2.95	13:40	13:57	14:01
2025/08/06	NOAA AR 4168	M1.06	16:56	17:02	17:06
2025/08/08	NOAA AR 4168	M1.02	18:56	19:10	19:17
2025/08/11	limb (NOAA AR 4168)	M1.0	22:12	22:18	22:22
2025/08/12	limb (NOAA AR 4168)	M1.51	00:42	00:59	01:18
2025/08/12	limb (NOAA AR 4168)	M1.83	01:18	01:23	01:27

During MSO's extended observing run, the most prolific flare-producing region, producing 75 flares (58 C-class and 16 M-Class) over its ∼10 day life. NOAA AR14168 arose on the eastern limb of the Sun on August 02, 2025, and remained on the disk until rotating off the western limb on August 12, 2025. During this time, MSO observed 18 of its C-class flares and 6 of its M-class flares (all M-class flares MSO observed during the Extended Observing Run originated from NOAA AR 4168). Unfortunately, during this time period, the MSO-Na DT was malfunctioning, and consequently, MSO-Na temporarily lost its magnetic observation capabilities. Although MSO-Na obtained intensitygrams and Dopplergrams, during these

flare no MSO-Na magnetograms were acquired. Figures 5.17 and 5.16 show magneto- and Dopplergrams from the M1.06 flare on August 6, 2025.

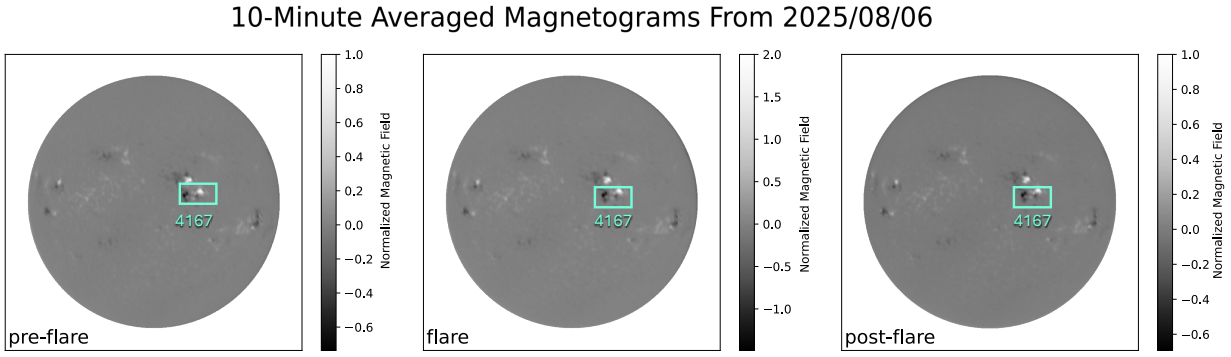

Figure 5.16 Ten-minute averaged magnetograms from MSO-K from 2025/08/06 exhibiting M1.6 flare in NOAA AR 4168 (cyan boxes). Magnetograms show one hour before the start of the flare (15:56 UTC, left), the max of the flare (16:56 UTC, center), and one hour after the end of the flare (17:56 UTC, right).

As described in Section 1.3, by measuring the strength and orientation of the magnetic field at the solar surface, magnetograms reveal the magnetic topology of active regions, including the total unsigned helicity, the total unsigned magnetic flux (R parameter), topological count of polarity inversion lines (D parameter), and the total free magnetic energy. These parameters not only allow us to better characterize and understand flares but have also been shown to be powerful flare prediction tools. Moreover, by characterizing the complexity of magnetically active regions (categories α, β, γ) can both indicate the presence and strength of an upcoming flare.

Observing flares at multiple heights in Doppler velocity allows us to investigate the acoustic wave dynamics of flaring regions and the possibility to use acoustic waves as flare precursors. Previous studies using multi-height MOTH data indicate anomalies in the acoustic

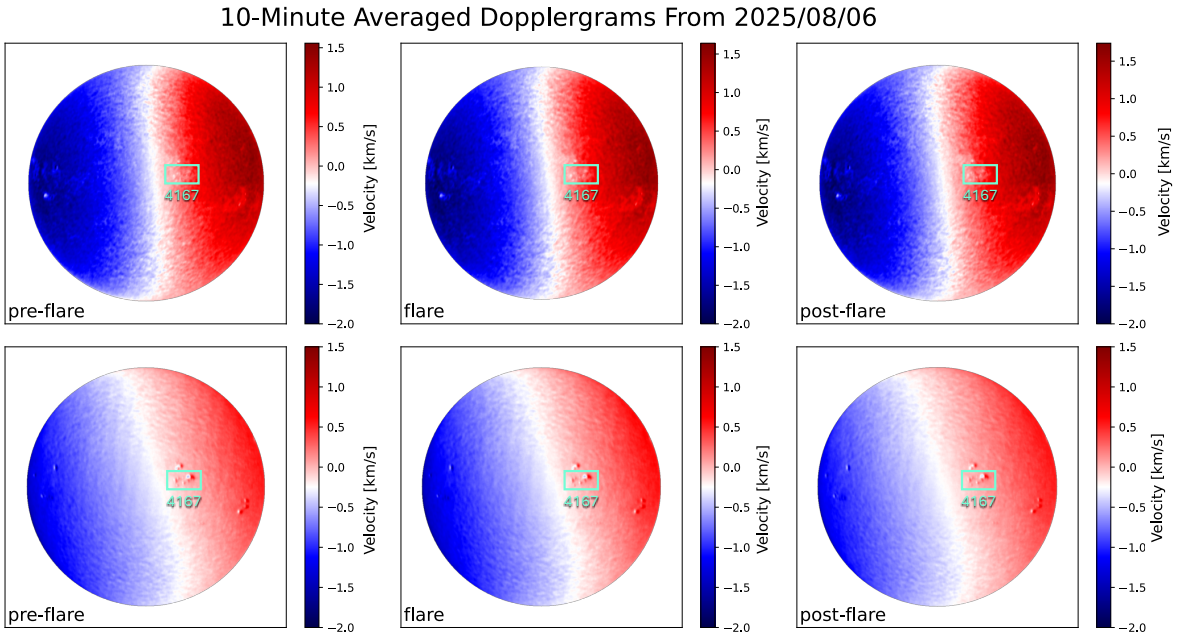

Figure 5.17 Ten-minute averaged Dopplergrams from MSO-Na (top) and MSO-K (bottom) on 2025/08/06. Dopplergrams show one hour before the start of the flare (15:56 UTC, left), the max of the flare (16:56 UTC, center), and one hour after the end of the flare (17:56 UTC, right).

wave propagation prior to flares. Finsterle et al. (2004c) reports a drop in the acoustic cut-off frequency before a flare, allowing high-frequency waves to propagate to the surface, and Aparna (2022) reports negative phase travel times of high-frequency waves prior to flares. We plan to use the multi-height GATES data to expand on these stories.

As a scaled-down version of the MOTH telescope, MSO was designed to extend the flare prediction studies enabled by earlier MOTH observations. The GATES Summer 2025 Campaign was approximately 1.5 times longer than the longest MOTH campaign (2002/2003; 260 hours) and was conducted during a substantially more active phase of the solar cycle. Consequently, the Summer 2025 Campaign was able to capture 2 times the number of flares

than 2002-2003 MOTH campaign. Despite this, the GATES' flare sample size remains under the required amount for statistical significance, so additional observations are required. When the GATES Network is fully operational, it will provide a strong dataset to contribute to both magnetic and velocity investigations of flare prediction.

CHAPTER 6
HELIUM 1083 NM MOF

As described in Section 1.3, expanding solar observations to the chromosphere is of great importance and interest for multiple subsets of heliophysics and space weather. To better solve the coronal heating problem, chromospheric and transition region diagnostics are required. Moreover, as the origin for many eruptive events, chromospheric velocity and magnetic field measurements are also integral to furthering space weather understanding and predictive capabilities. However, observing the chromosphere and transition region is challenging due to the limited number of spectral lines with sufficient chromospheric opacity. Furthermore, ground-based observations are further limited to the visible and IR wavelengths. Within these constraints, the most common diagnostic lines are the Ca II H & K lines (393.4 nm & 396.8 nm), the Hα 656.3 nm line, the Ca II infrared triplet lines (848.9nm, 854.2 nm, & 866.2 nm), and the He I D3 587.6 nm and He I 1083.0 nm lines (de la Cruz Rodríguez & van Noort 2017) (Figure 6.1).

Of these lines, we choose to focus on He I as a chromospheric probe and new MOF line for a variety of reasons. Firstly, although the quiet Sun formation height of the Ca II H line appears to coincide with the He I lines, this is only true in the quiet Sun regime. Moreover, the Ca II H and K lines are expected to be less effective for magnetic field measurements due to the lower strength of their Zeeman splitting (de la Cruz Rodríguez & van Noort 2017). Additionally, He I D3 and 1083 are usually optically thin and without a self-reversal in their line profiles (unlike Ca II H & K and Hα), which allows for a more straightfor-

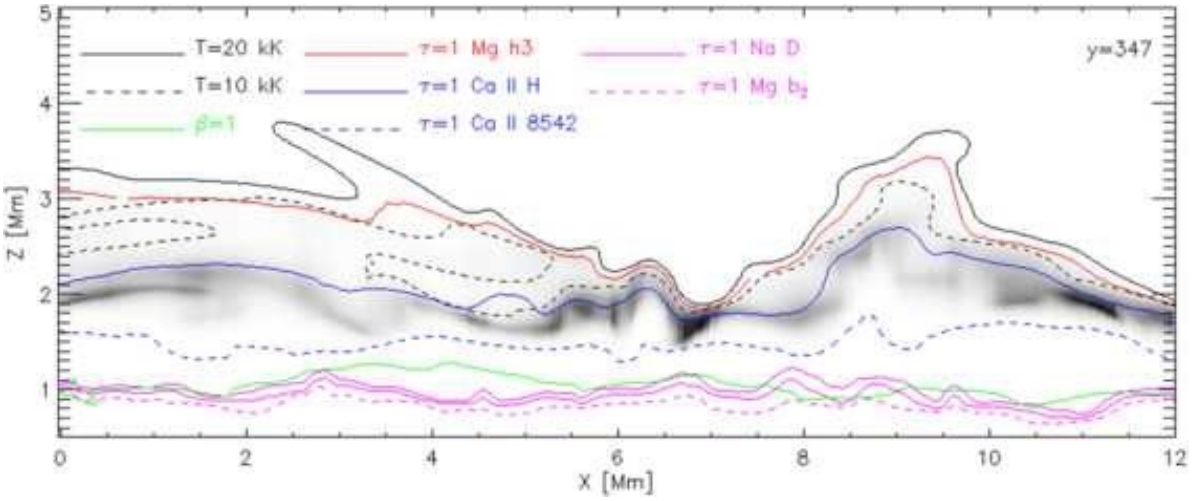

Figure 6.1 Common chromospheric diagnostics and their line-core formation heights in quiet Sun. The He line formation is given in grey-scale and has a broader, more continuous contribution because it is optically thin in the atmosphere. Reproduced from Libbrecht (2019), Courtesy of M. Carlsson (Institute for Theoretical Astrophysics, University of Oslo).

ward velocity measurement (Libbrecht et al. 2019). Furthermore, from the technical side, the GATES Network, through the MOTH team, has experience developing He MOFs for intensity observations (Section 6.2), providing a valuable basis for the MOF development.

6.1 *He I Formation and Diagnostic Potential*

In light atoms such as helium, the angular momentum (F) and electron spin (S) can become coupled, dividing a neutral atom in such a way that the states behave almost like two separate atoms. For neutral helium, this division results in the production of para-helium and ortho-helium. For para-helium, the two electrons have a total spin $S = 0$ and the corresponding energy levels are referred to as the singlet states. For ortho-helium, the two electrons have a total spin $S = 1$ and are referred to as the triplet states. Both the He I D3 and 1083 lines are transitions between energy levels in the ortho-helium triplet system (Figure 6.2). The He I

D3 line arises from the transition between the $1s2p^3P_{0,1,2}$ and $1s3d^3D_{1,2,3}$ energy states, and the 1083 line arises from the transition between the $1s2p^3S_1$ and $1s2p^3P_{0,1,2}$ energy states (Table 6.1).

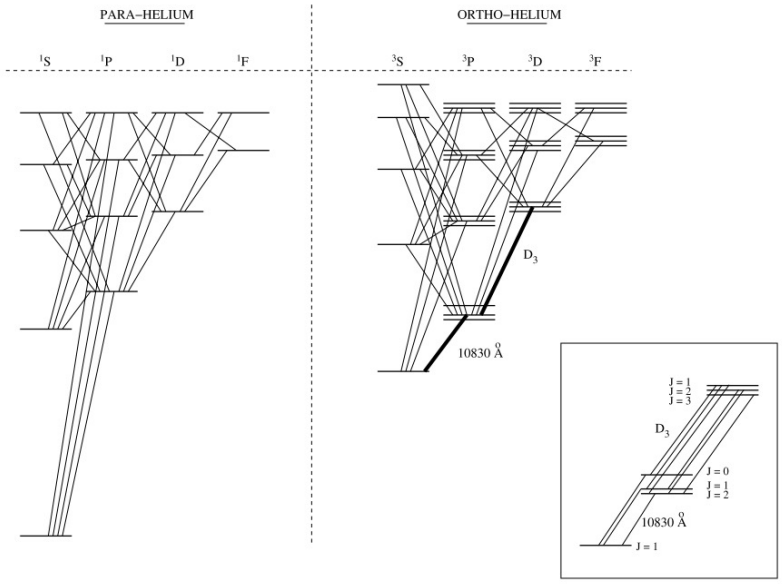

Figure 6.2 Grotrian Diagram of one of the energy levels of neutral helium from Centeno et al. (2008). The side panel shows a zoomed-in view of the He D3 and 1083 lines and their splitting.

Since electric dipole radiative transitions do not allow for a change in spin, both the singlet and triplet states are forbidden transitions. This, combined with the fact that, as a noble gas, helium has a very high first ionization energy of 24.587 eV, raises questions on how the triplet lines are populated. The two most common population mechanisms for ortho-helium are photoionization-recombination (PRM) and collisional excitation (CM). PRM occurs when electrons in the ground state of neutral helium are fully ionized by extreme ultraviolet radiation and subsequently recombine with the metastable triplet system (electron cascade). CM is the process of electrons in the ground state being excited through collisions

Table 6.1 Components of He I D3 and 1083. Information from NIST Atomic Spectral Database: (Kramida et al. 2024).

λ in Air $[nm]$	Atomic Levels
587.5599	1s2p $^3P_2$ - 1s3d $^3D_1$
587.5614	1s2p $^3P_2$ - 1s3d $^3D_2$
587.5615	1s2p $^3P_2$ - 1s3d $^3D_3$
587.5625	1s2p $^3P_1$ - 1s3d $^3D_1$
587.5640	1s2p $^3P_1$ - 1s3d $^3D_2$
587.5966	1s2p $^3P_0$ - 1s3d $^3D_1$
1082.9091	1s2s $^3S_1$ - 1s2p $^3P_0$
1083.0250	1s2s $^3S_1$ - 1s2p $^3P_1$
1083.0340	1s2s $^3S_1$ - 1s2p $^3P_2$

with free electrons. This process can either result in full ionization of the electrons followed by recombination down to the metastable states, or the excitation of electrons directly to the metastable triplet state (19.820 eV). Despite being a forbidden transition, the metastable ground state of the triple system (1s2s $^3S_1$) has an extremely long lifetime (on the order of 10^4 s) before it decays to the ground state of neutral helium. This makes the triplet state an advantageous ion to use in our MOF cell because once we populate the energy states of interest, electrons remain in that state long enough for observations to be conducted.

In addition to being a technically advantageous line for MOF development, the high ionization potential of He I and the PRM population mechanisms of the triplet lines make He I D3 and 1083 unique diagnostic tools for high-energy regions of the Sun, like the chromosphere and corona. The energy levels of these two lines are populated in proportion to the amount of incident EUV radiation originating in the transition region and the corona.

Consequently, these lines are sensitive to heating in those layers and are formed around 2 Mm in the solar atmosphere, making them one of the few effective chromospheric probes.

Helium lines have long been used for solar research. As early as 1939, Goldberg (1939) used chromospheric He I spectral lines from the 1932 eclipse to identify the increasing temperature with height in the chromosphere. Later studies such as Zirin (1975) identified limb brightening in both the D3 and 1083 lines, as well as darkening in the D3 emissions in coronal holes. Lites et al. (1985) showed that the He 1083 line can provide Doppler shift measurements above chromospheric active regions. de Toma et al. (2005) showed that coronal holes can be identified via brightenings in the He I 1083 nm line. More modern studies have used the He I triplet lines, most typically the 1083 line to investigate the dynamics of filaments (Kuckein et al. 2020), small-scale reconnection events like Ellerman bombs (Libbrecht et al. 2021a), and flares (Kuckein et al. 2025).

Despite its well-established use as a chromospheric diagnostic, there remains a lack of consistent solar observations conducted with He I – particularly with full-disk Doppler velocity and magnetic field measurements – due to the challenges of collecting data with high-resolution near-IR spectroscopy. The Mauna Loa Solar Observatory (MLSO) Chromospheric Helium Imager Photometer (CHIP; MacQueen et al. (1998)) observed the full solar disk in He 1083 from 1996 to 2013, and NSO's SOLIS (Keller et al. 2003) continued similar observations from 2006 to 2015, achieving full-disk He I 1083 nm line characteristics like full-disk Doppler velocity and vector magnetic field measurements as well as smaller FoV, high-resolution magnetic field measurements. The Swedish Solar Telescope (SST) has recently implemented

the Helium SpectroPolarimeter (HeSP) which can obtain full Stokes polarimetry, but over a small FoV (7.7" x 8.7") (Leenaarts et al. 2025). Additionally, the Vacuum Tower Telescope (VTT) can achieve full Stokes polarimetry (FoV 77" x 77") by employing the Tenerife Infrared Polarimeter attached to the Echelle spectrograph (Kuckein et al. 2015). Furthermore, space-based and ground-based coronal observations like the METIS coronagraph onboard SO (Antonucci et al. 2020; Müller et al. 2020), the Solar-C telescope's coronagraphic observations at the Haleakala High Altitude Observatory (Kuhn et al. 2007; Moise et al. 2010), and eclipse missions such as the Coronal HElium Emission Spectrograph Experiment (Molnar et al. 2025) have observed He I 1083 *nm* exclusively in the corona. These instruments all highlight the importance and difficulty of obtaining solar spectropolarimetric observations of He I 1083 *nm*. Despite them, there exists no currently operational telescope capable of achieving full-disk He I 1083 *nm* velocity and magnetic field measurements, a notable hole in chromospheric and space weather research that a He MOF has the unique capability to fill.

6.2 *History of the He Cell*

Although the basic design of a He, or other gaseous line, MOF is similar to that of an alkali metal MOF, there are a few key differences due to the required ionization of the gas in the cell. The optomechanical setup between the two types of cells remains the same: the MOF cell is placed in a magnetic assembly, which produces a longitudinal magnetic field, between two crossed polarizers (left panel of Figure 6.3). The differences lie in how the chosen spectral

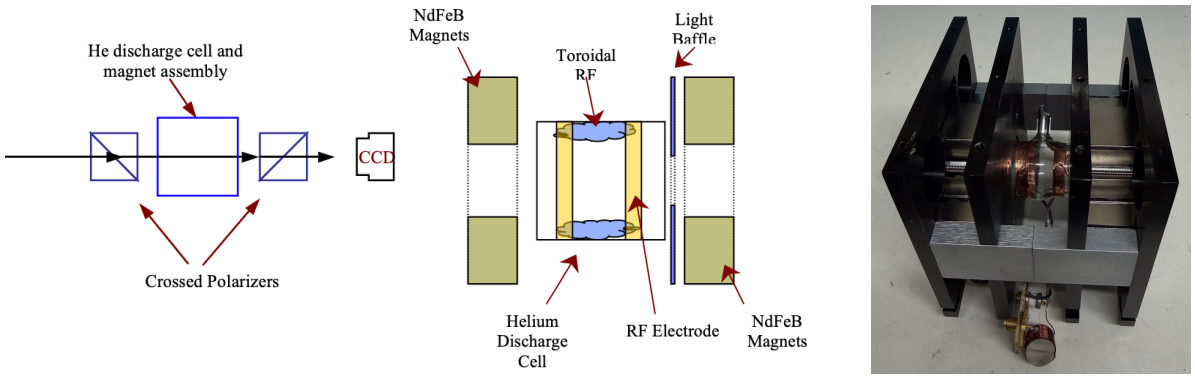

Figure 6.3 Schematics (reproduced from Murphy et al. (2005)) and images of a He MOF. Left: the basic assembly of the 2005 He MOF containing just an MOF section. Center: the basic schematic of the He MOF cell/magnet assembly. The presence of RF electrodes and a light baffle differ from a typical alkali MOF. Right: an image of the He MOF magnet assembly from the Eddy Co. in 2025.

lines are populated. In alkali-based MOFs, the cells are heated to create a vapor density of the atomic line of interest. In He-based MOFs, the Helium in the cell is ionized via a radio frequency (RF) electrode, producing He II, and allowing the metastable triplet lines of interest to be populated by recombination. Ionizing the cell with RF requires additional electronics in the form of the RF electrode wires and power circuit (right panel of Figure 6.3), and, because the He II emits light of its own, a light baffle is required to block excess He emission (center panel of Figure 6.3).

The He MOF was first developed by Murphy et al. (2005) utilizing the He I 1083 nm line. The instrument was constructed using a 40 mm long, 40 mm diameter cell filled with pure He at a pressure of 120 Pa, with a longitudinal magnetic field of 2 kG. The He discharge within the cell was produced by coupling an RF source at frequencies between 18 and 30 MHz to an electrode attached to the outside of the cell, in a two-band geometry; this produces a toroidal discharge close to the cell wall with the metastable He atoms diffusing

to the center of the cell (the beam path). The instrument consisted of the He cell in its magnetic assembly (MOF), placed between two crossed polarizers (P1 and P2), with a 10 *nm* interference filter (to block the residual light leaking through the polarizers and light from unwanted He transitions), and a CCD detector. Light was fed into the instrument using a heliostat and a 50 *mm*apeture; image resolution was seeing-limited, achieving > 10". The Murphy et al. (2005) He MOF achieved full-disk intensity images of the Sun (Figure 6.4) on July 22, 2004, operating at a cadence of one image every 35 *s*.

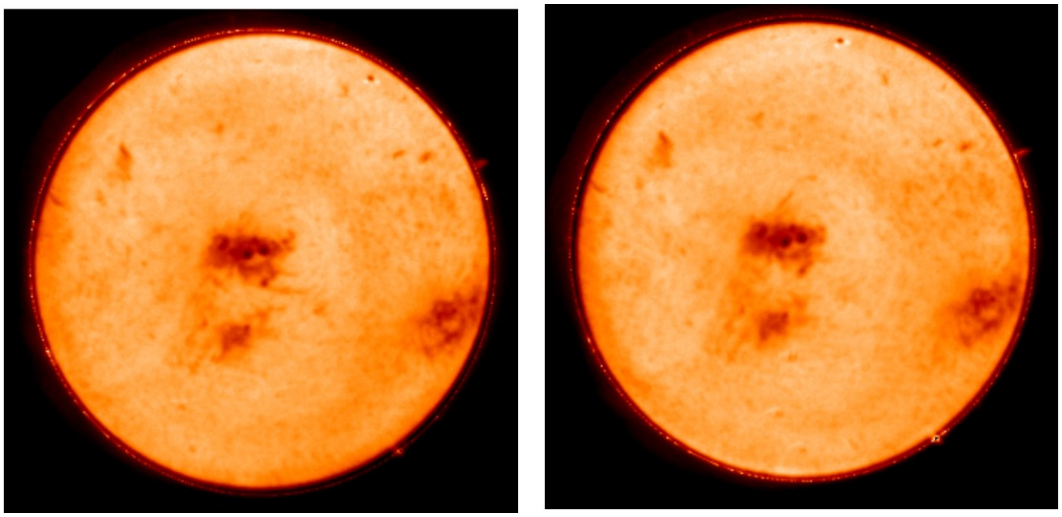

Figure 6.4 Two first-light intensity images taken using the He I 1083 *nm* MOF on July 22, 2004. The images were acquired using a 50 *mm* apeture and a single MOF cell; they were taken approximately 2 hours apart and are continuum subtracted. Reproduced from Murphy et al. (2005)

After the success of the He MOF first-light, the filter was planned to be upgraded to achieve Doppler velocity and magnetic field measurements to be included in the MOTH II instrument. The MOTH II planned to include the K and Na channels of the MOTH while adding the He MOF and a new Ca MOF as new channels to achieve simultaneous four-

height observations of the solar atmosphere. The MOTH II ended up consisting of just the original MOTH K and Na channels when being deployed to the South Pole, but while the MOTH was installed at the Mees Solar Observatory on Haleakalā in 2011, the He MOF was tested using the heliostat in the University of Hawaii Institute for Astronomy's Advanced Technology and Research Center (ATRC) in Pukalani, HI, USA, and new intensity images were acquired (Figure 6.5).

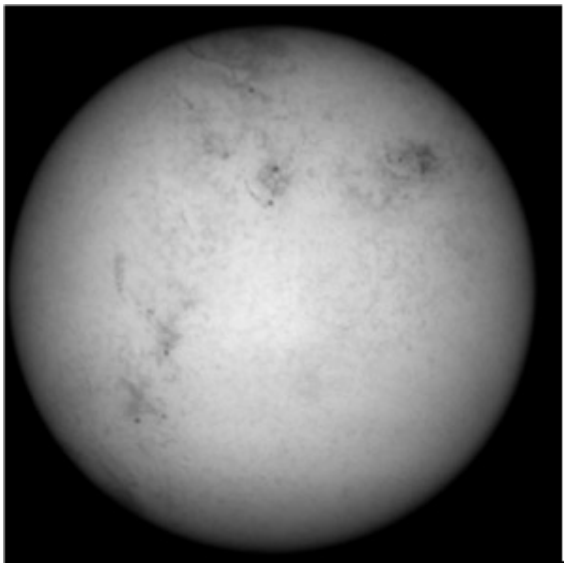

Figure 6.5 Intensity image of the Sun in He I 1083 *nm* acquired with a He MOF installed on the MOTH instrument when it was at the ATRC in Pukalani.

After the He observations from Pukalani, the MOTH team focused on K and Na MOF observations, beginning the development of MSO. The MOTH team, turned GATES Network, returned to the Doppler- and magnetic capability development of the He MOF in 2022. We had the preliminary intention to utilize the He I D3 line rather than the He I 1083 *nm* line to leverage the higher SNR (given current silicon detector technology achieves higher quantum efficiency and spectral response in visible wavelengths as compared to infrared) and

angular resolution achievable at this shorter, optical wavelength (Section 6.4). Ultimately, we reverted to focusing on the He I 1083 nm line (Section 6.5) and were able to achieve first-light images of full-disk Doppler- and magnetograms utilizing the new He I 1083 nm MOF (Section 4.2).

6.3 *Techniques to Enhance Metastable He Populations*

The biggest challenge when attempting to create the He I MOF function is reaching a critical population of He I in the cell before the line depopulates. Because the He I triplet lines are forbidden transitions, the presence of contaminants in the cells introduces non-resonant collisions which rapidly depopulate the He I lines. Even with vacuum cleaning the cell down to $\sim 1 \times 10^{-6}$ $torr$, contaminants such as water remain trapped in the crystalline structure of the glass. Over time, as the cell is irradiated with RF power, these contaminants will become unbound from the glass and migrate into the cell cavity, depopulating the forbidden He I lines. Moreover, as the cell is irradiated with RF power, the neutral He will dissolve into the glass, lowering the total viable population of He within the cell. To combat this, prior to placing the cell in the Figure 6.7 test bed, the He cell is "baked" while being flushed with pure He. This process involves repeatedly placing the cell inside a strong microwave while filling the cell with a high pressure (up to ~ 10 $torr$ of pure He and vacuuming the cell down to $\sim 1 \times 10^{-6}$ $torr$. For more information on this process refer to Appendix A.2.

Once the He cell had been properly cleaned,there are multiple ways to try to produce/enhance the metastable He population:

- Increase the neutral He pressure up to a critical point.
- Increase the RF power used to ionize the neutral He.
- Add alkali metals to create a sputtering-induced feedback loop of metastable population.
- Optically pump the He I 1083 nm line to enhance the triplet population.
- Increase the cell size.

The most straightforward way to populate the He I triplet is to ionize the neutral He in the cell, through the inclusion of an RF power source, and allow for the energy cascade of PRM to occur. With this in mind, there is a direct correlation between the population of He I triplet and the neutral He that is originally placed in the cell – increasing the fill pressure of he neutral He will increase the He I population. However, since the He I triplet is a metastable line, overfilling the cell with neutral He will actually cause the line to depopulate, as the fully ionized He ions become "contaminants" introducing non resonant collisions. For this reason, the neutral He fill pressure is kept below 6 $torr$. Moreover, the optimum neutral He fill pressure is determined to balance the emission (glow from the ionized He) and transmission (external light passing through the cell) of the cell when ionized. Figure 6.6 shows an example of this trade off. The peak transmission of the cell occurs with no He in the cell and rapidly decreases as He is added before reaching a critical inflection point and increasing once again. Conversely, the emission of the cell increases with pressure until all of neutral He in teh cell has been ionized. The pressure chosen to fill the cell is selected as the inflection point of the transmission curve; this point maximized the cell's transmission while minimizing the cell's

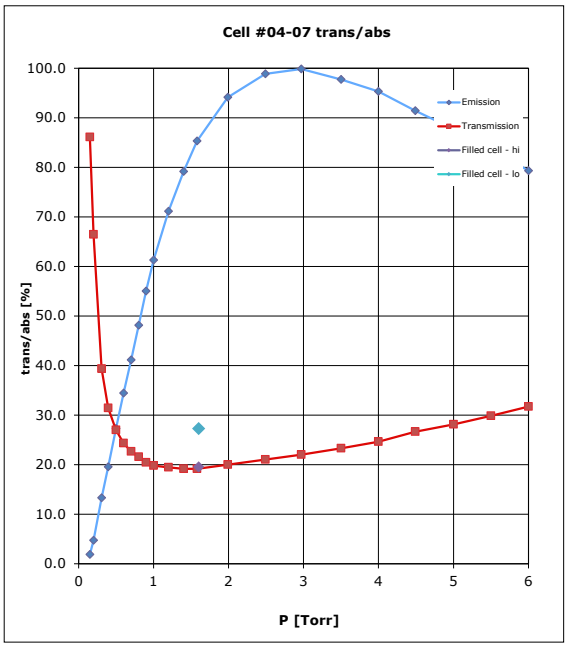

Figure 6.6 Transmission and emission curves of a He cell being filled by MSO team member Dr. Neil Murphy March 13, 2011. The filled cell point (1.6 *torr* was selected to match the inflection point of the cell transmission therefore minimizing the emission.

emission.

Once the fill pressure has been set, the next method to increase the metastable population is to increase the RF power. This will increase the percentage of neutral He that becomes ionized and consequently that populates the He triplet line through PRM. Similar to increasing the pressure within the cell, there is a critical point, once all the neutral He in the cell has been ionized, at which increasing the RF power is no longer beneficial. The right-hand panels of Figures 6.8 and 6.13 show examples from my lab-testing of this phenomenon.

If increasing the RF power still does not produce enough metastable He for MOF function, another method to theoretically bolster the metastable population is to add alkali metal vapor, with ionization energies close to the energy difference between ionized He II and the

He I triplet (4.78 eV), to the cell. When ionized He II collides with alkali metal atoms such as sodium (5.14 eV), potassium (4.34 eV), and rubidium (4.18 eV), the energy the He II ion provides the metal to ionize it will cause the He II ion to drop to the closest quantized energy state, which is the He I metastable triplet. An alternative to pure alkali metal is to introduce an alkali salt whose binding energy is similarly valued to the 4.78 eV He triplet energy difference. Section 6.4.2 describes this salt sputtering technique in more detail in context of its application to my He I D3 MOF tests at MSO.

The final way to attempt to enhance the metastable population without changing the physical construction of the cell is to optically pump the plasma with a laser. Optical pumping works by electronically exciting a medium with light, or specifically populating certain electronic levels. In the case of the He I triplet, the He I 1083 nm population can be directly enhanced using a He I 1083 nm laser. For the He I D3 line however, since the He I D3 transition cannot sustain a population inversion in neutral helium, lasers operating at this specific wavelength do not exist. Because of this, to optically pump the He I D3 line, the He I 1083 nm laser is still used since the He I D3 line typically populates after, and because of the 1083 nm population. Section 6.4.3 describes the optical pumping tests I conducted at MSO.

The previously mentioned techniques to enhance the metastable He population all leverage the ability to increase the creation mechanism of the He triplet. An alternative method to enhance the metastable population is to decrease the destruction mechanisms (e.g. collisional de-excitation) for the metastable ions. This requires eliminating as many contaminants

as possible (as is done through the cell cleaning) or increasing the mean free path for the metastable He ions. Increasing the mean free path can be achieved by increasing the overall size of the glass MOF cell which consequently lowers the collisional de-excitation from metastable He colliding with neutral or ionized He. Moreover, the larger cell size means the He plasma is produced further from the cell walls, resulting in less collisional de-excitation from wall collisions and preventing more He from dissolving into the glass. Altering the cell size required new cells to be produced and new, high-quality optical windows to be attached, so was outside the possible scope of my He MOF study. However, this technique remains as one of the primary next steps to the He MOF development the GATES team plans to enact.

6.4 *Development of the He I D3 MOF*

I began the development of the He I D3 MOF in 2022, with the construction of new He MOF cells. Testing began in the lab at the Eddy Co. using the set-up in Figure 6.7 to measure "MOF function". The He MOF testbed consisted of a He cell in a magnet assembly between two crossed linear polarizers (P1 and P2). A Na I D2 589 nm hollow cathode with a broad line width was used as a proxy "Sun" to introduce light into the system at the He I D3 wavelength (587.6 nm).

For these preliminary lab tests, "MOF function" is defined as any transmission of the He I D3 line through P2 after the emission from the cell was subtracted off. To achieve MOF function, there are two main parameters that can be altered: the magnetic field and the population of the species in the cell. A critical population of He I D3 must be reached in

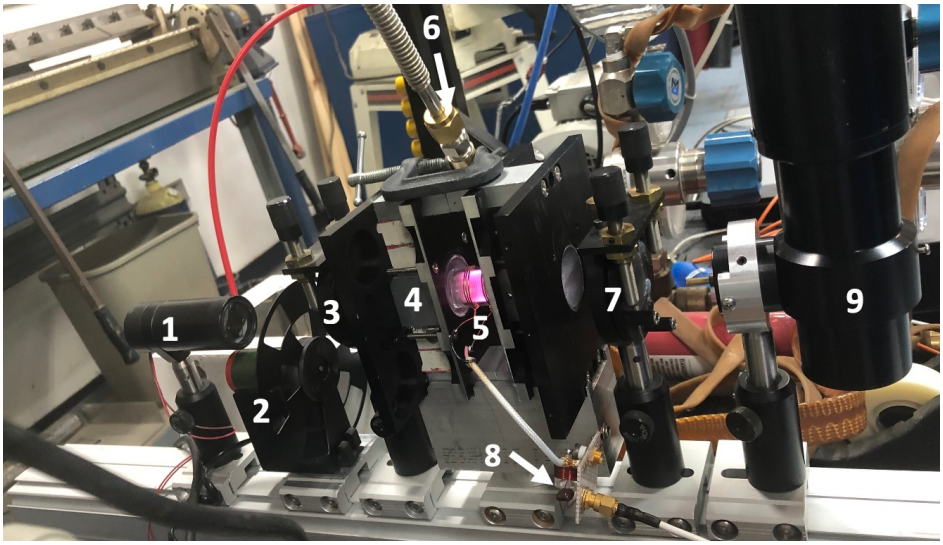

Figure 6.7 Lab setup for testing the He D3 MOF function consisting of a Na 589.0 nm hallow cathode (1), lock-in amplifier's chopper (2), colorPol polarizers (3 & 7), longitudinal magnets (4), MOF cell (5), tube to vacuum system (6), RF circuit (8), and detector (9)

the cell in order to produce the desired inverse Zeeman and Macaluso-Corbino effects and achieve MOF function. Since the MSO magnetic assemblies are constructed from permanent bar magnets, we chose to keep the magnetic field constant (at 3 kG) and alter the He I D3 population in the cell through methods like pressure and RF power changes. For these tests, the He cell was not yet sealed, and was connected to a vacuum system which allowed us to freely change the pressure of pure He within the cell.

6.4.1 *He I D3 MOF Testing: Cell Pressure and RF Power*

To determine the optimum fill pressure, the first MOF function test I conducted was varying the neutral He pressure. Radiating the cell with a constant RF power (3.2 mW), I tested various He pressures, ranging from 1.34 *torr* to 4.13 *torr* (left panel of Figure 6.8). Pressures less than 1.34 *torr* did not result in any ionization and are therefore not shown on the plot.

As pressure in the cell increased, the amount of D3 decreased due to collisional de-excitation. Even with lower pressures, no MOF function was measurable. Subsequently, I varied the RF power from 0.8 mW to 2 W to determine the relationship between RF power and He I D3 population (left panel of Figure 6.8). For the RF power test, the pressure was held constant at 2.2 $torr$. As expected, increasing the RF power proportionally increased the amount of He I D3 in the cell. However, even at the highest tested RF power, MOF function remained elusive.

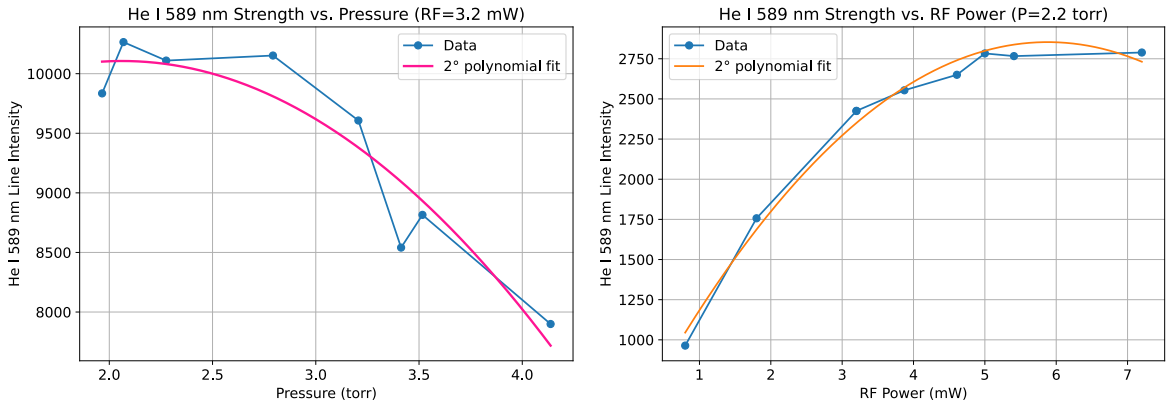

Figure 6.8 Left: D3 line strength versus pressure from May 24, 2022. He in the cell was ionized from 1.7 torr; all points are post-ionization. Right: D3 line strength versus RF power from May 27, 2022. Values measured of the cell emission in free space, not through the MOF testbed.

The most likely cause for the persisting lack of MOF function was a lack of the critical population of He I D3. However, due to its forbidden nature, and as shown by the pressure test in Figure 6.8, simply increasing the amount of He in the cell is not sufficient to critically increase the He I D3 population because the increasing population in the cell presents more opportunities for the He I D3 to collisionally de-excite. Therefore, as described in Section 6.3, the population of the He I D3 line specifically must be increased independently of the

total He pressure.

6.4.2 He I D3 MOF Testing: Alkali Salt Sputtering

The next test I ran to increase the He I D3 population was alkali salt sputtering. Leveraging the similarity between the binding energy of the salts (KCl: 4.78 eV or NaCl: 7.97) and the energy difference between He II (24.58 eV) and the He I triplet line (24.58 eV - 19.82 eV = 4.76 eV), this technique creates a feedback loop or collisions to enhance the He I D3 population. This process works by the He II colliding with the salt layer within the cell, breaking the KCl bond and consequently dropping 4.78 eV in energy. Due to the quantized nature of atomic energy states, the He atom will populate the energy level it is closest to: He I D3. In addition to the production of a He I D3 atom, the newly free K or Cl atoms hold the 4.78 eV from their binding energy. If one of these atoms collides with a He I D3 atom, they can re-ionize the He and restart the sputtering cycle. Figure 6.9 shows a schematic for this process.

Despite its higher binding energy, the first salt sputtering test was conducted with NaCl. This was done to test whether salt sputtering produced Na spectral lines – since the Fraunhofer lines are spectrally close to the He I D3 line, all three lines could be investigated at once using the Eddy Co. spectrometer. Unfortunately, this not only failed to produce sputter-induced Na lines, but also showed no enhancement in the He I D3 population (Figure 6.10).

The salt sputtering tests were limited by the technical ability to grow salt crystals in the cell. To ensure no contaminants (other than the salt) entered the cell, the crystals had to

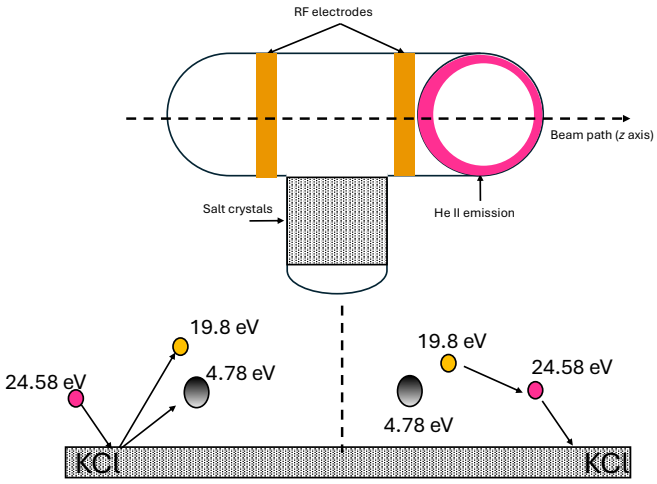

Figure 6.9 Top: diagram of a He cell tested for salt sputtering. Salt crystals were grown in the extended cell neck, which connected to a vacuum system. The He plasma exists in the horizontal cylinder of the cell. Bottom: schematic of the salt sputtering process.

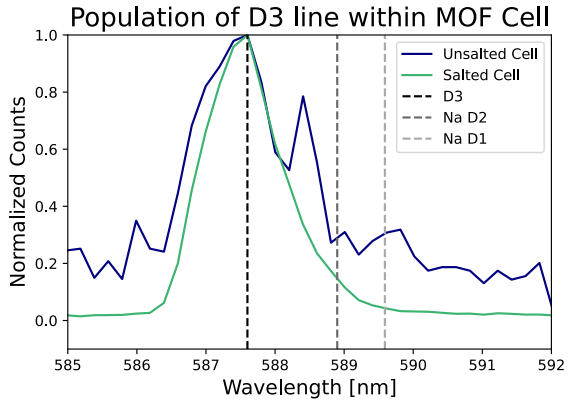

Figure 6.10 Spectra of the lit MOF cell (internal He pressure 10 torr), normalized to the D3 line obtained perpendicularly to the light path. The green spectrum shows the salted cell, used for the attempted sputtering technique. The lack of Na spectral features indicates that the salt sputtering technique was not working. The blue spectrum shows an unsalted cell, whose D3 population is produced exclusively through RF induction. The absolute strength of the D3 line in the unsalted cell was much weaker than in the salted cell, causing its normalized spectrum to look noisier.

be grown in a vacuum. Additionally, to prevent salt crystals from growing on the windows of the cell, thus making the cell unusable in the MOF, the saline solution was limited to the filling tube of the cell (Figure 6.11). Although maintaining the clear apertures of the cell windows, this placement of the salt is the most likely reason for the sputtering failures. As He II forms in a toroidal geometry around the main body of the cell, only a minimal amount reaches the filling tube to initiate sputtering. Because of this, and the challenges to grow salt crystals in the main body of the cell, salt sputtering was deemed a nonviable solution, and other methods, such as laser pumping, for He I D3 enhancement were pursued.

Figure 6.11 Cell connected to vacuum system to grow salt crystals in a clean cell. Saline water was pumped into the cell, and a central drainage tube (metal tube in the center of the cell) was placed for water evaporation. The knit band is connected to a heater to additionally aid in the efficient evaporation of the water. The saline solution was limited to the vertical component of the tube (filling tube) to prevent crystals from forming on the inner cell windows.

6.4.3 He I D3 MOF Testing: Optical Pumping

During the laser pumping tests, in addition to various laser powers, I tested multiple orientations of the laser, including parallel and perpendicular (from multiple entry positions) to the beam path. None of the configurations proved successful in enhancing the He I D3 population enough to produce MOF function. However, with the presence of the He laser, the He I 1083 *nm* was able to be scanned through (Figure 6.12). This presents an interesting potential for future MOFs to simplify their optical scheme and obtain vector magnetograms through line scanning.

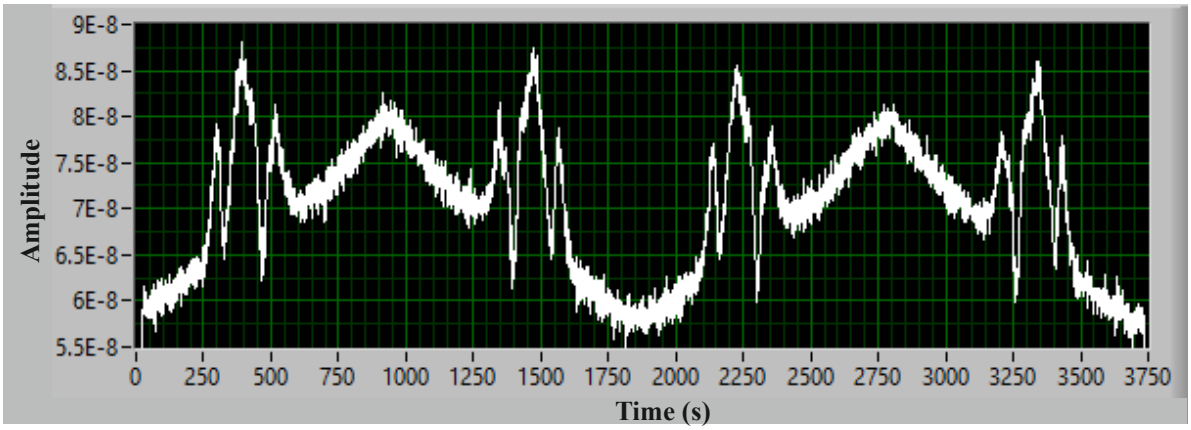

Figure 6.12 Optical scan of the He I 1083 *nm* line using the laser. The line is scanned in time by increasing the power level on the laser (current level). The laser was kept at a constant 25°C for these scans. The 4 line profiles shown are all of the He I 1083 *nm* line and depict the Zeeman splitting of the red and blue wings. The conversion between the scanning time and wavelength is 25 *s* to 0.1 *nm*.

6.5 *Development of the He I 1083 nm MOF*

With MOF function of the He D3 remaining elusive after various lab tests, I changed my focus to developing the He I 1083 *nm* MOF. Using the same lab setup as shown in Figure

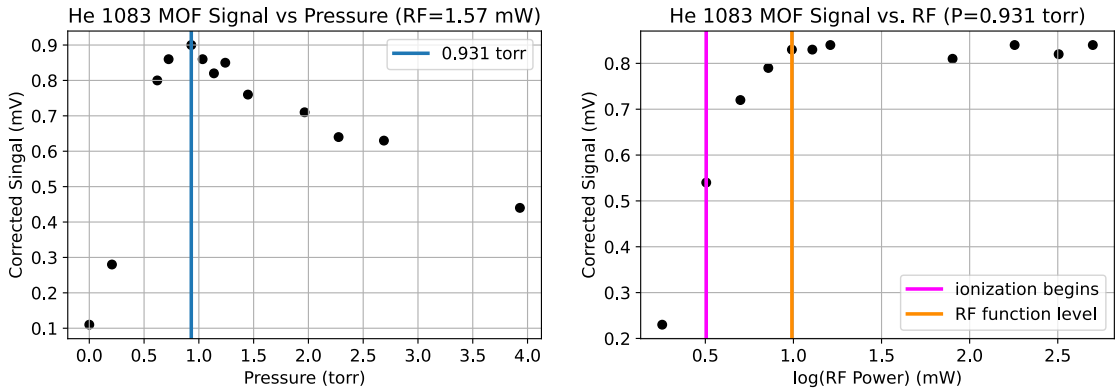

Figure 6.13 Lab tests conducted on the He 1083 *nm* MOF on July 12, 2022. Left: pressure vs. corrected signal (cell emission subtracted off) transmitting through P2, indicating the optimal pressure to operate the MOF at is 0.931 torr. Right: RF power vs. signal transmitted through P2. Pink line indicates when ionization began, and orange line indicates the power we operated at for the remainder of our tests (9.8 mW).

6.7 with the exception of changing the light source to a He I 1083 *nm* laser, I was able to immediately detect MOF function, and optimized the He pressure within the cell to 0.931 *torr* (left panel of Figure 6.13). Additionally, I ran tests to determine the optimal RF power required to operate the cell (right panel of Figure 6.13).

After the success of the lab tests of the He I 1083 *nm* MOF, my focus switched to the operation of the MSO-K and MSO-Na channels to bring the MSO telescope to a point suitable for observations (see Chapter 4). In 2025, I returned to the development of the He I 1083 *nm* MOF with the goal of testing the MOF on-sky as MSO-He. Using the He cells from the Murphy et al. (2005) He MOF experiment (filled with 0.90 *torr* of pure He), I constructed two new He MOF magnet assemblies, each with a magnetic field of 3 *kG*, consistent with the MSO-K and MSO-Na magnet assemblies, for the MSO-He MOF and WS (see Figure 6.3 for reference).

Due to structural limitations and to leverage the presence of an aligned MOF-based telescope channels' optics, MSO-He was slotted into the MSO-K channel. The preliminary on-sky observations I took to acquire He intensity images and consisted of the MSO-K channel with the He MOF in place of the K MOF and the He narrowband filter in place of the K narrowband filter. Additionally, I removed the WA to provide the maximum amount of transmission in a single solar disk image. During these tests, a notable ghost image offset from the solar disk was present. To combat this, the Eddy Co. created a new custom beam splitter to optimize the transmission around the 1083 nm line (see Appx. A for transmission curve) which I substituted into the MSO telescope before further testing. This substitution removed the ghost image and allowed us to acquire MSO-He first-light intensity images on October 7, 2025 (Figure 6.14).

Although the observed features differ due to probing different atmospheric heights, a rotational correction based on HMI intensitygrams (see Section 5.3.2) was successfully obtained for MSO-He. However, a discrepancy arose in the necessary correctional rotation between MSO-K and MSO-He. Since these two channels are mechanically the same, consisting in the same physical space, their correctional rotation should be identical. It is possible that the realignment of the WA when the MSO-He channel was installed could have slightly altered this value, or the discrepancy between the MSO-He features and HMI features resulted in an incorrect rotation. More alignment checks are planned to resolve this issue. Consequently, with the exception of Figure 6.15, all MSO-He observations presented in this document have been rotationally corrected by applying the MSO-K rotational correction.

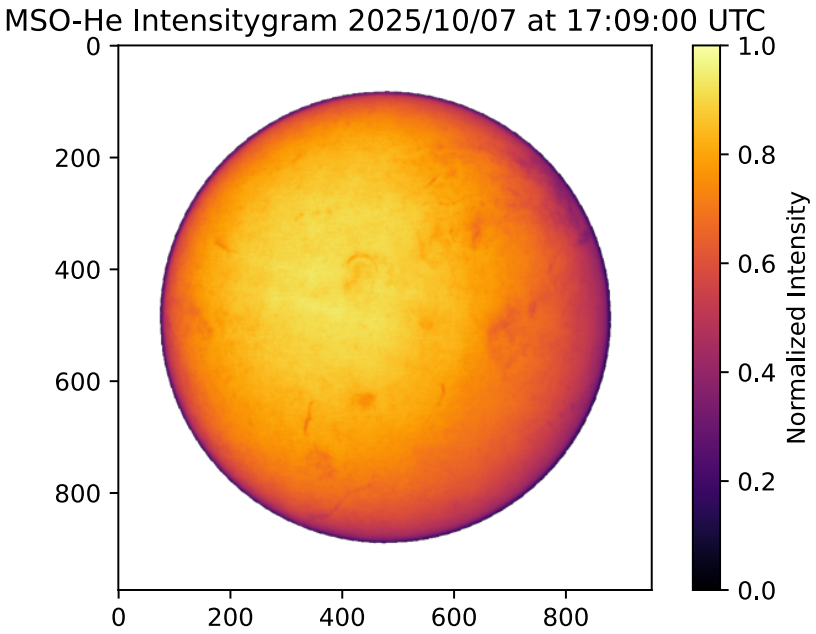

Figure 6.14 First-light image acquired with MSO-He on October 7, 2025. At this point, the K-WA was not in the optical path, and the K-QWPs were still in place, resulting in lower transmission RHCP and LHCP filtergrams with combined red and blue wings, respectively. The image shown above is the sum of these combined filtergrams, an effective intensitygram, summed over 2 minutes, and flat field corrected (no glow correction from cell emission).

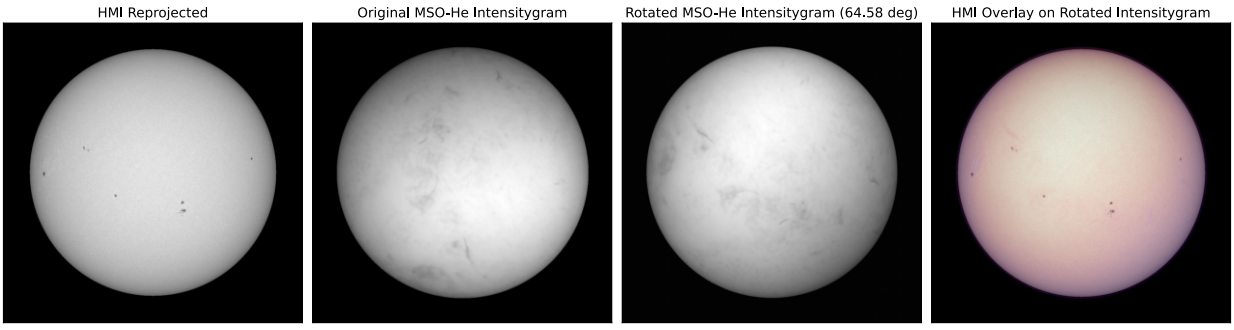

Figure 6.15 MSO-He rotational correction based on comparison to HMI intensitygrams. A discrepancy exists between the MSO-K and MSO-He computed rotational correction.

Following the first-light acquisitions, I replaced the WA, and installed the He WS to test for Doppler/magnetic signal. This test proved unsuccessful, attributed most likely to the presence of the K-QWPs. The QWP's phase retardance is wavelength-specific, following the function

$$\delta(\lambda) = \frac{2\pi\Delta}{\lambda} n(\lambda) d \tag{6.1}$$

where δ is the phase retardance, λ is the wavelength of the incident beam, $\Delta n = n_o - n_e$ is the difference between the ordinary/extraordinary indices of refraction, and d is the plate thickness. Therefore, attempting to operate MSO-K with QWPs optimized for a shorter wavelength will result in an under-retardance of the light, and therefore an elliptically polarized beam (rather than a linearly polarized beam) entering both P1 and the WA. Although the linear portion of this elliptical beam would be transmitted through P1 and the WA, it proved too weak to detect a Doppler or magnetic signal. Consequently, I installed new, near-IR (1064 nm QWPs) in MSO-He.

With the new QWPs installed, prior to attempting to acquire Doppler- and magnetograms, I ran an additional series of tests to determine the optimal RF power and capacitor tuning position to ionize the cells. The current RF power control for the cells (left panel of Figure 6.16) allows for both the frequency and power to be independently tuned. All tests and observations were conducted with an RF frequency of 28.5 MHz chosen because of its proximity to the Industrial, Scientific, and Medical (ISM) frequency standard and its ability to be conveyed across a meter-long wire without having to take transmission line behavior

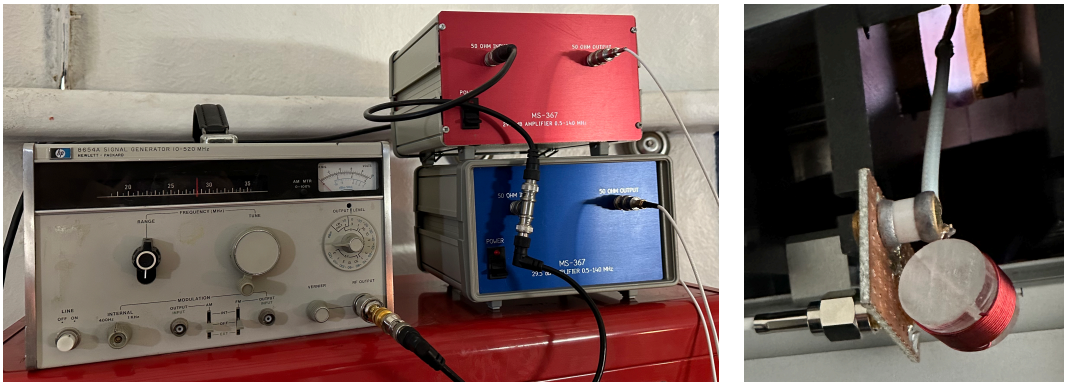

Figure 6.16 Left: RF power box and MOF/WS amplifiers. Right: RF electrode tuning circuit.

into account. The RF power is fed to two amplifiers, one for the MOF and one for the WS, such that the MOF and WS can be turned on and off independently. However, the boxes are coupled such that both cells are fed with the same RF power; because of this coupling, the only way to adjust one cell's RF power with respect to the other is to directly tune the capacitor on the cell's RF electrode tuning circuit (right panel of Figure 6.16).

I conducted two RF tests: RF power tuning (Figure 6.17) and RF circuit capacitor tuning (Figure 6.18). Both tests were conducted by acquiring five minutes of glow images (emission) followed by five minutes of flat field images (transmission) at the various power/capacitor settings. Transmission images were acquired in the form of flat field images to smooth out any solar features and prevent spurious signals. A Master Glow image was created by taking the mean of all of the emission images and was subsequently subtracted off of each transmission image. A central 100 x 100 pixel section from the disk center from each emission-correct transmission image was selected for analysis.

Figure 6.17 shows the mean intensity results of varying the MOF and WS cells' RF

powers from 0.8 mW to 320 mW. As described in Section 6.3, with increasing RF power the population of the metastable He I increases until there is no neutral He remaining in the cell. The increase in the metastable He I population consequently increases the overall transmission of the MOF cell. Based on the RF power test, an optimal ionization power of 12.8 mW was selected and used for all subsequent observations and tests.

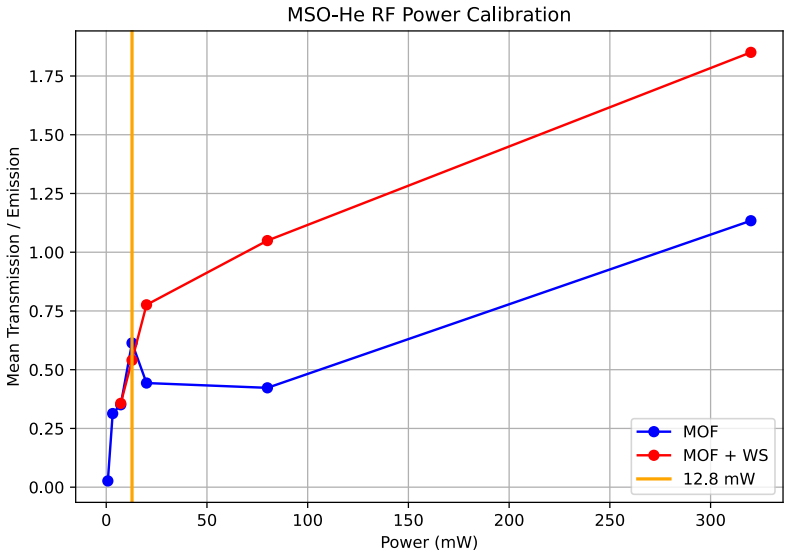

Figure 6.17 Ratio of mean intensity of glow-corrected transmission to emission versus RF power for MSO-He MOF. WS plot does not include powers less than 7.2 mW as the cell does not turn on for lower powers.Optimum RF power was selected by the inflection point in the transmission curve.

Figure 6.18 shows the mean intensity results of the MOF cell's capacitor tuning test for positions ranging from -4π to 10π rotations from its nominal position (position 0). This test was conducted with just the MOF, the RF power at 12.8 mW, and the MOF's capacitor tuned by hand. Tuning the capacitor effectively changes the amount of RF power being supplied to the cell. This allows for the MOF and WS's RF power to be tuned independently from one another while maintaining the coupling in their amplifier boxes. The

capacitor tuning test revealed the nominal MOF capacitor position as the optimal setting; this configuration was used for all subsequent observations.

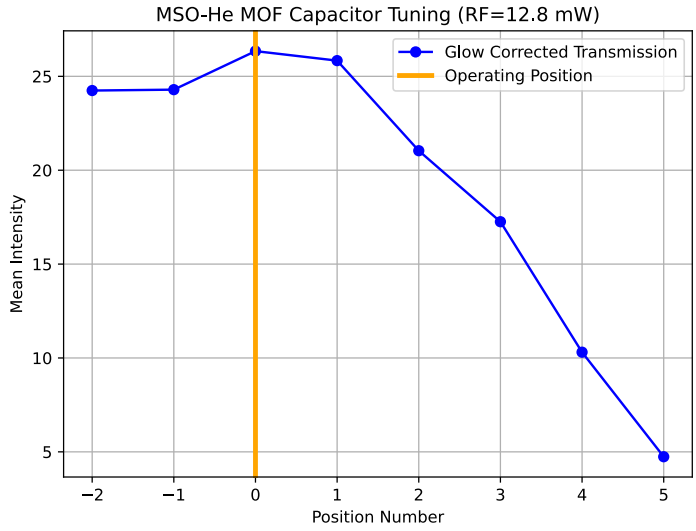

Figure 6.18 Mean intensity of glow-corrected MSO-He MOF transmission versus capacitor position. Each position refers to a π rotation of the capacitor's tuning screw. Position 0 (nominal position) was selected for operation based on its peak intensity.

6.6 *Solar Observations with MSO-He*

Phase 3 of the GATES 2025 Observing campaign focused on MSO-He observations. Its primary purpose was to show proof of concept for a fully operational He I 1083 nm MOF and acquire He Doppler- and magnetograms capable of resolving AR structures. The secondary goal was to acquire a fully chromospheric multi-height data set with MSO-Na and MSO-He operating simultaneously to investigate magnetic field dynamics and potential wave propagation across the chromosphere. From October 7, 2025, to October 29, 2025, MSO-He acquired 28 hours of He observations over 7 days. Of these observations, 20 hours had operational

MSO-He MOF and WS, attempting to collect Doppler- and magnetograms, and 23 hours acquired dual-height MSO-Na and MSO-He observations. During this time, MSO captured 4 C-class flares, two of which had both dual-height and Doppler/magnetic observational capabilities. Table 6.2 lists the specifics of the Phase 3 observing run.

Table 6.2 Parameters for MSO-He Observing campaign. Observation times are inclusive of both hours listed. Observations indicating no Doppler and magnetic capabilities apply only to MSO-He (which acquired intensity images); MSO-Na (if applicable) operated in Doppler- and magnetogram taking settings. Flare start times reported in UTC.

Date (MM/DD)	Time (PST)	Time (UTC)	Doppler/magnetic?	MSO-Na?	Flares
10/07	16 - 17	(+1) 0 - 1			
10/11	12 - 14	20 - 22		yes	
10/15	11 - 13	19 - 21			C5.1 @ 19:34 C5.1 @ 19:45
10/21	10 - 12	18 - 20	yes	yes	
10/23	09 - 15	17 - 23	yes	yes	
10/24	09 - 16	17 - 0 (+1)	yes	yes	C1.3 @ 18:33 C1.4 @ 20:00
10/29	10 - 12	18 - 20	yes	yes	

The large gaps in data acquisition days were due to both weather limitations and MSO-He testing days. In addition to the data acquisition days listed, MSO-He operated on October 10, 13, 17, and 20, testing various cell functions to tune the RF circuit parameters; each day also captured a few minutes of science data. The Phase 3 campaign culminated in a two-day extended dual-height observing run on October 23 and 24, 2025, during which 15 hours of MSO-Na/MSO-He observations were obtained.

After installing the He-QWPs and performing RF tuning, on October 21, 2025, I con-

ducted observations with MSO-He to acquire preliminary He I 1083 *nm* full-disk Doppler- and magnetograms. On this day, cloud coverage and telescope tracking issues prevented a clear signal from being acquired. However, the two-day observing run on October 23 and 24, 2025, was able to acquire the first preliminary He I 1083 *nm* full-disk magnetograms. Although MSO-He did attempt to also acquire Dopplergrams, the images were plagued with multiple fringing patterns which overwhelmed any Doppler signal. Figure 6.19 compares the MSO-He magnetogram to the MSO-He intensitygram and highlights magnetic activity corresponding to the active features in the intensitygram. See Section 7.1 for MSO-He magnetogram comparisons to GONG, BBSO, and HMI magnetograms.

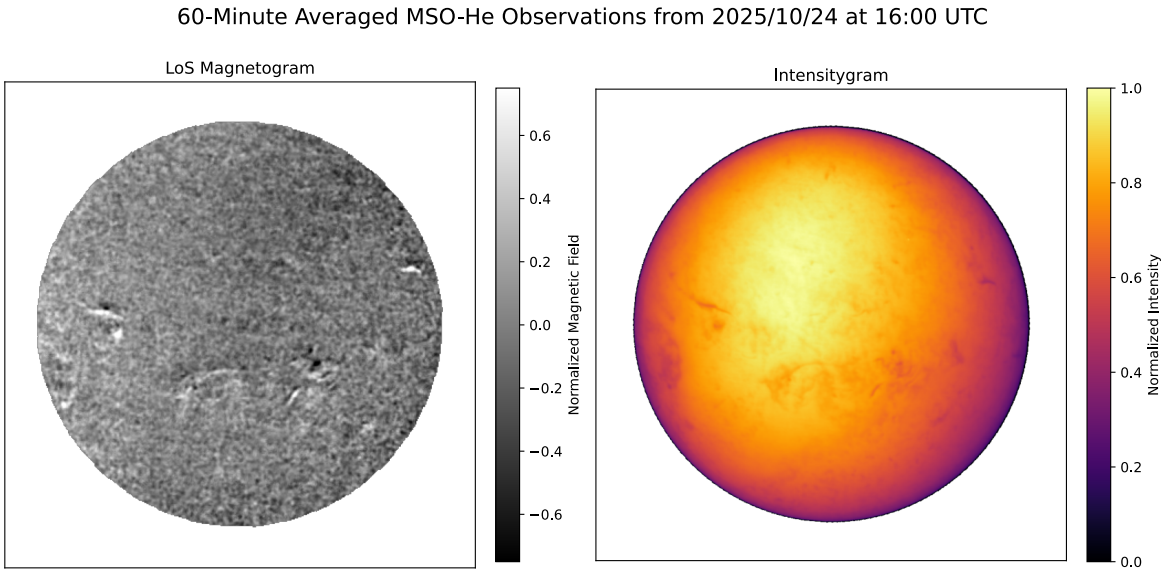

Figure 6.19 One-hour averaged magnetogram (left) and intensitygram (left) from MSO-He on October 24, 2025, at 17:00 UTC. Observations have been normalized/scaled according to the GATES pipeline; additionally, the magnetogram has been smoothed with a 4σ Gaussian.

Similar to the TSST-K, the MSO-He images exhibit a non-uniform intensity gradient present across the solar disk. This gradient appears to be caused by vignetting, potentially

from the baffles installed at the ends of the MOF and WS cells to minimize the glow noise from the cell emission. Further tests are necessary to mitigate this issue.

6.7 *Current Status and Future Work*

Phase 3 of the 2025 Observing Campaign showed promising ability for a He-MOF to obtain LoS magnetograms, but it was clear that full Doppler velocity and magnetic field observational capabilities have still not been achieved. Although the LoS magnetogram obtained with MSO-He does image magnetically active regions spatially correlated with confirmed ARs, it is clear that its MOF function is suboptimal. The lack of contrast between the ARs and quiet Sun, in addition to the inability to produce a LoS Dopplergram, indicates that the MOF passbands are not separated to the proper distance to correspond to the WS absorption bands, or the WS absorption bands are too shallow to properly transmit the individual filtergram wings. The position and depth of these passbands is dependent on the longitudinal magnetic field and the density of the metastable He population within the cell. Because of this, it is likely that in order to improve the MOF functionality of the MSO-He system, the metastable population within one, or both, of the cells needs to be adjusted – during the Phase 3 observing campaign, the MSO-He MOF and WS operated under the same conditions with a neutral He fill pressure of 0.9 $torr$, a magnetic field value of 3 kG, and an RF power of 12.8 mW.

To diagnose the validity of this theory, I developed a theoretical passband modeling code for the He I 1083 nm line, which models the transmission and absorption of the He MOF and

WS under the influence of the Inverse Zeeman and Macaluso-Corbino effects (Chapter 8) . The results of this model confirm that employing the same operational parameters for the He MOF and WS will not produce proper transmission passbands, and therefore optimum Doppler velocity and magnetic field observations is not possible. The model indicates that the number density of the metastable He in the WS must be notably higher than in the MOF section. This result motivates the next step in developing the He MOF; we will return to the techniques described in Section 6.3 to increase the WS's metastable He population and continue to test for Doppler velocity and magnetic field observational capabilities.

In addition to the minimal Doppler velocity and magnetic field observations acquired by this MSO-He test, the acquired images exhibited a few aberrations that need to be addressed prior to MSO-He's full integration into the GATES Network. First, notable vertical and horizontal fringing is present in individual filtergrams. Although not as prominent, these fringes are also visible in the MSO-K setup, and therefore are most likely caused by internal reflection from the polarization optics. These optics will need to undergo further precision polarization alignment to limit these fringes as much as possible to minimize the amount of post-processing filtering that is required. Second, MSO-He data reduction and calibration revealed a discrepancy in the rotational correction between MSO-K and MSO-He, which, given that the channels are physically mounted in the same place with no adjustments made to the primary imaging optics or camera, is expected to be the same and needs to be resolved. Despite these aberrations, the dataset acquired by Phase 3 proved incredibly useful for diagnosing the improvements necessary for the development of the He MOF while

still providing a rich multi-height chromospheric dataset.

The full-disk He I 1083 *nm* intensity images provide observations uniquely sensitive to large-scale magnetic and thermodynamic structures that connect the chromosphere to the corona. The MSO-He observations show clearly visible filamentary structures in absorption (dark features in the intensitygram of Figure 6.19). With extended observations, MSO-He allows for temporal and spatial tracking of their evolution and destabilization, which is critical for anticipating eruptive events such as coronal mass ejections. Additionally, the He I 1083 *nm* intensity observations can identify the presence of coronal holes, and therefore open magnetic field lines, that are primary sources of high-speed solar wind streams—key drivers of recurrent geomagnetic disturbances at Earth. Utilizing MSO-He as an intensity channel for coronal hole studies can provide insight into the spatial extent, evolution, and boundary dynamics of these open-field regions, which is essential for forecasting the timing and impact of high-speed solar wind streams at Earth.

Moreover, these scientific returns are significantly enhanced when these He intensity images are complemented by the full-disk Doppler- and magnetograms of MSO-Na. The MSO-Na Dopplergrams can reveal supergranular flows, wave propagation, and pre-eruptive dynamics spatially correlated with open field lines (as confirmed with the MSO-He observations). Additionally, the MSO-Na magnetograms constrain the low-chromospheric magnetic field that anchors high-chromospheric and coronal structures probed by the MSO-He observations. This multi-height dataset facilitates investigations of magnetic coupling, energy transport, and the buildup of eruptive instabilities.

At the conclusion of Phase 3 of the 2025 GATES observing campaign, I returned MSO to its MSO-K/MSO-Na status, so that additional multi-height Doppler velocity and magnetic field observations could be acquired. This required MSO-He to be temporarily dismantled. Despite this, given that the MSO-He and MSO-K share almost all optics, except for the QWPs, cells, and narrow-band filters, and because the MSO telescope enclosure is designed to be modularly disassembled while mounted, the change between MSO-K and MSO-He requires minimal effort. This allows the MSO team to continue He MOF development, addressing the fringing issues, metastable He population in the WS cell, and overall SNR, with the current MSO set-up in the near future.

The long-term plan for MSO, and other GATES nodes is to expand the telescope to allow for tri-channel observing. However, because of the limitations of their shared optics, it is currently impossible to observe with MSO-K and MSO-He simultaneously. Moreover, although the MSO-K optics and camera proved sufficient for preliminary MSO-He tests, He-specific optics and an IR-optimized camera would greatly improve the SNR and image quality of MSO-He. As the GATES Network expands, the MSO team plans to focus on realizing a full MSO-He channel that can run in conjunction with MSO-K and MSO-Na. This will require a structural redesign of the MSO optical scheme or an additional telescope, as the current MSO optical design and structural limitations only allow for two simultaneous channels. See Chapter 9 for more information about integrating He MOF into the GATES Network and its potential scientific contributions.

CHAPTER 7
DATA DISCUSSION AND PRELIMINARY ANALYSIS

7.1 *Magnetogram Analysis*

LoS magnetograms are a cornerstone of space weather and solar flare studies because they offer a direct link to the magnetic energy buildup and release mechanisms underlying solar eruptions, as they provide a measurement of the strength, polarity, and complexity of magnetic field lines in active regions. Preliminary quality checks of the GATES magnetograms were conducted through a comparison with GONG and SDO/HMI magnetograms. Since GONG and HMI provide photospheric magnetograms, these comparisons are most relevant to TSST-K and MSO-K. GONG produces 10-minute averaged magnetograms with a pixel scale of 2.5"/px, while HMI provides 12-minute averaged magnetograms at 0.5"/px. To allow for direct comparison, TSST-K (1.17"/px), MSO-K (2.39"/px), MSO-Na (2.29"/px) and HMI magnetograms were reprojected to match the GONG pixel scale using a linear coordinate-based interpolation. Figure 7.1 shows a comparison of all three GATES channels' magnetograms from July 31, 2025 at 15:30 UTC with the closest in time GONG and HMI magnetograms.

Magnetogram observations from MSO-He on October 24, 2025 were also compared to GONG and HMI for visual inspection. Figure 7.2 shows the MSO-He magnetogram compared to GONG BBSO and HMI from the same time (with the same initial observing time). Similar to Figure 7.1, HMI has been reprojected to match GONG's pixel scale using a linear coordinate-based interpolation; MSO-He (2.38"/px) remains in its original pixel scale due to

issues reprojecting arising from noise. Since GONG and HMI are photospheric instruments, the magnetic dynamics they are probing differ significantly from MSO-He. Consequently, it is not expected that GONG/HMI and MSO-He magnetic field measurements will be directly comparable. Despite this, a few of the notable active regions exhibiting magnetic activity spatially correlate in the magnetograms.

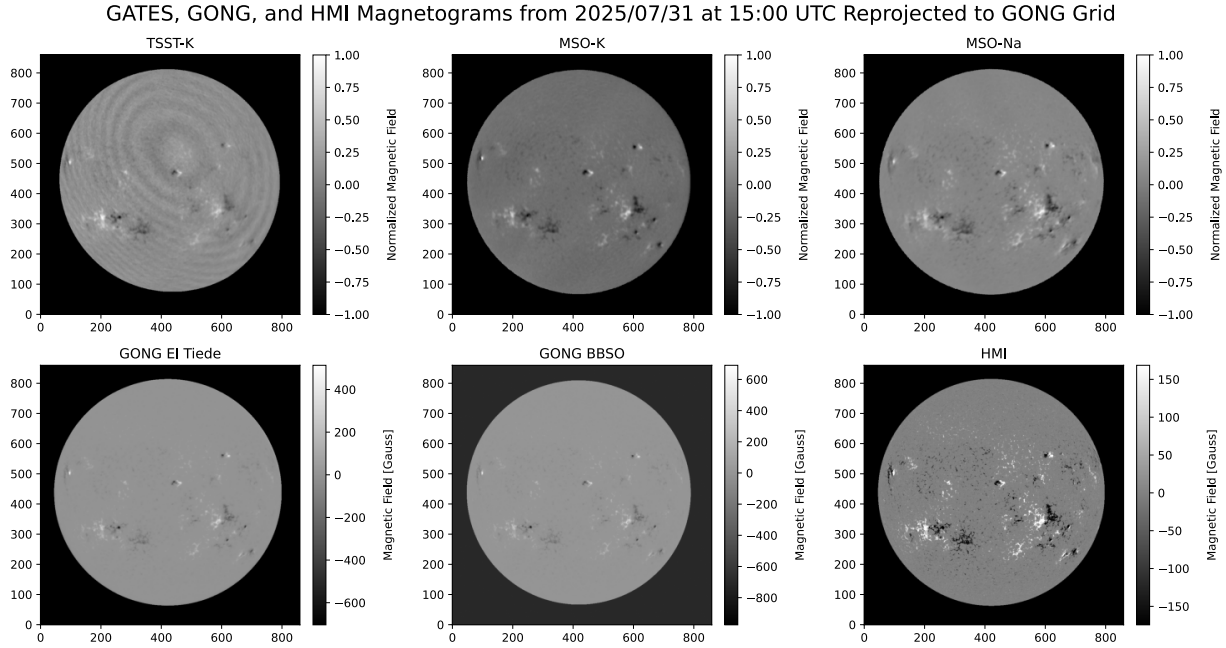

Figure 7.1 GATES magnetograms (top) compared to GONG/HMI magnetograms (bottom) from July 31, 2025 at 15:30 UTC. Both GONG El Teide Observatory and GONG BBSO are shown for their relatively proximity to the TSST-K and MSO.

7.1.1 Red/Blue Wing Magnetograms and the Magnetic Gradient

Aside from full LoS magnetograms, there is a benefit to investigating individual wings' magnetograms ($B_{Los:RW}$ and $B_{LoS:BW}$: see Equations 2.18). These magnetograms are constructed using the RHCP and LHCP states of a single wing's observations and are sensitive

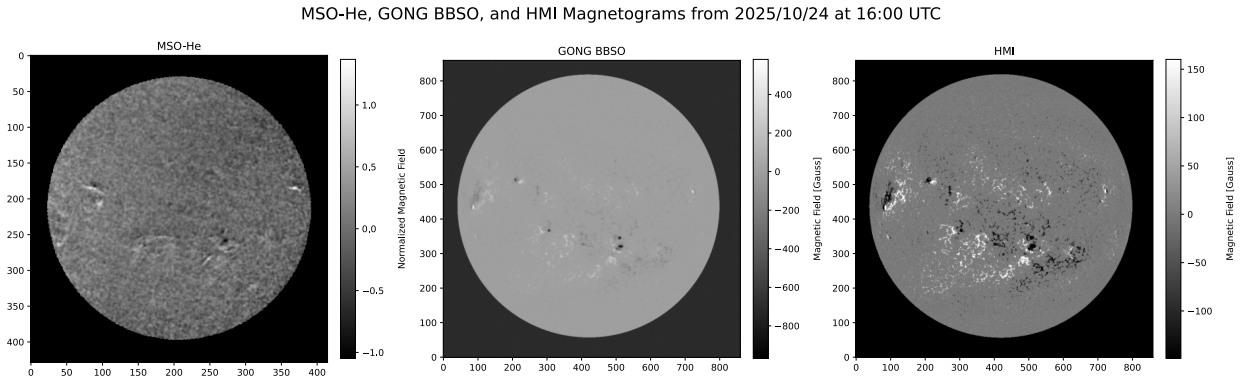

Figure 7.2 Comparison of MSO-He and GONG BBSO magnetograms from 2025/10/24 at 16:00 UTC. The MSO-He magnetogram is a 60-minute average, while the GONG and HMI magnetograms are 10-minute average.

to different magnetic features and plasma phenomena. RW magnetograms are sensitive to plasma with red-shifted Doppler velocity, and BW magnetograms are sensitive to plasma with blue-shifted Doppler velocity. The most obvious consequence of this is that the RW magnetograms are much more sensitive to magnetic activity on the western limb (the limb rotating away from Earth) and the BW to the eastern limb (top panels of Figure 7.3).

In addition to the component wing magnetograms, the magnetic gradient provides unique insight into the Sun's magnetic dynamics. The magnetic gradient is defined as the difference between the RW and BW magnetograms. While the total magnetogram describes the magnetic strength and polarity of the LoS component of the magnetic field, the magnetic gradient describes the non-radial motions of the plasma. Investigating the difference between the magnetic fields of spatially co-located red-shifted and blue-shifted plasma, the magnetic gradient reveals shearing and twisting in ARs. Figure 7.3 shows an example of the RW, BW, total magnetogram, and magnetic gradient from the MSO-Na channel.

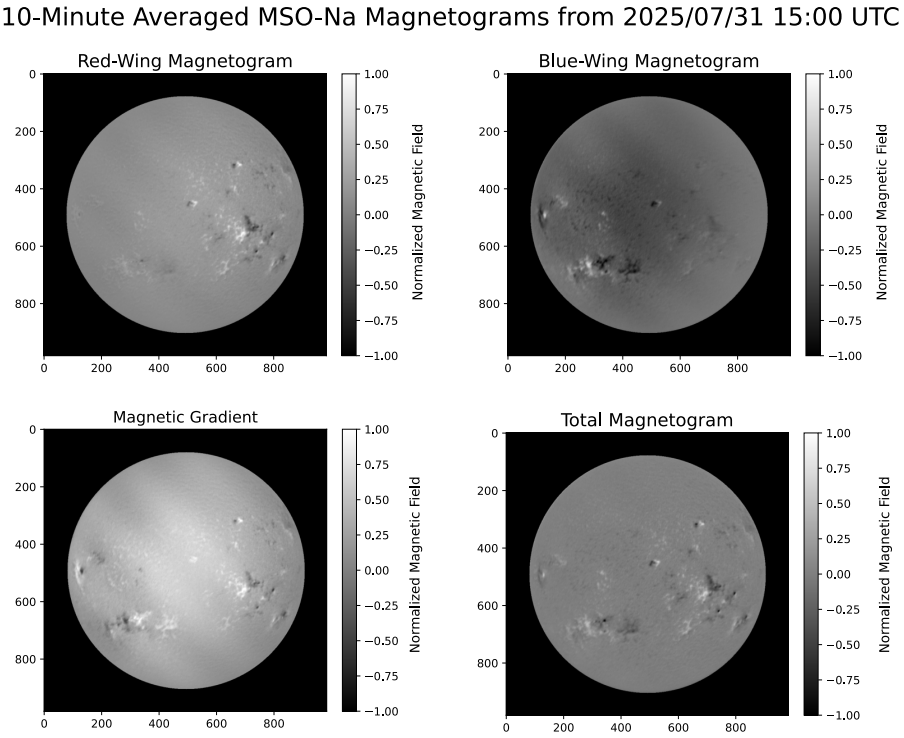

Figure 7.3 Ten-minute averaged magnetogram combinations from MSO-Na on July 31, 2025 at 15:00 UTC. The Magnetic gradient is the difference between the RW and BW magnetograms. The individual RW and BW magnetograms exhibit a central artifact (brighter in RW and darker in BW), which is caused by instrumental polarization. This cancels out in the total magnetogram, so it does not pose an issue to traditional magnetogram investigations.

Spatially, the magnetic gradient correlates with the total magnetogram. This is an indication of the presence of high-shear plasmas in magnetically active regions. Investigating smaller scales reveals a more nuanced view of the plasma dynamics within an active region (Figure 7.4). We can see that in addition to magnetic features on the western limb being stronger in the RW magnetogram, the RW magnetogram measures a stronger signal than the total magnetogram. Additionally, since the RW and BW magnetograms are constructed at independent wavelengths from each other, they provide views of two co-located slightly

different heights in the solar atmosphere. Although their atmospheric separation is small, this distinction allows for a single MOF channel to provide spatial analysis of magnetic dynamics.

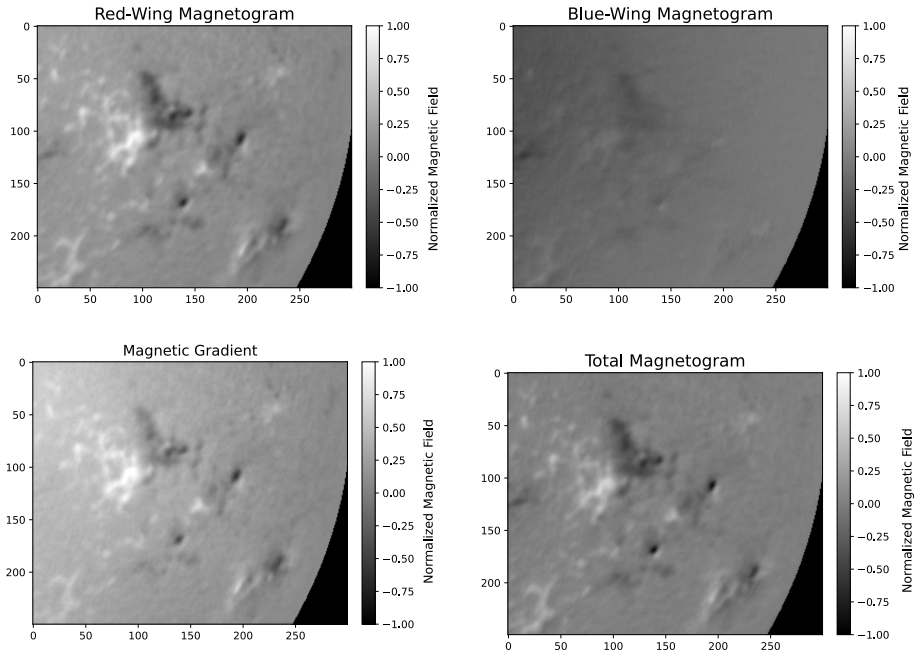

Figure 7.4 Zoomed-in views (FOV $\sim 15.3' \times 15.3'$) from the magnetograms in Figure 7.3 highlighting NOAA AR 4153, NOAA AR 4154, NOAA AR 4155, and NOAA AR 4157.

7.2 *Dopplergram Analysis*

LoS Dopplergrams are sensitive to a superposition of velocity contributions, including large-scale solar rotation, differential rotation, convection, oscillations, and localized flows associated with magnetic structures such as active regions, filaments, and supergranulation. Consequently, the prevailing signal in full-disk or Dopplergrams is the systematic east–west gradient produced by solar rotation, which ranges from $\sim \pm 2$ km/s across the solar disk. The (longitudinal) center of the Sun shows no rotation because the LoS component of the

velocity is zero; this produces a distinct zero-velocity line in LoS Dopplergrams (left-hand panels of Figure 7.5). This zero-velocity line is present in MSO-K and MSO-Na LoS Dopplergrams as a longitudinally parallel band. However, due to polarization-induced fringes and heliostat vignetting, the TSST-K Dopplergram zero-velocity line is plagued by spatial inhomogeneities that distort its overall shape.

The zero-velocity line is used for calibrating the LoS Dopplergrams to physical units and measuring the relative Earth-Sun radial velocity. By taking a latitudinal cross-section of a LoS Dopplergram, the 1D Doppler velocity spectrum exhibits a sinusoidal behavior due to the solar rotation. When modeling this sinusoid, the position of the zero-velocity line, corresponding to $\phi = 0$, exhibits a Doppler velocity offset. This offset is the result of the relative Earth-Sun radial velocity, solar redshift ($638 \pm 6\ m/s$ as observed in the photosphere by HARPS Fe: González Hernández et al. (2020)), and the pressure shift of the backfill gas (for GATES, argon) within the MOF cells. The right-hand panels of Figure 7.5 show this sinusoid fitting for each of the GATES channels on July 31, 2025.

In a standard LoS Dopplergram, the dominant signal of the solar rotation can obscure smaller-scale and more localized dynamical features in the velocity field, like supergranulation and p-mode oscillations. To isolate these features, a rotation-subtracted Dopplergram is constructed by modeling the large-scale rotational velocity field and subtracting it from the original LoS Dopplergram. As described in Section 5.3.3, this rotational velocity field model is produced by Gaussian smoothing the LoS Dopplergram. After subtracting the solar rotational model, the resulting residual Dopplergram highlights non-rotational flows, such as

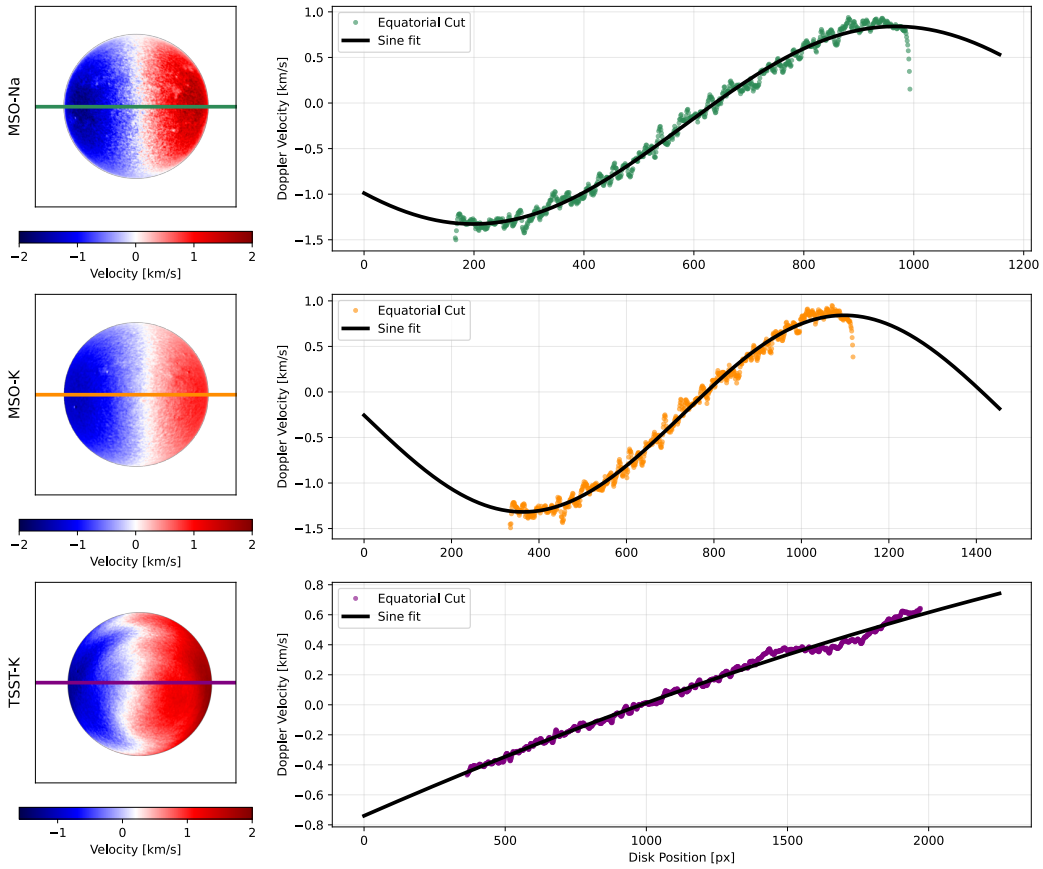

Figure 7.5 10-minute averaged Dopplergrams from 2025/07/31 at 15:00 UTC from all three active GATES channels. A 1D horizontal cross-section is plotted and fit with a sine curve. MSO-K and MSO-Na have a consistent 0.3 km/s vertical offset. However, the TSST-K model, produces an offset of -14 km/s likely due to inhomogeneity of the zero-velocity line effecting the Dopplergram calibrations.

supergranular outflows, and localized inflows and outflows around active regions. Rotation-subtracted Dopplergrams, therefore, enable more direct analysis of convective patterns, wave motion/power, and coupling between plasma flows and magnetic fields. Figure 7.6 shows LoS Dopplergrams and rotation-subtracted Dopplergrams computed from ten-minute averaged Dopplergrams on July 31, 2025 at 15:00 UTC. All three channels exhibit cellular structure consistent with supergranulation patterns.

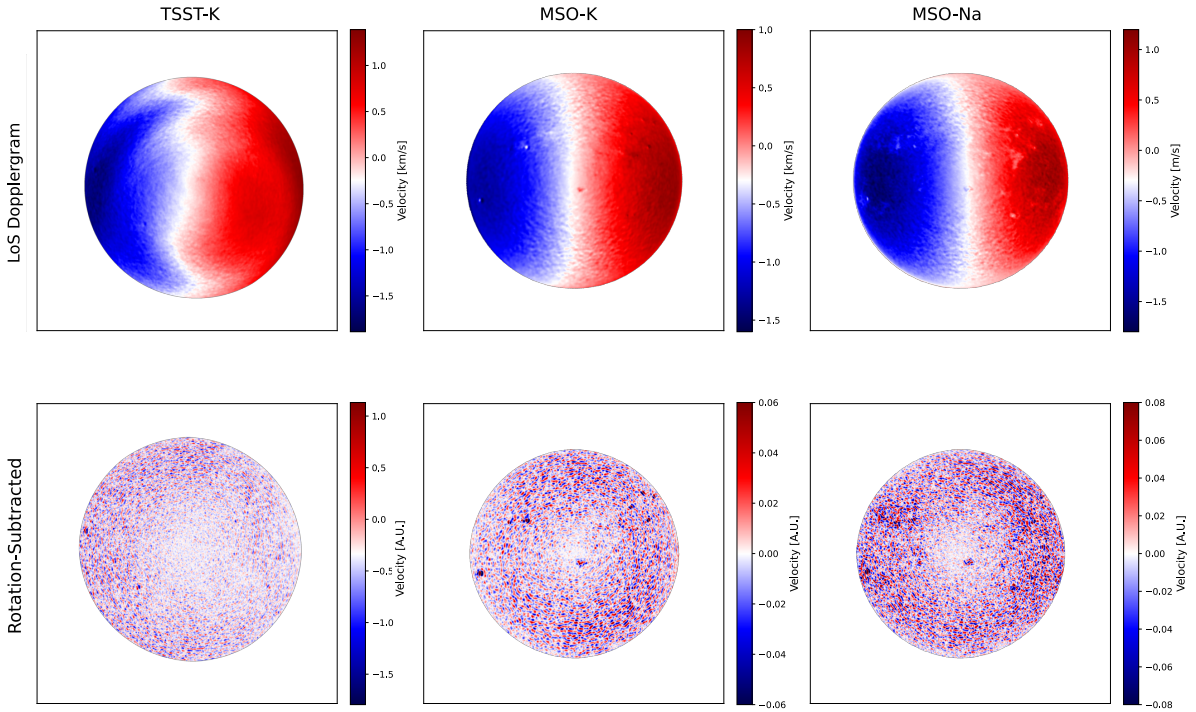

Figure 7.6 Ten-minute averaged GATES channels' LoS Dopplergrams (top) exhibiting the Sun's rotation and rotation-subtracted Dopplergrams (bottom) revealing supergranulation and p-mode patterns.

7.2.1 $k-\omega$ *Diagrams and Phase Spectra of Solar Atmospheric Oscillations*

In addition to mapping plasma flows at different heights in the solar atmosphere, Dopplergrams can be used to analyze wave phenomena and solar oscillations. Using a time series of rotationally subtracted Dopplergrams, a power spectrum, referred to as a $k-\omega$ diagram, can be computed to investigate and quantify the oscillatory velocity signals present in the solar atmosphere. To construct the power spectrum, using a Fourier Transform, the temporal signal at each spatial location is transformed from the time domain into the frequency domain, decomposing the velocity signal into its constituent frequencies and enabling periodic

components (frequencies with large powers) to be identified. The power at each frequency is then calculated as the magnitude of the corresponding Fourier component. Physically, the power spectrum represents how the energy of the velocity oscillations is distributed across different frequencies.

In a 2D $k-\omega$ diagram, power is concentrated along distinct ridges that trace the dispersion relations of the waves. Acoustic (p-modes) oscillations appear as a series of curved ridges between 2 - 5 mHz, with increasing order corresponding to higher frequency branches. Surface gravity waves (f-mode) form a prominent ridge at lower frequencies, typically lying below the p-mode ridges and following a characteristic dispersion relation. At very low frequencies and wavenumbers, signatures of large-scale flows or convective motions can be mapped. The location and shape of these features in $k-\omega$ space provide insight into the physical properties and wave propagation behavior in the solar interior and atmosphere.

Figure 7.7 presents 2D $k-\omega$ power diagrams of the MSO-K and MSO-Na channels from July 31, 2025. Both channels' spectra exhibit the characteristic p-mode ridges in the 2 - 5 mHz range. To better distinguish the various wave modes' physical regions on the $k-\omega$ diagram, I have overplotted three curves. The black horizontal line at 5.2 mHz marks the acoustic cut-off frequency – the highest frequency for which acoustic waves are trapped in the solar atmosphere; above this frequency, acoustic waves act as traveling waves and are free to propagate and escape. The cyan curve represents the f-mode ridge defined by the relation $\omega^2 = gk$, where g is the solar surface gravity and k is the horizontal wavenumber. The area below the cyan and black dotted line indicates where power is carried by atmospheric gravity

waves.

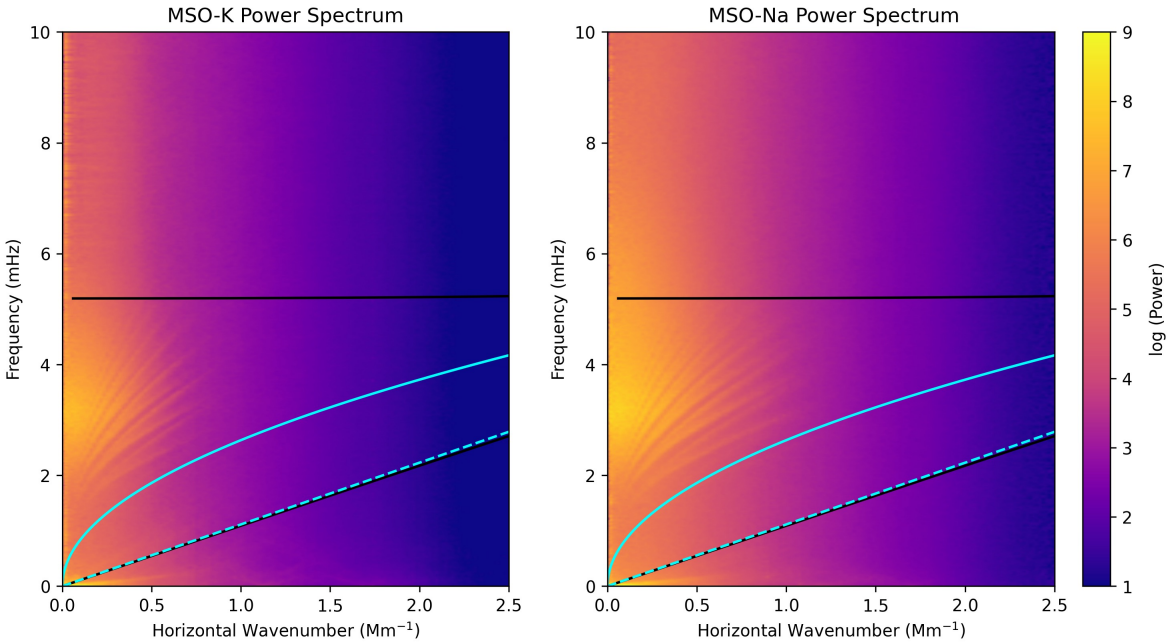

Figure 7.7 2D power spectra from MSO-K and MSO-Na obtained from 11 hours of data 2025/07/31 starting at 15:00 UTC. Both spectra exhibit characteristic p-mode ridges that trace the cyan f-mode curve and extend towards the black acoustic cut-off frequency line at 5.2 mHz.

To enable cross-spectrum analysis, both channels' spatial resolutions were rebinned to match MSO-K (2.39"$/px$ corresponding to 1.71 mm/px). Using a 200 x 200 pixel patch in the center of the solar disk and 11 hours of continuous 45 s cadence Dopplergrams (rebinned from the standard 5 s MSO cadence to account for missed frames and to reduce computation cost), we are able to Nyquist sample 11.1 mHz frequencies with a frequency resolution of 0.025 mHz and Nyquist sample 2.9 Mm^{-1} spatial frequencies with a spatial frequency resolution of 0.0029 Mm^{-1}.

In power spectra derived from solar Dopplergram time series, the most prominent signal is produced by the global acoustic (p-mode) oscillations, which appear as a strong, broad peak

centered around $\sim$3 mHz (5-minute period) in 1D power spectra. These modes typically occupy a frequency band spanning roughly 2 - 6 mHz, where the oscillation power reaches its maximum due to the efficient excitation of acoustic waves by near-surface convection. Figure 7.8 shows 1D power spectra constructed spatially averaging the 200 x 200 pixel patches used to compute the $k-\omega$ diagrams of Figures 7.7 and 7.9. The 1D power spectra indicates a peak frequency of $\sim$3.1 mHz for both the K and Na observations, with an increased overall power for the Na channel; this observation is consistent with previous atmospheric seismology studies such as Aparna (2022) and Finsterle et al. (2004a) which found the relative oscillatory power of a given frequency increases with height in the solar atmosphere.

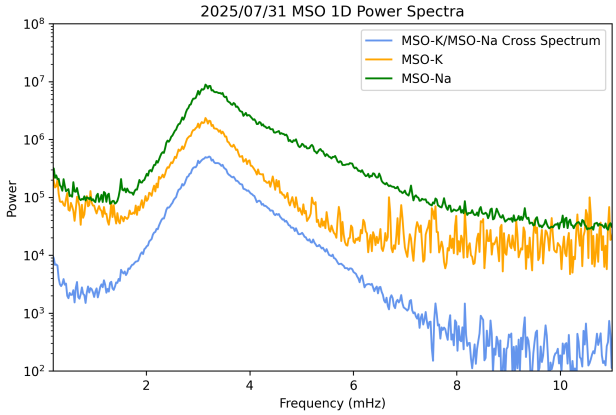

Figure 7.8 1D power spectra obtained from 11 hours of MSO-K, MSO-Na, and cross spectra of MSO K-Na observations on 2025/07/31. The peak oscillation frequency measured for each channel is 3.14 mHz, 3.13 mHz and 3.12 mHz for MSO-K, MSO-Na, and the cross spectrum, respectively.

By cross-correlating the temporal signal at a given pixel in the MSO-K spectrum with that in the corresponding pixel of the MSO-Na spectrum, we can produce a cross-spectrum $k-\omega$ diagram and determine the phase difference between the two Doppler signals. The cross-spectrum $k-\omega$ power diagram (left-hand panel of Figure 7.9) describes the correlation

between the wave signals at the two atmospheric heights, which helps determine what signals are real and how much energy is traveling between the two heights. The cross-spectrum $k-\omega$ phase diagram (right-hand panel of Figure 7.9) provides information about the direction and speed of wave propagation between two atmospheric layers. The sign of the phase difference corresponds to the direction of propagation (positive for upwards and negative for downwards), while the magnitude of the phase difference combined with the frequency gives the vertical phase speed of the wave. Assuming vertically propagating waves, we interpret this phase difference as arising from the phase travel time between the two observing heights.

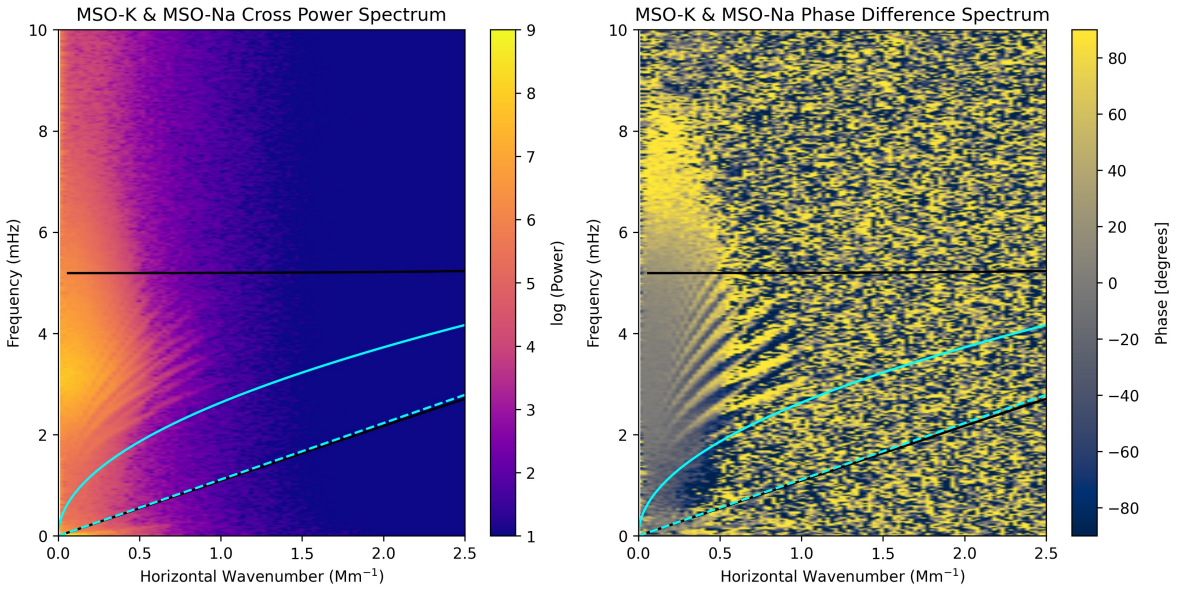

Figure 7.9 Cross-spectrum $k-\omega$ power (left) and phase difference (right) diagrams from MSO-K and MSO-Na on July 31, 2025. The strong phase signal of the p-mode frequency indicates there are waves propagating between the K I photospheric and Na I D2 chromospheric heights.

By collapsing the cross-phase spectrum to one dimension, it is possible to model the propagating acoustic wave(s) between the two atmospheric heights and obtain physical

characteristics of the solar atmosphere. Jefferies et al. (2019) used MOTH II Na and K Dopplergrams to model a single wave traveling upward originating from the base of the photosphere. Chaturmutha et al. (2024) builds on this one-wave model, introducing a second wave, a reflected downward-traveling wave, with an amplitude R_{atm} with respect to the upward-traveling wave. Both studies utilized MOTH Dopplergrams – Jefferies et al. (2019) using MOTH II Na, MOTH II K, and HMI Fe and Chaturmutha et al. (2024) using MOTH II Na and HMI Fe – to verify their respective models. Applying these models to the July 31, 2025 MSO observations, we are able to infer atmospheric parameters such as the distance d_z, radiative damping time t_r, and the sound speed c_s between the two atmospheric heights the MSO-K and MSO-Na channels probe. Figure 7.10 shows the 11-hour 1D MSO cross-spectra fit with both the one-wave (Jefferies et al. 2019) and two-wave (Chaturmutha et al. 2024) models. Table 7.1 lists the atmospheric parameters from these two models.

Table 7.1 Fit parameters from the one-wave and two-wave models provided by Varun Chaturmutha. Although not directly comparable to Chaturmutha et al. (2024)'s results due to the difference in the height, HMI's Fe and MSO-K's channels are probing, I provide Chaturmutha et al. (2024)'s one- and two-wave model outputs for their MOTH Na - HMI Fe data set for comparison.

2025 GATES MSO K - MSO Na					
	d_z $[km]$	t_r $[s]$	c_s $[km/s]$	R_{atm}	RMSE
One-wave	346	101.85	6.81		49.07
Two-wave	376	92.96	6.19	0.12	47.77
2017 MOTH Na - HMI Fe (Chaturmutha et al. 2024)					
	d_z $[km]$	t_r $[s]$	c_s $[km/s]$	R_{atm}	Reduced χ^s
One-wave	520 ± 2.5	140 ± 5.3	7.1 ± 0.041		36.24
Two-wave	480 ± 2.5	79 ± 2.8	6.7 ± 0.044	0.12 ±0.0039	2.19

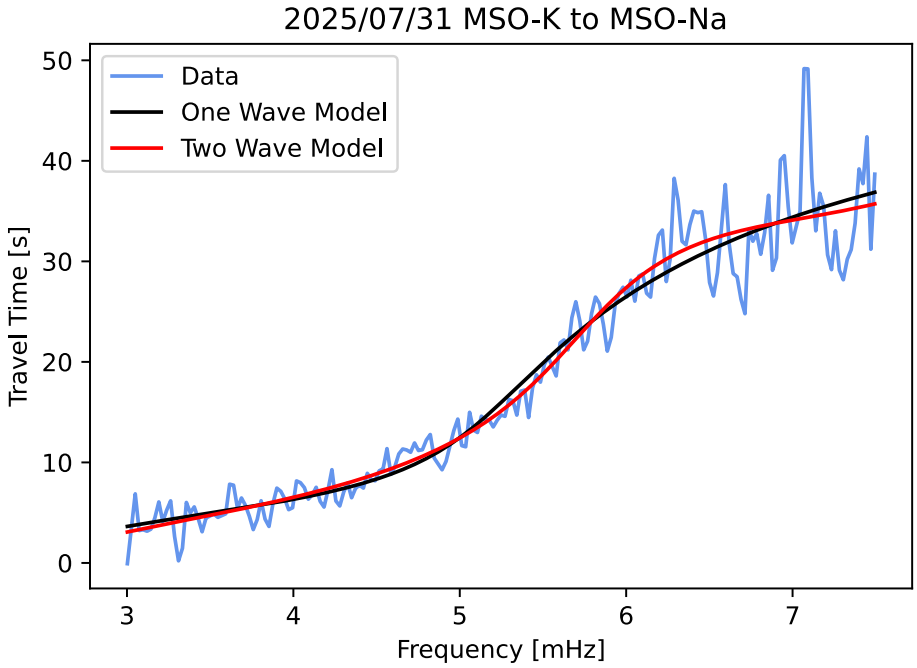

Figure 7.10 1D phase cross-spectra (blue curve) from the July 31, 2025 MSO-K and MSO-Na data converted to travel time compared to the one-wave (black) and two-wave (red) propagating acoustic wave models. Consistent with the findings of Chaturmutha et al. (2024), the two-wave model fits the data better than the one-wave model, supporting the presence of wave reflection in the chromosphere.

In addition to analyzing the phase and power spectra of the MSO-K and MSO-Na channels, I investigated the ability to utilize individual LHCP and RHCP Dopplergrams of the MSO-Na channel as independent height probes. To remain spatially consistent with the K - Na analysis, the Na LHCP and RHCP channels were again rebinned to match MSO-K's spatial resolution, and a 200 x 200 pixel patch was selected from the disk center. However, due to computational limitations, the LHCP - RHCP data set only spans 3 hours on July 31, 2025, corresponding to a frequency resolution of 0.0926 mHz. Figure 7.11 shows the $k - \omega$ power spectra for the individual MSO-Na LHCP and RHCP Dopplergrams. As is

consistent with the full MSO-Na power spectrum (right-hand panel of Figure 7.7 both Na channels indicate notable p-mode ridges. Figure 7.12 shows the cross-spectrum power and phase $k - \omega$ diagrams.

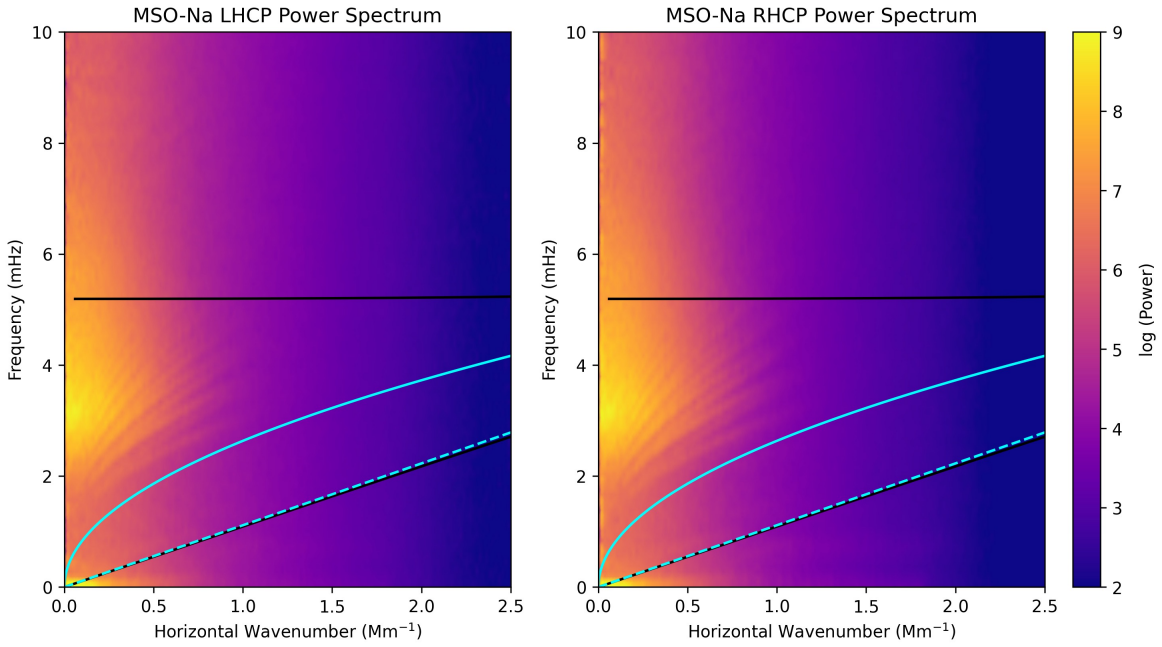

Figure 7.11 2D power spectra from MSO-Na LHCP and RHCP Dopplergrams obtained from 3 hours of data 2025/07/31 starting at 15:00 UTC.

The most notable result from these calculations is the presence of p mode ridges in the phase difference $k - \omega$ diagram. This difference indicates that the two polarization states (corresponding to the solar Zeeman split red and blue wings) are formed at slightly different heights in the solar atmosphere. This enables MSO-Na to operate independently as a dual-height instrument. Furthermore, the fact that the different LHCP and RHCP observations are sampling different heights in the solar atmosphere provides observational access to the vertical contribution function of the Na I D2 line.

As shown in Chapter 8, varying the temperature and magnetic field within the MOF

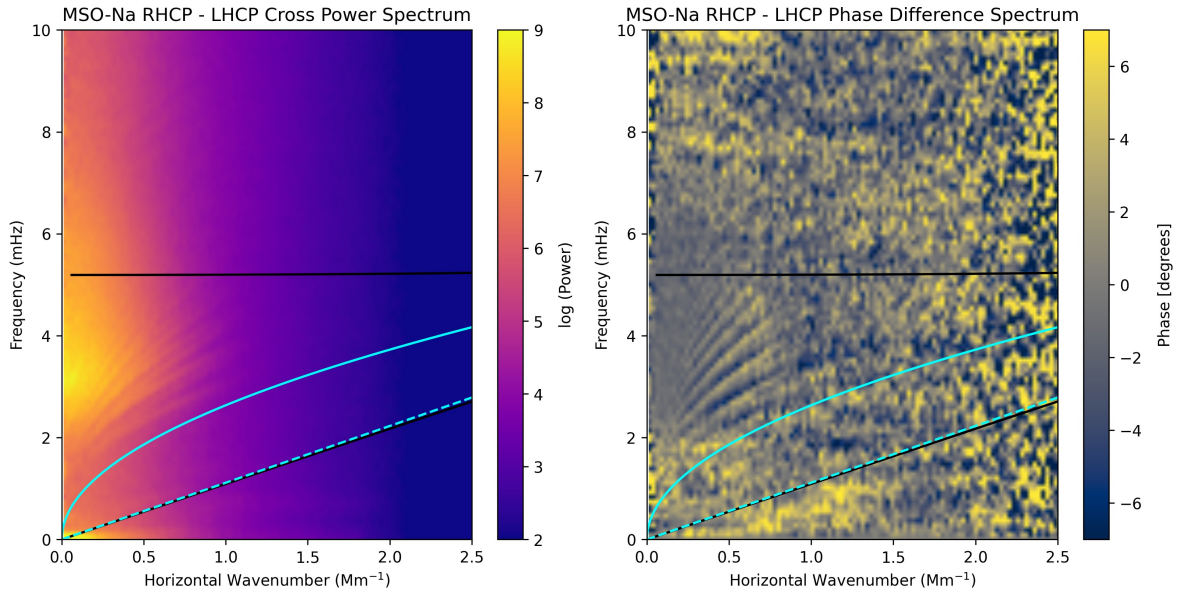

Figure 7.12 Cross-spectrum $k - \omega$ power (left) and phase (right) diagrams from MSO-Na LHCP and RHCP Dopplergrams obtained from 3 hours of data 2025/07/31 starting at 15:00 UTC. The presence of a phase difference between the Dopplergrams of the two polarization states' channels indicates that they probe slightly different heights in the solar atmosphere.

and WS cells will shift the position of the passbands, thus imaging different portions of the line. By varying the temperature within the Na cell, we can scan across the Na line and map the solar contribution function observationally over a period of time. Moreover, if, rather than varying the operating temperature of the MOF cells over time, we construct a multi-Na-channel MOF-based instrument with each Na channel operating at a different temperature/magnetic field, we can instantaneously map the Na I D2 contribution function over the entire solar disk and investigate differences in ARs versus quiet Sun.

7.3 *He Intensitygram Analysis*

In an attempt to capture multi-height dynamics of the chromosphere, MSO-Na was run alongside MSO-He during the observing run on October 24 and 24, 2025. An unidentified error occurred in the acquisition of MSO-Na magnetograms, resulting in magnetic sensitivity limited to the eastern limb of the MSO-Na solar disk. Additionally, the dominating fringe pattern on the MSO-He Dopplergram prevents any meaningful comparison between the two heights' LoS velocity fields at this time. Despite this, comparing the two channels' intensitygrams still provides interesting insight into the solar chromosphere. Figures 7.13 and 7.14 present hour-averaged intensitygrams from MSO-Na and MSO-He compared to two AIA channels (304 Å and 193 Å).

In MSO-Na (probing the low chromosphere $\sim$ 700 km), the penumbras of the active regions' sunspots are visible as dark points while plage regions in the surrounding areas appear as bright patches. Observing higher in the chromosphere ($\sim$ 2 Mm), MSO-He intensitygrams are dominated by dark, diffuse fibril patterns. AIA 304 Å overlaps with MSO He observing from the top of the chromosphere through the transition region ($\sim 2-10$ Mm) observing filaments, prominences, and the base of coronal structures. AIA 193 Å probes the corona ($\sim 10-100$ Mm) observing bright coronal loops and active regions as well as dark coronal holes. The MSO-He 1083 nm is an optically thick line, sensitive to the column density and absorption along the LoS and not just local emission meaning notable contrast can be observed even when the plasma is not very hot. Conversely, the AIA 304Å line is typically optically thin meaning its observed intensity is proportional to the emission along the line

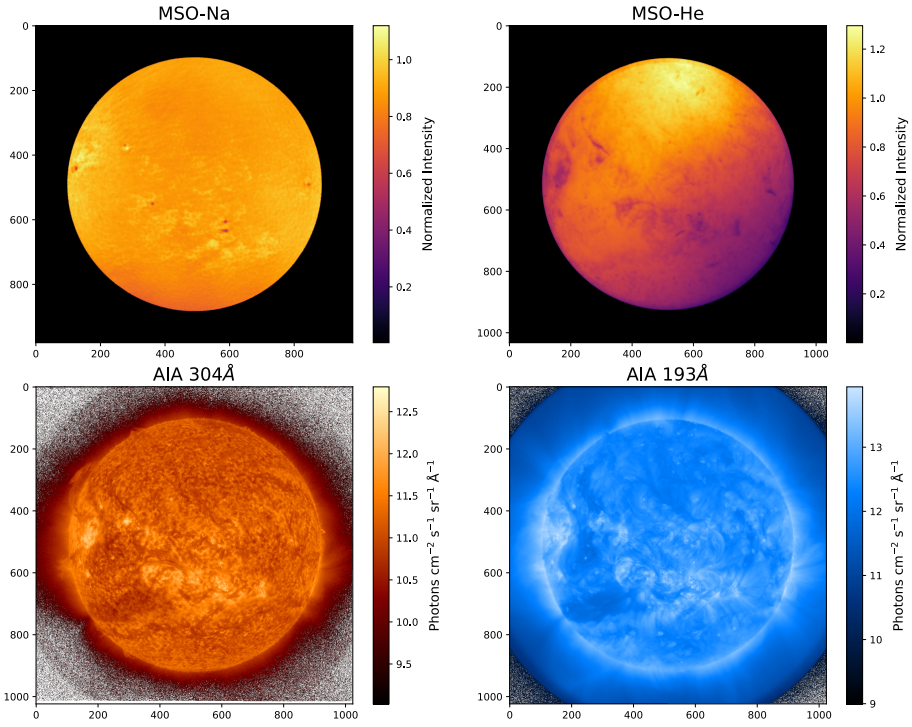

Figure 7.13 Normalized intensitygrams from MSO-Na and MSO-He channels on October 24, 2025 16:00 UTC compared to AIA 304Å and 193 Å at the same time.

of sight which allows for multiple features along the line of sight to be observed. Figure 7.14 shows a zoomed-in view of these intensitygrams (FoV $\approx 16' \times 16'$) containing NOAA AR 4257 and NOAA AR 4262 to highlight the difference between the observed features at different atmospheric heights.

Figure 7.14 highlights the bridge He I 1083 *nm* observations provide between the low chromosphere and transition region/corona. The dark filaments present in the MSO-He observations spatially correlate to the bright plage present in MSO-Na. Although the observation of these plage regions with just MSO-Na is a good indication of activity higher in the solar atmosphere, it provides no morphological information about the structures. MSO-He introduces this morphological information, mapping the extent of the filaments tied to the

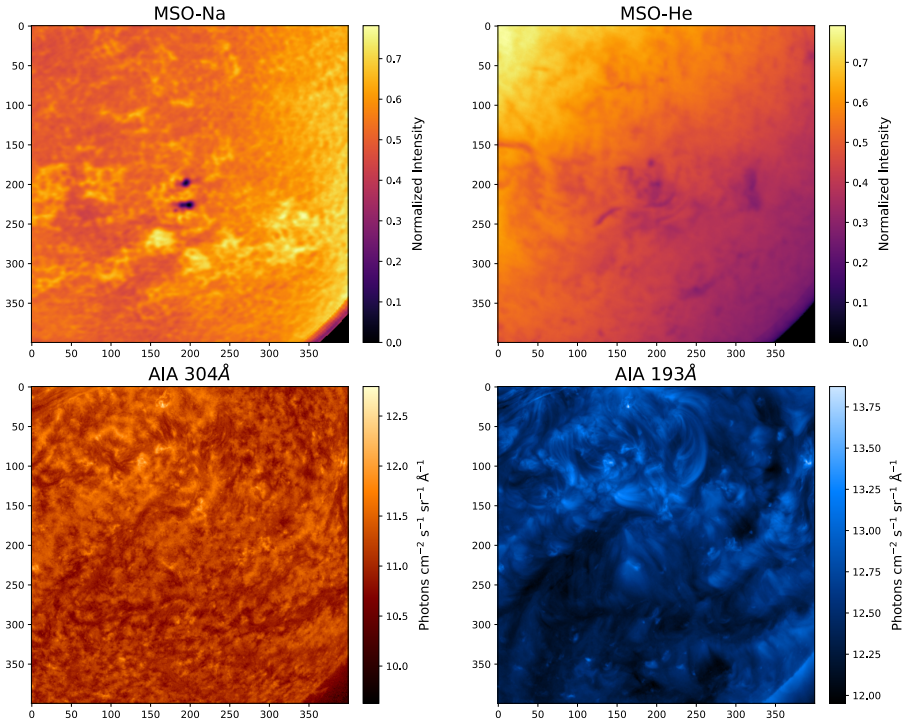

Figure 7.14 Zoomed in view of MSO-Na and MSO-He intensitygrams from Figure 7.13 highlighting NOAA AR4 4257 and NOAA AR 4262. FoV for both images is $\sim 16' \times 16'$.

coronal loops seen in the higher/hotter AIA images.

In addition to mapping filaments in the upper chromosphere, the He I 1083 nm line can be used as a coronal hole diagnostic because of its sensitivity to coronal EUV irradiance above the chromosphere. Since coronal holes emit less EUV, the He I 1083 nm absorption is weaker and consequently, coronal holes appear as brightenings in He I 1083 nm, which spatially correlate to the presence of open magnetic field lines. During the Phase 3 observing campaign, a sizable coronal hole was present in the Southern Hemisphere of the solar disk from October 22 to November 2, 2025, spatially constant with NOAA AR 4267. Figure 7.15 shows MSO-He intensitygrams compared to AIA 304 Å and AIA 193 Å intensity images from October 24, 2025 and October 29, 2025 in an attempt to identify this coronal hole.

Despite clearly identifying EUV brightenings (appearing dark in MSO-He intensitygrams), such as the active region on the eastern limb on October 24 or the coronal loop near disk center on October 29, the MSO-He data does not obviously identify any coronal holes. The intensity gradient across the disk, potentially caused by vignetting, is likely overwhelming any potential coronal hole detections, and is the next planned step in improving the MSO-He data. Despite this, the temporal evolution of filaments is clearly present in MSO-He intensitygrams and provides the GATES Network with a more extended view of the solar atmosphere.

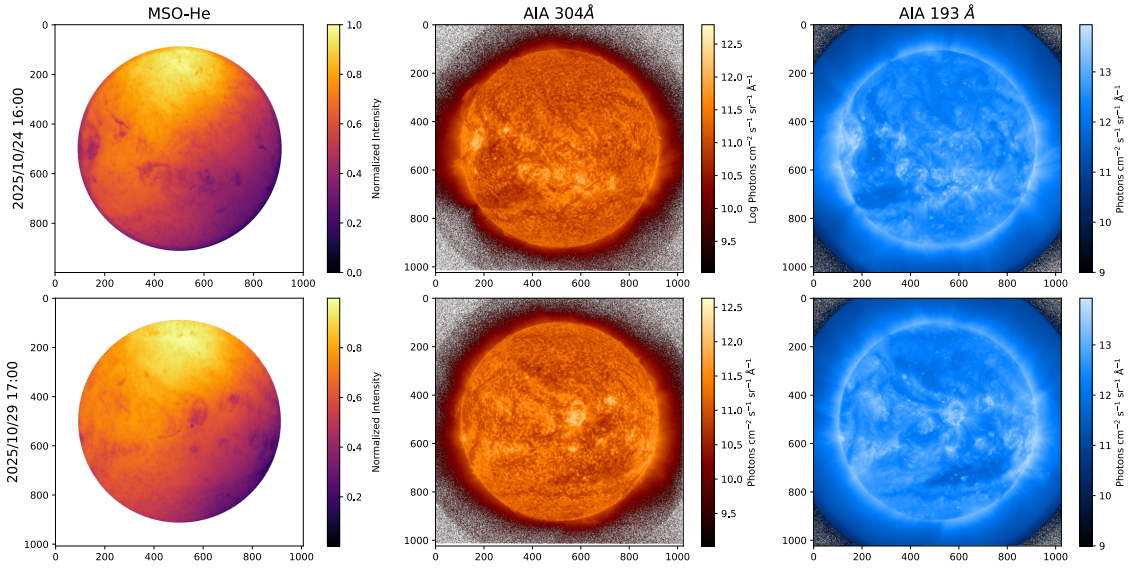

Figure 7.15 MSO-He intensitygrams compared to AIA 304Å and 193Å from October 24, 2025, and October 29, 2025. Although coronal hole-induced brightening is not visible in MSO-He, notable coronal structures present in the GOES images are identified by MSO-He.

CHAPTER 8
MOF PASSBAND MODELING

One of the critical steps in MOF application is the spectral calibration. This calibration is necessary for understanding the exact position of the passbands and, consequently, is needed for transforming data into physical units. In addition to measuring the instrument's spectral response, modeling the expected performance provides a basis for selecting cell temperature/RF power and magnetic field strength for certain cell setups. As part of my dissertation work, I have adapted an MOF-modeling code developed by S. Tomczyk for Na and K MOFs to model the He I 1083 nm MOF. This chapter details how the code works and the results from the He update.

8.1 *Hyperfine Structure and the Zeeman Effect*

The first necessary component of modeling the MOF passband functionality is to model the components of our lines of choice. For the alkali metals, this corresponds to hyperfine components associated with each transition. The Na I D2 line arises from the $3^2S_{1/2} \rightarrow 3^2P_{3/2}$ transitions and the K I 769.9 nm line arises from the $4^2S_{1/2} \rightarrow 4^2P_{1/2}$ transition; each of these transitions has additional hyperfine structure (Steck 2000; Tiecke 2019). The hyperfine interactions originate from the coupling of the nuclear spin I with the total electronic angular momentum $F = J+I$. When an external magnetic field is applied, each hyperfine component splits into $2F+I$ sublevels (Sargsyan et al. 2014). The energy shift, and consequently the wavelength shift, of these sublevels is correlated to the intensity of the magnetic field and can be straightforwardly computed by

$$E = \frac{hc}{\lambda} = am_J m_I + \mu_B(g_J m_J + g_I m_I)B \tag{8.1}$$

where a is the magnetic dipole hyperfine constant in units $ergs$, m_J is the magnetic quantum number of the electronic angular momentum, m_I is the magnetic quantum number of the nuclear spin, μ_B is the Bohr magneton in units erg/G, g_J is the electronic Landé g-factor, g_I is the nuclear g-factor, and B is the magnetic field in units G.

Figures 8.1 and 8.2 depict the hyperfine splitting of the K I and Na I D2 lines. The levels are grouped according to their angular momentum F in low-field regimes (anomalous Zeeman) and grouped by the magnetic quantum number M_J in the strong-field regime (Paschen-Back). For the case of GATES' MOFs, we are operating using a longitudinal magnetic field on the order of a few kG, so are mainly interested in the Incomplete Paschen-Back Splitting (IPBS) regime with the transitions in which $\Delta M_J = \pm 1$, which correspond to the $\sigma\pm$ Zeeman components. These transitions are caused by the interaction of the cell species with circularly polarized light.

The He I 1083 nm line is a triplet formed from the $2^3S_1 \rightarrow 2^3P$ transition. Although it does not have hyperfine components as the alkali metals, each triplet state has fine components arising from spin–orbit coupling that splits the upper term into $J = \{0, 1, 2\}$ fine-structure components. These components exhibit energy splitting in the presence of a magnetic field and, consequently, must be measured separately to determine the entire passband function. Figure 8.3 shows the fine splitting structure of the He I 1083 nm line considering IPBS; for a more thorough description of the He I triplet and its formation, see section 6.1.

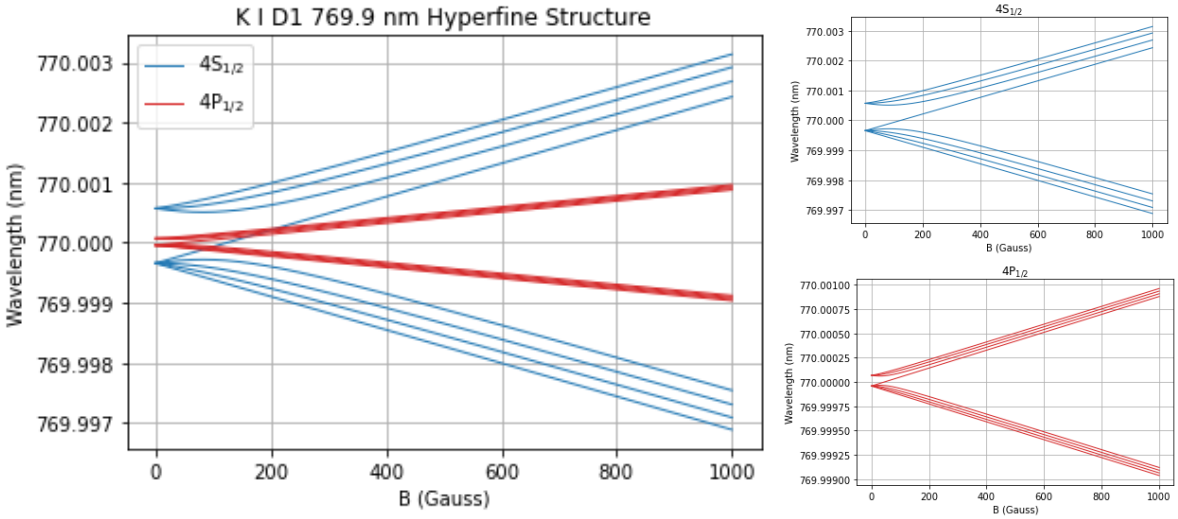

Figure 8.1 Right: Hyperfine splitting of the K I 769.9 nm line. Left: Zoom in plots of the $4S_{1/2}$ and $4P_{1/2}$ sublevels' splitting. Each of the K orbital levels split into 2 components giving 4 hyperfine components which split according to $\sigma^{\pm}$ states.

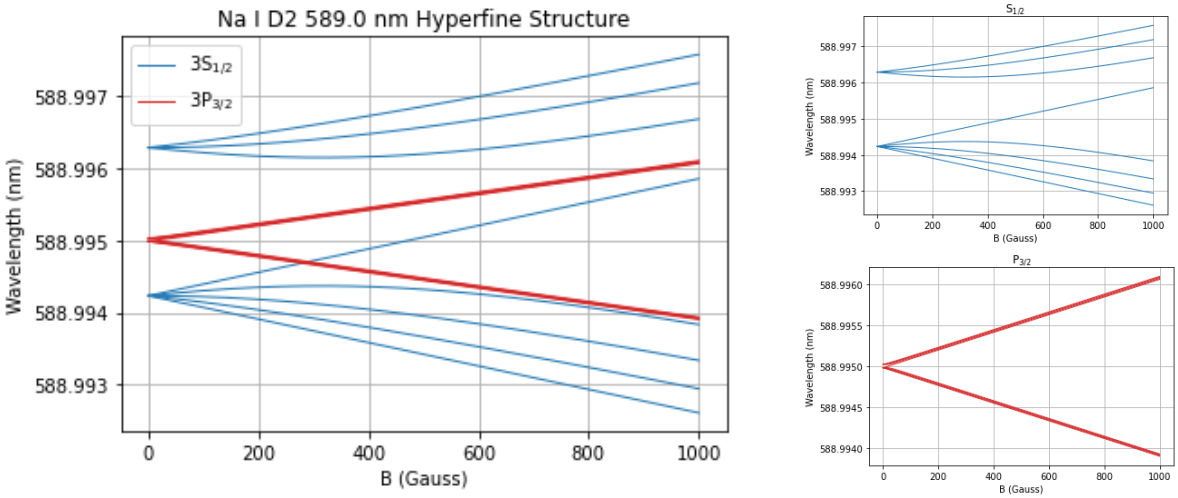

Figure 8.2 Right: Hyperfine splitting of the Na I D2 589.0 nm line. Left: Zoom in plots of the $3S_{1/2}$ and $3P_{3/2}$ sublevels' splitting. Just like the K hyperfine splitting, each component then splits according to $\sigma^{\pm}$ states.

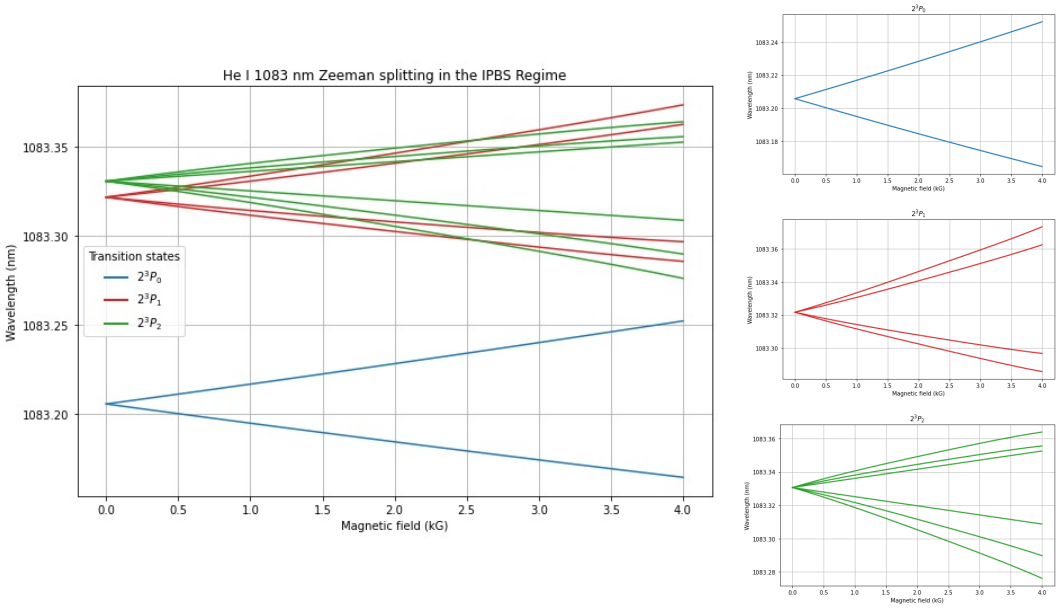

Figure 8.3 Fine splitting of the He triplet under consideration of IPBS.The symmetry of the fine splitting about the transition's rest wavelength arises from the $\sigma^{\pm}$ states.

8.2 *Modeling Inputs*

The original MOF model allowed selection of the Na D1, D2, or K D1 line when selecting the MOF and WS species. The updated version of the model I produced allows for all of these, as well as each of the He I triplet states. To properly model the He MOF, each triplet state's passband is calculated separately and linearly combined, with the wavelength shift set to its respective zero point. Once a species has been selected, there are two main inputs for the program: the magnetic field in Gauss at the center of the cell and the size of the beam in *cm*. The strength of the magnetic field determines the amount of Zeeman splitting that occurs in the spectral line. The size of the beam determines the vapor pressure within a reservoir cell, as the vapor density varies radially along the cell. The alkali metals additionally have the temperature of the gas in $^{\circ}C$ at the center of the cell (different than

the heating temperature of the cell), where the He model takes the number density of the metastable He at the center of the cell in g/cm^{-3} which was numerically selected based off of the optimum number density output of the K cells. The reference system was chosen to have the z axis along the length of the cell and have the origin at the center of the cell.

MOF and WS cells sit in the presence of a longitudinal magnetic field produced by permanent bar magnets. The longitudinal magnetic field is set by a value B_{max} which is reached in the center of the cell. The field distribution is then assumed to drop 10% over the length of the magnetic assembly central separation ($W \sim \pm 1.5\ cm$), and then drop to 0 outside of this range for the remainder of the length of the cell (L). This function is modeled below in Figure 8.4.

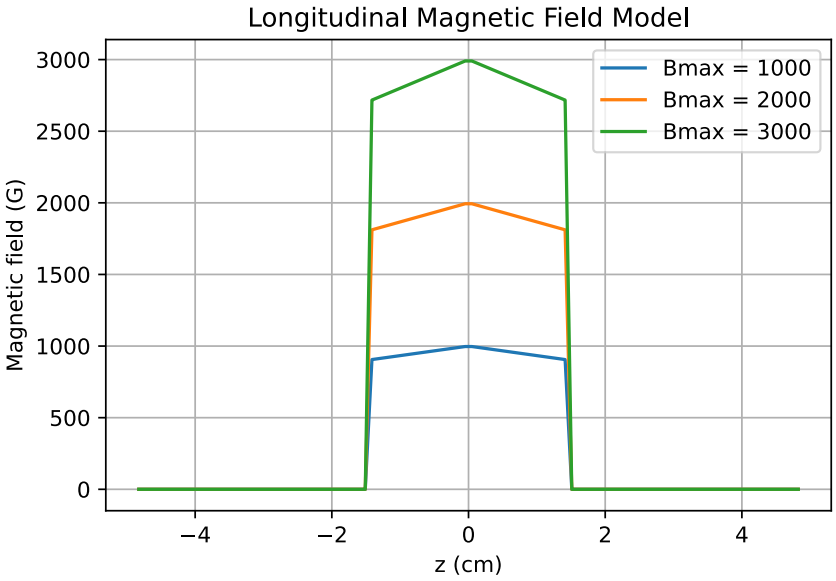

Figure 8.4 Model for the longitudinal magnetic field along the z axis within the MOF and WS cells. Field is modeled by at 10% from B_{max} along the central extent of the magnetic assembly's separation W, and is 0 otherwise.

For the alkali metals, the secondary input to the model is temperature. This is the vapor

temperature of the cell, rather than the external input temperature the cells are heated to, and it is used to calculate the maximum vapor pressure along the z-axis according to:

$$P(mmHg) = 10^{\left(a - \frac{0.5223 \cdot b}{T}\right)} \tag{8.2}$$

where b is the enthalpy of vaporization, a is an empirical constant, both obtained from (Lide 2004) and T is the temperature in Kelvin. This pressure is used to calculate the number density following:

$$N(\frac{ng}{cm^3}) = \frac{133.315 \cdot P}{k_B T \cdot 10^6} \cdot mu \cdot 10^{-3} \tag{8.3}$$

where k_B is the Boltzmann constant, m is the atomic mass in atomic mass units u. The density of the species is highly concentrated at the center of the cell (longitudinally) and is limited by the width of the reservoir/ring; it is therefore modeled as a box function with width W (the same acting extent of the longitudinal magnetic field). In a reservoir cell, radially along the cell, the density distribution is set by the mean free path of the species of choice, and is therefore larger on the edges of the cells (near the rings/reservoirs) than in the center. Currently, this distribution is modeled as a constant minus a Gaussian:

$$\text{dist}(r) = 2 - e^{\left(-\frac{1}{2}\left(\frac{r}{s_l}\right)^2\right)} \tag{8.4}$$

where r is the radial length along the cell, and s_l is the standard deviation of the Gaussian and is also set equal to 0.4. We do not currently have experimental data to constrain this

distribution, so this distribution was chosen to represent a purely theoretical cell. Ring cells are designed to produce a constant vapor density across the radial axis. As such, their radial density distributions are modeled as a constant across the acting length W of the cell. Figure 8.5 depicts the model distribution of density in the MOF cell along both the z and r axes.

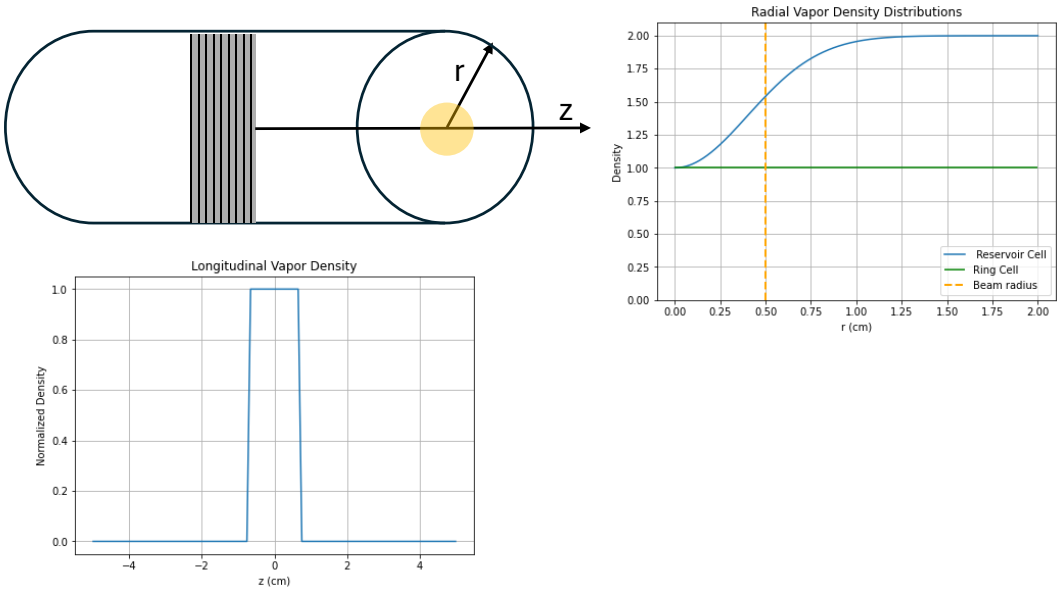

Figure 8.5 Diagram of a ring cell with the r and z axes shown. Radial (right) and longitudinal (bottom) vapor density distributions shown. Radial distributions for both the reservoir (blue) and ring (green) cells are shown with a line marking the beam radius.

To consider the variation of densities and magnetic fields along the z axis of the cells, the program divides the cell into a user-set equal number of partitions. At each of these parts, the program computes the absorption coefficient at line center (k_0), the optical thickness ($\tau^{\pm}$), and the phase shift ($\phi^{\pm}$) of the fine/hyperfine lines red- or blueshifted by the Zeeman effect, polarized with RHCP or LHCP. These are calculated at each part using the following equations:

$$k_0 = \frac{\sqrt{\pi}}{m_e c^2} e^2 f \rho(z) \frac{\lambda_0^2}{\Delta\lambda_d} \tag{8.5}$$

$$\frac{d\tau^{\pm}}{dz} = \frac{k_0}{2} \sum_i \frac{f_i^{\pm}}{f} H(a, y_i^{\pm}) \tag{8.6}$$

$$\frac{d\phi^{\pm}}{dz} = k_0 \sum_i \frac{f_i}{f} R(a, y_i^{\pm}) \tag{8.7}$$

where m_e is the mass of the electron, c is the speed of light, e is the charge of the electron, f is the oscillation frequency of the fine/hyperfine components (tabulated in the program) λ_0 is the central wavelength of the line, $\Delta\lambda_d$ is the Doppler width (defined in Equation 8.10), $H(a, v)$ is the Hjerting function, $R(a, v)$ is the Rachkovsky functions. The Hjerting function is another name for the Voigt function (a line profile which is a convolution of a Gaussian core and Lorentzian wings) and is calculated using equation 8.8 (Finn & Mugglestone 1965). The Rachkovsky function is the generalization of the Hjerting function to include the effects of a magnetic field (Zeeman splitting); in the model, the Rachkovsky function is numerically calculated using the tabulated values from Beckers (1969).

$$H(a, v) = \frac{a}{\pi} \int_{-\infty}^{+\infty} \frac{e^{-y^2}}{(v - y)^2 + a^2} \, dy \tag{8.8}$$

The inputs of the Hjerting and Rachkovsky functions, a (Equation 8.11) and v (Equation 8.12) are the ratio of the natural width (Equation 8.9) to the Doppler width (Equation 8.10)

and the line shift from its laboratory wavelength in Doppler units, respectively.

$$\Delta\lambda_\gamma = \frac{\gamma}{c}\lambda_0^2 \tag{8.9}$$

$$\Delta\lambda_d = \lambda_0\sqrt{\frac{2k_BT}{muc^2}} \tag{8.10}$$

$$a = \frac{\Delta\lambda_d}{4\pi\Delta\lambda_\gamma} \tag{8.11}$$

$$v_i = \frac{\lambda - \lambda_{0i}}{\Delta\lambda_d} \tag{8.12}$$

λ_{0i} is the unshifted wavelength of the fine/hyperfine component, and λ is the Zeeman splitting defined by the relation

$$\Delta\lambda = g_{eff}\frac{\lambda^2}{hc}\mu_B B = 4.668\times10^{-10}e_{eff}\lambda^2 B \tag{8.13}$$

where μ_B is the Bohr magneton, B is the magnetic field, and g_{eff} is the effective Landè g-factor for the considered transition (listed in the program as an input, computed from Equation 2.5). Once this model has been computed for each partition of the cell, the total transmission of the MOF/WS is calculated by the following:

$$T_{MOF}(\lambda) = \frac{1}{8}(e^{-\tau^+} - e^{-\tau^-})^2 + \frac{1}{2}e^{-(\tau^+ + \tau^-)}\sin^2\frac{\delta}{2} \tag{8.14}$$

$$T_{WS}^{\pm}(\lambda) = e^{-\tau^{\pm}} \tag{8.15}$$

where $\tau^{\pm}$ are the RHCP or LCHP optical depths calculated above and δ is the difference between the phase shifts of the RHCP and LHCP states. The output of the MOF transmission modeling is the transmission of the spectral line as a function of wavelength for the given selection of input temperatures (Figure 8.6). The WS model produces two outputs: the absorption as a function of wavelength for the red and blue passbands and the final transmission profile as a function of wavelength for the red and blue wings at varying input temperatures (Figure 8.7).

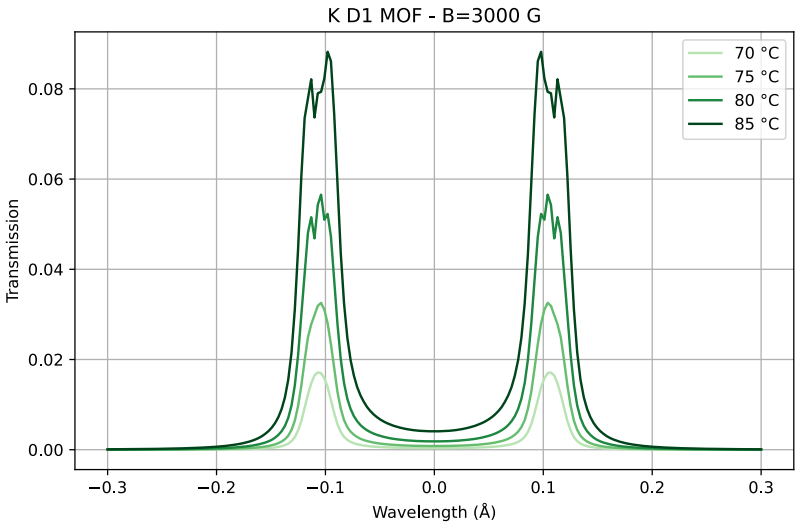

Figure 8.6 Model of MOF cell at multiple temperatures. Taking temperature steps of 0.1°C, a MOF vapor temperature of 75°C was chosen for its passband separation $\sim$ 0.1Å and overall transmission of $\sim$ 5%.

Figures 8.6 and 8.7 show example outputs for the MSO-K (ring cell) channel. To determine the optimal MOF transmission, transmissions at temperature steps of 0.1°C were

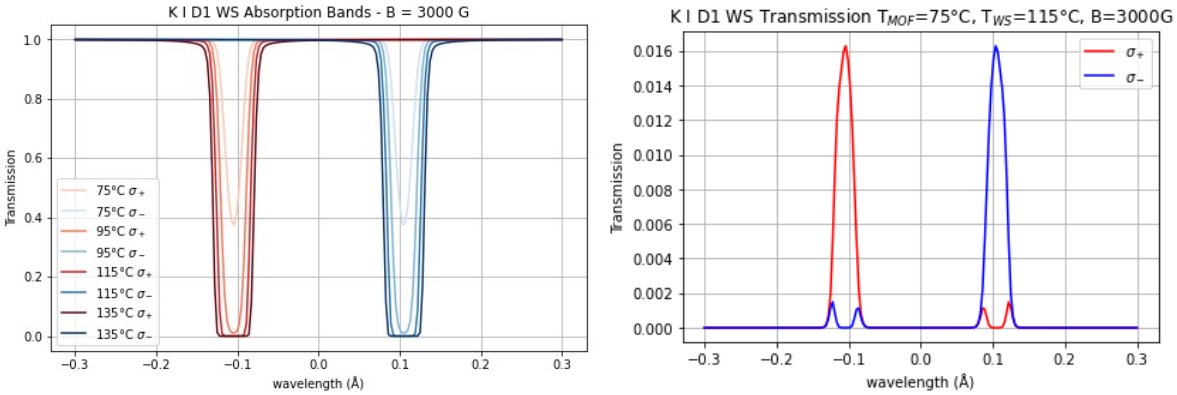

Figure 8.7 Left: example WS absorption bands at various temperatures. Right: transmission profile of a system running the MOF at 75°C and WS at 115°C. Optimal WS vapor temperature chosen by comparing passband crosstalk and absorption band saturation.

computed from 65°C to 95°C. The chosen vapor temperature of the MOF, 75°C, was selected due to its passband separation ~ 0.1 Å its overall transmission of $\sim 5\%$, and its minimal self-reversal in the individual wings (as becomes present in the model at higher temperatures, but isn't physically accurate). To determine the optimal WS transmission, a similar approach was conducted: transmissions at temperature steps of 1°C were computed from 75°C to 135°C. 115°C was selected because it has fully saturated absorption bands and low passband crosstalk (see Section 8.4).

8.3 *Helium Modeling*

Since the He cells are not heated to create a vapor, but are rather ionized through RF power, the inputs of the model are adjusted to reflect this. Rather than taking the temperature as an input, the He setting takes the number density (at the center of the cell) as its input. This number density is not the fill pressure of He's density in the cell, but rather is the density specifically of the metastable He I triplet. For preliminary models of the He cell,

we employed the output number density of the optimized K cell models as the preliminary input He density. The program uses the same theoretical model to calculate the MOF and WS transmission and absorption profiles over a list of density inputs.

As the He line is a triplet, to obtain the true transmission of the He cells, the transmissions of each triplet state must be calculated individually and then combined with the appropriate wavelength shift. Figure 8.8 shows the individual triplet states' MOF transmissions, their composite, and how they compare to an MOF transmission profile calculated without separating the triplet states (referred to as "combined setting"). Figure 8.9 shows the "combined setting" and individual transitions' composite MOF and WS transmissions at the selected optimal densities.

The He transmission model was run in the ring cell mode with both the MOF and WS magnetic fields $B_{max} = 3\ kG$ to match MSO-He. The number density of the He MOF cell was set by the output density of the K MOF cell ran at 75°C ($7.05 \times 10^{10}\ cm^{-3}$). The WS density was chosen by stepping through densities ranging from $10^{10}\ cm^{-3}$ to $10^{10}\ cm^{-18}$ using the combined setting; an optimum WS density of $2.29 \times 10^{17}\ cm^{-3}$ was chosen.

8.4 *"Crosstalk" Computation*

An additional upgrade made to the passband model is to compute the "crosstalk" between the red and blue wings through the WS. "Crosstalk" is used to define the quantity of the red wing's transmission overlapping the blue wing and vice versa, and is calculated by taking the ratio of the red wing transmission: blue wing transmission when $\lambda > 0$ (or the inverse

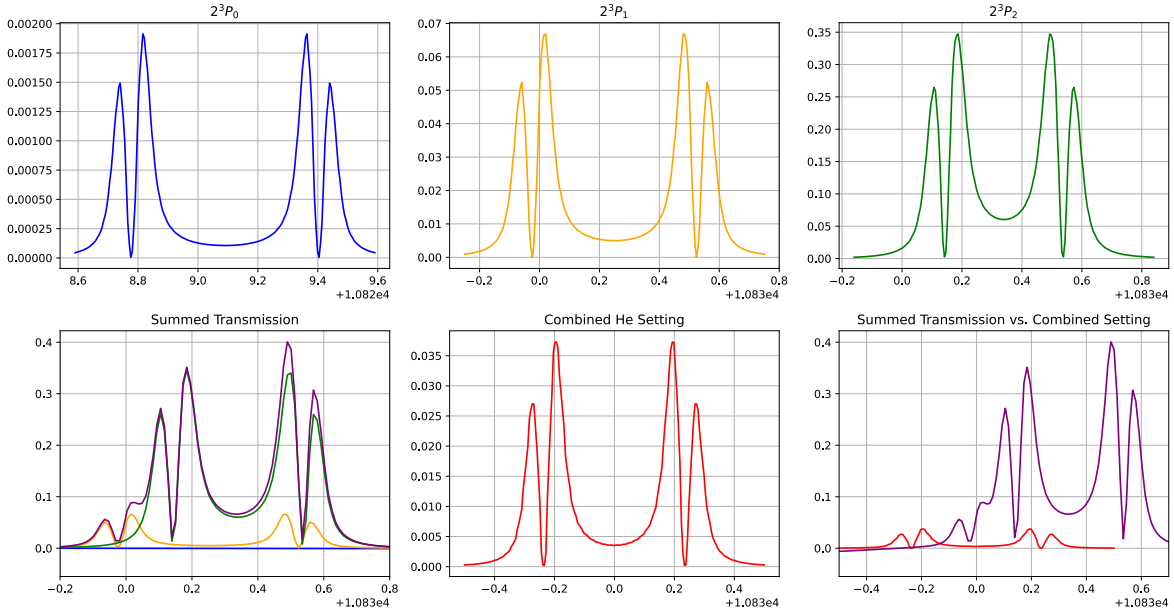

Figure 8.8 Top: individual He transitions' MOF passbands. Bottom: comparison between the individual transitions (same color code as top) and their sum (purple) compared to the combined He setting's passband. The combined setting produces a very similar shape to the summed passband, but at an order of magnitude lower transmission, and with a notable wavelength shift as it is centered on the rest wavelength of He I 1083 nm rather than the individual transitions' rest wavelengths.

when $\lambda < 0$). It is used to validate the optimal density of species in the cell. The acceptable amount of crosstalk varies for different MOF operating modes. Cacciani mode, operating with higher overall cell temperatures, produces twice the total transmission compared to Tomczyk mode. However, the lower magnetic field values for the WS in Cacciani mode result in higher crosstalk compared to Tomczky mode.

In a theoretical model, crosstalk will increase indefinitely with increasing cell density, because the WS absorption bands become more saturated. Therefore, we define the optimum level of crosstalk to be the inflection point of the crosstalk vs. number density function. In the model, the crosstalk is computed by taking the integral of the final WS's red-wing

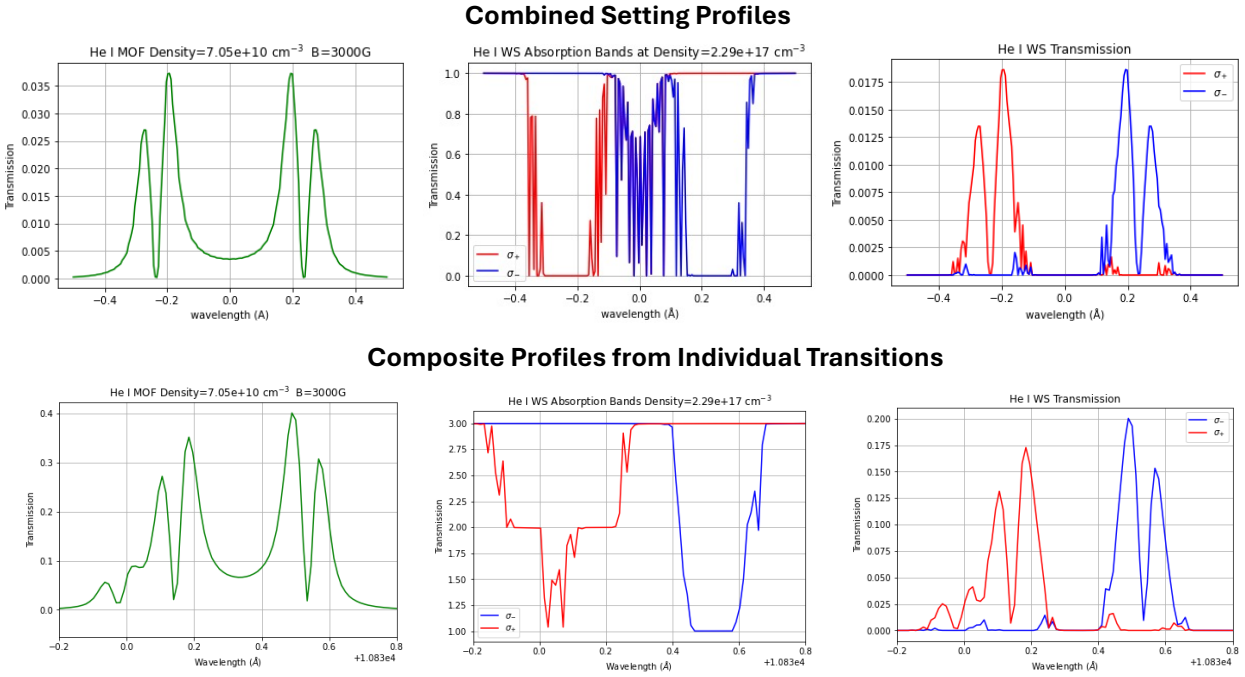

Figure 8.9 Combined He setting MOF transmission (left), WS absorption (center), and total transmission (right) for combined setting and composite triplet setting.

transmission for $\lambda > 0$ compared to the integral blue-wing transmission for $\lambda > 0$ (and the inverse for $\lambda < 0$). Figure 8.10 depicts the K and He crosstalks from the model runs in Figures 8.6 and 8.9, respectively.

8.5 *Discussion and Future Work*

The critical results from my development of the model are the He cell outputs. The results of the He model indicate that full MOF functionality – independent red and blue transmission profiles through the WS – is possible at MSO-He's current operational longitudinal magnetic field. However, for optimum MOF functionality, the WS must have a critical population of metastable He notably higher than that of the MOF. Currently, the He MOF and WS cells

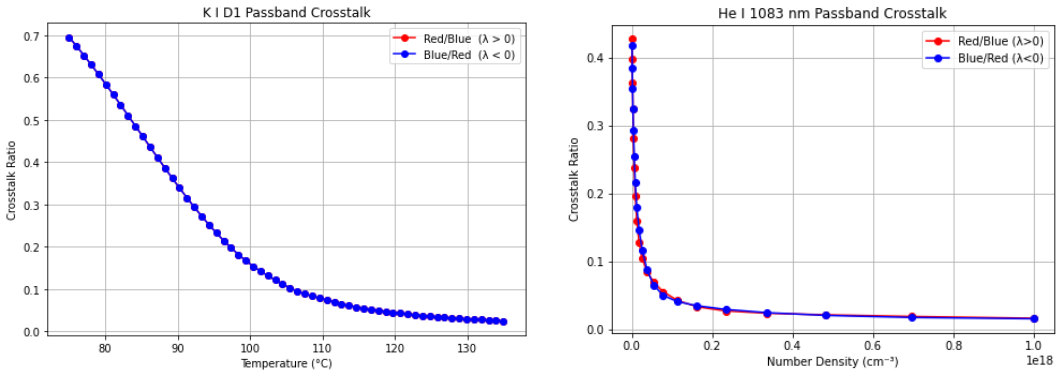

Figure 8.10 Crosstalk plots for K (left) and He (right) for WS temperatures/number densities. K WS temperatures were spaced linearly and He WS number densities were spaced logarithmically. The optimum WS temperature/number density is chosen near the inflection point the the crosstalk plot to minimize the passband crosstalk without over-saturating. The K plot appears to only have the blue ratio because the two ratios exactly overlap.

are back-filled with the same neutral He pressure (0.90 *torr*) and employ the same magnetic field strength (3 *kG*). Consequently, to adjust the density of metastable He in the WS, it is possible, and necessary, to use methods other than varying the fill pressure – such as varying the RF power, increasing the cell length, adding alkali metals to the cell, or laser pumping (as explained in Ch. 6). The results from the He modeling motivate the immediate next steps of the He MOF development to focus on the operational parameters of the WS cell. See Section 9.2.1 for further details.

Although useful for informing the development of the He MOF, the passband model is still limited in its ability to properly depict the real operation of the GATES' MOF cells. Firstly, the radial and longitudinal density distributions are empirically derived and assume a constant beam radius along the entire length of the cell. To improve accuracy, an experimental measurement of the density distributions in both ring cells and reservoir cells must be performed. One method to achieve this is to illuminate the cells with a wavelength-

relevant laser at varying radial positions, measure the output intensity, and calculate the vapor density as defined by the Beer-Lambert Law, $I = I_0 e^{-\sigma n l}$, where I_0 is the initial intensity of the laser, σ is the absorption cross section of the vapor, n is the vapor's number density, and l is the path length.

In addition to experimentally verifying the vapor density distribution within the cells, making the model more physically accurate requires a more proper solar beam radius. Although the constant beam radius is a sufficiently accurate assumption for the TSST-K given that both the MOF and WS cells are traversed by a collimated beam, the MSO optical design does not place the MOF and WS cells in collimated space, and therefore, if the vapor density is experimentally measured to be anything other than the theoretical constant value for ring cells, the varying beam size needs to be considered. Furthermore, the model's radial density distribution is set by a single value calculated at the radial extent, R of the light beam; a more realistic model requires computing the radial density in expanding rings over the range $0 \rightarrow R$.

Secondly, we plan to update the model inputs such that the model takes the cells' heating temperature (for Na and K) or RF power (for He) and computes the central vapor temperature or gas density, respectively. This will make the model more physical and make it more applicable to our experimental spectral calibrations. Finally, we aim to expand the suite of species the program supports to assist GATES' planned expansion into additional observational wavelengths, such as Ca (see Section 9.3).

CHAPTER 9
FUTURE WORK

9.1 *Future of TSST*

The Summer 2025 GATES observing campaign showed that the TSST is capable of producing full-disk Dopplergrams with sufficient spatial and temporal resolution to detect supergranulation patterns and p-mode oscillation frequencies (Section 7.2). Additionally, the TSST's full-disk magnetograms provide enough resolution to conduct active region PIL analysis (Section 7.1). Despite these notable results, the overall operation of the TSST channels require additional testing to ensure optimum image quality prior to final commissioning. The next stage of TSST development will emphasize performance optimization, operational automation, readying the system for deployment at the ORM, and completing its integration into the SWERTO Service. To achieve these goals, we plan several key developments:

- Perform brief TSST-K observations directly from an equatorial mount to determine the instrument's true image quality, independent of any aberrations introduced by the heliostat.
- Upgrade the MOF and WS cells with higher optical quality windows to minimize interference fringes. Potentially introduce wedged or anti-reflectance-coated windows to further prevent interference fringes.
- Improve the precision and stability of the optical alignment to ensure long-term, repeatable, diffraction-limited image quality.

- Conduct a new, comprehensive polarization and spectral characterization of the TSST-K to re-establish the aligned rotational position of the polarizers, HWPs, and QWPs.
- Execute thermal modeling and testing of the telescope box to ensure thermal and imaging stability under observing conditions; improve thermal maintenance techniques if necessary.
- Integrate robotic arm for covers and flat field filters on both the TSST-Hα and TSST-K.
- Improve the TSST-Hα image quality through the installation of a larger camera sensor or a focal reducer to ensure full-disk imaging without introducing focal distortions.
- Complete the acquisition algorithm, including camera and optomechanical component control for both TSST channels, integrating data updates to SWERTO, and ensuring proper fail-safes implementation for emergency shutdown.
- Employ the flare detection and notification algorithm.
- Test the full TSST on an equatorial mount at the University of L'Aquila to simulate observational conditions at the final site at the ORM and access the acquisition algorithm.

These steps will determine if our imaging aberrations and observational limitations, such as the elliptical fringing and filtergram switching time, can be resolved using the current optical scheme. Should these steps prove insufficient for data quality improvement, we consider the possibility to adjust the optomechanical scheme to implement an LCVR in place of HWP1 and a polarizing beamsplitter after the WS. This change will simplify the operation of the TSST-K and reduce the operational time to switch between filtergram states,

thus greatly improving our temporal resolution and observational fill factor. Additionally, this adjustment streamlines the GATES nodes' MOF channel designs, making the TSST-K and MSO channels more operationally comparable.

In tandem with these developments, ADS is working to complete the TSST dome and mount so that all telescope components will be ready for deployment by 2028. Once fully deployed to ORM, the TSST will constitute the first permanent node of the GATES Network and will be integral to establishing the network's communal automation. Furthermore, the TSST will constitute a valuable node in the next generation of ground-based solar monitoring networks.

9.2 *Future of MSO*

The next phase of MSO will focus on instrument automation, expansion, and possible relocation. The team at MSO is working to form a collaboration with larger California observatories to mount the MSO telescope. We plan to integrate the current MSO telescope (MSO-K and MSO-Na) into a commercially available dome, similar to the one being realized for the TSST, so that the MSO node can be fully automated, and the control software will be standardized across GATES. Furthermore, the relocation of the MSO telescope would allow for the Mojave Solar Observatory itself to be used as a test bed for new MOF developments such as the He and Ca MOFs. Prior to this stage,at MSO we plan the following advancements:

- Digitize the control of all telescope components.

- Conduct a new, comprehensive polarization and spectral characterization of MSO-K and MSO-Na to re-establish the optimum rotational alignment of the polarizers, HWPs, and QWPs to ensure the maximum precision of polarization alignment (see Appx. C.3).
- Execute thermal modeling and testing of the telescope box to ensure thermal and imaging stability under observing conditions; improve thermal maintenance techniques if necessary.
- Integrate the Python data acquisition algorithm to improve SNR and simplify computational resources.
- Automate the full telescope control and data acquisition to allow for integration into a fully automated GATES Network and SWERTO service.
- Produce optics and mechanics for a full He-specific channel to perform further He MOF tests, leveraging the results of the He MOF modeling to achieve better Doppler and magnetic signal.
- Conduct temporal stability analyses on the photometric response, thermal drift, and pointing precision of the telescope.

The current telescope control at MSO (Appendix D) can run automatically throughout the day; however, the start-up and calibration procedure currently relies on manual adjustments. Currently, the dome, telescope mount, cameras, and HWPs can be controlled digitally/remotely and therefore automated. However, the camera positioning, mounted on a digitized mount, currently uses an analog control switch, and the MOF and WS tempera-

tures, controlled by a PTC10 unit, are also not accessible remotely. Moreover, the filters used for calibration image acquisition (flat-field and dark) must be changed manually. Therefore, the first improvement planned at MSO is the digital integration of all of the adjustable telescope components. We plan to integrate robotic arms for the flat field filter and dark shield, similar to the one proposed for the TSST.

Although currently a capable tool for acoustic wave observations, the expansion of MSO's automatic capabilities will help establish the synoptic coverage that GATES proposes allowing MSO to more readily contribute to continuous space weather studies. Moreover, the multi-height observational capabilities position MSO to make significant contributions to the field of helioseismology while, like the TSST, constituting a valuable node in the next generation of ground-based solar monitoring networks.

9.2.1 *Future of MSO-He*

Motivated by the results of the He MOF passband modeling (Section 8.3), the next steps for improving the He MOF functionality focus on changing the operating parameters of the He WS to increase the population of metastable He. To achieve this, at MSO we plan the following steps:

- Produce more precise cell-window baffles to minimize the amount of cell "glow" that is transmitted through the beam-path contaminating the true signal.
- Conduct RF-capacitor tuning tests including Doppler- and magnetogram observations to determine optimum passband separation rather than peak total transmission.

- Model and experimentally confirm the optimum magnetic field to operate the WS at.
- Test varying cell lengths to minimize the loss function of the metastable He and increase their population.
- Conduct further laser pumping tests to enhance the metastable population.

While we continue the development of the He MOF technology, MSO maintains the ability to produce full-disk He 1083 nm intensitygrams. These intensity observations provide valuable insight into chromospheric dynamics and coronal hole and magnetic structure mapping (see Section 7.3), and in conjunction with MSO-Na, can provide information on spatial variations throughout the chromosphere. Thanks to the modular design of the MSO telescope, while we work to expand its infrastructure to house all three channels (K, Na, and He), it is possible to switch the MSO-K for the MSO-He between observing days. Consequently, we plan to continue conducting dual-height MSO-Na and MSO-He observations allowing MSO-He to contribute valuable scientific observations even while its full MOF capabilities are being improved.

9.3 *Future of GATES*

The expansion of the GATES Network focuses on three avenues: becoming fully automatic, increasing the heights in the atmosphere we can observe, and expanding our synoptic coverage. As described in Section 9.1, I am working with the TSST team to fully automate the operation of the TSST instruments and dome (through the collaboration of ADS International). This is a key step forward for GATES, as it will allow the expansion of future nodes

without requiring as much manpower. Once tested with the TSST, the automatic control algorithm will be implemented at MSO and all future GATES nodes.

The secondary goal of the GATES Network is to expand our tomographical coverage in the solar atmosphere. As described in Section 9.2, at MSO, we are working to improve the He MOF operation so that it can be integrated into a fully operational GATES node. As described in Section 9.2.1, motivated by results of the Phase 3 observing campaign and the He passband modeling, the team at MSO is working to improve the He MOF operation so that it can be integrated into a fully operational GATES channel. Furthermore, the GATES collaboration plans to continue the development of the Ca MOF that was started by the MOTH team in the early 2000s. As a magnetically sensitive, strong absorption in the solar chromosphere, the addition of Ca to the GATES MOF suite adds an additional height of Doppler- and magnetogram observations. The inclusion of Ca and He in GATES' suite of MOF channels will greatly expand our observational capabilities and provide a more complete tomographic map of the solar atmosphere, allowing for more precisely mapping physical heights such at the $\beta \sim 1$ layer (Section 1.4). Moreover, the successful development of the He MOF unlocks the potential to move beyond alkali-metal-based MOFs and investigate other gaseous elements like hydrogen.

The third goal for GATES' expansion is to increase our synoptic coverage through the addition of new collaborations/telescope nodes. GATES has multiple proposed collaborations currently underway. These collaborations include the University College of the Cayman Islands (UCCI) and Samarkand State University (SSU). All of the proposed nodes are planned

to initially include an $H\alpha$ channel with future expansions of MOF channels and have been chosen strategically to strengthen GATES' synoptic capabilities. Figure 9.1 depicts the future observational coverage of the GATES Network once the first phase (Hα telescope installation) of the new collaborations is complete.

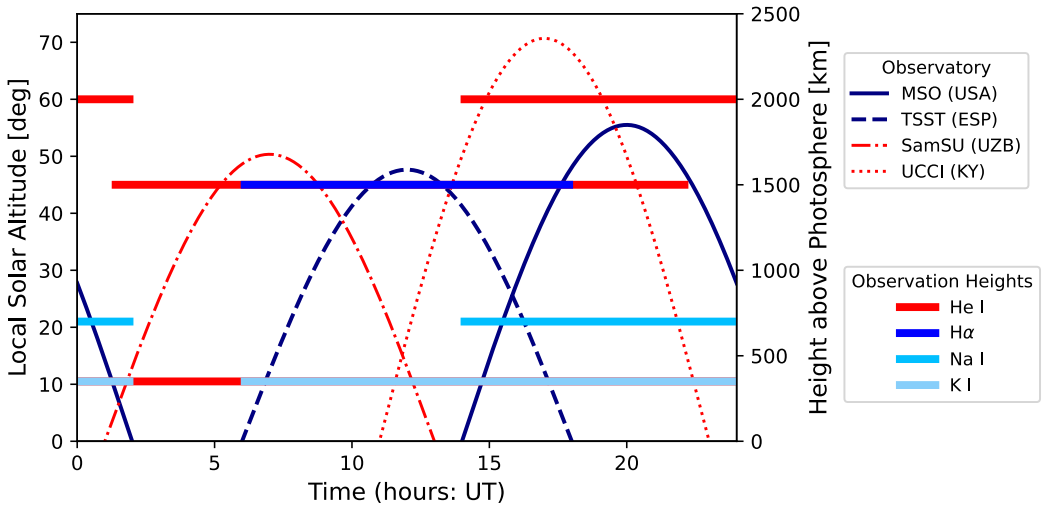

Figure 9.1 Observational coverage of the GATES Network, considering its expansions with UCCI, and SSU. Blue lines represent the current observational times/atmospheric heights of the GATES Network (on the equinox). Red lines indicate the potential node and telescope expansions.

We submitted a proposal of partnership in October 2025 to bring a GATES node to the UCCI in Georgetown, Grand Cayman. The proposed GATES node at UCCI will contain an Hα telescope and a single MOF channel, which can later be upgraded to a dual-channel system. UCCI already possesses $H\alpha$ instrumentation and has expertise in its operation. This makes UCCI an ideal new node for the GATES Network, given its ability to introduce immediate, high-quality observations for the GATES Network and work alongside TSST-Hα to conduct real-time flare detection and forecasting with extended temporal coverage.

UCCI resides at an optimal longitude (UTC - 5) for the GATES Network; UCCI sits in the middle of the TSST and MSO coverages. Its positioning notably strengthens GATES' current temporal coverage by reducing gaps in solar observations and minimizing the need for any single node for true synoptic coverage, thereby enabling more complete studies of solar phenomena as they evolve.

In addition to the UCCI proposal, the GATES collaboration has also prepared a proposal for a joint program between UTOV and SSU. Under the budgetary constraints of the program to which this proposal was submitted, the proposed GATES node at SSU will include an Hα node of the GATES Network. Once the Hα node has been fully implemented into GATES and the collaboration with SSU has been established, we plan to expand the SSU site to include one or more MOF channels. SSU occupies an advantageous longitude (UTC + 5) to expand GATES' temporal coverage and will set a precedent for expanding GATES' nodes to locations in middle Asia.

9.3.1 *GATES Data Storage and Accessibility*

With the planned synoptic coverage of the GATES Network, one of the largest issues we will run into is data storage and accessibility. Currently, all GATES data is stored on hard drives at the primary administrative sites: MSO and UTOV. Both sites host a full backup of both nodes' data and are accessible to the GATES Network via remote access. Although this method has proved sufficient for showing a proof-of-concept of the network, a long-term solution for data storage and accessibility must be created.

Assuming a consistency in data acquisition (despite the different operating modes, both

the TSST and MSO produce a single 16-bit $\sim$ 2000 x 2000 pixel image every 5 s; TSST produces one filtergram and MSO produces four filtergrams saved to the same array), each GATES channel (ex. MSO-K) will produce $\sim$0.12 TB of raw data per ten-hour observing day (assuming an average of eight hours of observation, two hours of calibrations, and a 15% overhead). Moreover, over the course of the night while the data are calibrated, these quantities double. Although acquiring data at this cadence is advantageous for high-frequency studies and wave investigations, it is clear that storing all GATES data at this cadence indefinitely will become unfeasible given our current infrastructure.

Given GATES' current data storage capabilities, we can manage $\sim$ 1 year of continuous observations from all four tested channels (TSST-Hα, TSST-K, MSO-K, MSO-Na), assuming an average ten-hour observing day with 15% overhead. This does not account for data compression or non-observation days due to weather, infrastructure, etc. Consequently, our effective storage capacity is over a year's worth of data once the current GATES nodes are fully operational. We project this to be a sufficient period of time to be able to expand GATES' storage capabilities.

9.4 *Further Scientific Questions*

Although the main science driver for the development of the GATES Network is space weather monitoring and prediction, the unique dataset the network produces can be applied to many different solar studies. Multi-height Dopplergrams can be used for acoustic wave propagation studies. These studies can provide insights into phenomena such as flare

precursor events (Aparna 2022) and coronal heating (Arregui 2015). Moreover, GATES magnetograms and Hα intensity images will provide valuable datasets for future flare forecasting studies, whether that be through R^* and D parameter analysis (Cicogna et al. 2021), Hα intensity gradient studies (Henney et al. 2011), or general ML/AI training sets (Goodwin et al. 2024).

As I exhibited in Section 7.2.1, the GATES data I acquired at MSO during Phase 2 of the 2025 observing campaign have proven sufficient for contributing to atmospheric seismology studies through the detection of acoustic p-modes phase-travel times between two solar atmospheric heights. With this data quality confirmed, I am imminently investigating the phase travel time of acoustic waves in flaring and non-flaring regions between the MSO-K and MSO-Na observations. Moreover, Figure 7.12 shows the ability to use the MSO-Na RHCP and LHCP Dopplergrams as two independent channels to probe two heights in the atmosphere. Consequently, by shifting the MOF and WS passband locations (through varying the cell temperature/magnetic field), it is possible to scan through the Na I D2 line. This result motivates the development of a new Na MOF-based instrument to sample multiple points in the solar Na I D2 line, thereby observationally mapping the contribution function of the Na I D2 line in the solar atmosphere.

Perhaps the most unique advancement GATES' data is poised to make is the inclusion of upper-chromospheric Doppler- and magnetogram measurements through the introduction of the He-MOF. This filter will enable a more extensive local helioseismic study of the chromosphere, providing better mapping of the $\beta \sim 1$ layer (Rosenthal et al. 2002), greater

insight into the coronal heating problem (Klimchuk 2006), and potential to address the problem of height dependence of magnetic fields in sunspots (Balthasar 2018). Moreover, He I 1083 nm observations will greatly contribute to the study of reconnection events like EBs (Libbrecht et al. 2021b) and coronal hole studies (Caplan et al. 2023).

In addition to its broader scientific impact, GATES data will be incorporated into several forthcoming studies conducted by the GATES teams at GSU and UTOV, in collaboration with the Radiation in Earth, Sun, and Space Surroundings (RES3) and Remote Sensing for Space Sciences (RSSS) Laboratories, with integration anticipated in the near future. Chaturmutha et al. (2024) presents a study on wave reflection in the lower solar chromosphere utilizing MOTH Dopplergrams; they are ready to expand their model with the inclusion of a longer, more magnetically active dataset such as GATES'. Additionally, Goodwin et al. (2024) is looking to expand their ML model of real-time solar flare prediction by including GATES magnetograms in their training and testing sets. Hamilton et al. (2024) uses simulations and radiative transfer to develop diagnostics of propagating acoustic waves; they look forward to using GATES data to validate their model. Finally, the updated SWERTO Service at UTOV looks to include all GATES data into their space weather monitoring service, thus making it accessible to the general public.

CHAPTER 10
CONCLUSION

In this dissertation work, I have introduced the GATES Network: a ground-based network of MOF-based telescopes designed for space weather studies. GATES currently consists of two telescope nodes, TSST and MSO, and has multiple active expansions in development. Each node has been designed using commercially available parts and to operate as a completely automatic facility enabling efficient and cost-effective network expansion. The scientific goal of the GATES Network is to provide high-cadence, synoptic observations of intensity, LoS magnetic field, and Doppler velocity, enabling detailed studies in solar magnetic fields and evolution, investigating acoustic wave propagation throughout the solar atmosphere, and providing real-time space weather monitoring and forecasting.

In the first part of this work (Chapters 1 and 2), I introduced the scientific background, observational motivations, and historical attempts behind synoptic solar and space weather observations. I presented a description of space weather and current prediction capabilities to provide context for the necessity of full-disk Doppler- and magnetograms that the GATES Network provides. Additionally, I provide an overview of the theoretical principles, operational features, and past observations with MOFs to underline the unique developments MOF-based instruments can make to the field.

In the second part of this work (Chapters 3, 4, and 5), I introduced each of the GATES nodes (TSST and MSO) and the network as a whole. The TSST is a dual-channel telescope that acquires full-disk K Doppler- and magnetograms and Hα images of the Sun. MSO

is a dual MOF channel telescope that acquires full-disk K and Na Doppler- and magnetogram. Moreover, through the development of a new He MOF, MSO can operate as a fully chromospheric observatory, acquiring full-disk Na Doppler- and magnetograms and full disk He intensity- and magnetograms. My work with these nodes focused on optomechanical improvement and alignment, conducting observing campaigns, and performing preliminary data reduction/analysis. These chapters concentrated on the design of the telescopes, the organization of the GATES Network, the data reduction pipeline, and our Summer 2025 observing campaign.

In the third part of this work (Chapters 6 and 7), I present some of the novel developments of the GATES Network and its data. Chapter 6 details the various attempts during this PhD to develop a He I MOF. My work with the He I MOF consisted of lab-testing a new He I D3 MOF, and sky-testing a He I 1083 nm MOF, expanding its observational capabilities to include Doppler velocity and magnetic field measurements. Installing the He I 1083 nm MOF at MSO, I was able, for the first time, to acquire full-disk He I magnetograms using an MOF. Notable interference patterns currently limit the quality of these data, but nonetheless provide a valuable step forward in expanding the suite of operational of MOFs. Chapter 7 presents comparisons of GATES data to other instruments such as GONG, HMI, and AIA. Additionally, I present examples of magnetic field/ Doppler velocity field gradients and power spectrum analyses from the MSO-Na and MSO-K channels. The MSO channels data can able to produce cross power and phase spectra exhibiting characteristic p-mode oscillation ridges, indicating its ability to effectively contribute to solar atmospheric seismology studies.

Moreover, investigating the phase cross spectrum of the MSO-Na RW and BW Dopplergrams reveals a slight phase difference between the two wings, thus showing the two Na wings can be used as independent channels to probe different heights.

In the fourth part of this work (Chapter 8), I described the modeling side of my project, which complements the technical development of the GATES' MOF instrumentation. The model computes the passbands produced by the MOF and WS of various MOF species. My work with this model (originally developed by S. Tomczyk) focused on translating it from IDL/Matlab into Python, realizing a more physical description of our MOF cells, and expanding its capabilities to include He I 1083 nm. The He results from this model indicate that the optimum pressure to operate the He MOF cells at differs from MSO's current status. This model result provides the immediate next steps for further development of the He MOF. Moreover, this model can be used for all MOF species active in the GATES Network to predict and validate spectral characterizations.

Finally, in Chapter 9, I detailed the future plans for the GATES Network and its data. TSST is in the final stages of instrument alignment (with both channels) and dome realization with the collaboration of ADS International. With the TSST, we are investigating the possibility of implementing a more streamlined optical scheme utilizing LCVRs rather than mechanically rotating HWPs to simplify the TSST-K operation and allow for increased temporal resolution. Moreover, we are working to realize our automatic operation procedure into a functional, open-source algorithm before employing it at MSO as well. MSO maintains data-taking capabilities, currently reverting to its original K-Na design. At MSO, we are

working to progress the capabilities of the He MOF further and fully integrate it into the MSO telescope without sacrificing the MSO-K channel. In addition to the planned improvements to both active GATES nodes, multiple new collaborations are under development to expand the network's observational capabilities. Furthermore, I report some of the primary science goals of the GATES Network and how GATES data will be integrated into current studies – most notably, flare prediction (Goodwin et al. 2024) and acoustic/gravity wave modeling (Chaturmutha et al. 2024; Hamilton et al. 2024) studies being conducted by the RSSS and RES3 groups at GSU who are imminently planning to introduce GATES data into their studies.

The GATES data demonstrate the powerful impact that compact MOF-based instruments can have on flare and other space weather studies. With a spatial resolution comparable to other ground-based space weather networks, such as the GONG Project, and increased temporal resolution, the GATES Network will contribute a rich dataset which can be implemented into flare forecasting techniques. Additionally, the multi-height dataset acquired by MSO has been shown to be capable of detecting phase differences of acoustic waves at varying heights in the solar atmosphere, thus exhibiting MSO's capability to contribute to solar atmospheric seismology studies. Furthermore, the successful dual-site observing campaign and cross-site calibration of the two GATES nodes provide proof-of-concept for the GATES Network's observing capabilities. The procedures and instrumental resources developed during this work, including passband modeling, data acquisition, calibration, and reduction, provide a robust framework for the future development and expansion of the GATES Net-

work. Ultimately, the progress presented in this work provides a stable foundation for the GATES Network and establishes its significant capacity to contribute novel synoptic, space weather studies.

Appendices

A Full Parts list of the TSST-K

The TSST was designed as a low-cost, easily reproducible telescope. As such, it utilizes commercially available parts as much as possible. The majority of the TSST-K's optomechanical components come from Thorlabs. The filters come from Edmund optics and Andover, and the camera used is from Basler (see Appx. B). TSST-K houses a few custom-made parts that were designed and produced with the collaboration of the Mechanical Workshop at UTOV.

A Optical Elements

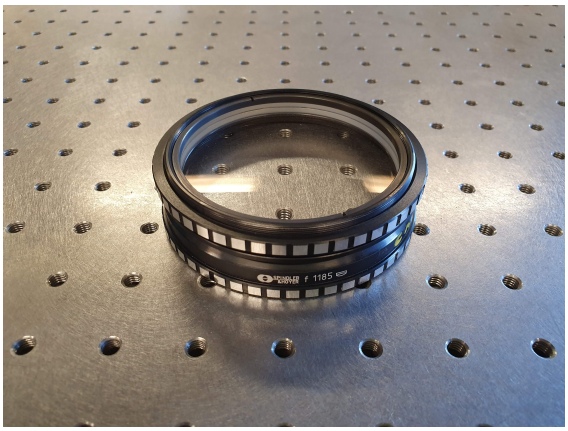

Figure 1 *L1*: *Spindler & Hoyer* doublet in its mount.

Table 1 L1 optical specifications.

Focal Length	1185 mm
Diameter	80 mm
Thickness	11.8 mm
Transmission	95%
Glass	SSK4A and SF8
Optical Quality	$\lambda/4$

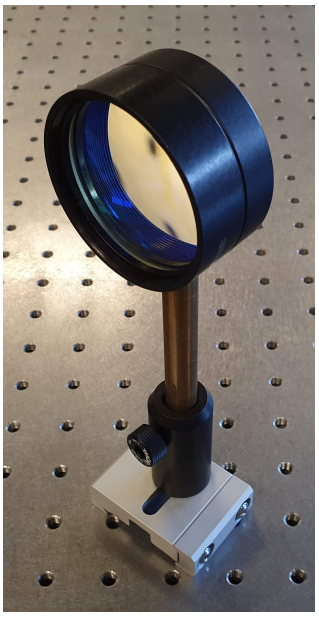

Figure 2 *L2, L3, L4, L5*: Thorlabs AC508-200-B-ML Achromatic Doublets.

Table 2 Thorlabs AC508-200-B-ML[a] optical specifications.

Focal Length	200 mm
Diameter	50.8 mm
Thickness	13.2 mm
Transmission	97%
Optical Quality	$\lambda/4$

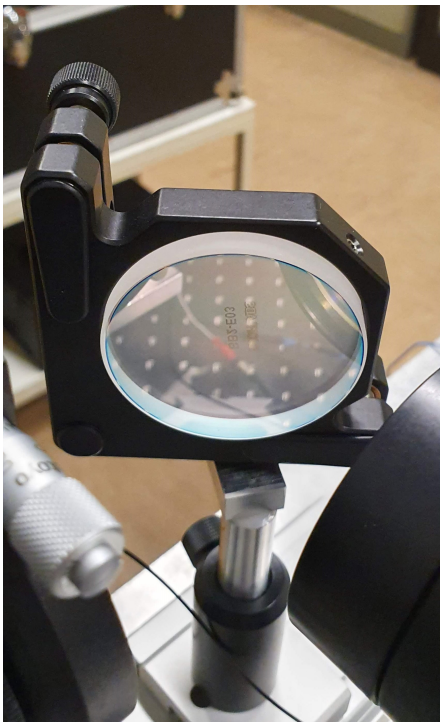

Figure 3 *M1, M2*: Thorlabs KM200-E3 Dielectric Mirrors.

Table 3 Thorlabs KM200-E3[b] Dielectric Mirrors optical specifications.

AR Coating	750 - 1100 nm
Diameter	80 mm
Thickness	12 mm
Reflectivity	99%
Optical Quality	$\lambda/10$

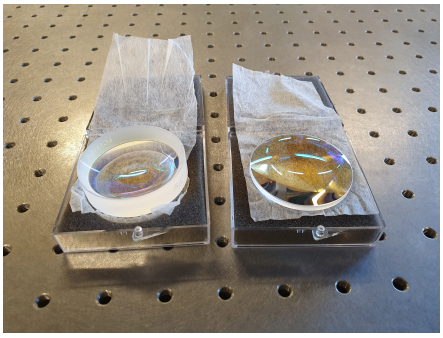

Figure 4 *CL*: Corrective lens for CAM comprised of Thorlabs LC1315-B plano-concave lens (left) and Thorlabs LB1309-B biconvex lens (right).

Table 4 Thorlabs LC1315-B[c] and Thorlabs LB1309-B[d] optical specifications.

	LC1315-B	LB1309-B
Focal Length	-75 mm	75 mm
Diameter	50.8 mm	50.8 mm
Thickness	3.5 - 13 mm	3 - 11.8 mm
Reflectivity	97%	97 %
Optical Quality	$\lambda/4$	$\lambda/4$

Figure 5 *IR*: cut filter from Edmund optics in its mount.

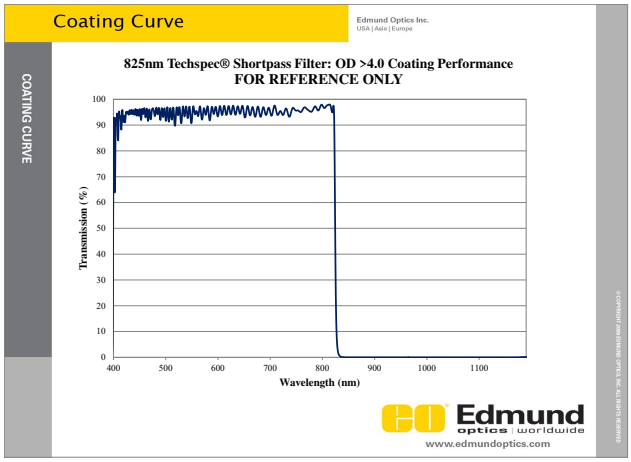

Figure 6 IR filter passband.

Table 5 IR filter[e] specifications.

Cut-off Wavelength	825 nm
Diameter	50 mm
Thickness	5 mm
Transmission	95%
Optical Quality	$< \lambda/4$

Figure 7 UV: cut filter from Edmund optics in its mount.

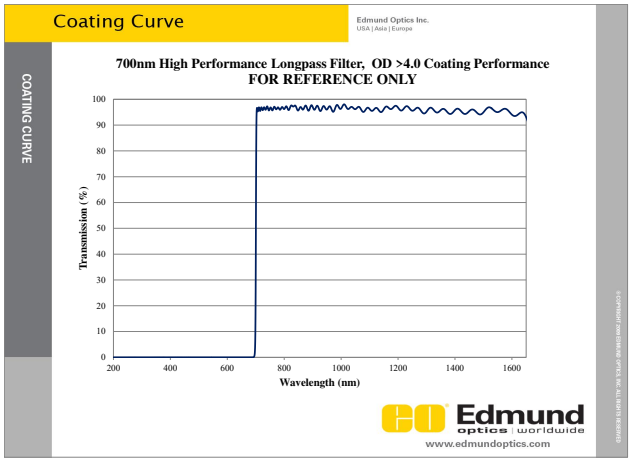

Figure 8 UV filter[f] passband.

Table 6 UV filter specifications.

Cut-off Wavelength	700 nm
Diameter	50 mm
Thickness	5 mm
Transmission	95%
Optical Quality	$< \lambda/4$

Figure 9 K: broadband filter from Edmund optics in its mount.

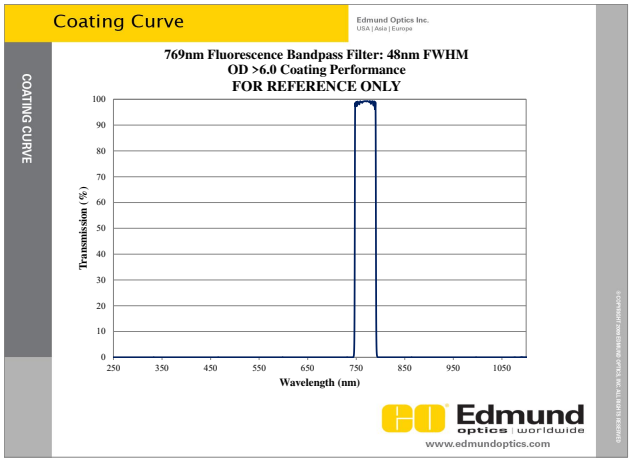

Figure 10 K filter passband.

Table 7 K filter[g] specifications.

Central Wavelength	769 nm
Passband Width	41 nm
Diameter	50 mm
Thickness	3.5 mm
Transmission	95%
Optical Quality	$< \lambda/4$

Figure 11 *IF*: narrowband filter from Andovercorp in its mount.

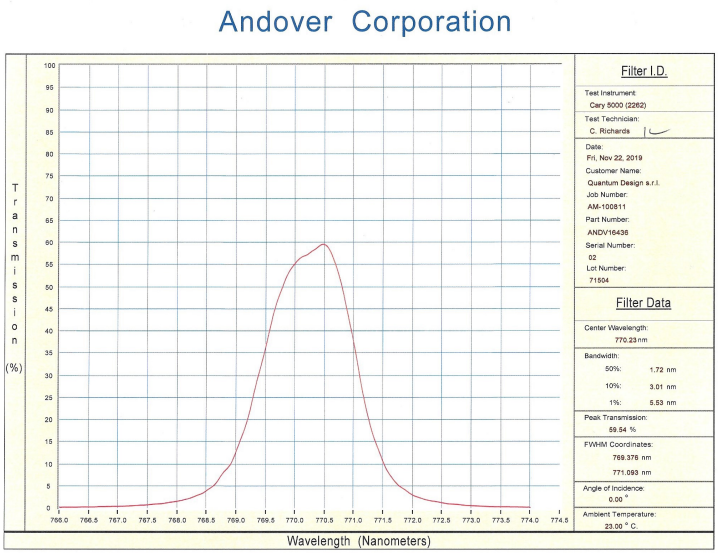

Figure 12 IF passband.

Table 8 IF^h specifications.

Central Wavelength	772.23 nm
Passband Width	1.72 nm
Diameter	25 mm
Thickness	5 mm
Transmission	55%
Optical Quality	$< \lambda/4$

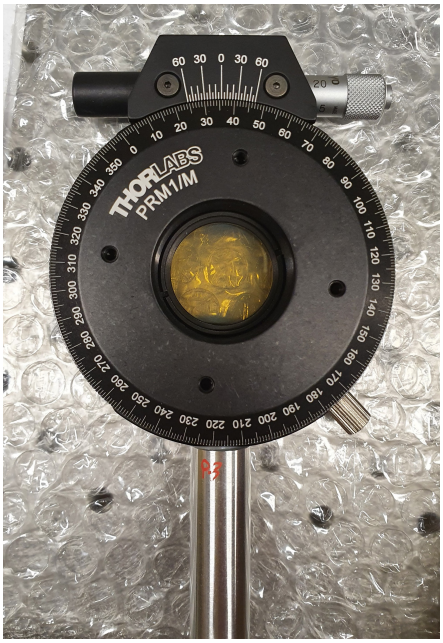

Figure 13 *P1, P2*: Thorlabs LPVIS100 nanoparticle linear film polarizer in rotating holder.

Table 9 Thorlabs LPVIS100^i nanoparticle linear film polarizer optical specifications.

AR Coating	550 - 1500 nm
Diameter	25 mm
Thickness	2 mm
Transmission	$\sim 80\%$
Extinction Ratio	$\sim 10^7$
Optical Quality	$\lambda/4$

Figure 14 *QWP1, QWP2* (left): Thorlabs AQWP10M-980 Quartz Zero-Order Achromatic Quarter-Wave Plate. *HWP1, HWP2* (right): Thorlabs AHWP10M-980 Quartz Zero-Order Achromatic Halve-Wave Plate.

Table 10 Thorlabs AQWP10M-980[j] and AHWP10M-980[k] optical specifications.

AR Coating	690 - 1200 nm
Diameter	25.4 mm
Thickness	1.57 mm
Transmission	97%
Optical Quality	$\lambda/4$

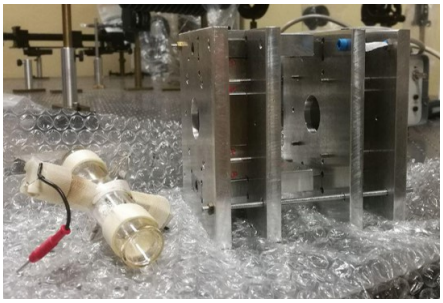

Figure 15 *MOF, WS*: cell of the filter section (MOF) and wing selector (WS) with externally wired heating filament next to magnetic enclosure.

Table 11 MOF and WS cell optical specifications.

Length	100 mm
Diameter	20 mm
Thickness (Optical Windows)	16.8 mm
Material	BK7
Optical Quality (Windows)	$\lambda/4$

B Mechanical Elements

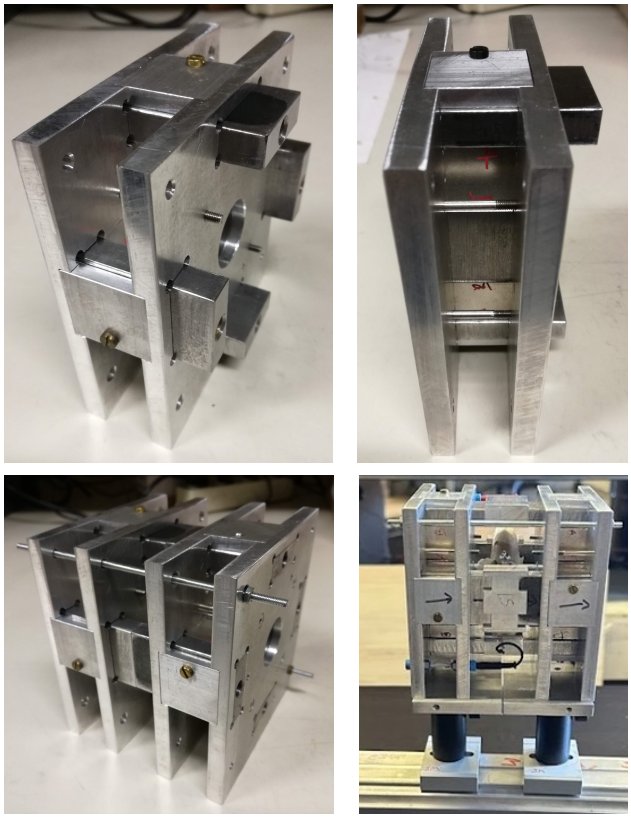

Figure 16 The MOF and WS magnetic enclosures designed to hold the vapor cells at the proper beam height and maintain a constant longitudinal magnetic field via permanent bar magnets. The MOF enclosure has two magnets and the WS enclosure has four magnets.

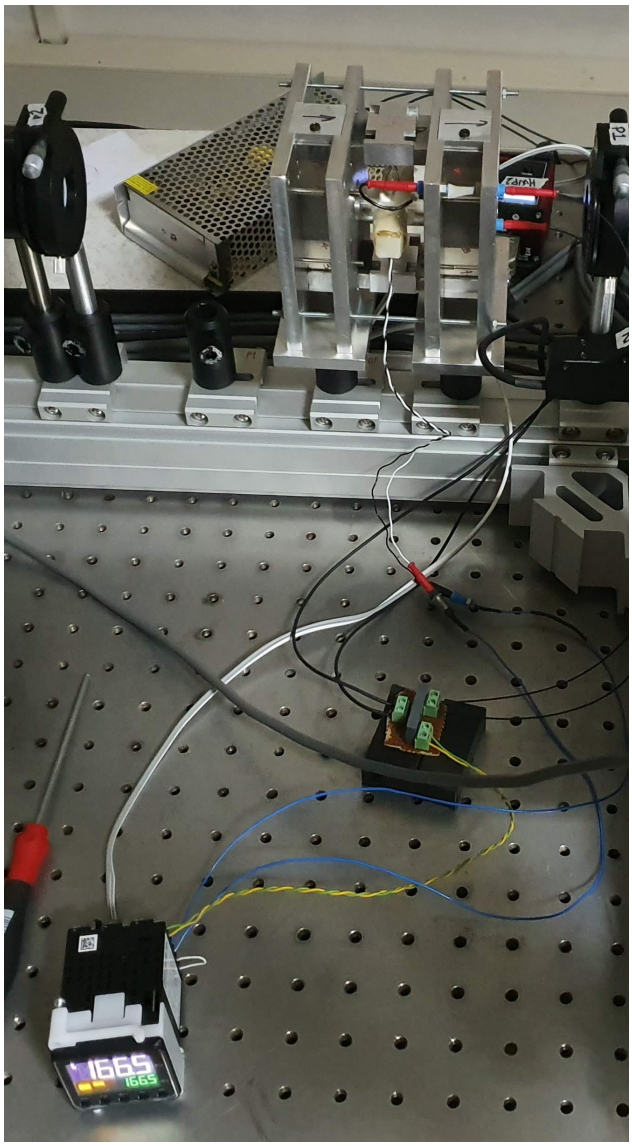

Figure 17 The MOF and WS cells' temperatures are maintained by an OMRON E5CC^{l} controller connected to a 24 V power supply and a PID circuit.

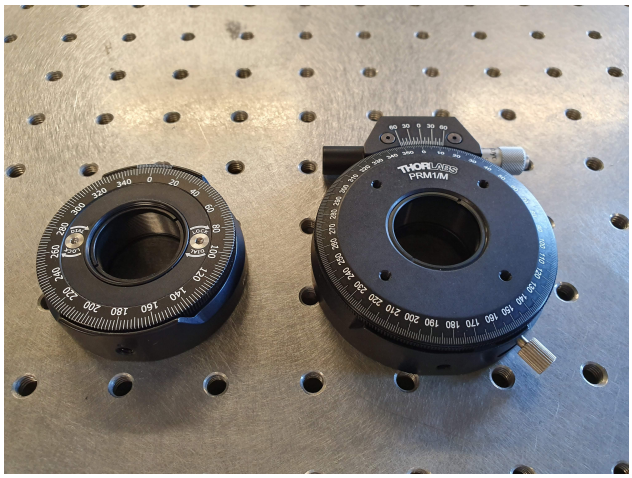

Figure 18 Manual rotating mounts for the QWPs (Thorlabs RPS1D/M^m: left) and the polarizers (Thorlabs PRM1/M^n: right). The rotating mounts have 5 *arcmin* and 2.5 *arcmin* rotational precision, respectively.

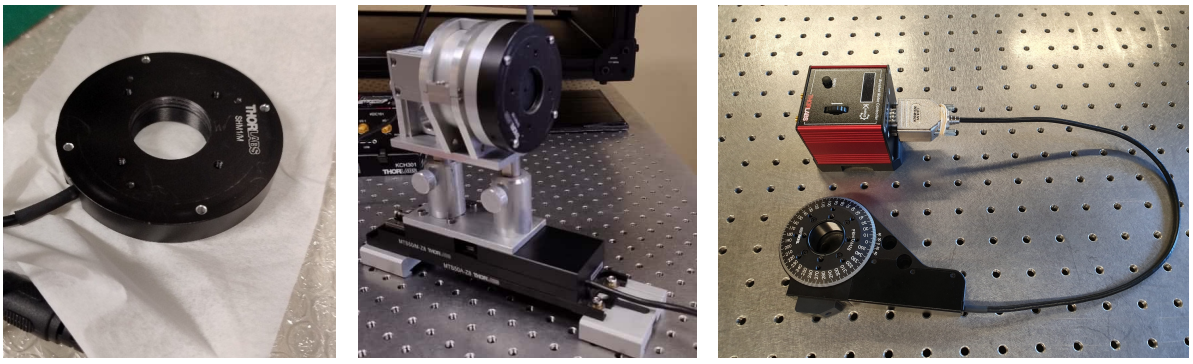

Figure 19 Motorized elements: a) The camera shutter is a Thorlabs SHB1T^o low reflectance automated shutter placed in front of CL. b) The camera is mounted on a Thorlabs MTS50/M-Z8^p motorized linear stage to allow for the image focus to be adjusted as needed; the linear stage has a maximum speed of 2.4 mm/s and a minimum step size of 15 μm over a range of 50 mm. c) The HWPs are mounted in Thorlabs KPRM1E/M^q motorized rotational mounts to allow for the different filtergrams to be acquired. The rotational mounts have a maximum speed of 25deg /s and a minimum increment of 1.8'.

Table 12 References for full optomechanical specifications.

a. L2, L3, L4, L5	Thorlabs AC508-200-B-ML
b. M1, M2	Thorlabs KM200-E3
c. CL1	Thorlabs LC1315-B
d. CL2	Thorlabs LB1309-B
e. IR	Edmund Optics IR Cut Filter
f. UV	Edmund Optics UV Cut Filter
g. K	Edmund Optics K Filter
h. IF	Andovercorp Filter
i. P1, P2	Thorlabs LPVIS100
j. HWP1, HWP2	Thorlabs AHWP10M-980
k. QWP1, QWP2	Thorlabs AQWP10M-980
l. Cell Heaters	OMRON E5CC
m. QWP Rotator	Thorlabs RPS1D/M
n. Polarizer Rotator	Thorlabs PRM1.M
o. Shutter	Thorlabs SHB1T
p. Linear Stage	Thorlabs MTS50/M
q. Rotational Mount	Thorlabs KPRM1E

B Basler a2A4504-18umPRO Specifications, Performance, and Acquisition Procedures

The Basler a2A4504-18umPRO is a monochromatic CMOS detector-based camera with a global shutter, which TSST uses for both the TSST-K and TSST-Hα channels (two individual cameras). When upgrading the TSST from the Dalsa Pantera 1M60 camera, this particular Basler camera was chosen for its compact size, its spectral response and QE at both the Hα and K wavelengths, and its programming flexibility – specifically its manufacturer-developed Python library, pypylon. At the K wavelength, the absolute QE of the detector is approximately 25% and its spectral response is approximately 0.55, while at the Hα wavelength, the detector's QE is approximately 50% and its spectral response is approximately 0.9. The manufacturer reported spectral response and QE plots can be found in Figure 20 and Table 13 reports additional specifications (for complete camera specifications, refer to the Basler website).

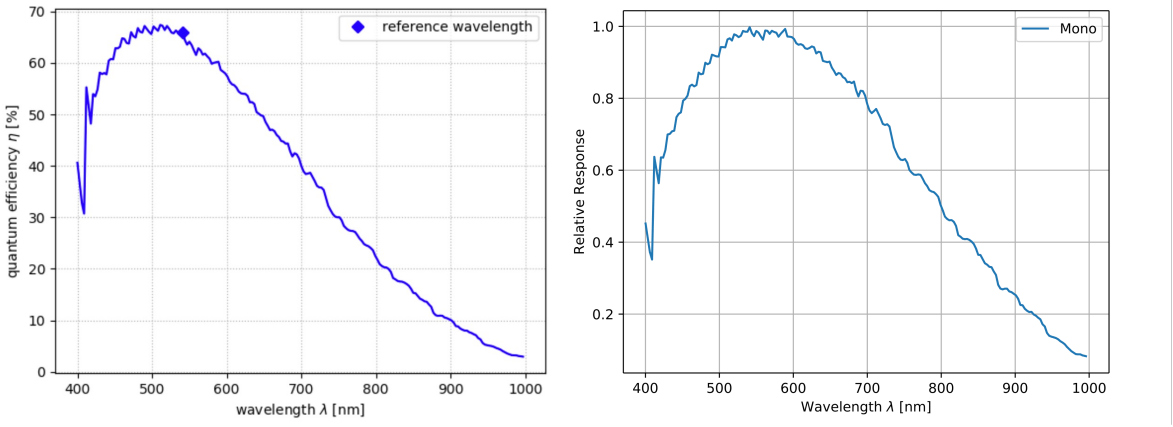

Figure 20 Absolute QE (left) and spectral response (right) of the Basler a2A4504-18umPRO cameras.

Table 13 Manufacturer-reported specifications for the TSST Basler a2A4504-18umPRO camera. a) The TSST acquisition procedure operates using 12-bit pixel depth. b) The TSST acquisition procedure operates with a frame rate of 16 fps. c) The TSST acquisition procedure operates with an exposure time of 62.5 ms for each frame for a total integration time of 5 s.

Sensor model	Sony IMX541
Sensor Type	CMOS
Resolution	4512 x 4512
Shutter Type	Global Shutter
Pixel Size	2.74 μm x 2.74 μm
Sensor Bit Depth[a]	8-bit, 10-bit, 12-bit, 16-bit
Maximum Frame Rate[b]	1000
Exposure Time[c]	16 μs to 10 s

The TSST data acquisition algorithm was written in Python by Andrea Chiodini. In addition to controlling the data acquisition of the camera, the acquisition code controls all of the mechanical parts (i.e. the HWP rotators, the camera's linear stage). The acquisition is such that one filtergram has acquisition time $5s$ and is made up of a collection of exposures of 62.5 ms. These exposures are saved in a multi-dimensional .fits file named with the starting time of the acquisition and the filtergrams type (R_+, R_-, B_+, B_-). The control code then rotates the HWP and begins the next $5s$ acquisition. The acquisition code automatically cycles through all four filtergram states and can be set to repeat the cycle for a user-specified amount of time.

During scientific acquisitions in the 2025 summer, the specific acquisition procedure utilized a cycle length of 50 s per Doppler/magnetogram, which was composed of acquiring 80

frames over a 5 s exposure for each filtergram. This exposure time was chosen to match MSO's cadence, and the cycle length was chosen to be comparable to HMI's fast 45-s cadence (we were limited to a 50 s exposure due to frame saving and HWP rotational times, which impose a 6.25 s acquisition cadence on each filtergram). Moreover, during acquisition modes, we binned the camera both vertically and horizontally, summing over 2x2 pixels, to better match the pixel scale of MSO. Using this strategy provided an average filtergram measurement with a gradient of 300 to 700 counts across the solar disk and a background of 30 counts.

C Full Parts List of MSO

Before joining the GATES Network, MSO was the private observatory of the Eddy Company, a producer of optical monitoring systems. Similar to the TSST-K, a large portion of the MSO telescope's optics come from Thorlabs or Edmund optics. However, a large portion of the optomechanical components and control mechanisms were custom-made by the Eddy Co. The two main structural channels of the MSO telescope (MSO-K and MSO-Na) are mirrors of each other, so for brevity, only the MSO-K optical components are listed. The major differences between MSO-K and MSO-Na optics are that the MSO-K optics are coated with AR-B anti-reflective coating while MSO-Na optics are coated with AR-A coating. Moreover, aside from the MOF and WS replacement, MSO-He was created by implementing alternatively coated BS and QWPs; I report the coating specifications for both MSO-K and MSO-He.

A Optical Elements

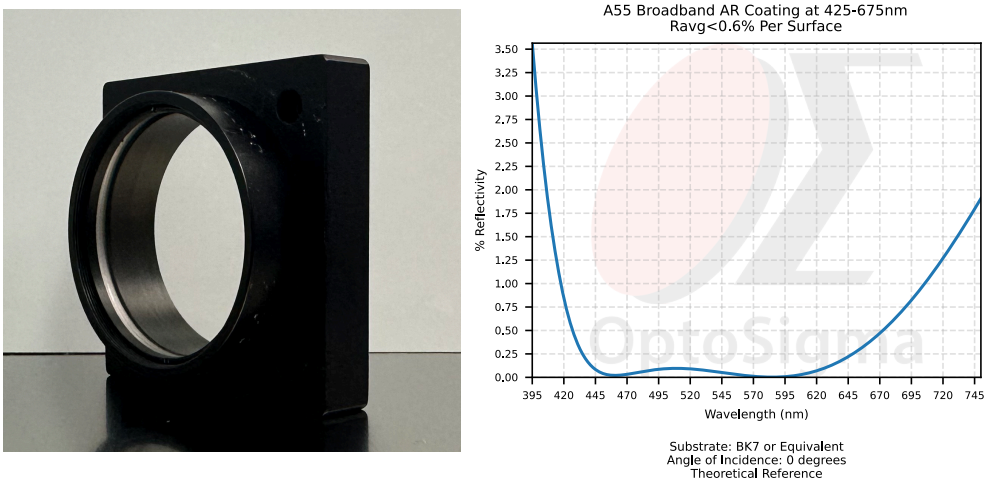

Figure 21 *L1*: Optosigma 026-1590[a] achromatic doublet in its mount (left) and its anti-reflective coating (right).

Table 14 L1 optical specifications.

Focal Length	100 mm
Diameter	50 mm
Thickness	8.3 mm
Anti-Reflection Coating	425 - 675 nm

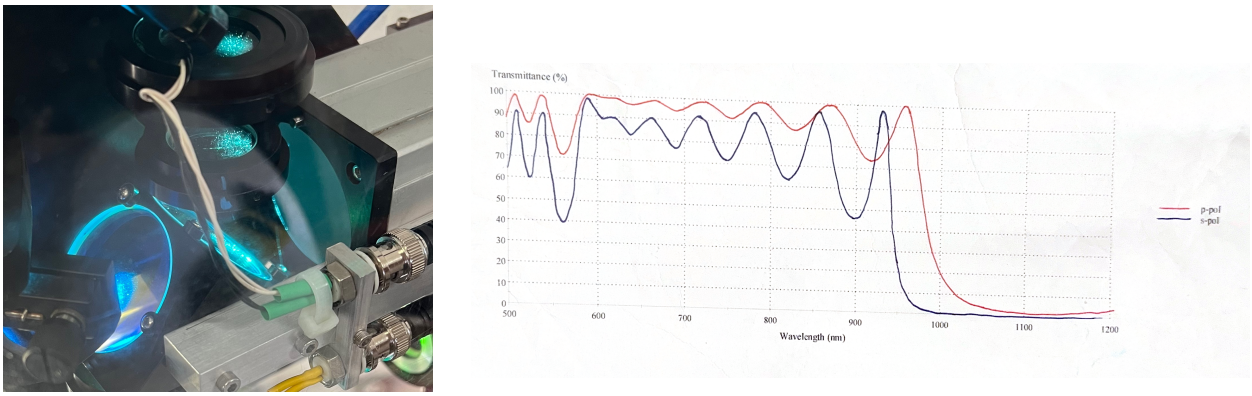

Figure 22 *BS*: The BS (left) is a custom-coated optic that is designed for 50/50 transmission between the Na and K wavelengths. As such, the first optic (reflects up to MSO-K and transmits to MSO-Na) is coated to reflect over 90% of the p-polarization in the 770 nm regime, while the second optic (reflects down to MSO-Na) is coated for the same transmission in the 589 nm regime. When the MSO-K channel was substituted for the MSO-He, a different BS was coated to optimize the NIR performance; its transmission performance can be seen on the right.

Figure 23 *QWP1, QWP2*: K QWP (left) in its mount for QWP1 and in its plain optic form for QWP2 are Meadowlark I9121 quarter-wave plates. When substituted for MSO-He, the QWPs are replaced with Thorlabs WPQ10ME-633 polymer zero-order quarter-wave plates (right).

Table 15 Thorlabs WPQ10ME-633[b] optical specifications

AR Coating	1050 - 1700 nm
Diameter	25.4 mm
Thickness	3.2 mm
Transmission	$\geq$98%
Optical Quality	$\lambda/4$

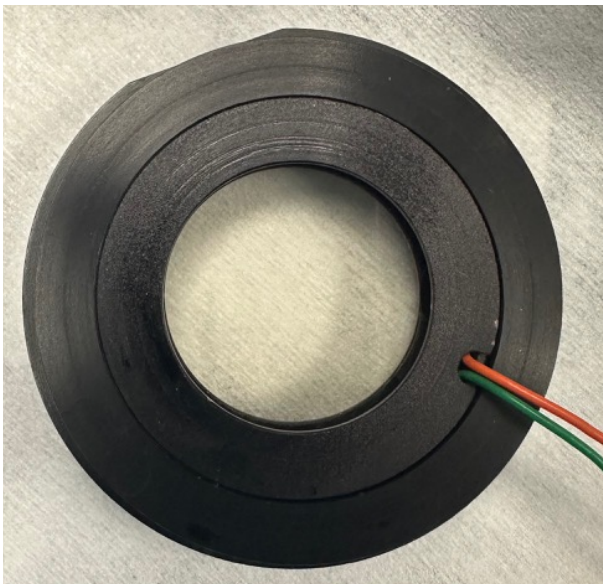

Figure 24 *HWP (DT)*: The MSO HWP is an LCVR from Display Tech (DT). To optimize for each channel, MSO-K has two DTs stacked, compared to MSO-Na's one.

Figure 25 *M1*: M1 is a custom 24.5 mm diameter optic made by the Eddy Co. Each channel's optic is coated to maximize transmission at their respective wavelengths.

Figure 26 *L2,L3*: Thorlabs AC254-200-B Achromatic Doublets.

Table 16 Thorlabs AC254-200-B[c] optical specifications.

Focal Length	200 mm
Diameter	25.4 mm
Thickness	8.0 mm
Transmission	97%
Optical Quality	$\lambda/4$

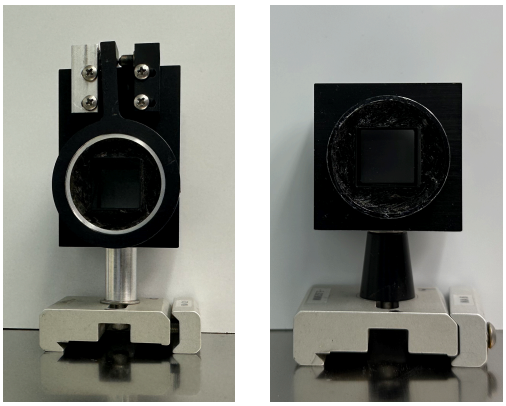

Figure 27 *P1, P2*: calcite polarizers with an extinction ratio 10^{-7}. P1 is mounted in a custom, spring-loaded enclosure for fine-tune adjustments. Both polarizers can rotate freely 360° when unlocked.

Figure 28 *L4, L5*: Thorlabs AC254-150-B Achromatic Doublets. L4 and L5 are mounted within the same enclosure.

Table 17 Thorlabs AC254-150-B[d] optical specifications.

Focal Length	150 mm
Diameter	25.4 mm
Thickness	8.0 mm
Transmission	97%
Optical Quality	$\lambda/4$

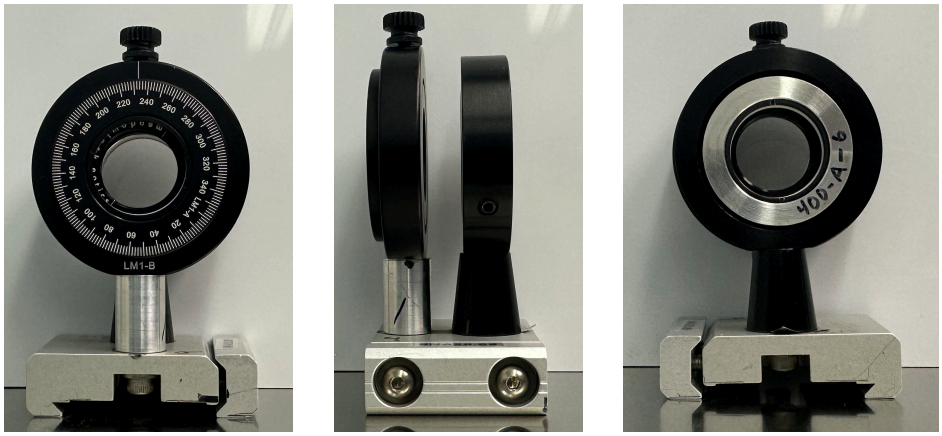

Figure 29 *QWP2, L6* are mounted on the same base but in independent enclosures. QWP2 is free to rotate 360° and can lock in place. L6 is a Thorlabs AC254-400-B Achromatic Doublet.

Table 18 Thorlabs AC254-400-B[e] optical specifications.

Focal Length	400 mm
Diameter	25.4 mm
Thickness	8.0 mm
Transmission	97%
Optical Quality	$\lambda/4$

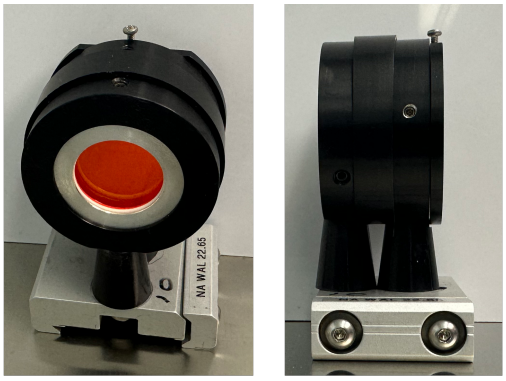

Figure 30 *Filter, L7, WA*: A narrowband filter, L7, and WA are mounted in the same enclosure. The MSO-K and MSO-Na filters are custom made optics[f] and the MSO-He[g] is an Alluxa Optics 1083-1.4 OD3 filter. L7 is a Thorlabs AC254-400-B Achromatic Doublet (see Table A) and the WA is a Karl Lambrecht custom 3-degree Wollaston Prism[h].

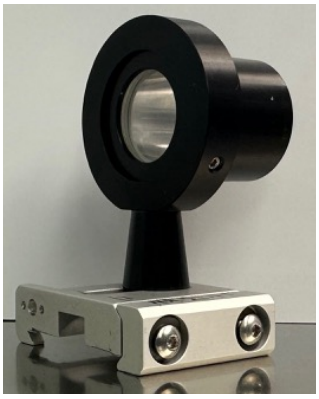

Figure 31 *L8, L9*: Thorlabs AC254-150-B and AC254-100-B Achromatic Doublets; mounted on the same base and enclosure.

Table 19 Thorlabs AC254-100-B^i optical specifications.

Focal Length	100 mm
Diameter	25.4 mm
Thickness	8 mm
Transmission	97%
Optical Quality	$\lambda/4$

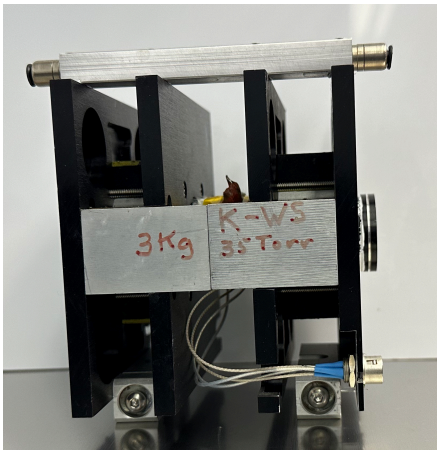


Figure 32 *MOF, WS*: MSO-K WS cell and magnet enclosure (left). Example alaki ring cells (center) and He cell (right).

Table 20 MOF and WS cell optical specifications for alkali cells.

Length	96.5 mm
Diameter	19 mm
Coating (Optical Windows)	V-coated to less than 0.2% reflectivity
Material	BK7
Optical Quality (Windows)	$\lambda/10$

Table 21 References for full optomechanical specifications.

a. L1	Optosigma 026-1590
b. He QWP	Thorlabs WPQ10ME-633
c. L2, L3	Thorlabs AC254-200-B
d. L4, L5, L8	Thorlabs AC254-150-B
e. L6, L7	Thorlabs AC254-400-B
f. MSO-K and MSO-Na Filter	Eddy Co.
g. MSO-He Filter	1083-1.4 OD3
h. WA	Karl Lambrecht custom 3-degree WA
i. L9	Thorlabs AC254-100-B

B Mechanical/Electrical Elements

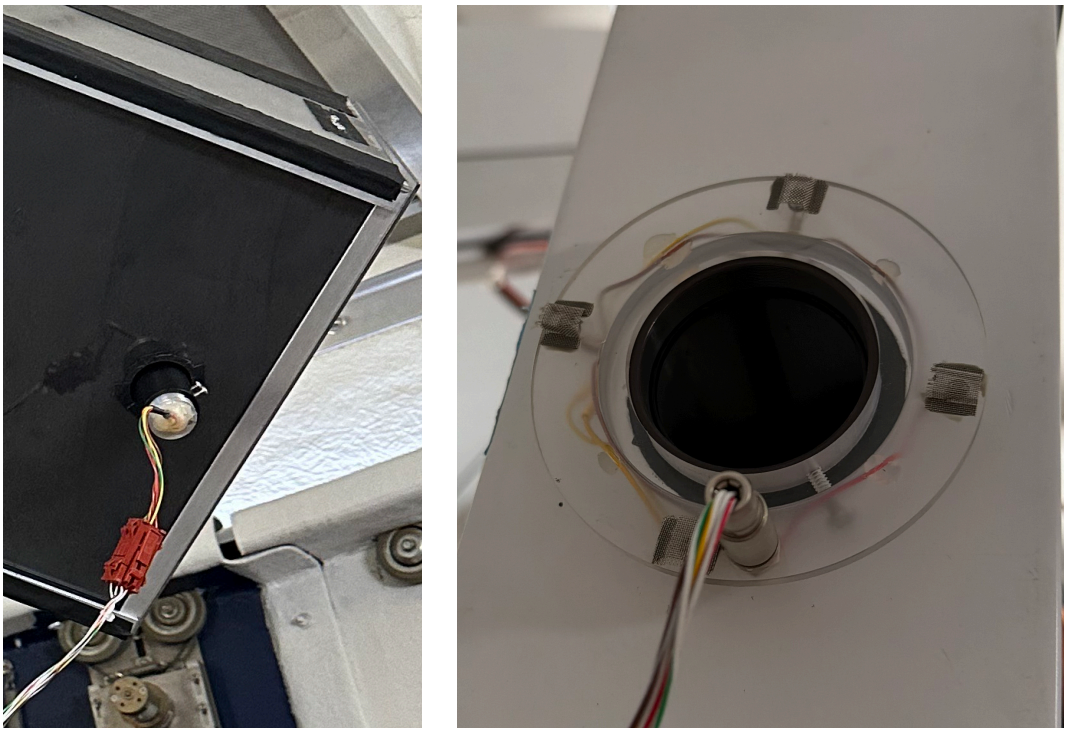

Figure 33 *Tracking diodes for the MSO telescope* Left: fine tracking quad diode, which uses the excess beam from the BS. Right: photodiodes on the front aperture of the telescope to lock the dome tracking to the telescope.

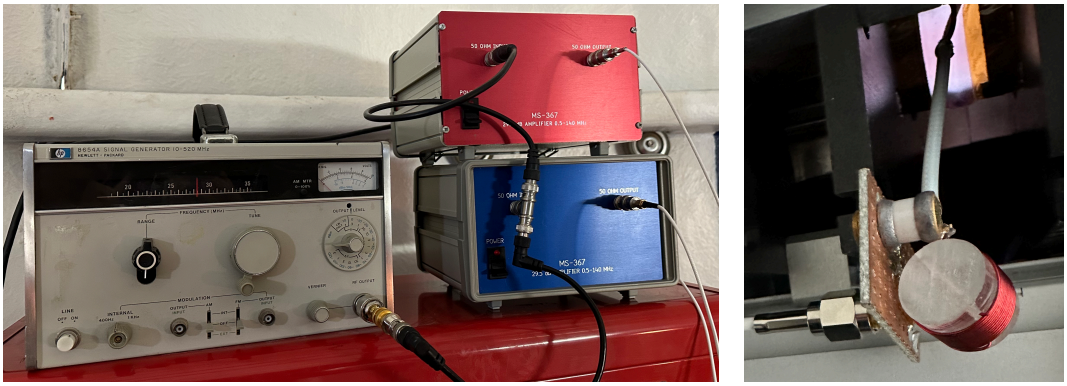

Figure 34 *RF circuit for He cell ionization* Left: RF generator tunable to Hz frequencies and dB output levels. The red and blue boxes are amplifiers for MOF and WS cells. They can operate independently from each other. Right: tunable circuit which connects to the cell.

Figure 35 *MSO Electronic Controls*: A) oscillascope for fine-tracking quad diode alignment; B) DT drivers; C) dome power; D) camera mount control with x, y, z axis motorized control; E) power box for camera mount control; F) PTC10 unit for MOF and Ws heating; G) computers for dome, MSO-K and MSO-Na control.

D Alvium 1800 U-508M Specifications, Performance, and Acquisition Control

The Alvium 1800 U-508M camera is a monochromatic CMOS detector-based camera with a global shutter, which MSO uses for both the MSO-K and MSO-Na channels, as well as the MSO-He tests. This camera was chosen for its compact size, its spectral response and QE at both the K and Na wavelengths, and programming flexibility. At both the K and Na wavelengths, the absolute QE of the detector is over 40%, and the spectral response is greater than 0.2 A/W. Moreover, the entire Alvium camera suite is designed so that its cameras' SDK is fully compatible with all major software providers; consequently, this has allowed us to readily standardize the MSO camera control algorithm to match TSST's Python infrastructure. The manufacturer reported spectral response and QE plots can be found in Figure 36, and Table 22 reports additional specifications (for full specifications, refer to theAluvium website).

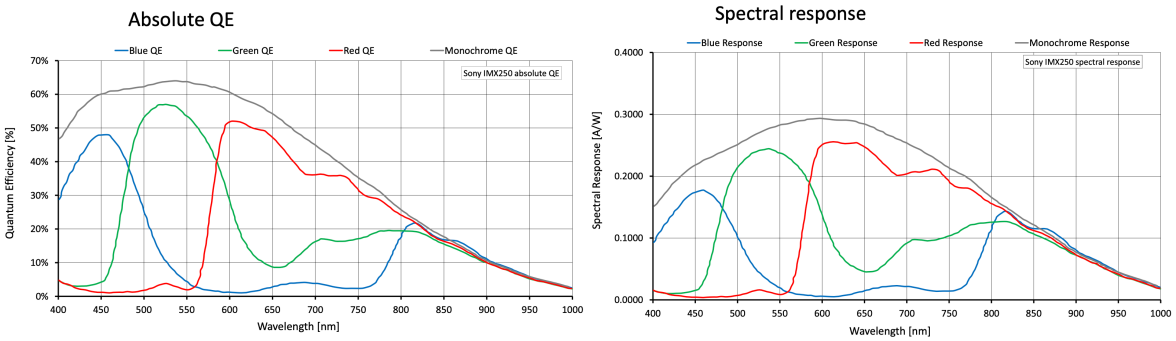

Figure 36 Absolute QE (left) and spectral response (right) of the Alvium 1800 U-508 cameras. MSO is operating with the monochromatic cameras whose response curves are represented in grey.

For the Summer 2025 observing campaign, the data acquisition algorithm at MSO was written in LabVIEW by Dr. Neil Murphy. LabVIEW, a graphical system design and devel-

Table 22 Manufacturer-reported specifications for the MSO Alvium 1800 U 508m camera. a) The MSO acquisition procedure operates using 12-bit camera that is converted to 16-bit data. b) The MSO acquisition procedure operates with an exposure time of 100 ms per frame, which is summed over the exposure burst during the 5 s acquisition time.

Sensor model	Sony IMX250
Sensor Type	CMOS
Resolution	2464 (H) x 2056 (V)
Shutter Type	Global Shutter
Pixel Size	3.45 μm x 3.45 μm
Sensor Bit Depth[a]	8-bit, 10-bit, 12-bit
Maximum Frame Rate	84 fps
Exposure Time[b]	27 μs to 10 s

opment platform distributed by National Instruments, was chosen for its ease of creating/interacting with Graphical User Interfaces (GUIs); the MSO LabVIEW allows users to view live filtergram, Dopplergram, magnetogram, and waveform (2D horizontal slices across the camera detector) images (Figure 37). The MSO acquisition is such that both red-wing (or blue-wing) filtergrams are imaged simultaneously on the same detector. Over the exposure time of 5 s, the LCVR – controlled by the LabVIEW algorithm, triggered by the camera – alternates the HWP's orientation at a rate of 10 - 20 Hz so that both red and blue wings (of both polarization states) are imaged with a user-set number of frames over a burst of time within the 5 s cadence. The system is set to take a burst of images and then use the remaining time in the 5 s cadence to read out the array. This extended read-out time is required for the communication time between the LabVIEW GUI and the main Python camera communication. For the Summer 2025 campaign, all MSO channels operated, acquiring

10 frames per acquisition. These frames are summed by their respective wavelengths, and the two resultant images are stitched together to a single, two-dimensional .fits file titled with the acquisition start time. Using this strategy provided an average filtergram intensity of 1600 - 2400 counts across the solar disk with a background of 240 counts for MSO-Na and 5000 - 7000 counts across the solar disk with a background of 700 counts for MSO-K.

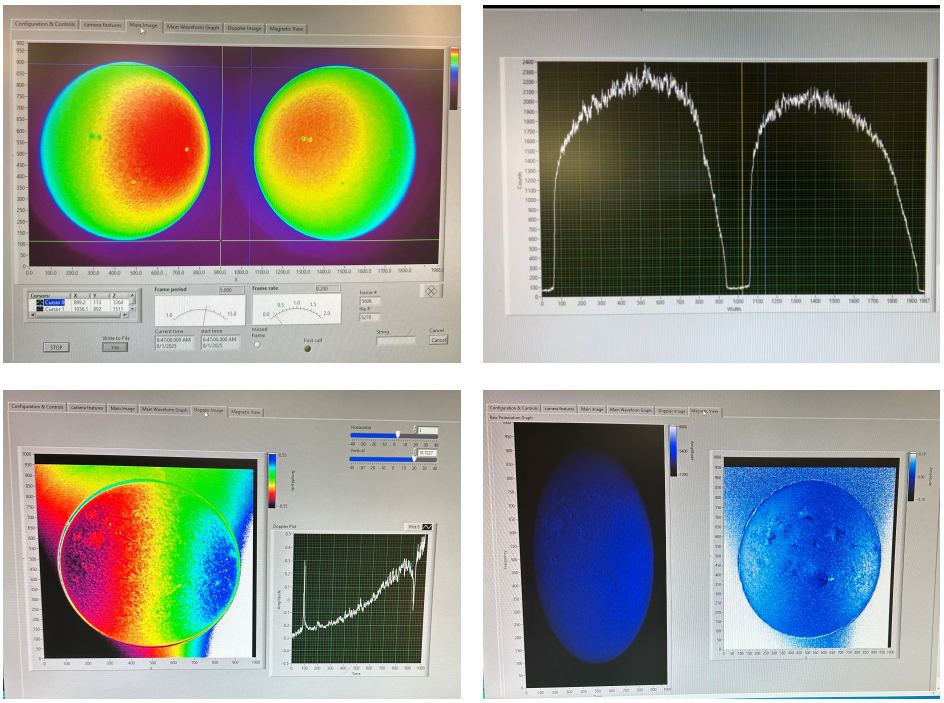

Figure 37 Example still frames from the LabVIEW GUI. The upper-left panel shows the intensity tab, which contains 2 filtergrams. The upper-right panel shows the waveform tab, which displays a horizontal cut across the center of the filtergrams. The bottom left shows the Dopplergram and the horizontal cut plot. The bottom right shows a single polarization state and a magnetogram.

In an effort to improve the efficiency of the MSO image acquisition, match the operational language of the TSST (and consequently the GATES Network), and be overall more open-source/accessible, MSO is developing a Python-based control algorithm. This Python algorithm, also developed by Dr. Neil Murphy, operates similarly to the LabVIEW algorithm,

alternating the HWP position, populating the four filtergrams into a single two-dimensional array, and saving the full $5s$ acquisition to a single .fits file named after the acquisition's start time. The main differences between teh Python control and the LabVIEW control are the presence of a GUI and the DT control. The Python algorithm does not have a GUI, but since the entirety of the camera control and data saving is completed within the same algorithm/application, the extended read-out time is not necessary. This means that filtergram images can be acquired for the entirety of the 5 s acquisition, not just for a burst.

I tested the Python algorithm on July 22, 2025, obtaining an hour of MSO-K and MSO-Na data. For each acquisition, the average numerical unit intensity of the filtergrams was 98,009, compared to 4,251 obtained with the LabVIEW algorithm (Figure 38). Moreover, the Python control algorithm decreases RAM usage which will allow for both MSO-K and MSO-Na channels to be safely controlled via a single computer when the Python control is fully implemented.

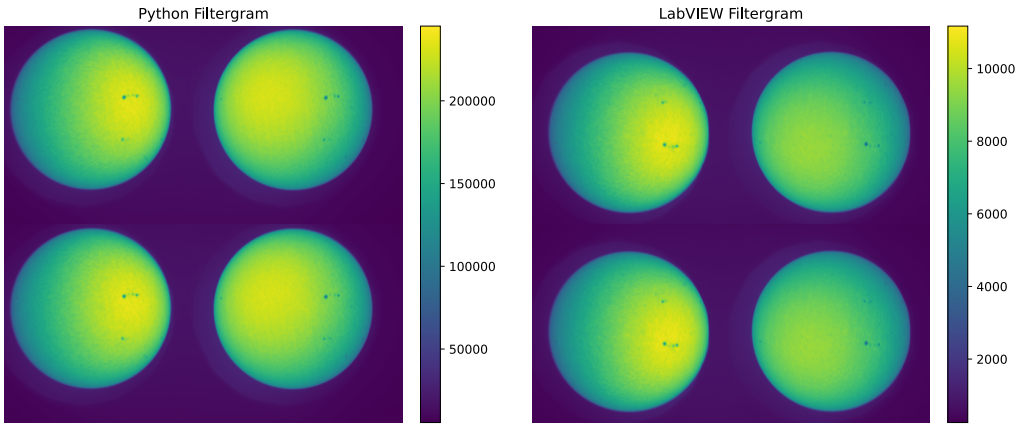

Figure 38 A comparison of the efficiency of the MSO Python control algorithm (filtergrams on the left) compared to the LabVIEW control algorithm (filtergrams on the right) for the MSO-K. For a given $5s$ acquisition time, the Python filtergrams are 23x brighter.

E Python Code for Data Reduction

The Python code in the following pages takes level 0 data inputs – dark, leakthrough, flat field, cell glow (in case of He), and raw filtergram images – and produces level 3 data – calibrated Dopplergrams and magnetograms. I based this reduction pipeline on the MOTH data reduction pipeline from Forte et al. (2020) and the PMODE data reduction pipeline from Gulledge (2022). The pipeline allows selection of TSST or MSO data and is compatible with the data-saving standards of both GATES' nodes as of January 2026. For brevity, the code included here contains only the MSO cells. The TSST reduction cells follow a similar logic, but have an additional step of cumulatively summing the raw data frames into a single exposition. Additionally, the TSST calibration images are separated by filtergram state, so the TSST calibration pipeline holds each filtergram in its own dictionary until it joins the MSO reduction at the point of batch processing the filtergram files into Doppler- and magnetograms.

```
"""
MSO Reduction

@author: Fallon
"""
import numpy as np
import numpy.fft as fft

import matplotlib.pyplot as plt
from matplotlib import colors

from astropy.io import fits

from scipy.signal import argrelextrema
from scipy.signal import find_peaks
from scipy.signal import medfilt2d
```

```
from scipy.ndimage import rotate
from scipy.ndimage import shift
from scipy.ndimage import gaussian_filter
from scipy.ndimage import fourier_shift
from scipy.ndimage import shift as shift_image


from skimage.registration import phase_cross_correlation
from skimage import measure, filters, morphology
from skimage.draw import circle_perimeter
from skimage.filters import sobel
from skimage import filters, feature
from skimage.transform import rescale
from scipy.ndimage import shift as ndi_shift

import os
import sys
import time
import glob

from pathlib import Path

import cv2

from pathlib import Path
from tqdm import tqdm


#%% Inputs

home=Path(r"D:\MSO") #pick the node of GATES
element="Na"
year="2025"
month="10"
date="2025_10_24"
date_us="10_24_2025"

direct=home /element /month / date
calibration_direct=direct / "Calibrations"

#%% Na/K inputs

cadence=5 #5 s cdence at MSO
rotational_correction=101.3 #determined by log-polar cross correlation to HMI
```

```
#TSST=-49.04, MSO-K=MSO-He=80.35, MSO-Na=101.3

#%% functions
def save_to_fits(data,filename,direct,header=None):
    if header is None:
      hdu=fits.PrimaryHDU(data=data)
      hdul=fits.HDUList([hdu])
    else:
      hdu=fits.PrimaryHDU(data=data,header=header)
      hdul=fits.HDUList([hdu])
    ##output_filename=direct+filename+'.fits'
    output_filename = direct / f"{filename}.fits"
    hdul.writeto(output_filename, overwrite=True)

    print('File saved!')


def open_fits(f):
    hdus=fits.open(f)
    hdr = hdus[0].header
    data_fits = hdus[0].data
    return hdus,hdr,data_fits


def save_multi(frames_list,filename,save_directory,frame_start_list=None):

    hdus = [fits.PrimaryHDU()]
    for i in range(len(frames_list)):
        hdu = fits.ImageHDU(frames_list[i])
        hdu.header['FRAME'] = i # Optional: label each HDU with a frame index
        #hdu.header['START']=frame_start_list[i]
        hdus.append(hdu)

    # Write to FITS file
    hdul = fits.HDUList(hdus)
    #hdul.writeto('/Users/Fallon/Desktop/multi_frame.fits', overwrite=True)
    direct=save_directory
    output_filename=direct+filename+'.fits'
    #output_filename=direct+frame_type+'_'+frame_start_list[0]+'_multi.fits'
    hdul.writeto(output_filename, overwrite=True)
    print('File saved!')


def load_multifits(directory,filtergram):
```

```
    fits_files = glob.glob(os.path.join(directory, "*"+filtergram+"*.fits"))
    data_frames = [] # Will hold frames grouped by file

    for file_path in fits_files:
        try:
            with fits.open(file_path) as hdul:
                frames = [hdu.data for hdu in hdul if hdu.data is not None]
            data_frames.append(frames)
        except Exception as e:
            print(f"Error reading {file_path}: {e}")
    data_frames=np.array(data_frames)
    converted_data_frames=data_frames.astype(np.int64)
    return converted_data_frames


def apply_calibrations(fgram,master_dark,master_leak,master_flat):
    gram_dcorr=fgram-master_dark
    gram_lcorr=gram_dcorr-master_leak
    gram_fcorr=gram_lcorr/master_flat
    return(gram_fcorr)


def apply_calibrations_He(fgram,master_dark,master_leak,master_flat,
                          master_glow):
    gram_dcorr=fgram-master_dark
    gram_lcorr=gram_dcorr-master_leak
    gram_gcorr=gram_lcorr-master_glow
    gram_fcorr=gram_gcorr/master_flat
    return(gram_gcorr)

def read_fit_files_to_array(directory):

    pattern = os.path.join(directory, "*.fit")
    fit_files = sorted(glob.glob(pattern)) # Optional: sort for consistency

    data_list = []

    for file_path in fit_files:
        try:
            with fits.open(file_path) as hdul:
                data = hdul[0].data
                if data is not None:
                    data_list.append(data)
                else:
                    print(f"Warning: No data in primary HDU of {file_path}")
```

```
        except Exception as e:
            print(f"Failed to read {file_path}: {e}")

    if not data_list:
        raise ValueError("No valid .fit data found in directory.")

    try:
        return np.stack(data_list)
    except ValueError as e:
        raise ValueError(f"Inconsistent image shapes: {e}")

def load_fits_images(directory: Path):
    """Load all 2D FITS images from a directory as float32 arrays."""
    files = list(directory.glob('*.fit'))
    data_list = []

    for f in files:
        try:
            with fits.open(f, memmap=False) as hdul:
                data = hdul[0].data
            if data is None or not isinstance(data, np.ndarray) or \
            data.ndim != 2:
                print(f"      Skipping {f} (invalid or empty data)")
                continue
            data_list.append(data.astype(np.float32))
        except Exception as e:
            print(f"   Error reading {f}: {e}")
            continue

    if data_list:
        stacked = np.array(data_list)
        print(f"{directory.name} all loaded, shape: {stacked.shape}")
        return stacked
    else:
        print(f"      No valid FITS files found in {directory}")
        return np.array([])


def process_hour(hour, direct, reduced_direct, master_dark, master_leak,
                 master_flat, master_glow):
    """
    Process all FITS files for a given hour directory.
    """
    # Define paths
    data_direct = direct / hour
```

```
    reduced_direct_hour = reduced_direct / hour

    # Create output directory if it doesn't exist
    reduced_direct_hour.mkdir(parents=True, exist_ok=True)

    print(f"\nProcessing hour: {hour}")
    print(f"Input directory: {data_direct}")
    print(f"Output directory: {reduced_direct_hour}")

    # Get list of FITS files
    fgrams = sorted(data_direct.glob('*.fit'))

    for f in tqdm(fgrams, desc=f"Processing {hour}"):
        try:
            hdr, hdus, gram = open_fits(f)

            calibrated_gram = apply_calibrations_He(
                gram, master_dark, master_leak, master_flat, master_glow
            )

            root = Path(f).stem
            save_to_fits(calibrated_gram, root + '_calibrated',
                         reduced_direct_hour)

            # Clean up
            del hdr, hdus, gram, calibrated_gram

        except (OSError, IOError) as e:
            error_msg = str(e).lower()
            if any(word in error_msg for word in ["truncated",
                                                  "buffer too small",
                                                  "segment is too short"]):
                print(f"Skipped {f} due to truncation/buffer error: {e}")
                continue
            else:
                print(f"Error processing {f}: {e}")
                continue

        except Exception as e:
            print(f"Unexpected error processing {f}: {e}")
            continue
def MSO_filtergrams(data):

    if data.ndim == 3:
        # Multiple frames case
```

```
        F, X, Y = data.shape
        Rr, Br, Rl, Bl = [], [], [], []

        for i in range(F):
            frame = data[i]
            mid_x, mid_y = X // 2, Y // 2
            Rr.append(frame[0:mid_x, 0:mid_y])
            Br.append(frame[mid_x:, 0:mid_y])
            Rl.append(frame[0:mid_x, mid_y:])
            Bl.append(frame[mid_x:, mid_y:])

        Rr = np.array(Rr)
        Br = np.array(Br)
        Rl = np.array(Rl)
        Bl = np.array(Bl)

        combined = np.stack([Rr, Br, Rl, Bl], axis=1) # shape (F, 4, X/2, Y/2)
        return Rr, Br, Rl, Bl, combined

    elif data.ndim == 2:
        # Single frame case
        X, Y = data.shape
        mid_x, mid_y = X // 2, Y // 2

        Rr = data[0:mid_x, 0:mid_y]
        Br = data[mid_x:, 0:mid_y]
        Rl = data[0:mid_x, mid_y:]
        Bl = data[mid_x:, mid_y:]
        combined=np.stack([Rr,Br,Rl,Bl],axis=0)

        return Rr, Br, Rl, Bl, combined

    else:
        raise ValueError("Input must be 2D (X, Y) or 3D (F, X, Y)")



def process_filtergrams(images, output_basename="output", save_dir=".",
                        min_radius=390, max_radius=420, dp=1.2,
                        param1=10, param2=30, invert=False, show_debug=False,
                        r_target=None):

    save_dir = Path(save_dir)
    doppler_dir = save_dir / "Dopplergrams"
    magneto_dir = save_dir / "Magnetograms"
```

```
intensity_dir = save_dir / "Intensitygrams"
for d in [doppler_dir, magneto_dir, intensity_dir]:
    d.mkdir(parents=True, exist_ok=True)

centers_radii = []
masked_centered_images = []
aligned_images = []
scaled_images = []

h, w = images[0].shape
center_target = np.array([w//2, h//2])

for idx, img in enumerate(images):
    # Normalize
    p1, p99 = np.percentile(img, [1, 99])
    norm = np.clip((img - p1) / (p99 - p1), 0, 1)
    if invert:
        norm = 1 - norm

    norm_blur = filters.gaussian(norm, sigma=1.5)
    frame_8bit = (255 * norm_blur).astype(np.uint8)

    # Detect circle
    circles = cv2.HoughCircles(
        frame_8bit, cv2.HOUGH_GRADIENT, dp=dp,
        minDist=1000, param1=param1, param2=param2,
        minRadius=min_radius, maxRadius=max_radius
    )
    if circles is None:
        raise RuntimeError(f"No circle found in image {idx}")
    cx, cy, r = np.uint16(np.around(circles[0,0]))
    centers_radii.append([cx, cy, r])

    # Shift image
    shift_x = center_target[0] - cx
    shift_y = center_target[1] - cy
    aligned = ndi_shift(img, shift=(shift_y, shift_x), order=1,
                        mode='constant', cval=0)
    aligned_images.append(aligned)

    # Masked image
    yy, xx = np.indices(aligned.shape)
    mask = np.sqrt(((xx - center_target[0])**2 +
                    (yy - center_target[1])**2)) <= r
    masked_centered = np.where(mask, aligned, np.nan)
```

```
        masked_centered_images.append(masked_centered)

        # Optional scaling
        if r_target is not None:
            scale = r_target / r
            rescaled = rescale(aligned, scale, order=1, preserve_range=True,
                               anti_aliasing=True, mode='constant')
            # Crop/rescale to original shape
            rh, rw = rescaled.shape
            y_offset = max(0, (rh - h)//2)
            x_offset = max(0, (rw - w)//2)
            cropped = rescaled[y_offset:y_offset+h, x_offset:x_offset+w]
            fixed = np.zeros((h, w), dtype=img.dtype)
            fixed[:cropped.shape[0], :cropped.shape[1]] = cropped
            scaled_images.append(fixed)
        else:
            scaled_images.append(aligned)

        if show_debug:
            import matplotlib.pyplot as plt
            plt.figure(figsize=(10,4))
            plt.subplot(1,3,1)
            plt.imshow(img, cmap='gray')
            plt.scatter(cx, cy, c='r')
            plt.title('Original')
            plt.axis('off')
            plt.subplot(1,3,2)
            plt.imshow(aligned, cmap='gray')
            plt.title('Aligned')
            plt.axis('off')
            plt.subplot(1,3,3)
            plt.imshow(masked_centered, cmap='gray')
            plt.title('Masked & Aligned')
            plt.axis('off')
            plt.show()

    centers_radii = np.array(centers_radii)
    masked_centered_images = np.array(masked_centered_images)
    aligned_images = np.array(aligned_images)
    scaled_images = np.array(scaled_images)

    return centers_radii, masked_centered_images, aligned_images
```

```
def process_filtergrams_scaling(images,
                      min_radius=380, max_radius=420, dp=1.2,
                      param1=10, param2=30,
                      invert=False,
                      show_debug=False,
                      r_target=400):

    centers_radii = []
    masked_centered_images = []
    aligned_images = []
    scaled_images = []

    h, w = images[0].shape
    center_target = np.array([w//2, h//2]) # where to place the disk center

    for idx, img in enumerate(images):
        # Normalize to [0,1]
        p1, p99 = np.percentile(img, [1, 99])
        norm = np.clip((img - p1) / (p99 - p1), 0, 1)
        if invert:
            norm = 1 - norm

        # Gaussian smoothing
        norm_blur = filters.gaussian(norm, sigma=1.5)

        # Convert to 8-bit for Hough
        frame_8bit = (255 * norm_blur).astype(np.uint8)

        # Detect circle
        circles = cv2.HoughCircles(
            frame_8bit,
            cv2.HOUGH_GRADIENT,
            dp=dp,
            minDist=1000,
            param1=param1,
            param2=param2,
            minRadius=min_radius,
            maxRadius=max_radius
        )

        if circles is None:
            raise RuntimeError(f" No circle found in image {idx}.")

        cx, cy, r = np.uint16(np.around(circles[0,0]))
        centers_radii.append([cx, cy, r])
```

```
# Shift image so disk center is at image center
shift_x = center_target[0] - cx
shift_y = center_target[1] - cy
aligned = ndi_shift(img, shift=(shift_y, shift_x), order=1,
                    mode='constant', cval=0)
aligned_images.append(aligned)

# Rescale to match target radius
scale = r_target / r
rescaled = rescale(aligned, scale, order=1, preserve_range=True,
                   anti_aliasing=True, mode='constant')

# Crop or pad to match original shape
rescaled_fixed = np.zeros((h, w), dtype=img.dtype)
rh, rw = rescaled.shape

# Compute cropping/padding coordinates
y_offset = max(0, (rh - h) // 2)
x_offset = max(0, (rw - w) // 2)

# Crop if larger
rescaled_cropped = rescaled[y_offset:y_offset + h,
                            x_offset:x_offset + w]

# Pad if smaller
rescaled_fixed[:rescaled_cropped.shape[0],
               :rescaled_cropped.shape[1]]= rescaled_cropped

scaled_images.append(rescaled_fixed)

# Create mask for rescaled image
yy, xx = np.indices(rescaled_fixed.shape)
mask = np.sqrt(((xx - w//2)**2 + (yy - h//2)**2)) <= r_target
masked_centered = np.where(mask, rescaled_fixed, np.nan)
masked_centered_images.append(masked_centered)

# Create mask for just aligned image
yy, xx = np.indices(aligned.shape)
mask = ((xx - center_target[0])**2 + (yy - center_target[1])**2) \
    <= r**2
masked_centered_a = np.where(mask, aligned, np.nan)
# masked_centered_images.append(masked_centered)
```

```
        if show_debug:
            import matplotlib.pyplot as plt
            plt.figure(figsize=(12, 4))
            plt.subplot(1, 4, 1)
            plt.imshow(img, cmap='gray')
            plt.title(f'Original {idx}')
            plt.axis('off')
            plt.scatter(cx, cy, c='r')

            plt.subplot(1, 3, 2)
            plt.imshow(aligned, cmap='gray')
            plt.title('Aligned & Scaled')
            plt.axis('off')

            plt.subplot(1, 3, 3)
            plt.imshow(masked_centered, cmap='gray')
            plt.title('Masked & Scaled')
            plt.axis('off')
            plt.show()


    return (
        np.array(centers_radii),         # (N, 3)
        np.array(masked_centered_images), # (N, H, W)
        np.array(aligned_images),        # (N, H, W)
        np.array(scaled_images)          # (N, H, W)
    )




def compute_and_plot_combinations(aligned_imgs):
    """
    aligned_imgs: np.array of shape (4, H, W), ordered [Rr, Br, Rl, Bl]
    """
    Rr, Br, Rl, Bl = aligned_imgs
    eps = 1e-6 # small value to avoid divide-by-zero

    # Combinations
    magnetoR = Rr - Rl
    magnetoB = Br - Bl
    DopR = Rr - Br
    DopL = Rl - Bl

    Dopplergram = ((Br - Rr) / (Rr + Br + eps)) + ((Bl - Rl) / (Rl + Bl + eps))
```

```
    Magnetogram = ((Br - Rr) / (Rr + Br + eps)) - ((Bl - Rl) / (Rl + Bl + eps))

    # Prepare for plotting
    images = [magnetoR, magnetoB, Magnetogram, DopR, DopL, Dopplergram]
    titles = ["Magneto R", "Magneto B", "Magnetogram", "Doppler R",
              "Doppler L", "Dopplergram"]
    cmaps = ['Greys','Greys','Greys','seismic','seismic','seismic']

    fig, axs = plt.subplots(2, 3, figsize=(16, 10))
    axs = axs.flatten()

    for i, ax in enumerate(axs):
        im = ax.imshow(images[i], cmap=cmaps[i], origin='lower')
        ax.set_title(titles[i])
        ax.axis('off')
        plt.colorbar(im, ax=ax, shrink=0.75)

    plt.tight_layout()
    plt.show()

    return {
        'magnetoR': magnetoR,
        'magnetoB': magnetoB,
        'DopR': DopR,
        'DopL': DopL,
        'Dopplergram': Dopplergram,
        'Magnetogram': Magnetogram
    }

def save_grams_multi(root_dir, base_name, masked, aligned, product_name):
    hdu_primary = fits.PrimaryHDU(masked)
    hdu_aligned = fits.ImageHDU(aligned, name="ALIGNED")
    hdul = fits.HDUList([hdu_primary, hdu_aligned])
    hdul.writeto(root_dir / f"{base_name}_{product_name}.fits", overwrite=True)

def process_filtergrams(images, output_basename="output", save_dir=".",
                        min_radius=390, max_radius=420, dp=1.2,
                        param1=10, param2=30, invert=False, show_debug=False,
                        r_target=None):

    save_dir = Path(save_dir)
    doppler_dir = save_dir / "Dopplergrams"
    magneto_dir = save_dir / "Magnetograms"
    intensity_dir = save_dir / "Intensitygrams"
    for d in [doppler_dir, magneto_dir, intensity_dir]:
```

```
    d.mkdir(parents=True, exist_ok=True)

centers_radii = []
masked_centered_images = []
aligned_images = []
scaled_images = []

h, w = images[0].shape
center_target = np.array([w//2, h//2])

for idx, img in enumerate(images):
    # Normalize
    p1, p99 = np.percentile(img, [1, 99])
    norm = np.clip((img - p1) / (p99 - p1), 0, 1)
    if invert:
        norm = 1 - norm

    norm_blur = filters.gaussian(norm, sigma=1.5)
    frame_8bit = (255 * norm_blur).astype(np.uint8)

    # Detect circle
    circles = cv2.HoughCircles(
        frame_8bit, cv2.HOUGH_GRADIENT, dp=dp,
        minDist=1000, param1=param1, param2=param2,
        minRadius=min_radius, maxRadius=max_radius
    )
    if circles is None:
        raise RuntimeError(f"No circle found in image {idx}")
    cx, cy, r = np.uint16(np.around(circles[0,0]))
    centers_radii.append([cx, cy, r])

    # Shift image
    shift_x = center_target[0] - cx
    shift_y = center_target[1] - cy
    aligned = ndi_shift(img, shift=(shift_y, shift_x), order=1,
                        mode='constant', cval=0)
    aligned_images.append(aligned)

    # Masked image
    yy, xx = np.indices(aligned.shape)
    mask = np.sqrt(((xx - center_target[0])**2 + (yy - center_target[1])**2))
        <= r
    masked_centered = np.where(mask, aligned, np.nan)
    masked_centered_images.append(masked_centered)
```

```
        # Optional scaling
        if r_target is not None:
            scale = r_target / r
            rescaled = rescale(aligned, scale, order=1, preserve_range=True,
                               anti_aliasing=True, mode='constant')
            # Crop/rescale to original shape
            rh, rw = rescaled.shape
            y_offset = max(0, (rh - h)//2)
            x_offset = max(0, (rw - w)//2)
            cropped = rescaled[y_offset:y_offset+h, x_offset:x_offset+w]
            fixed = np.zeros((h, w), dtype=img.dtype)
            fixed[:cropped.shape[0], :cropped.shape[1]] = cropped
            scaled_images.append(fixed)
        else:
            scaled_images.append(aligned)

        if show_debug:
            import matplotlib.pyplot as plt
            plt.figure(figsize=(10,4))
            plt.subplot(1,3,1)
            plt.imshow(img, cmap='gray')
            plt.scatter(cx, cy, c='r')
            plt.title('Original')
            plt.axis('off')
            plt.subplot(1,3,2)
            plt.imshow(aligned, cmap='gray')
            plt.title('Aligned')
            plt.axis('off')
            plt.subplot(1,3,3)
            plt.imshow(masked_centered, cmap='gray')
            plt.title('Masked & Aligned')
            plt.axis('off')
            plt.show()

    centers_radii = np.array(centers_radii)
    masked_centered_images = np.array(masked_centered_images)
    aligned_images = np.array(aligned_images)
    scaled_images = np.array(scaled_images)


    return centers_radii, masked_centered_images, aligned_images

def make_grams(imgs,debug):
    Rr, Br, Rl, Bl = imgs
    eps = 1e-6 # small value to avoid divide-by-zero
```

```
# Combinations
magnetoR = Rr - Rl
magnetoB = Br - Bl
DopR = Rr - Br
DopL = Rl - Bl

Dopplergram = ((Br - Rr) / (Rr + Br + eps)) + ((Bl - Rl) / (Rl + Bl + eps))
Magnetogram = ((Br - Rr) / (Rr + Br + eps)) - ((Bl - Rl) / (Rl + Bl + eps))
Intensitygram = Rr + Br + Rl +Bl

Dop_stack=np.stack([Dopplergram,DopR,DopL],axis=0)
Mag_stack=np.stack([Magnetogram,magnetoR,magnetoB],axis=0)

Dop_stack_cal=[]
Mag_stack_cal=[]

for i in Dop_stack:
    rot_dop=rotate_with_nan(i, rotational_correction)
    scale_dop=normalize_and_scale(rot_dop,'doppler',scale=True)
    scale_dop.append(Dop_stack_cal)
for i in Mag_stack:
    rot_mag=rotate_with_nan(i, rotational_correction)
    scale_mag=normalize_and_scale(rot_mag,'magneto',-1,1,scale=True)
    scale_mag.append(Mag_stack_cal)
Dop_stack_cal=np.array(Dop_stack_cal)
Mag_stack_cal=np.array(Mag_stack_cal)

Igram_rot=rotate_with_nan(Intensitygram,rotational_correction)
Intensitygram_norm=normalize_and_scale(Igram_rot,'igram',scale=False)

if debug == True:
  images = [magnetoR, magnetoB, DopR, DopL, Dopplergram, Magnetogram]
  titles = ["Magneto R", "Magneto B", "Doppler R", "Doppler L",
            "Dopplergram", "Magnetogram"]

  fig, axs = plt.subplots(2, 3, figsize=(16, 10))
  axs = axs.flatten()

  for i, ax in enumerate(axs):
      im = ax.imshow(images[i], cmap='seismic', origin='lower')
      ax.set_title(titles[i])
      ax.axis('off')
      plt.colorbar(im, ax=ax, shrink=0.75)
```

```
      plt.tight_layout()
      plt.show()

    return Dop_stack_cal,Mag_stack_cal,Intensitygram_norm


def batch_process_fits(file_list, save_dir):
    for file_path in file_list:
        print(f"Processing: {file_path}")

        masked_dir = save_dir / "Masked"
        unmasked_dir = save_dir / "Unmasked"

        masked_doppler_dir = masked_dir / "Dopplergrams"
        masked_magneto_dir = masked_dir / "Magnetograms"
        masked_intensity_dir = masked_dir / "Intensitygrams"

        unmasked_doppler_dir = unmasked_dir / "Dopplergrams"
        unmasked_magneto_dir = unmasked_dir / "Magnetograms"
        unmasked_intensity_dir = unmasked_dir / "Intensitygrams"

        # Create them
        for d in [
                masked_doppler_dir, masked_magneto_dir, masked_intensity_dir,
                unmasked_doppler_dir, unmasked_magneto_dir,
                unmasked_intensity_dir]:
            d.mkdir(parents=True, exist_ok=True)



        with fits.open(file_path, memmap=False) as hdul:
            data = hdul[0].data
            if data.ndim != 2:
                raise ValueError(f" got shape {data.shape}")

            # Split the data into quadrants
            X, Y = data.shape
            mid_x, mid_y = X // 2, Y // 2

            Rr = data[0:mid_x, 0:mid_y]   # Top-left
            Rl = data[0:mid_x, mid_y:]    # Top-right
            Br = data[mid_x:, 0:mid_y]    # Bottom-left
            Bl = data[mid_x:, mid_y:]     # Bottom-right

            filtergrams = [Rr, Br, Rl, Bl]
```

```
            base_name = os.path.splitext(os.path.basename(file_path))[0]

            try:
                centers_radii, masked_centered_images, aligned_images= \
                    process_filtergrams(filtergrams)

                aligned_dop_stack,aligned_mag_stack,aligned_intensity= \
                    make_grams(aligned_images,debug=True)
                fits.writeto(unmasked_doppler_dir/ f"{base_name}_doppler.fits",
                            aligned_dop_stack,overwrite=True)
                fits.writeto(unmasked_magneto_dir/ f"{base_name}_magneto.fits",
                            aligned_mag_stack,overwrite=True)
                fits.writeto(unmasked_intensity_dir /
                            f"{base_name}_intensity.fits",aligned_intensity,
                            overwrite=True)

                masked_dop_stack,masked_mag_stack,masked_intensity= \
                make_grams(masked_centered_images,debug=True)
                fits.writeto(masked_doppler_dir/
                            f"{base_name}_masked_doppler.fits",
                            masked_dop_stack,overwrite=True)
                fits.writeto(masked_magneto_dir/
                            f"{base_name}_masked_magneto.fits",
                            masked_mag_stack,overwrite=True)
                fits.writeto(masked_intensity_dir /
                            f"{base_name}_masked_intensity.fits",
                            masked_intensity,overwrite=True)

            except RuntimeError as e:
                print(f"      Skipping {file_path}: {e}")

            # Free memory explicitly
            del hdul, data, Rr, Br, Rl, Bl, filtergrams

def rotate_with_nan(image, angle, reshape=True):
    nan_mask = np.isnan(image)
    # Temporarily replace NaNs with 0 (or any neutral value)
    image_filled = np.where(nan_mask, 0, image)
    # Rotate the filled image
    rotated = rotate(image_filled, angle, reshape=reshape, order=1)
    # Rotate the mask to know where NaNs should be
    rotated_mask = rotate(~nan_mask, angle, reshape=reshape, order=0). \
    astype(bool)
    # Reapply NaNs to the rotated image
    rotated[np.logical_not(rotated_mask)] = np.nan
```

```
    return rotated
def normalize_and_scale(arr,gram='default',smin=-1,smax=1,scale=True):
    arr=arr.astype(float).copy()

    if gram.lower()=='intensity':
        min_val=np.nanmin(arr)
        max_val=np.nanmax(arr)
        arr_norm=(arr-min_val)/(max_val-min_val)
        arr_norm[np.isnan(arr)]=np.nan
        return arr_norm if scale else arr_norm

    else:
        max_abs=np.nanmax(np.abs(arr))
        arr_norm=arr/max_abs
        arr_norm[np.isnan(arr)]=np.nan

    if not scale:
        return arr_norm

    if gram.lower()=='doppler':
        arr_rescaled=arr_norm*2
    else:
        arr_rescaled=((arr_norm+1)/2)*(smax-smin)+smin
    arr_rescaled[np.isnan(arr)]=np.nan
    return arr_rescaled

def limb_darkening_correction(image, center=None, radius=None):
    #basic limb darkening correction
    ny, nx = image.shape

    if center is None:
        x0, y0 = nx / 2, ny / 2
    else:
        x0, y0 = center

    if radius is None:
        radius = min(nx, ny) / 2

    y, x = np.indices(image.shape)
    r = np.sqrt((x - x0)**2 + (y - y0)**2)

    mu = np.sqrt(1 - (r / 410)**2)
    mu[r > radius] = np.nan
```

```
    # Simple limb darkening model (can be tuned)
    # I( )/I(1) = 1 - u * (1 - )
    u = 0.6
    limb_profile = 1 - u * (1 - mu)

    corrected = image / limb_profile

    plt.imshow(limb_profile)

    return corrected

def resample(data, resample_time, cadence_seconds=5):

    frames_per_chunk = (resample_time * 60) // cadence_seconds # minutes
    n_frames, x, y = data.shape
    n_chunks = n_frames // frames_per_chunk

    # Trim to a multiple of chunk size
    trimmed_data = data[:n_chunks * frames_per_chunk]

    # Reshape and sum
    reshaped = trimmed_data.reshape(n_chunks, frames_per_chunk, x, y)
    summed = reshaped.sum(axis=1)

    return summed

def fit_2d_poly(x, y, z, deg=3):
    """
    Fit a 2D polynomial of given degree to the data points (x, y, z).
    Returns the fitted values on the original grid.
    """
    # Build design matrix
    G = []
    for i in range(deg + 1):
        for j in range(deg + 1 - i):
            G.append((x**i) * (y**j))
    G = np.stack(G, axis=-1)

    # Solve least squares
    coeffs, _, _, _ = np.linalg.lstsq(G, z, rcond=None)

    return coeffs
def model_rotation_field(dopplergram, mask, deg=3):
    """
    Fit and return the smooth rotation pattern in the masked dopplergram.
```

```
    """
    yy, xx = np.indices(dopplergram.shape)
    x = xx[mask].ravel()
    y = yy[mask].ravel()
    z = dopplergram[mask].ravel()

    # Fit polynomial
    coeffs = fit_2d_poly(x, y, z, deg=deg)

    # Reconstruct model on full grid
    G_full = []
    for i in range(deg + 1):
        for j in range(deg + 1 - i):
            G_full.append((xx**i) * (yy**j))
    G_full = np.stack(G_full, axis=0)

    model = np.tensordot(coeffs, G_full, axes=1)

    return model
#%% Create reduced directories

reduced_direct = direct / "Reduced_data"
master_calibration_direct = calibration_direct / "master_calibrations"

reduced_direct.mkdir(parents=True, exist_ok=True)
master_calibration_direct.mkdir(parents=True, exist_ok=True)

print(f"Directory '{reduced_direct}' created successfully.")
print(f"Directory '{master_calibration_direct}' created successfully.")

#%% load all calibration images
file_types=['Darks','Leakthrough','Flats','Solo_MOF','Glow/MOF','Glow/MOF_WS']
directs = {f"directory_{i}": calibration_direct / i for i in file_types}

calibration_data = {}
for ft in file_types:
    dir_path = directs[f"directory_{ft}"]
    calibration_data[ft] = load_fits_images(dir_path)

#%% create mean calibration images
#darks
mean_dark=np.mean(calibration_data['Darks'],axis=0)
med_dark=medfilt2d(mean_dark,kernel_size=3)
save_to_fits(med_dark, 'master_dark',master_calibration_direct)
```

```
#glow
mean_glow_mof=np.mean(calibration_data['Glow/MOF'],axis=0)
#save_to_fits(mean_glow_mof,'master_glow_mof',master_calibration_direct)

mean_glow_mof_ws=np.mean(calibration_data['Glow/MOF_WS'],axis=0)
#save_to_fits(mean_glow_mof_ws,'master_glow_mof_ws',master_calibration_direct)

#leakthrough
mean_leak=np.mean(calibration_data['Leakthrough'],axis=0)
med_leak=medfilt2d(mean_leak,kernel_size=3)
leak_dcorr=med_leak-med_dark
save_to_fits(leak_dcorr,'master_leak',master_calibration_direct)

#flats
flat_sum=0
for f in calibration_data['Flats']:
    flat_dcorr=f-med_dark
    #flat_lcorr=flat_dcorr-mean_leak
    #flat_gcorr=flat_dcorr-mean_glow_mof
    flat_sum+=flat_dcorr
flat_blur=gaussian_filter(flat_sum,sigma=4)
flat_norm=flat_blur/np.max(flat_blur)
flat_norm[flat_norm==0]==0.001
save_to_fits(flat_norm,'master_flat_norm',master_calibration_direct)

mean_flat=np.mean(calibration_data['Flats'],axis=0)
flat_dcorr=mean_flat-med_dark
flat_lcorr=flat_dcorr-mean_leak
flat_gcorr=flat_lcorr-mean_glow_mof
save_to_fits(flat_gcorr,'master_flat',master_calibration_direct)

#%% apply calibrations to all hours folders

hdrs,hdus,master_dark=open_fits(master_calibration_direct/
                            f'master_dark.fits')
hdrs,hdus,master_leak=open_fits(master_calibration_direct/
                            f'master_leak.fits')
hdrs,hdus,master_flat=open_fits(master_calibration_direct/
                            f'master_flat_norm.fits')
hdrs,hdus,master_glow=open_fits(master_calibration_direct/
                            f'master_glow_mof_ws.fits')

hour_dirs = [p.name for p in direct.glob(f"{date_us}_*") if p.is_dir()]

master_glow=np.zeros_like(master_flat)
```

```
for hour in sorted(hour_dirs):
    process_hour(hour, direct, reduced_direct, master_dark, master_leak,
                 master_flat, master_glow)

#%% Make intensity, doppler, and magnetograms and saves to new folders
#loops through all of the hours

hour_dirs = [p for p in reduced_direct.glob(f"{date_us}_*") if p.is_dir()]

for hour in sorted(hour_dirs):
    file_list = sorted(hour.glob('*.fit*'))
    save_dir = hour / 'Grams'
    save_dir.mkdir(parents=True, exist_ok=True)

    batch_process_fits(file_list, save_dir)

#%%
'''
Below are cells to resample the cadence and do rotational subtraction from the
Dopplergrams
'''
#%%Resample grams
direct=save_dir /r'Grams'
dop_direct=direct /r'Dopplergrams'
mag_direct=direct / r'Magnetograms'
inten_direct=direct / r'Intensitygrams'
dops=sorted(dop_direct.glob('*doppler*.fits'))
mags=sorted(mag_direct.glob('*magneto*.fits'))
intens=sorted(inten_direct.glob('*intensity*.fits'))

dgram=np.zeros((984,982))
mgram=np.zeros((984,982))
igram=np.zeros((984,982))

dgrams=[]
dgramr=[]
dgraml=[]

mgrams=[]
mgramr=[]
mgramb=[]

igrams=[]
```

```
for f,g,h in zip(dops,mags,intens):
    with fits.open(f) as hdul:
        data_dop = hdul[0].data
    dgram += data_dop[0]
    dgramr.append(data_dop[1])
    dgraml.append(data_dop[2])
    dgrams.append(data_dop[0])
    with fits.open(g, memmap=False) as hdul:
        data_mag = hdul[0].data
    mgram += data_mag[0]
    mgramr.append(data_mag[1])
    mgramb.append(data_mag[2])
    mgrams.append(data_mag[0])
    with fits.open(h, memmap=False) as hdul:
        data_inten = hdul[0].data
    igram += data_inten
    igrams.append(data_inten)

dgrams=np.array(dgrams)
dgramr=np.array(dgramr)
dgraml=np.array(dgraml)

mgrams=np.array(mgrams)
mgramr=np.array(mgramr)
mgramb=np.array(mgramb)

igrams=np.array(igrams)


fits.writeto(os.path.join(save_dir, "60min_dopplergram_sum.fits"),dgram,
            overwrite=True)
fits.writeto(os.path.join(save_dir, "60min_magnetogram_sum.fits"),mgram,
            overwrite=True)
fits.writeto(os.path.join(save_dir, "60min_intensitygram_sum.fits"),igram,
            overwrite=True)

fits.writeto(os.path.join(save_dir, "Dopplergrams.fits"),dgrams,
            overwrite=True)
fits.writeto(os.path.join(save_dir, "RHCP_Dopplergrams.fits"),dgramr,
            overwrite=True)
fits.writeto(os.path.join(save_dir, "LHCP_Dopplergrams.fits"),dgraml,
            overwrite=True)

fits.writeto(os.path.join(save_dir, "Magnetograms.fits"),mgrams,
            overwrite=True)
```

```
fits.writeto(os.path.join(save_dir, "RW_magnetograms.fits"),mgramr,
            overwrite=True)
fits.writeto(os.path.join(save_dir, "BW_magnetograms.fits"),mgramb,
            overwrite=True)


#%% SUM UP FOR 10 MINUTES
resample_time=10 #10 minute resample

dopplergrams_resampled=resample(dops,resample_time,cadence)
magnetograms_resampled=resample(mags,resample_time,cadence)

for i, f in enumerate(magnetograms_resampled, start=1):
    filename = f"10min_resampled_magnetogram_{i}.fits"
    save_to_fits(f, filename, save_dir)
for i, f in enumerate(dopplergrams_resampled, start=1):
    filename = f"10min_resampled_dopplergram_{i}.fits"
    save_to_fits(f, filename, save_dir)


#%% rotational subtraction
dopplergram=dopplergrams_resampled[0]

mask = ~np.isnan(dopplergram)
rotation_model = model_rotation_field(dopplergram, mask, deg=3)
residual_dopplergram = dopplergram - rotation_model

fits.writeto(os.path.join(save_dir, "rotation_subtracted_doppler.fits"),
           residual_dopplergram, overwrite=True)
```

F Miscellaneous GATES Testing and Procedures

To make this document as comprehensive as possible regarding the production, operation, and maintenance of the GATES Network, I include in this appendix a collection of resources and images that do not clearly fit in other sections. Topics covered in this final appendix include cell cleaning, flat field testing, and telescope alignment.

A Cell Cleaning

A.1 Alkali Metal Cells (Example: TSST-K WS)

When stored vertically for long periods of time or if quickly rotated vertically while being heated, the alkali metal cells, particularly the reservoir cells, run the risk of having the deposited metal migrating within the cell. This migration can cause multiple problems. Primarily, if the metal has solidified outside of the heated regime of the cell, it will not vaporize, and the proper vapor pressure for MOF function will not be reached. Secondly, if the migrated metal solidifies in a particularly dense shape, it might vignette the beam. However, as long as the metal has not condensed on the windows of the cell, the metal should be able to be manually moved back to the reservoirs to return the cells to their previous function.

During the TSST-K's storage from 2020 to 2023, potassium deposits in the WS migrated out of their reservoirs into the body of the cell, forming a deposit outside the heated zone of the cell and thereby preventing proper vaporization. Detailed below is the procedure used to clean the TSST-K's WS cell. This procedure is best performed with two people.

1. Remove the cell from the magnet enclosure. It is crucial to ensure the magnet enclosure is opened in parallel using the brass magnet-pulling screws.

2. Remove any heat-resistant tape to expose the migrated potassium and the heating filament (retain the piece between the wells to protect the connecting wire).

3. Unwind the heating filament to expose the glass of the reservoir.

4. Hold the cell at an angle such that the reservoir in which you are redepositing the potassium is below the migrated potassium, and the cross wire remains on the top of the cell (so that the potassium in the reservoir does not form a path to flow out of the reservoir when heated.

5. Using a soldering iron, heat the area with the migrated metal to liquefy it. Simultaneously, gently tap the cell to agitate the liquid metal so that it will flow toward the reservoir (to be done in small spurts). NOTE: Thin deposits of metal in the body of the cell are more difficult to move as their mass does not reach a critical weight to overcome their surface tension. Therefore, it is advantageous to combine larger deposits with smaller ones before migrating everything back to the reservoir.

6. Rewind the heating filaments and reapply the heat-resistant tape.

7. Heat cell to full temperature to allow for preliminary tape melting. Ensure that the cell's reservoirs remain parallel to the table.

8. Place the cell back in the magnet enclosure, once again using the brass screws to close.

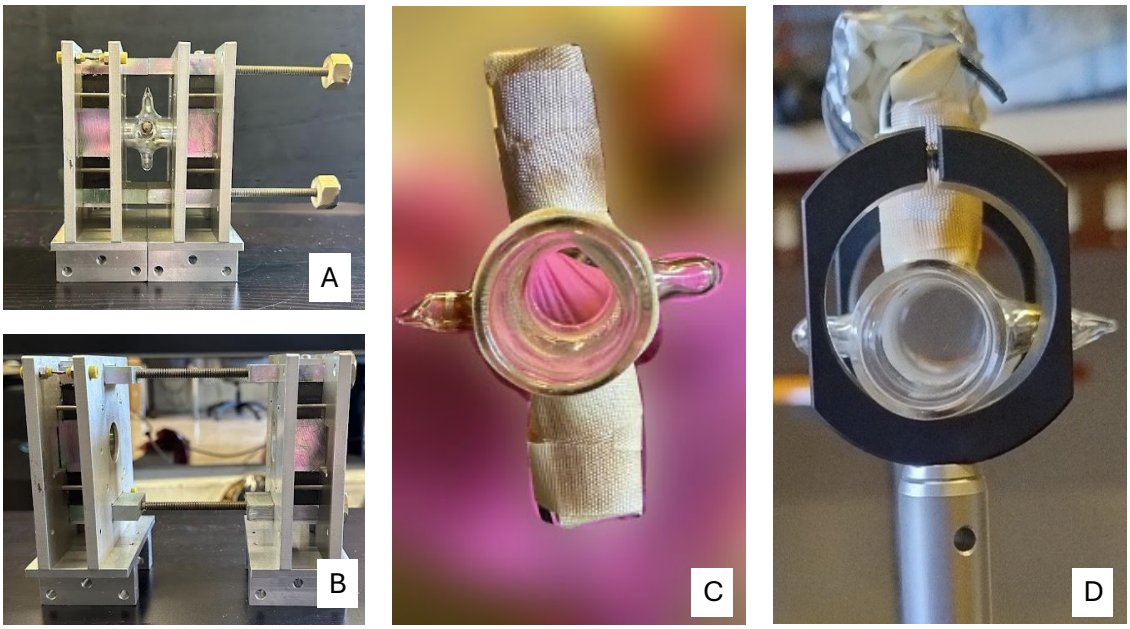

Figure 39 Images taken during the process of cleaning the TSST-K WS on May 26, 2025. A) magnet enclosure closed and B) open with designated brass screws. C) cell prior to cleaning, with migrated potassium visible in the upper right quadrant. D) cell after cleaning during heating test of step 7.

A.2 He Cells

Unlike the alkali metal cells the He cell "cleaning" is a preventative measure to take during the process of filling the cell. Since the He I 1083 nm line is a metastable line, and contaminants in the cell will cause rapid depopulation of the He triplet. These contaminants most notably arise from species being agitated out of the glass of the cell during the repeated process of ionizing the He with RF power. Over time, these contaminants will lower the critical population of metastable He and lower the cells' function. To combat this, during the process of filling the He cells, we flush the cells with pure He while irradiating with microwaves so that He is absorbed into the glass. This extends the cell's lifetime by making the "contaminant" that agitates out of the glass is He itself.

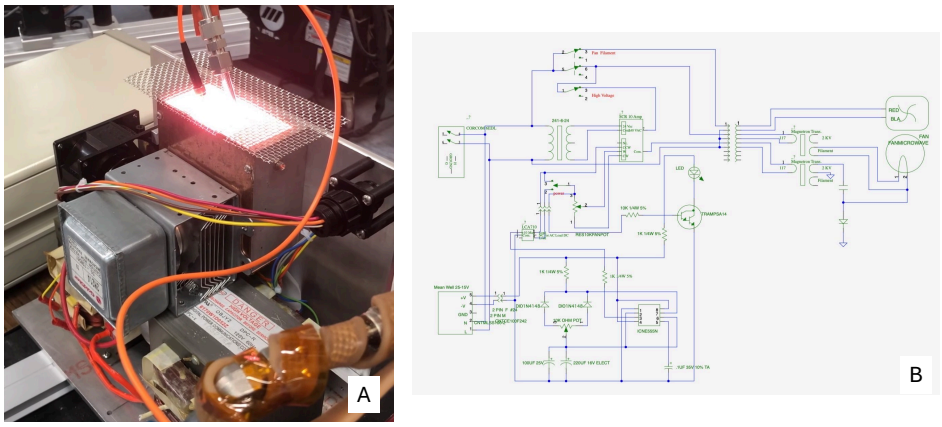

Figure 40 A) Image taken during the process of He cell cleaning using the microwave oven described in the circuit diagram in B).

Figure 40 depicts the set-up for cleaning and irradiating the He cells completed in May 2022. Through the process of cleaning the cells, we were able to significantly reduce the contaminant oxygen lines by. Although this cell is not the same as the one that was used for the October 2025 He MOF observation tests, a similar cleaning process was performed on those cells when they were created. The exact process for cleaning the He cells is as follows:

- Physically wash the cell with deionized water to remove any dust.
- Connect the open end of the cell to a vacuum and bake the cell at high (300° - 400°) for a few days to remove any remaining liquid water.
- Fill the cell with a high pressure ($\sim$ 10 torr) of pure He gas. Using a spectrometer measure the contaminants in the cell. At this point there should be notable molecular lines.
- Flush the cell quickly with high pressure then let it sit under vacuum for a few minutes. Repeat this step 2-3 times, or until the molecular lines decrease.
- The most notable remaining contaminants are the result of water: Hα and O I 777

nm will be the most prominent/useful. Continue quickly flushing the cells with a lower pressure of He gas (∼3 - 3.5 torr) followed by time under vacuum to lower these contaminants' lines.

- Keep the cell under vacuum for 2+ hours.
- Repeat He flushing as necessary until contaminant lines remain negligible after extended vacuum time. In order to prevent non-resonant collisions (which produce higher energy and can more quickly become dangerous for the integrity of the cell in the microwave), repeating this step is critical.
- Place the He cell in the microwave oven and continue to repeatedly flush quickly with He. This step is to dissolve He into the glass so that when the cells are scientifically operated (irradiated with RF power), the gaseous He in the cell necessary for producing metastable lines does not then dissolve into the glass.
- Fill the cell with the desired pressure of neutral He ($\sim 1 - 2\ torr$) before sealing the glass tube.

B Flat Field Acquisition

Flat field correction is done to correct for pixel-to-pixel variations in device sensitivity. Conceptually, the procedure is simple: a perfectly uniform, or "flat" image is acquired with the complete observing system by observing a flat target. Any nonuniformities in the acquired image are then consequently caused by different sensitivities in the system, and can be corrected for in science images by dividing the science image by the flat field image. In practice, achieving these perfectly flat images in complicated by multiple factors. Firstly, it is difficult

to acquire a perfectly uniform target. Secondly, instrument sensitivity responses tend to vary with wavelength. Finally, it is difficult to ensure that the "complete observing system" remains unchanged between calibrations and science acquisition.

To acquire the "flattest" images, flat field images are typically taken one of two ways: sky flats or dome flats. Sky flats refer to images taken on the (relatively) bright twilight sky to acquire a uniform image. Dome flats are taken by imaging an illuminated flat portion of the dome. However, for solar observations, these methods do not provide sufficient accuracy in representing the scientific observations (in terms of beam geometry, light level, or temperature distribution inside of the instrument) (Hölken et al. 2024), and consequently, it is standard to use the Sun itself as the illumination source. As the Sun is inherently a non-uniform source, methods must be taken to achieve a flat image. Typically, when acquiring a flat field image from an extended, non-uniform source, it is done by shifting the image on the sensor and acquiring a mean of multiple images (Tyson 1986) or least squares estimate (KLL method: Kuhn et al. (1991)).

Although we plan to implement a KLL method for future flat field acquisition, for GATES' preliminary observing runs in the summer of 2025, we simply used a diffusive filter applied to the front of the telescopes' entrances. We tested multiple LEE Filters with various diffusive properties (Table 23). We chose to use the LEE 250 with the TSST and the LEE 253 with MSO to maximize transmission while still ensuring a maximally diffused image.

Table 23 A comparison of the reported properties of the LEE Filters' Diffusion Pack. "Transmission Y" denotes the percentage of light transmitted by the filter. "Stop" is a photographic term which describes the amount of light reduction; each stop cuts the light by 50% (i.e. 1/2 stop cuts the light by 25%).

Filter No.	Transmission Y	Absorption	Stop
216	36	-	1.5
250	60	0.22	0.75
251	80	0.1	-
253	-	-	<0.25
400	36	0.44	1.5
410	71	-	0.5

C GATES Alignment Procedures

C.1 TSST Alignment

The alignment procedure for the TSST has been detailed in Appendix F of Chiodini (2025). The telescope is aligned optically utilizing an elliptical 656 *nm* laser, two custom pinhole dimes (used as targets), and a shearing interferometer (to ensure collimation). The alignment procedure is undertaken on the optical bench in the SPSW Lab at UTOV to ensure maximum stability, maintain proper optical cleanliness, and allow for the use of the heliostat for full alignment.

C.2 MSO Optical Alignment

The MSO telescope is aligned in the Eddy Co. clean room to also enable proper optics cleaning. The alignment is performed optically in two steps utilizing an elliptical 532 nm laser. Firstly, each optic is aligned individually using two pinholes and a flat mirror to

ensure aligned transmission and back reflection (Figure 41 top). Subsequently, the laser is mounted to the front of the telescope with an extending rail (Figure 41 bottom) so that the two channels can be co-aligned; in this step, all optics' alignment is double-checked to ensure that the combination of optics is not causing beam deviation. Both of these alignment steps utilize two precision targets which have pinholes drilled at 5.585 cm above the rail height (the nominal beam height). The full procedure for aligning the telescope can be found below.

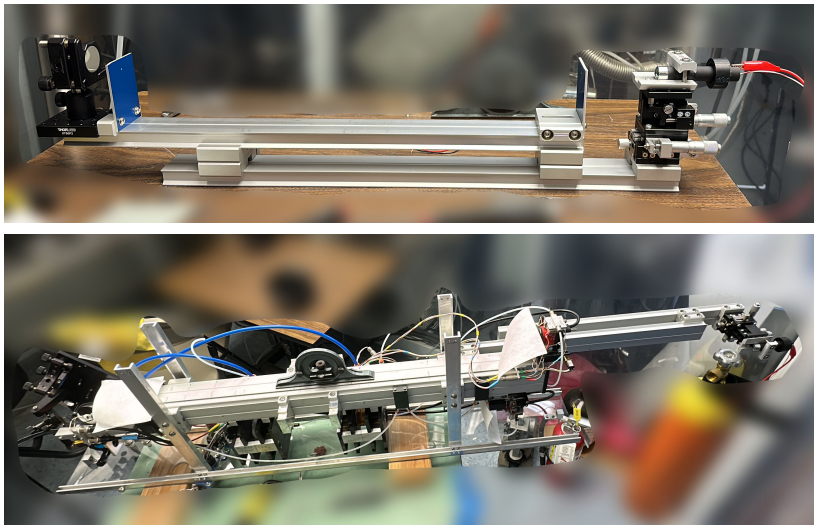

Figure 41 Top: individual optic alignment rail featuring the 532 nm laser, the precision pinhole targets, and the flat mirror. Bottom: aerial view of the full telescope alignment featuring the rail extension holding the 532 nm rail (right).

1. *Laser Alignment: Initial*

   (a) Mount the laser, pinholes, and flat mirror in the orientation depicted in Figure 41.

   (b) With the laser mounted on the XYZ adjustable plates, adjust the laser's position such that the beam is aligned through both pinholes and its reflection off the flat mirror returns through pinhole 1.

2. *Individual Optic Alignment*

(a) Mount each optic individually at the center of the rail with proper orientation (note: since the Na channel is "upside down" for the alignment procedure, its optics will be oriented "backwards" on the alignment rail).

(b) Align each optic such that its transmission properly passes through pinhole 2 and any front reflections off the optics properly pass through pinhole 1.

(c) If an adjustment is needed, place a shim under the mount of the optic.

(d) For polarization optics (ex., polarizers, QWP, HWP), align with just the optic's reflection on pinhole 1.

3. *Laser Alignment: on Telescope*

(a) Cover the cameras to protect the CMOS detectors from the laser

(b) Attach the rail extender (removing both pinholes and the flat mirror) to the main telescope rail using 2 double dovetail clamps for maximum rigidity (clamps go in place of pinhole 2 and the flat mirror from the individual optic set-up).

(c) Using level, ensure the rail extender is flat with respect to the main telescope rail.

(d) Attach irises to both ends of the main telescope rail (an iris typically is already attached to the mirror-side of the rail as part of the optical scheme), and close them to their smallest positions.

(e) Adjust the height of the laser so that the beam properly passes through iris 1 (at the front aperture of the telescope).

(f) Ensure the beam properly passes through the second iris (if properly aligned in step 1, only the height adjustment should be required).

(g) Keep iris 1 fully closed to serve as a pinhole for the laser.

4. *Mirror Alignment*

(a) With all optics except the BS and M removed, place the pinholes at the front and end of the rail.

(b) Align the M_K so that the beam remains flat and passes through each pinhole.

(c) Move pinholes to Na channel and align M_{Na} with the same procedure.

(d) If achieving a simultaneous alignment with both channels mirrors proves unsuccessful, adjust the BS by slightly tightening/loosening its 3 set screws.

(e) Return to aligning the two mirrors until a sufficient alignment is reached with both channels

5. *Individual Channel Alignment*

(a) Mount a pinhole at the CAM end of the rail.

(b) Mount the first optic in the beampath (QWP1) and adjust position using shims until its transmitted beam is aligned with the pinhole.

(c) Continue adding each optic in its proper distance in the beampath, adjusting their position with shims to maintain the flat beam.

(d) Skip P2, the MOF, and WS to allow for the beam to remain present for the back optics.

(e) Once all other optics are in place, place P2 and check its reflection back to iris 2 for beam alignment.

(f) Place the MOF and WS magnet assemblies back in place.

(g) Remove P2 to perform CAM alignment.

(h) Uncover the CAM, ensure the power of the laser is low, and adjust camera height (via motorized XYZ mounts) such that the image is in the center of the detector.

(i) Replace P2.

(j) Repeat procedure for other channel.

(k) Remove the laser's rail and iris 1.

(l) Replace L1 (directly screws to the front of the rail).

(m) Rebuild the enclosure box.

C.3 MSO Polarization Alignment

The beginning of the polarization alignment of the telescope is the alignment of P1 to allow for strictly linearly polarized light to pass through. Currently, this is done by placing the optic on a precision bench and

The polarization alignment of the MSO channels occurs when the telescope is mounted in the MSO dome, utilizing the Sun and the various tabs of the LabVIEW GUI (referred to as GUI here for brevity). The entire procedure is performed with both the MOF and WS off. In addition to the channel's optics, the alignment procedure utilizes two test polarizers (TP1 and TP2). These test polarizers may have lower extinction ratios than the actual P1 and P2. It is worth noting that any time a polarizer is removed, it is good practice to cover the CMOS so as not to overwhelm the detector with the incoming solar radiation.

1. *Polarizer Alignment*

(a) Align P1 mechanically with a precision bench so to ensure the optic square is parallel

to the bench and therefore allows pure linear polarized light through.

(b) Mount both P1 and P2 onto the telescope.

(c) Remove QWP1 and DT from the beam path.

(d) Using the waveform tab on the GUI, rotate polarizer 2 until a minimum amount of light passes through the system.

2. *Align QWP1 and DT*

(a) Replace P2 with TP2, and minimize the system transmission (if using test polarizers with extinction ratios similar to the actual system polarizers, proceed to slightly uncross TP2).

(b) Insert TP1 at the front of the telescope aperture (TP1 is mounted on a tube that fits exactly into the primary aperture) and rotate it to produce a maximum solar image brightness (best with waveform GUI tab).

(c) Insert DT and ensure it is connected to the driver.

(d) Using the magnetic field tab on the GUI, rotate the DT until the solar image is maximized (note location) and minimized (note location). The DT alignment position is the middle of these two positions. If utilizing a GUI with the individual polarization states, rotate the ST until one of the views disappears; this is the aligned position for DT.

(e) Re-insert QWP1 and follow the same procedure as 2d to align the QWP.

(f) Remove TP1 and TP2 (replace P2 in its place).

3. *Align QWP2*

(a) Replace P1 with TP2, and minimize the system transmission (should be 90° rotation from its current position).

(b) Rotate QWP1 until the two solar images are equal brightness (using the waveform tab on the GUI).

4. *Align the WA*

(a) Rotate the WA until the 2 solar images are even on the filtergram tab of the GUI.

(b) Replace P1.

REFERENCES

Abbasvand, V. et al. 2020, A&A, 642, A52

Agnelli, G., Cacciani, A., & Fofi, M. 1975, Solar Physics, 44, 509

Alfvén, H. 1942, Nature, 150, 405

Alvarez-Herrero, A. et al. 2011, in Society of Photo-Optical Instrumentation Engineers (SPIE) Conference Series, Vol. 8160, Polarization Science and Remote Sensing V, ed. J. A. Shaw & J. S. Tyo, 81600Y

Anastasiadis, A., Lario, D., Papaioannou, A., Kouloumvakos, A., & Vourlidas, A. 2019, Philosophical Transactions of the Royal Society of London Series A, 377, 20180100

Angryk, R. A. et al. 2020, Scientific Data, 7, 227

Antonucci, E. et al. 2020, A&A, 642, A10

Aparna, V. 2022, PhD thesis, Georgia State University

Appourchaux, T. 1987, Solar physics, 109, 393

Arregui, I. 2015, Philosophical Transactions of the Royal Society of London Series A, 373, 20140261

Aufdenberg, J. P. 2003, in Encyclopedia of Physical Science and Technology, 3rd edn., ed. R. A. Meyers (New York: Academic Press), 1–10

Babcock, H. W. 1961, ApJ, 133, 572

Bailén, F. J., Orozco Suárez, D., & del Toro Iniesta, J. C. 2023, Ap&SS, 368, 55

Balthasar, H. 2018, Sol. Phys., 293, 120

Barghouty, N., & Falconer, D. 2015, Magnetogram Forecast: An All-Clear Space Weather Forecasting System, NASA Technical Report 20160008033, NASA Marshall Space Flight Center

Barnes, G. et al. 2016, ApJ, 829, 89

Basu, S. 2016, Living Reviews in Solar Physics, 13, 2

Basu, S., Antia, H. M., & Tripathy, S. C. 1999, ApJ, 512, 458

Beckers, J. M. 1969, Sol. Phys., 9, 372

Berrilli, F. et al. 2010, Advances in Space Research, 45, 1191

Berrilli, F. et al. 2018, in IAU Symposium, Vol. 335, Space Weather of the Heliosphere: Processes and Forecasts, ed. C. Foullon & O. E. Malandraki, 348–351

Bertello, L. et al. 2022, Multi-height Measurements Of The Solar Vector Magnetic Field: A White Paper Submitted To The Decadal Survey For Solar And Space Physics (Heliophysics) 2024-2033

Bertello, L., Pevtsov, A., Tlatov, A., & Singh, J. 2016, Sol. Phys., 291, 2967

Bjørgen, J. P., Sukhorukov, A. V., Leenaarts, J., Carlsson, M., de la Cruz Rodríguez, J., Scharmer, G. B., & Hansteen, V. H. 2018, A&A, 611, A62

Blamont, J. E., & Roddier, F. 1961, Physical Review Letters, 7, 437

Bobra, M. G., Sun, X., Hoeksema, J. T., Turmon, M., Liu, Y., Hayashi, K., Barnes, G., & Leka, K. D. 2014, Sol. Phys., 289, 3549

Bornmann, P. L., & Shaw, D. 1994, Sol. Phys., 150, 127

Brooks, D. H., Baker, D., van Driel-Gesztelyi, L., & Warren, H. P. 2018, Nature Com-

munications, 9, 1466, uses full-disk solar observations to study disk-integrated coronal composition variation with solar cycle

Brosius, J. W., & Viall, N. M. 2020, in AGU Fall Meeting Abstracts, Vol. 2020, AGU Fall Meeting Abstracts, SH037–0004

Cacciani, A. 1981, Space Science Reviews, Volume 29, Issue 4, pp. 403-404, 29, 403

Cacciani, A., Cimino, M., & Fofi, M. 1971, in Symposium-International Astronomical Union, Vol. 43, Cambridge University Press, 94–98

Cacciani, A., Comari, M., Furlani, S., Hanslmeier, A., Messerotti, M., Moretti, P., Pettauer, T., & Veronig, A. 1998, in Three-Dimensional Structure of Solar Active Regions, Vol. 155, 265–269

Cacciani, A., di Martino, V., Hanslmeier, A., Messerotti, M., Moretti, P. F., Pettauer, T., & Veronig, A. 1998, in Astronomical Society of the Pacific Conference Series, Vol. 155, Three-Dimensional Structure of Solar Active Regions, ed. C. E. Alissandrakis & B. Schmieder, 229–233

Cacciani, A., Dolci, M., Giuliani, C., & Moretti, P. 1998a, in Structure and Dynamics of the Interior of the Sun and Sun-like Stars, Vol. 418, 381

Cacciani, A., & Fofi, M. 1978, Sol. Phys., 59, 179

Cacciani, A., Hanslmeier, A., Messerotti, M., Moretti, P., Otruba, W., Pettauer, T., & Rodgers, W. 1998bin , n/a

Cacciani, A., Jefferies, S. M., Finsterle, W., Rapex, P., Knox, A., Giebink, C., & di Martino, V. 2003, in ESA Special Publication, Vol. 517, GONG+ 2002. Local and Global

Helioseismology: the Present and Future, ed. H. Sawaya-Lacoste, 243–245

Cacciani, A., Marmolino, C., Moretti, P. F., Oliviero, M., Severino, G., & Smaldone, L. A. 1997, Mem. Soc. Astron. Italiana, 68, 467

Cacciani, A., Moretti, P., & Smith, E. 1995, in GONG 1994. Helio-and Astro-Seismology from the Earth and Space, Vol. 76, 440

Cacciani, A., & Moretti, P.-F. 1994, in Instrumentation in Astronomy VIII, Vol. 2198, SPIE, 219–228

Cacciani, A., Paverani, E., Smith, E., & Zirin, H. 1991, in Solar Polarimetry, 133–141

Cacciani, A., Rapex, P., Dolci, M., Reale, F., Landi, E., Stenflo, J., Bianda, M., & Moses, D. 2001, in Solar encounter. Proceedings of the First Solar Orbiter Workshop, Vol. 493, 177–181

Cacciani, A., Ricci, D., Rosati, P., Rhodes, E. J., Smith, E., Tomczyk, S., & Ulrich, R. K. 1990a, Nuovo Cimento C Geophysics Space Physics C, 13, 125

Cacciani, A., Varsik, J., & Zirin, H. 1990b, Sol. Phys., 125, 173

Calchetti, D. 2021, PhD thesis, University of Rome Sapienza

Calchetti, D., Viavattene, G., Berrilli, F., Del Moro, D., Giovannelli, L., & Oliviero, M. 2020a, in Journal of Physics Conference Series, Vol. 1548, Journal of Physics Conference Series, 012005

Calchetti, D. et al. 2020b, in Society of Photo-Optical Instrumentation Engineers (SPIE) Conference Series, Vol. 11445, Ground-based and Airborne Telescopes VIII, ed. H. K. Marshall, J. Spyromilio, & T. Usuda, 114452T

Calcines Rosario, A., Green, L. M., Smith, A., & Long, D. M. 2023, Aerospace, 10, 1028

Caplan, R. M., Mason, E. I., Downs, C., & Linker, J. A. 2023, ApJ, 958, 43

Centeno, R., Trujillo Bueno, J., Uitenbroek, H., & Collados, M. 2008, ApJ, 677, 742

Chaplin, W. J. et al. 1999, MNRAS, 308, 405

Charbonneau, P. 2020, Living Reviews in Solar Physics, 17, 4

Charbonneau, P., Christensen-Dalsgaard, J., Henning, R., Larsen, R. M., Schou, J., Thompson, M. J., & Tomczyk, S. 1999, ApJ, 527, 445

Charbonneau, P., Tomczyk, S., Schou, J., & Thompson, M. J. 1998, ApJ, 496, 1015

Chaturmutha, V., Fleck, B., & Jefferies, S. M. 2024, ApJ, 966, 200

Chen, P. F. 2011, Living Reviews in Solar Physics, 8, 1

Chiodini, A. 2025, Master's thesis, Tor Vergata Università degli studi di Roma

Choudhuri, A. R., Schussler, M., & Dikpati, M. 1995, A&A, 303, L29

Christensen-Dalsgaard, J. 2002, Reviews of Modern Physics, 74, 1073

Christensen-Dalsgaard, J. 2002, Rev. Mod. Phys., 74, 1073

——. 2021, Living Reviews in Solar Physics, 18, 2

Cicogna, D. et al. 2021, ApJ, 915, 38

Cimino, M., Cacciani, A., & Fofi, M. 1970, Solar Physics, 11, 319

Cimino, M., Cacciani, A., & Sopranzi, N. 1968, Sol. Phys., 3, 618

Cimino, M., Cacciani, A., & Sopranzi, N. 1968, Solar Physics, 3, 618

Cranmer, S. R. 2009, Living Reviews in Solar Physics, 6, 3

Cui, Y., Li, R., Zhang, L., He, Y., & Wang, H. 2006, Sol. Phys., 237, 45

de la Cruz Rodríguez, J., & Socas-Navarro, H. 2011, A&A, 527, L8

de la Cruz Rodríguez, J., & van Noort, M. 2017, Space Sci. Rev., 210, 109

De Pontieu, B. et al. 2022, The Astrophysical Journal, 926, 52

de Toma, G., Holzer, T. E., Burkepile, J. T., & Gilbert, H. R. 2005, ApJ, 621, 1109

Domingo, V., Fleck, B., & Poland, A. I. 1995, Sol. Phys., 162, 1

Duda, R. O., & Hart, P. E. 1972, Communications of the ACM, 15, 11

Duvall, T. L., J., & Harvey, J. W. 1983, Nature, 302, 24

Duvall, T. L., J., Jefferies, S. M., Harvey, J. W., & Pomerantz, M. A. 1993, Nature, 362, 430

Dwivedi, B. N. 2003, Dynamic sun (Cambridge University Press), n/a

Elsworth, Y., Broomhall, A.-M., Gosain, S., Roth, M., Jefferies, S. M., & Hill, F. 2015, Space Sci. Rev., 196, 137

Erdélyi, R. et al. 2022, Journal of Space Weather and Space Climate, 12, 2

Falkenberg, T. V., Vršnak, B., Taktakishvili, A., Odstrcil, D., MacNeice, P., & Hesse, M. 2010, Space Weather, 8, S06004

Faraday, M. 1846, Philosophical Transactions of the Royal Society of London, 136, 1

Finn, G. D., & Mugglestone, D. 1965, MNRAS, 129, 221

Finsterle, W., Jefferies, S. M., Cacciani, A., Rapex, P., Giebink, C., Knox, A., & Dimartino, V. 2004a, Solar Physics, 220, 317

——. 2004b, Sol. Phys., 220, 317

Finsterle, W., Jefferies, S. M., Cacciani, A., Rapex, P., & McIntosh, S. W. 2004c, ApJ, 613, L185

Formicola, I., Longobardo, A., Pinto, C., & Cerulo, P. 2007, Measure of Solar oscillations and supergranulation with Magnetic-Optical Filter

Forte, R. et al. 2020, Journal of Space Weather and Space Climate, 10, 63

Fossat, E. et al. 1992, A&A, 266, 532

Fresnel, A.-J., & Putland, G. R. t. 2021, Memoir on the double refraction that light rays undergo in traversing the needles of quartz in the directions parallel to the axis

Fröhlich, C. 2002, Advances in Space Research, 29, 1409

Gallagher, P. T., Moon, Y.-J., & Wang, H. 2002, Sol. Phys., 209, 171

Gary, G. A. 2001, Solar Physics, 203, 71

Georgoulis, M. K. 2012, in Astrophysics and Space Science Proceedings, Vol. 30, The Sun: New Challenges, ed. V. N. Obridko, K. Georgieva, & Y. A. Nagovitsyn, 93

Giovannelli, L. et al. 2020a, Journal of Space Weather and Space Climate, 10, 58

——. 2020b, Journal of Space Weather and Space Climate, 10, 58

Gizon, L., & Birch, A. C. 2005, Living Reviews in Solar Physics, 2, 6

Glover, A., Daly, E., Hilgers, A., & Berghmans, D. 2002, European Review, 10, 249

Goldberg, L. 1939, ApJ, 89, 673

González Hernández, J. I. et al. 2020, A&A, 643, A146

Goodwin, G. T., Sadykov, V. M., & Martens, P. C. 2024, ApJ, 964, 163

Gough, D. O. et al. 1996, Science, 272, 1296

Gulledge, D. J. 2022, PhD thesis, Georgia State University

Haberreiter, M., Schmutz, W., & Kosovichev, A. 2008, The Astrophysical Journal, 675, L53

Hale, G. E. 1922, MNRAS, 82, 168

Hale, G. E., Ellerman, F., Nicholson, S. B., & Joy, A. H. 1919, ApJ, 49, 153

Hamilton, J., Sadykov, V. M., Kitiashvili, I., & Wray, A. A. 2024, in AGU Fall Meeting Abstracts, Vol. 2024, AGU Fall Meeting Abstracts, SH21G–2917

Hannah, I. G., Hudson, H. S., Battaglia, M., Christe, S., Kašparová, J., Krucker, S., Kundu, M. R., & Veronig, A. 2011, Space Sci. Rev., 159, 263

Harvey, J. W. et al. 1996, Science, 272, 1284

Hathaway, D. H. 2015, Living reviews in solar physics, 12, 4

Henney, C. J., MacKenzie, D., Hill, F., Mills, B., & Pietrzak, J. 2011, in AAS/Solar Physics Division Meeting, Vol. 42, AAS/Solar Physics Division Abstracts #42, 22.33

Hill, F. 1989, ApJ, 343, L69

Hölken, J., Doerr, H.-P., Feller, A., & Iglesias, F. A. 2024, A&A, 687, A22

Huang, Z., Tóth, G., Sachdeva, N., & van der Holst, B. 2024, ApJ, 965, 1

Hubeny, I., & Mihalas, D. 2014, Theory of Stellar Atmospheres: An Introduction to Astrophysical Non-equilibrium Quantitative Spectroscopic Analysis, Princeton Series in Astrophysics (Princeton, NJ: Princeton University Press), 944

Ireland, J., Young, C. A., McAteer, R. T. J., Whelan, C., Hewett, R. J., & Gallagher, P. T. 2008, Sol. Phys., 252, 121

Jefferies, S. M., Armstrong, J. D., Cacciani, A., Giebink, C. A., Rodgers, W., & Murphy, N. 2005, in AGU Spring Meeting Abstracts, Vol. 2005, SH13C–12

Jefferies, S. M., Fleck, B., Murphy, N., & Berrilli, F. 2019, ApJ, 884, L8

Jefferies, S. M., McIntosh, S. W., Armstrong, J. D., Bogdan, T. J., Cacciani, A. r., & Fleck, B. 2006, ApJ, 648, L151

Jing, J., Tan, C., Yuan, Y., Wang, B., Wiegelmann, T., Xu, Y., & Wang, H. 2010, ApJ, 713, 440

Keller, C. U., Harvey, J. W., & Giampapa, M. S. 2003, in Society of Photo-Optical Instrumentation Engineers (SPIE) Conference Series, Vol. 4853, Innovative Telescopes and Instrumentation for Solar Astrophysics, ed. S. L. Keil & S. V. Avakyan, 194–204

Keller, C. U., Harvey, J. W., & Giampapa, M. S. 2003, in Innovative telescopes and instrumentation for solar astrophysics, Vol. 4853, SPIE, 194–204

Keller, C. U., Schüssler, M., Vögler, A., & Zakharov, V. 2004, ApJ, 607, L59

Kiepenheuer, K. O. 1953, in The Sun, ed. G. P. Kuiper, 322

Klein, K. G. et al. 2023, Space Sci. Rev., 219, 74

Klimchuk, J. A. 2006, Sol. Phys., 234, 41

Klimchuk, J. A. 2015, Philosophical Transactions of the Royal Society A: Mathematical, Physical and Engineering Sciences, 373, 20140256

Konow, F. et al. 2024, in Ground-based and Airborne Instrumentation for Astronomy X, Vol. 13096, SPIE, 3007–3016

Korsós, M. B., Ludmány, A., Erdélyi, R., & Baranyi, T. 2015, ApJ, 802, L21

Kosovichev, A., & Sadykov, V. 2023, Proceedings of the International Astronomical Union, 19, 275, publisher Copyright: © The Author(s), 2024.

Kramida, A., Yu. Ralchenko, Reader, J., & and NIST ASD Team. 2024, NIST Atomic

Spectra Database (ver. 5.12), [Online]. Available: https://physics.nist.gov/asd [2026, January 16]. National Institute of Standards and Technology, Gaithersburg, MD.

Krivova, N. A., Solanki, S. K., Fligge, M., & Unruh, Y. C. 2003, A&A, 399, L1

Kuckein, C. et al. 2025, A&A, 699, A121

Kuckein, C., Collados, M., Sainz, R. M., & Ramos, A. A. 2015, in IAU Symposium, Vol. 305, Polarimetry, ed. K. N. Nagendra, S. Bagnulo, R. Centeno, & M. Jesús Martínez González, 73–78

Kuckein, C., González Manrique, S. J., Kleint, L., & Asensio Ramos, A. 2020, A&A, 640, A71

Kuhn, J. R., Arnaud, J., Jaeggli, S., Lin, H., & Moise, E. 2007, ApJ, 667, L203

Kuhn, J. R., Lin, H., & Loranz, D. 1991, PASP, 103, 1097

Künzel, H. 1960, Astronomische Nachrichten, 285, 271

Kurokawa, H. 1989, Space Sci. Rev., 51, 49

Landeros, J. A., Kirk, M. S., Arge, C. N., Boucheron, L. E., Zhang, J., Uritsky, V. M., Grajeda, J. A., & Dupertuis, M. 2025, Sol. Phys., 300, 10

Lawrence, J. S., Ashley, M. C. B., Tokovinin, A., & Travouillon, T. 2004, Nature, 431, 278

Leenaarts, J., Carlsson, M., & Van Der Voort, L. R. 2012, The Astrophysical Journal, 749, 136

Leenaarts, J. et al. 2025, A&A, 696, A3

Leighton, R. B. 1969, ApJ, 156, 1

Libbrecht, T. 2019, PhD thesis, Stockholm University

Libbrecht, T., Bjørgen, J. P., Leenaarts, J., de la Cruz Rodríguez, J., Hansteen, V., & Joshi, J. 2021a, A&A, 652, A146

——. 2021b, A&A, 652, A146

Libbrecht, T., de la Cruz Rodríguez, J., Danilovic, S., Leenaarts, J., & Pazira, H. 2019, A&A, 621, A35

Lide, D. R., ed. 2004, CRC Handbook of Chemistry and Physics: A Ready-Reference of Chemical and Physical Data, 85th edn. (Boca Raton, FL, USA: CRC Press), 2712

Lites, B. W., Keil, S. L., Scharmer, G. B., & Wyller, A. A. 1985, Sol. Phys., 97, 35

Lockyer, J. N. 1868, Proceedings of the Royal Society of London Series I, 17, 131

Macaluso, D., & Corbino, O. M. 1898, Il Nuovo Cimento, 8, 257

MacQueen, R. M., Blankner, J. G., Elmore, D. F., Lecinski, A. R., & White, O. R. 1998, Sol. Phys., 182, 97

Magrì, M., Oliviero, M., & Severino, G. 2008, Solar Physics, 247, 15

McIntosh, P. S. 1990, Sol. Phys., 125, 251

Meadowlark Optics, I. 2019, High Speed Liquid Crystal Variable Retarder Specifications, Technical product data sheet, typical LC rise time 50 µs and fall time 500 µs at 532 nm, sub-millisecond performance

Meredith, R. 2022, Scientific American

Merenda, L., Lagg, A., & Solanki, S. K. 2011, A&A, 532, A63

Moise, E., Raymond, J., & Kuhn, J. R. 2010, ApJ, 722, 1411

Molnar, M. E., Casini, R., Bryans, P., Berkey, B., & Tyson, K. 2025, Sol. Phys., 300, 88

Moretti, P., Berrilli, F., Bigazzi, A., Jefferies, S., Murphy, N., Roselli, L., & Di Mauro, M. 2010, Astrophysics and Space Science, 328, 313

Moretti, P. F., Cacciani, A., Hanslmeier, A., Messerotti, M., Oliviero, M., Otruba, W., Severino, G., & Warmuth, A. 2001, A&A, 372, 1038

Moretti, P. F. et al. 1997, in Astrophysics and Space Science Library, Vol. 225, SCORe'96 : Solar Convection and Oscillations and their Relationship, ed. F. P. Pijpers, J. Christensen-Dalsgaard, & C. S. Rosenthal, 293–296

Müller, D., Marsden, R. G., St. Cyr, O. C., & Gilbert, H. R. 2013, Sol. Phys., 285, 25

Müller, D. et al. 2020, A&A, 642, A1

Murphy, N., Jefferies, S., Fleck, B., Berrilli, F., Velli, M., Lightsey, E. G., Gizon, L., & Braun, D. 2017, Solar Activity Investigation (SAI): A 6U CubeSat Mission Concept, Research publication, Georgia Institute of Technology, gT Digital Repository

Murphy, N., Smith, E., Rodgers, W., & Jefferies, S. 2005, in ESA Special Publication, Vol. 592, Solar Wind 11/SOHO 16, Connecting Sun and Heliosphere, ed. B. Fleck, T. H. Zurbuchen, & H. Lacoste, 511

Öhman, Y. 1960, Scientia, 54, 142

Oliviero, M., Dolci, M., Severino, G., Straus, T., Cacciani, A., & Moretti, P. F. 1998, in IAU Symposium, Vol. 185, New Eyes to See Inside the Sun and Stars, ed. F.-L. Deubner, J. Christensen-Dalsgaard, & D. Kurtz, 53

Oliviero, M., Severino, G., Berrilli, F., Moretti, P., & Jefferies, S. 2011, in Solar Physics and Space Weather Instrumentation IV, Vol. 8148, SPIE, 305–316

Oliviero, M., Severino, G., & Esposito, G. 2010, Astrophysics and Space Science, 328, 325

Osterbrock, D. E. 1961, ApJ, 134, 347

Parenti, S. 2014, Living Reviews in Solar Physics, 11, 1

Parker, E. N. 1988, ApJ, 330, 474

Parnell, C. E., & De Moortel, I. 2012, Philosophical Transactions of the Royal Society A: Mathematical, Physical and Engineering Sciences, 370, 3217

Pellizzoni, A. et al. 2024, in Society of Photo-Optical Instrumentation Engineers (SPIE) Conference Series, Vol. 13094, Ground-based and Airborne Telescopes X, ed. H. K. Marshall, J. Spyromilio, & T. Usuda, 130941R

Pesnell, W. D., Thompson, B. J., & Chamberlin, P. 2012, in The solar dynamics observatory (Springer), 3–15

Peter, H. et al. 2021, Experimental Astronomy, 54

Petrie, G. J. D., & Patrikeeva, I. 2009, ApJ, 699, 871

Pevtsov, A. A., Martinez Pillet, V., Warner, M., Gosain, S., & Bertello, L. 2024, in Society of Photo-Optical Instrumentation Engineers (SPIE) Conference Series, Vol. 13096, Ground-based and Airborne Instrumentation for Astronomy X, ed. J. J. Bryant, K. Motohara, & J. R. D. Vernet, 1309618

Piazzesi, R., Berrilli, F., Del Moro, D., & Egidi, A. 2012, Memorie della Societa Astronomica Italiana Supplement, v. 19, p. 109 (2012), 19, 109

Pietarila, A., Hirzberger, J., Zakharov, V., & Solanki, S. K. 2009, A&A, 502, 647

Pomerantz, M., Wyller, A., & Kusoffsky, U. 1981, in Solar instrumentation: What's next?,

ed. R. B. Dunn, 379

Pötzi, W., Veronig, A., & Temmer, M. 2018, Solar Physics, 293, 94

Pötzi, W., Veronig, A. M., Riegler, G., Amerstorfer, U., Pock, T., Temmer, M., Polanec, W., & Baumgartner, D. J. 2015, Solar physics, 290, 951

Rajaguru, S. P., Couvidat, S., Sun, X., Hayashi, K., & Schunker, H. 2013, Sol. Phys., 287, 107

Reale, F. 2010, Living Reviews in Solar Physics, 7, 5

Reames, D. V. 2013, Space Sci. Rev., 175, 53

Rhodes, Edward J., J., Cacciani, A., Garneau, G., Misch, T., Progovac, D., Shieber, T., Tomczyk, S., & Ulrich, R. K. 1988, in Flare Research at the Next Solar Maximum: Workshop 1: Scientific Objectives, NASA Goddard Space Flight Center, nASA Technical Reports Server, Document ID 19890006485

Rhodes Jr, E. J., Cacciani, A., Garneau, G., Misch, T., Progovac, D., Shieber, T., Tomczyk, S., & Ulrich, R. K. 1988, in NASA, Goddard Space Flight Center, Max 1991: Flare Research at the Next Solar Maximum. Workshop 1: Scientific Objectives, n/a

Rhodes Jr, E. J., Cacciani, A., Tomczyk, S., Ulrich, R. K., Blamont, J., Howard, R. F., Dumont, P., & Smith, E. J. 1984, Advances in Space Research, 4, 103

Righi, A. 1906, Il Nuovo Cimento, 12, 247

Riley, P. et al. 2014, Sol. Phys., 289, 769

Rimmele, T. R. et al. 2020, Sol. Phys., 295, 172

Rochus, P. et al. 2020, A&A, 642, A8

Rodgers, W., Murphy, N., & Jefferies, S. M. 2005, in AGU Spring Meeting Abstracts, Vol. 2005, SH13C–13

Rosenthal, C. S. et al. 2002, ApJ, 564, 508

Sakurai, T., Tanaka, K., Miyazaki, H., Ichimoto, K., Sakata, A., & Wada, S. 1990, in Progress of Seismology of the Sun and Stars, ed. Y. Osaki & H. Shibahashi, Vol. 367, 277

Santamarina Guerrero, P., Orozco Suárez, D., Bailén, F. J., & Blanco Rodríguez, J. 2024, A&A, 688, A67

Sargsyan, A., Hakhumyan, G., Leroy, C., Pashayan-Leroy, Y., Papoyan, A., Sarkisyan, D., & Auzinsh, M. 2014, Journal of the Optical Society of America B Optical Physics, 31, 1046

Schrijver, C. J. 2007, ApJ, 655, L117

Schrijver, C. J., & Zwaan, C. 2008, Solar and Stellar Magnetic Activity

Schwenn, R. 2006, Living Reviews in Solar Physics, 3, 2

Shaw, C. L., Gulledge, D. J., Swindle, R., Jefferies, S. M., & Murphy, N. 2022, Frontiers in Astronomy and Space Sciences, 9, 768452

Shibata, K. et al. 2007, Science, 318, 1591

Singh, K. A. P., Nishida, K., & Shibata, K. 2024, ApJ, 962, L35

Skumanich, A., Lites, B. W., & Martínez Pillet, V. 1994, in NATO Advanced Study Institute (ASI) Series C, Vol. 433, Solar Surface Magnetism, ed. R. J. Rutten & C. J. Schrijver, 99

Sobotka, M., Vázquez, M., Bonet, J. A., Hanslmeier, A., & Hirzberger, J. 1999, ApJ, 511, 436

Solanki, S. K., Inhester, B., & Schüssler, M. 2006, Reports on Progress in Physics, 69, 563

Speziali, R. et al. 2021, Journal of Space Weather and Space Climate, 11, 22

Spiegel, E. A., & Zahn, J.-P. 1992, A&A, 265, 106

Stahl, H. P., & Allison, M. 2020, in Society of Photo-Optical Instrumentation Engineers (SPIE) Conference Series, Vol. 11450, Modeling, Systems Engineering, and Project Management for Astronomy IX, ed. G. Z. Angeli & P. Dierickx, 114500Z

Stangalini, M., Moretti, P. F., Berrilli, F., Del Moro, D., Jefferies, S. M., Severino, G., & Oliviero, M. 2011, in Society of Photo-Optical Instrumentation Engineers (SPIE) Conference Series, Vol. 8148, Solar Physics and Space Weather Instrumentation IV, ed. S. Fineschi & J. Fennelly, 81480U

Stangalini, M., Piazzesi, R., Speziali, R., & Dal Sasso, L. 2018, in Ground-based and Airborne Telescopes VII, Vol. 10700, SPIE, 467–473

Stebbins, R., & Wilson, C. 1983, Sol. Phys., 82, 43

Steck, D. A. 2000, Sodium D Line Data, `https://steck.us/alkalidata/sodiumnumbers.pdf`, revision 1.6 (14 October 2003), originally posted 27 May 2000

Straus, T., Fleck, B., Jefferies, S. M., Cauzzi, G., McIntosh, S. W., Reardon, K., Severino, G., & Steffen, M. 2008, ApJ, 681, L125

Straus, T., Fleck, B., Jefferies, S. M., McIntosh, S. W., Severino, G., Steffen, M., & Tarbell, T. D. 2009, in Astronomical Society of the Pacific Conference Series, Vol. 415, The Second Hinode Science Meeting: Beyond Discovery-Toward Understanding, ed. B. Lites, M. Cheung, T. Magara, J. Mariska, & K. Reeves, 95

Su, J. T., Jing, J., Wang, S., Wiegelmann, T., & Wang, H. M. 2014, The Astrophysical Journal, 788, 150

Temmer, M. 2021, Living Reviews in Solar Physics, 18, 4

Temmer, M., Veronig, A., Hanslmeier, A., Otruba, W., & Messerotti, M. 2001, A&A, 375, 1049

Thomas, J. 1999, in Astronomical Society of the Pacific Conference Series, Vol. 183, High Resolution Solar Physics: Theory, Observations, and Techniques, ed. T. R. Rimmele, K. S. Balasubramaniam, & R. R. Radick, 1

Tiecke, T. G. 2019, Properties of Potassium, `https://tobiastiecke.nl/archive/PotassiumProperties.pdf`, version 1.03, June 2019, unpublished atomic physics reference document

Tomczyk, S., McIntosh, S. W., Keil, S. L., Judge, P. G., Schad, T., Seeley, D. H., & Edmondson, J. 2007, Science, 317, 1192

Tomczyk, S., Streander, K., Card, G., Elmore, D., Hull, H., & Cacciani, A. 1995, Sol. Phys., 159, 1

Tyson, J. A. 1986, Journal of the Optical Society of America A, 3, 2131

Usoskin, I. G. 2017, Living Reviews in Solar Physics, 14, 3

van Driel-Gesztelyi, L., & Green, L. M. 2015, Living Reviews in Solar Physics, 12, 1

Vernazza, J. E., Avrett, E. H., & Loeser, R. 1981, Astrophysical Journal Supplement Series, vol. 45, Apr. 1981, p. 635-725., 45, 635

Viavattene, G., Calchetti, D., Berrilli, F., Del Moro, D., Giovannelli, L., Pietropaolo, E.,

Oliviero, M., & Terranegra, L. 2020, arXiv e-prints, arXiv:2006.04921

Vogt, E., Oliviero, M., Severino, G., & Straus, T. 1999, in Magnetic Fields and Solar Processes, Vol. 448, 405

Vojna, D., Slezák, O., Lucianetti, A., & Mocek, T. 2019, Applied Sciences, 9, 3160

Welsch, B. T., Li, Y., Schuck, P. W., & Fisher, G. H. 2009, ApJ, 705, 821

Withbroe, G. L. 1983, ApJ, 267, 825

Yan, X.-L., Qu, Z.-Q., & Kong, D.-F. 2011, Monthly Notices of the Royal Astronomical Society, 414, 2803–2811

Youssef, M. 2012, NRIAG Journal of Astronomy and Geophysics, 1, 172

Zeeman, P. 1897, Nature, 55, 347

Zhang, H., & Bao, S. 1999, ApJ, 519, 876

Zirin, H. 1975, ApJ, 199, L63